Universidade de Aveiro Departamento de Química
2014

REDA MOHAMED ABDELHAMEED

Modificação pós-síntese de materiais híbridos metalo-orgânicos

Post-synthetic modification of metal–organic frameworks

Universidade de Aveiro Departamento de Química
2014

REDA MOHAMED ABDELHAMEED

Post-synthetic modification of metal–organic frameworks

Tese apresentada à Universidade de Aveiro para cumprimento dos requisitos necessários à obtenção do grau de Doutoramento em Química, realizada sob a orientação científica dos Doutores Joao Rocha e Artur M. S. Silva, ambos Professores Catedráticos do Departamento de Quimica da Universidade de Aveiro

Apoio financeiro do POPH – QREN.

Apoio financeiro da FCT e do FSE no âmbito do III Quadro Comunitário de Apoio.

As for the foam, it vanishes, [being] cast off; but as for that which benefits the people, it remains on the earth.

o júri/the jury

presidente / president

Prof. Doutor António Manuel Rosa Pereira Caetano
Professor Catedrático, Universidade de Aveiro

vogais / examiners committee

Prof. Doutor João Carlos Matias Celestino Gomes da Rocha
Professor Catedrático, Universidade de Aveiro (orientador)

Prof. Doutor Luís António Ferreira Martins Dias Carlos
Professor Catedrático, Universidade de Aveiro

Prof. Doutor Verónica de Zea Bermudez
Professora Catedrática da Universidade de Trás-os-Montes e Alto Douro

Prof. Doutor Susana Paula Graça Costa
Professora Auxiliar, Escola Ciências, Universidade do Minho

Prof. Doutor Ana Margarida Gomes da Silva
Investigador Auxiliar, Requimte, Faculdade de Ciências, Universidade do Porto

Agradecimentos/ acknowledgements

I thank my supervisors, Professor João Rocha and Professor Artur M. S. Silva, for offering me a Ph.D. opportunity and their confidence to join their research groups. I am deeply indebted to them for their excellent mentorship during the four years of my Ph.D. project; they have taught me how to develop new scientific thoughts, and to organize, write and present good scientific communications. I am grateful to them for respecting my ideas and choices in the development of my Ph.D. I also thank them for translating this thesis abstract into Portuguese.

I would like to thank Professor Luis D. Carlos, Drs. R. A. S. Ferreira and V. T. Freitas for their advice and assistance in the photoluminescence measurements. I wish to acknowledge the help provided by Prof. Pierre Rabu and also I would like to thank the Labex NIE, Strasbourg, France for granting aid and A. Derory for technical support in magnetic measurement. Assistance provided by Dr. Fa Nian Shi and Sérgio M. Santos was greatly appreciated. I would also like to extend my thanks to the staff and the technicians of the laboratory of the chemistry department for their help.

I thank: Fundação para a Ciência e a Tecnologia (FCT, Portugal) for awarding me a Ph.D. research grant (SFRH/BD/51269/2010)]; the European Union, QREN, FEDER, COMPETE, for funding the Organic Chemistry Research Unit (QOPNA) (project PEst-C/QUI/UI0062/2013) and the Laboratório Associado Centro de Investigação em Materiais Cerâmicos e Compósitos - CICECO (project PEst-C/CTM/LA0011/2013); and the Portuguese National NMR Network (RNRMN). I further acknowledge the COST Action MP1202. I would like to offer my special thanks to Dr. Oulid Talhi. Finally, I wish to thank my parents and my wife for their support and encouragement throughout my study.

palavras-chave

IRMOF-3; NH_2-MIL-125; Materiais híbridos metalo-orgânicos; Modificação pós-sintese; Emissores de radiação visível e do infravermelho próximo; Lantanídeos; Fotocatálise

resumo

A modificação pós-síntese de estruturas metalo-orgânicas compreendendo na transformação do ligando orgânico presente é uma nova e promissora via para a engenharia de centros ópticos, permitido sintonizar as propriedades de emissão de luz de materiais na região do visível e do infravermelho próximo. Nesta dissertação, procedeu-se à modificação pós-sintética da estrutura isorreticular metal-orgânica-3 (IRMOF-3) com 2-cloro-2-oxoacetato de etilo, acetoacetato de etilo, pentano-2,4-diona, 3-(2-hidroxifenil)-3-oxopropanal, ácido 2-cloroacético, ácido glioxílico, metilvinil cetona e (etoximetileno)malonato de dietilo, seguida da quelação com iões lantanídeos trivalentes, a qual originou interessantes emissores de luz na região do infravermelho próximo (Nd^{3+}) e do visível (Eu^{3+}, Tb^{3+}). O IRMOF-3 foi usado como um caso de estudo devido quer à sua a estrutura cristalina que apresenta considerável microporosidade, quer à presença de grupos amino livres no ligando benzenodicarboxilato (bdc), que são passíveis de modificação. Os materiais foram caracterizados por análise elementar, difracção de raios X de pós, microscopias óptica, electrónica de varrimento e de transmissão, espetroscopias de infravermelho com transformadas de Fourier e de ressonância magnética nuclear (estados líquido e sólido). As propriedades de luminescência dos materiais Ln-IRMOF-3-modificados foram estudadas à temperatura ambiente. A presença do anel aromático bdc, β-dicetonato e oxalato reforça a sensibilização do Ln^{3+} através da transferência de energia do ligando para o metal (efeito antena). No que respeita à fotocatálise, sintetizaram-se novos materiais metal-orgânicos (Cr-MIL-125-AC, Ag-MIL-125-AC) através de uma reação sólido-vapor. Estes materiais apresentam uma excelente atividade fotocatalítica para a degradação de azul de metileno até 6,52 vezes maior que o fotocatalisador comercial hombikat UV-100. Estes resultados abrem a porta a novos estudos que visam melhorar a actividade fotocatalítica de materiais metalo-orgânicos.

keywords

IRMOF-3; NH_2-MIL-125; Metal–organic frameworks; Post-synthetic modification; Near-infrared and visible light emitters; Lanthanides; Photocatalytic activity

abstract

Post-synthetic modification (PSM) of metal-organic frameworks encompassing the chemical transformation of the linker present is a promising new route for engineering optical centres and tuning the light emission properties of materials, both in the visible and in the near infrared (NIR) spectral regions. Here, PSM of isoreticular metal-organic framework-3 (IRMOF-3) with ethyl oxalyl monochloride, ethyl acetoacetate, pentane-2,4-dione, 3-(2-hydroxyphenyl)-3-oxopropanal, 2-chloroacetic acid, glyoxylic acid, methyl vinyl ketone and diethyl (ethoxymethylene)malonate followed by chelation of trivalent lanthanide ions afforded intriguing near infrared (Nd^{3+}) and visible (Eu^{3+}, Tb^{3+}) light emitters. IRMOF-3 was used as a case in point due to both its highly porous crystalline structure and the presence of non-coordinating amino groups on the benzenedicarboxylate (bdc) linker amenable to modification. The materials were characterised by elemental analysis, powder X-ray diffraction, optical, scanning and transmission electron microscopy, Fourier transform infrared spectroscopy, and liquid and solid-state nuclear magnetic resonance. The solid-state luminescence properties of Ln-modified-IRMOF-3 were investigated at room temperature. The presence of the bdc aromatic ring, β–diketonate and oxalate enhanced the Ln^{3+} sensitization via ligand-to-metal energy transfer (anthena effect). As far as photocalysis is concerned, we have synthesized metal−organic frameworks (Cr-MIL-125-AC, Ag-MIL-125-AC) by a green method (solid–vapors reactions). The resulting functionalized materials show a photocatalytic activity for methylene blue degradation up to 6.52 times larger than that of the commercial photocatalyst hombikat UV-100. These findings open the door for further research for improving the photocatalytic performance of metal-organic frameworks.

Table of Contents

Part I: General introduction

Part II: Synthesis and Post-Synthetic Modification

List of Figures

Abbreviations

bdc	benzene-1,3-dicaboxylate
BET	Brunauer, Emmet, Teller
btapa	1,3,5-benzene tricarboxylic acid tris[N-(4-pyridyl)amide
btb	4,4',4''-benzene-1,3,5-triyl-tribenzoate
btc	benzene-1,3,5-tricarboxylate
btt	benzene-1,3,5-tris(1H-tetrazole)
CMK	Carbon Meta structure at KAIST
COSY	Correlation Spectroscopy
d	doublet
DABCO	1,4-diAzabicyclo[2.2.2]octane
DFT	Density Functional Theory
DMF	dimethylformamide
DMOF	DABCO Metal-Organic Framework
EDS	Energy Dispersive Spectroscopy
GC	Gas Chromatography
HKUST	Hong-Kong University of Science and Technology
ICP	Inductively Coupled Plasma
IR	Infrared
IRMOF	IsoReticular Metal-Organic Framework
Ln	Lanthanide
Ln^{3+}	Trivalent lanthanide ion
m	multiplet
MAS	Magic Angle Spinning
MIL	Matériaux de l'Institut Lavoisier
MOF	Metal-Organic Framework
NMR	Nuclear Magnetic Resonance
PL	Photoluminescence
ppm	parts per million
PSM	post-synthetic modification

PXRD	Powder X-Ray Diffraction
s	singlet
SBU	Secondary Building Unit
SEM	Scanning Electron Microscopy
t	triplet
TEM	Transmission electron microscopy
TMS	trimethylsilane
$TMSN_3$	Trimethylsilyl azide
UiO	University of Oslo
UMCM-1	University of Michigan Crystalline Material-1
UV	Ultraviolet
UV-Vis-NIR	Ultraviolet-visible-near infrared
XRD	X-ray diffractogram
ZIF	Zeolitic Imidazolate Framework

Preface

This thesis describes the Ph.D. work I have carried out at the University of Aveiro, in the period September 2010 to September 2014, on the post-synthetic modification of metal-organic frameworks as a promising new route for engineering optical centres and tuning light emission and the photocatalytic properties of materials.

Metal-organic frameworks are hybrid materials consisting of organic linkers bridging metal clusters, having very high surface areas, in excess of 5000 m^2g^{-1}, and a variety of chemical functionalities. Metal-organic frameworks have potential applications in the absorption and separation of gas molecules (such as CO_2, N_2, CH_4, and H_2), microelectronics, sensing, ion conductivity, optics, pollutant sequestration, drug delivery, contrast agents, micromotors, bioreactors and catalysis.

An outstanding feature of nanoporous metal-organic frameworks is that the chemical makeup of the channel walls may be adjusted by post-synthetic modification of the organic linkers. In this way, new organic functionalities and metal cations may be introduced enabling or improving gas sorption, catalytic activity or light emission, among others. The challenges in the area encompass not only the development of new solids but also improvements in the formulation and processing of the materials, including tailoring the morphology and surface chemistry of the frameworks to fit the proposed applications. In this work, we have performed a series of post-synthetic modifications of amino-functionalized metal-organic frameworks and used a combination of X-ray diffraction, transmission electron microscopy, Fourier transform infrared spectroscopy, liquid and solid-state nuclear magnetic resonance, and elemental analysis in the characterization of the structure, morphology and composition of the final materials. Photoluminescence spectroscopy was used to characterize the light-emission properties.

The objectives of this PhD thesis are:

- Synthesis, characterization and post-synthetic modification of the channel walls of amino functionalized metal-organic frameworks (IRMOF-3 and NH_2-MIL-125);

- Use of the post-synthetic modified nanoporous metal-organic frameworks as suitable platforms for engineering light-emitting devices by chelating lanthanide (Ln^{3+}) centres;

- Study of the photoluminescence properties (*e.g.*, emission and excitation spectra, and excited-state lifetimes) and magnetic properties of Ln^{3+}-doped metal-organic frameworks;

- Study of the photocatalytic properties of Ag and Cr modified-NH_2-MIL-125.

This thesis is divided in four parts. The first part consists of two chapters providing general background information on metal-organic frameworks and their post-synthetic modification.

The second part describes the work I have performed on the synthesis and post-synthetic modification of IRMOF-3 and NH_2-MIL-125, encompassing two chapters. Chapter II.1 is devoted to the design of near-infrared and visible light emitters by post-synthetic modification of IRMOF-3. The amino group of this material was covalently modified with pentane-2,4-dione, 3-(2-hydroxyphenyl)-3-oxopropanal, ethyl oxalyl monochloride, 2-chloroacetic acid, glyoxylic acid, diethyl (ethoxymethylene)malonate, ethyl acetoacetate and methyl vinyl ketone (vapour) (Scheme 1), followed by the coordination to lanthanide ions (Eu^{3+}, Tb^{3+} and Nd^{3+}). The resultant materials are near-infrared and visible light-emitters, whose photoluminescence properties were studied in collaboration with the group of Prof. Luís Carlos (Physics Department). The magnetic properties of some modified Ln^{3+}-IRMOF-3 were studied in collaboration with the group of Prof. Pierre Rabu (Institut de Physique et Chimie des Matériaux de Strasbourg, Université de Strasbourg, France). In chapter II.2, I show that post-synthetic modification may be used to enhance the photocatalytic activity of MIL-125 by doping with Cr^{3+} ions (hole acceptors) and Ag nanoparticles (electron acceptors) (Scheme 2).

The third part describes in detail the experimental procedures and methods used, including the description of the synthesis and post-synthetic modification of IRMOF-3 and NH_2-MIL-125 and their structure characterization**.**

The thesis draws to an end with some general conclusions and outlook for the future. A considerable amount of supporting information for the second-part chapters is presented in extensive annexes.

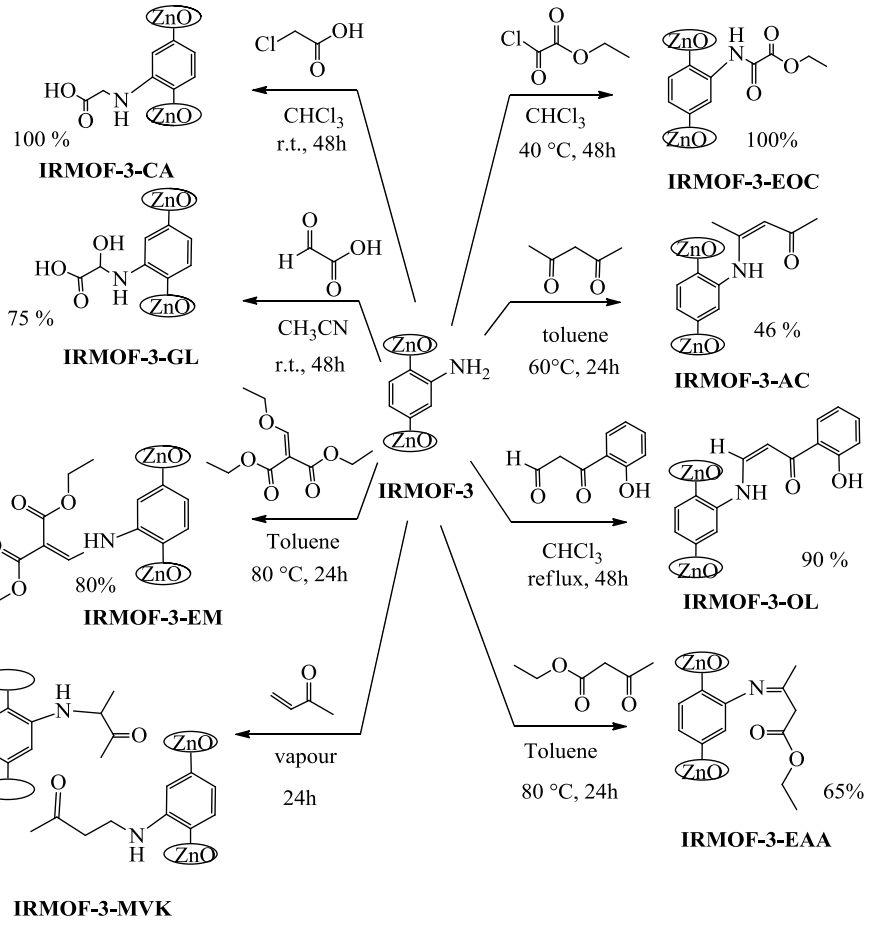

Scheme 1. Post-synthetic modifications of IRMOF-3.

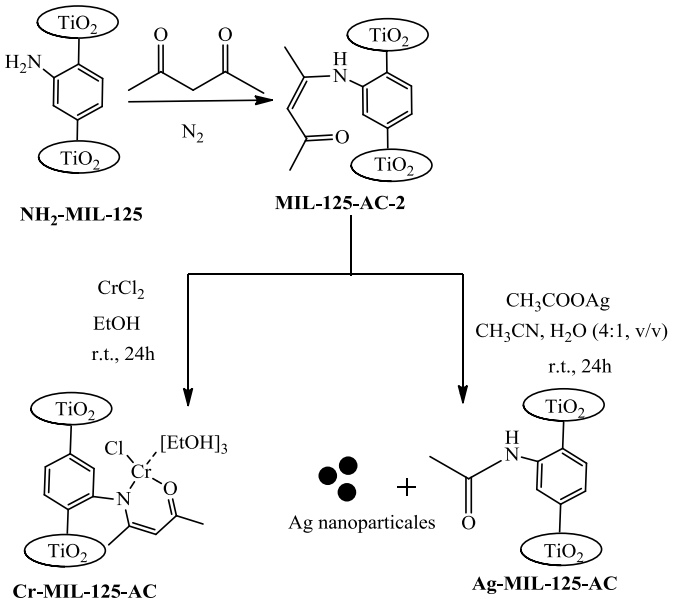

Scheme 2. Post-synthetic covalent modification of NH_2-MIL-125 with acetylacetone vapour followed by coordination to chromium or doping with Ag nanoparticles.

Chapter I.1: Metal-organic frameworks [MOFs]

- Terminology, Synthesis, and properties of MOFs
- Applications
  1- Biological applications.
  2- Gas Storage and Separation.
  3- Catalysis.
- References

Terminology, Synthesis, and properties of MOFs

Metal–organic frameworks or porous coordination polymers (PCP) are crystalline compounds consisting of metal ions linked by organic molecules to form one-, two-, or three-dimensional structures (Figure I.1.1).[1]

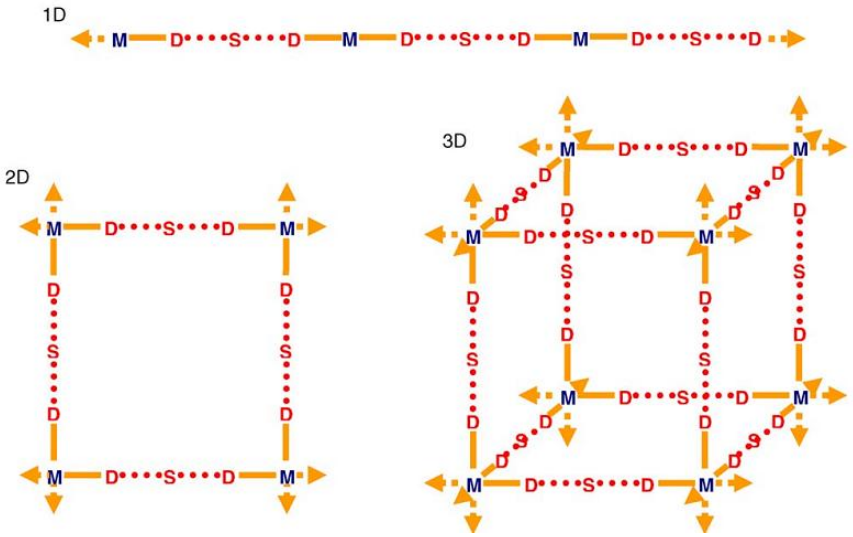

Figure I.1.1. Dimensionality of MOFs structures (M, metal ions; D, donor groups of the ligand; S, spacer within the ligand.

The first important aspect to be considered in the design of MOFs is the secondary building unit (SBU), a small unit constructed from one or more metal ions and the donor atoms of multidentate linkers, creating rigid entities repeated throughout the whole network. Figure I.1.2 shows some examples of SBUs that are commonly encountered in metal carboxylate MOFs. SBUs are not introduced directly, but are formed *in situ* under specific synthetic conditions.[1]

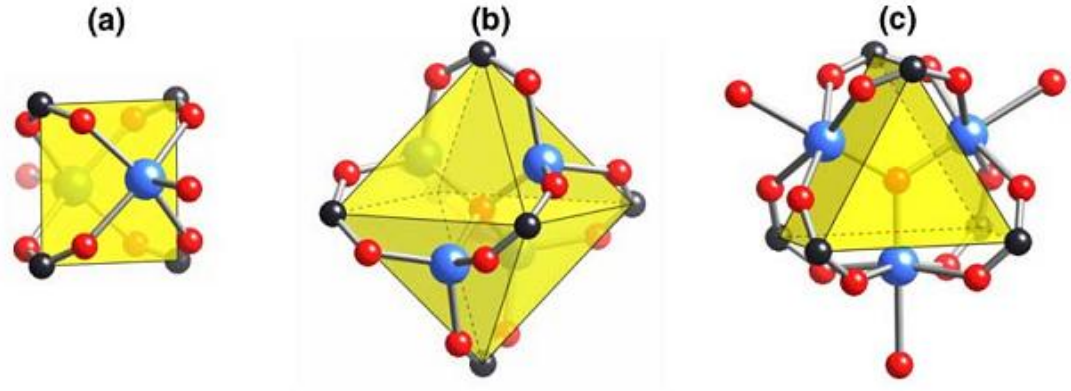

Figure I.1.2 SBUs: [a] the square ‘‘paddlewheel’’, with two terminal ligand sites, [b] the octahedral ‘‘basic zinc acetate’’ cluster, and [c] the trigonal prismatic oxo-centered trimer, with three terminal ligand sites.[1]

The second important aspect is the organic ligands; so far, the most commonly used linkers are aromatic carboxylates because they have rigid organic skeleton and strong coordination ability toward many metals. Figure I.1.3 shows some organic ligands based on carboxylic acids, phosphonic acid, *N*-heterocyclic and mixed functional groups.[2-3]

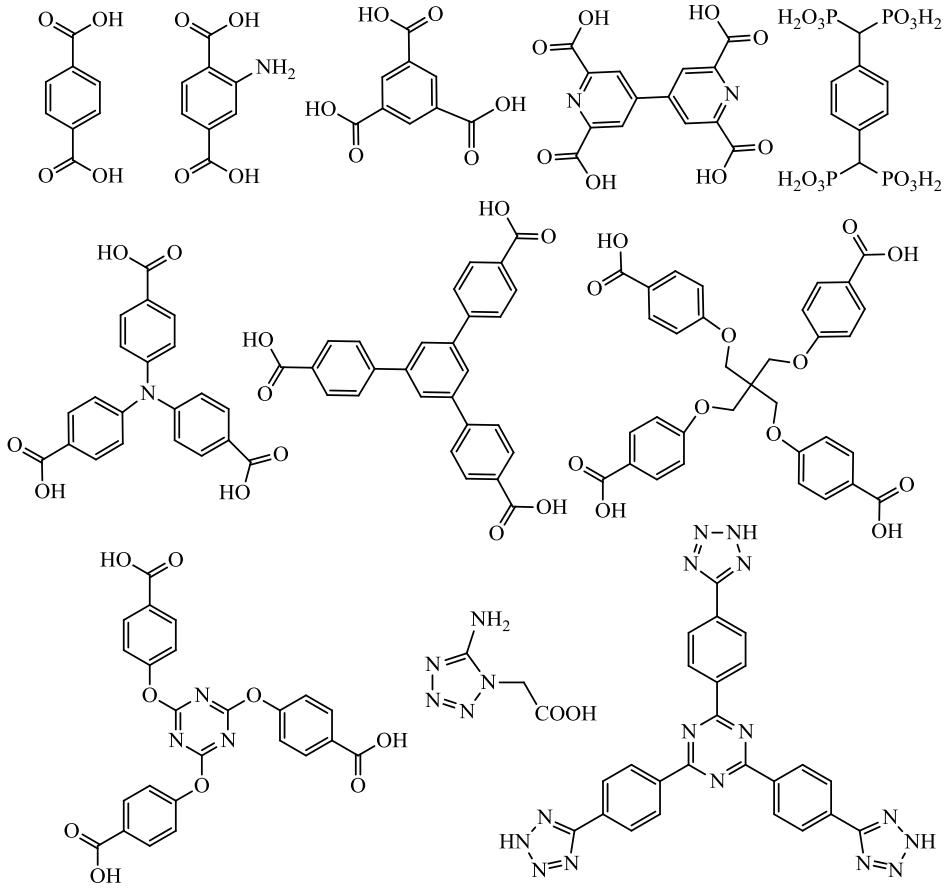

Figure I.1.3. Some selected ligands used in the preparation of MOFs.

Many MOFs synthesis methods have been proposed, such as solvothermal, hydrothermal, microwave, sonochemical and mechanochemical methods.[4] Solvothermal synthesis is a method of producing MOFs by heating a mixture of a ligand and a metal salt in a solvent leading to the production of high quality crystals. The most used solvents in these syntheses are diethylformamide (DEF) and dimethylformamide (DMF). Hydrothermal synthesis uses water as the reaction medium and occurs under high pressure on steel pressure vessels called autoclaves. The advantage of the hydrothermal method is producing stable MOFs with good-quality crystal growth. The disadvantages of this method include the need of expensive autoclaves and the impossibility of observing the crystal as it grows. Microwave heating is used to accelerate the rate of chemical reactions.

Ni and Masel were the first to synthesize MOFs via microwave irradiation.[5a] They produced IRMOF-1 (MOF-5), −2, and –3 in very short reaction times in the form of microcrystalline products. The sonochemical method consists on the application of ultrasounds to prompt chemical reactions and processes. MOF-5 crystals were prepared for the first time using a sonochemical method. The reaction time for MOF-5 was substantially reduced and significantly smaller crystals were obtained. Their physicochemical properties were similar to the crystals prepared under conventional convective heating. Sonochemical synthesis of MOF-5 has many benefits, the equipment is cheaper than a microwave unit, the energy consumption is low since no induction period is needed before sonicator stabilization, and the reaction time is very short. Successful implementation of the economic 1-methyl-2-pyrrolidone (NMP) as the solvent for the synthesis MOF-5 instead of DEF was an added advantage of this solvothermal synthesis, which can be beneficial for large scale production. Mechanochemistry offers a solvent-free access for the preparation of MOFs. For industrial MOFs production, electrochemical synthesis can be used. The principle of MOFs electrochemical synthesis relies on providing the metal ion by anodic dissolution into synthesis mixtures that include organic linkers and electrolytes.[5b]

MOFs have many advantages for gas storage and catalysis applications[6] like its high surface areas (in excess of 5000 m^2 g^{-1}), accessible permanent porosities, tunable structures, and high chemical and/or thermal stability. Moreover, they have ultrahigh porosity and high thermal and chemical stability. They can be synthesized into a wide variety of structures with a wide range of pore sizes. They can be synthesized to be superhydrophobic.

Applications

1- Biological applications.

MOFs as Drug Delivery Vehicles: This field of research is still very new. MOFs were used for drug delivery due to the functional groups and pores in the frameworks. Figure I.1.4 shows the mechanism of drug loading into MOFs and its slow release. MIL is used as drug delivery agent because it has a pore size of 25-34 Å and surface areas of 3100-5900 m^2/g and possibility of functionalization. Horcajada *et al.*[7,8] found that MIL-100 could uptake 0.35 g of ibuprofen/g of dehydrated MIL-100, whereas MIL-101 could uptake 1.4 g of ibuprofen/g of dehydrated MIL-101.

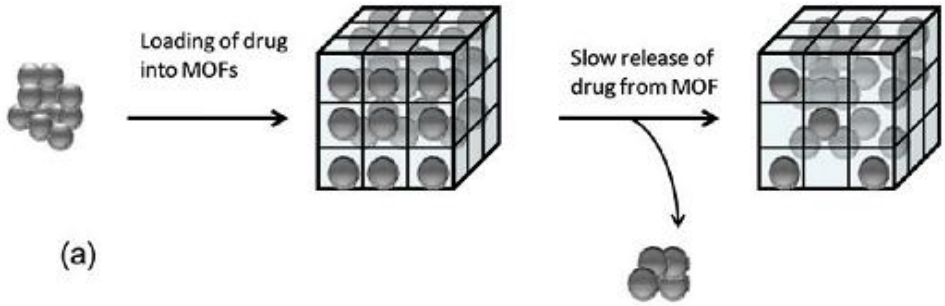

Figure I.1.4. Generalized scheme for the use of MOFs as drug delivery vehicles.

MOFs for NO storage: MOFs play an important role in storage of nitric oxide (NO), which has application in medicine. Figure I.1.5 shows the difference between MOFs in adsorption of NO. Al-MIL-53 and Cr-MIL-53 do not possess open metal sites in their structure and they adsorb small amounts of NO at room temperature compared to CPO-27-Co, CPO-27-Ni, and HKUST-1.

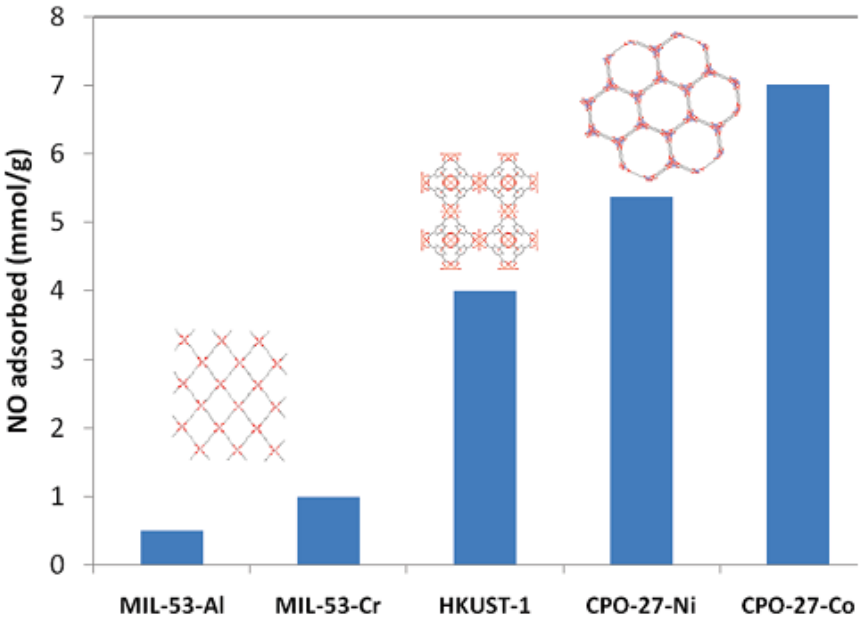

Figure I.1.5. Amounts of NO adsorbed by different MOFs at room temperature at 1 bar pressure.[9-11]

MOFs as potential imaging agents: Iron-based MOFs have a potential application as magnetic resonance imaging (contrast) agents. Horcajada *et al.*[12] studied the *in vitro* cytotoxicity of MOFs using an MTT assay, which showed comparable results with that of the currently available nanoparticulate systems. Figure I.1.6 shows that the treated organs appeared darker than the untreated controls.

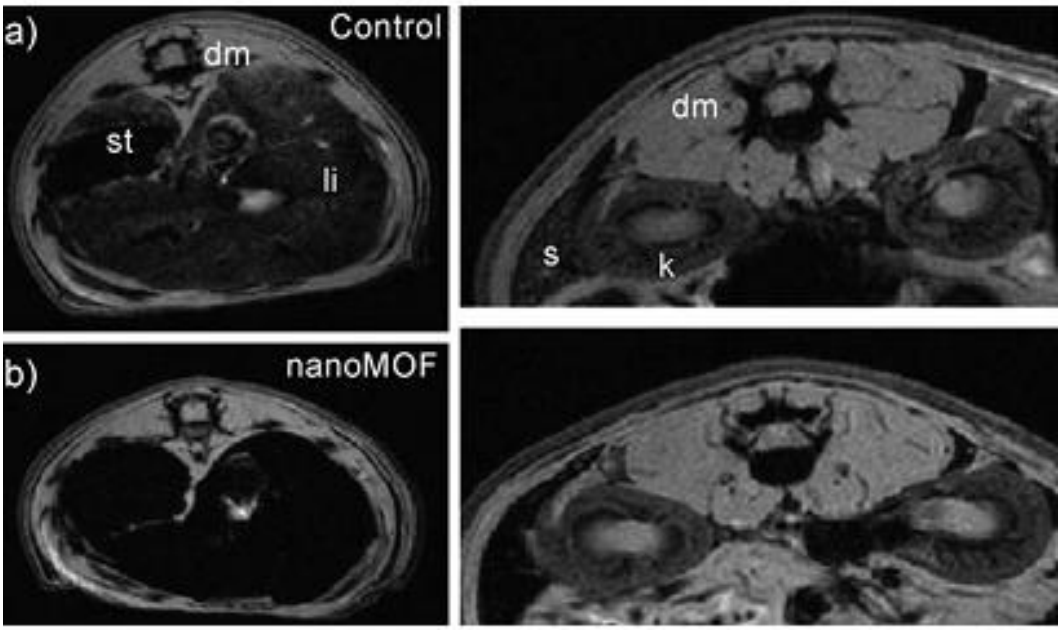

Figure I.1.6. Magnetic resonance images after exposure of rats to iron based MOFs, acquired with a gradient echo sequence for [a] control rats, and [b] rats injected with 220 mg kg^{-1} in liver (left) and spleen (right) regions (dm: dorsal muscle; k: kidney, li: liver; s: spleen; st: stomach).[12]

2- Gas Storage and separation

Due to high surface areas, vacant coordination sites on metal ions, and strong surface dipole moments of MOFs, they can be used as gas adsorbents. For example, Yaghi *et al.*[13] studied six MOFs (MOF-5, IRMOF-3, MOF-74, MOF-177, MOF-199, and IRMOF-62) as selective adsorbents for eight harmful gases: sulfur dioxide, ammonia, chlorine, tetrahydrothiophene, benzene, dichloromethane, ethylene oxide, and carbon monoxide. The results showed that pore functionality plays a dominant role in determining the dynamic adsorption performance of MOFs.

$Zn(bdc)(4,4'\text{-Bipy})_{0.5}$ (MOF-508; bdc = 1,4-benzenedicarboxylic acid, 4,4'-Bipy = 4,4'-bipyridine) was prepared by the solvothermal reaction of H_2bdc, 4,4'-Bipy, and $Zn(NO_3)_2$ and H_2O in DMF/ethanol at 90°C for 24 h. MOF-508 has an interpenetrated 3D pillared-layer structure with 1D open channels. MOF-508 was tested for the chromatographic separation of natural gas. A chromatographic column of 120 cm was packed with single crystals of MOF-508 with sizes of 25–100 mm (3 g) under 60 psi of pressure with helium as the carrier gas over the temperature range of 40–150°C. Four experiments were done, separation of: a) n-pentane and n-hexane, b) 2-methylbutane and n-pentane, c) 2,2-dimethylbutane, 2-methylpentane, and n-hexane, and d) an alkane mixture containing 2-

methylbutane (1), n-pentane (2), 2,2-dimethylbutane (3), 2-methylpentane (4), and n-hexane (5) (Figure I.1.7). The study results showed good GC separation capability. [14]

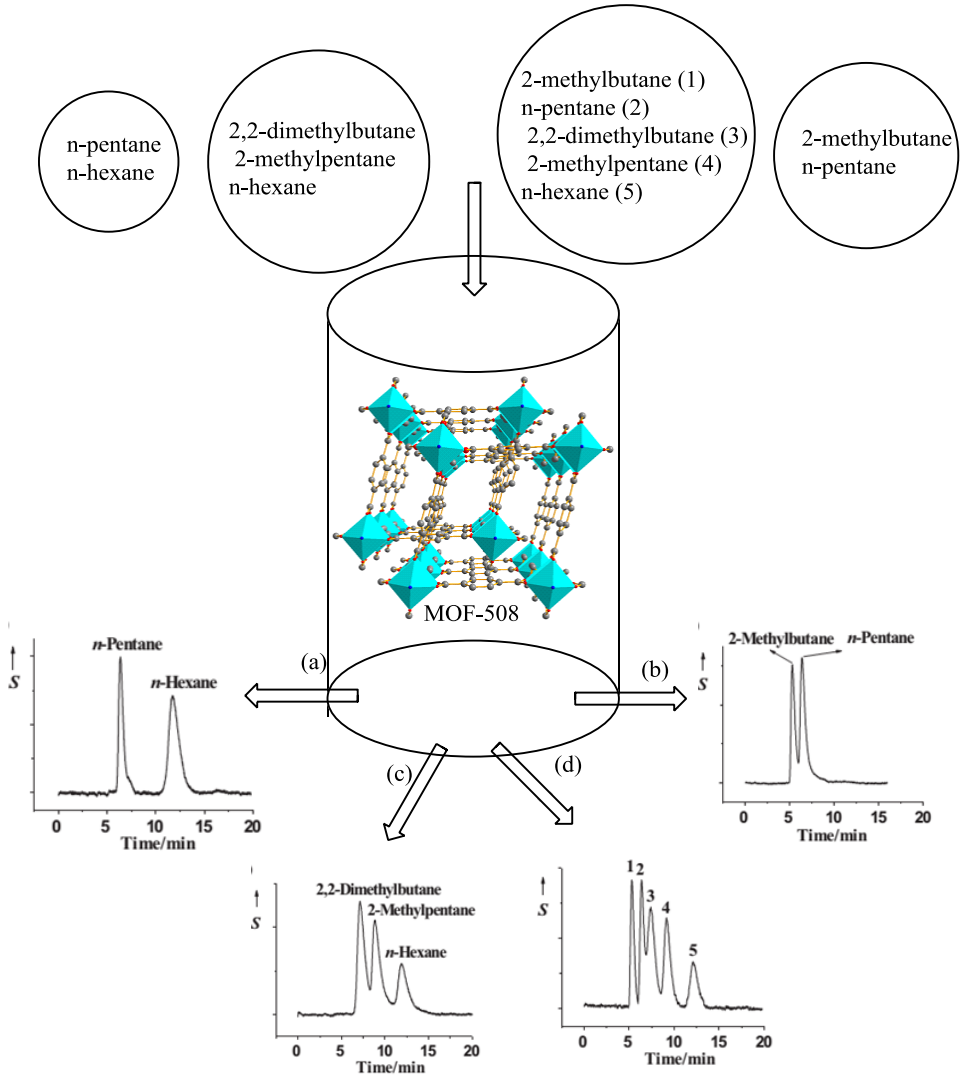

Figure I.1.7. Chromatograms of alkane mixtures separated on a MOF-508 column, S = thermal conductivity detector response.

3- Catalysis

Metal-organic frameworks play an important role in catalysis and photocatalysis,[15-22] here I will discuss the type of organic reactions catalyzed by MOFs.

Lewis Acid catalysis: The organic reactions catalyzed by Lewis acids are based on acceptor of electron pairs by metal centers to increase the reactivity of a substrate. MOFs with metal cations can be used as catalysts after removal of the solvents they contain to leave a vacant co-ordination site, a Lewis acid. As an example, the water molecules were removed from HKUST-1, [$Cu_3(btc)_2(H_2O)$, btc = 1,3,5-benzenetricarboxylate], by heat activation and the

dehydrated MOF was tested on catalyzed benzaldehyde cyanosilylation, isomerization of α-pinene oxide, citronellal cyclization, and rearrangement of ethylene acetal of 2-bromopropiophenone. The results show high the selectivity and catalytic activity.[23,24]

Brønsted Acid catalysis: The selectivities and reactivities of Brønsted acids play an important role in catalysis of various organic reactions. Due to the drawback of homogeneous Brønsted acids (difficulties in separation from the product, equipment corrosion, and environmental pollution), a heterogeneous catalyst is often used. For example, MIL-100 [$M_3OF_{0.85}(OH)_{0.15}(H_2O)_2(btc)_2$, M= Fe^{3+} or Cr^{3+}] show M-OH Brønsted sites of medium acidity and several types of Lewis centers. It is used for Friedel–Crafts benzylation catalysis and the results show high catalytic activity (Scheme I.1.1).[25]

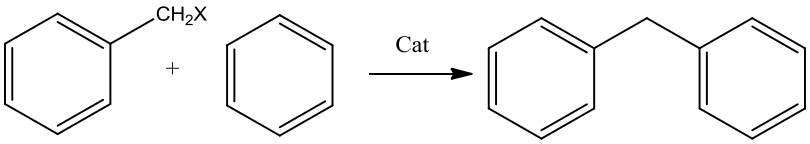

Scheme I.1.1. Friedel–Crafts benzylation

Base catalysis: $[Cd\text{-}(4\text{-btapa})_2(NO_3)_2].6H_2O.2DMF)_n$, 4-btapa = 1,3,5-benzene tricarboxylic acid tris[N-(4-pyridyl)amide] has been synthesized by the reaction of $Cd(NO_3)_2{\cdot}4H_2O$ with a tridentate ligand, (4-btpa). The product was used as catalyst in the Knoevenagel condensation reaction of benzaldehyde with active methylene compounds (malononitrile, ethyl cyanoacetate, and cyanoacetic acid *tert*-butyl ester) (Scheme I.1.2).[26] The results show that the conversion of malononitrile to adduct is 98% and the reaction occurs in the channels and not on the surface of MOFs.

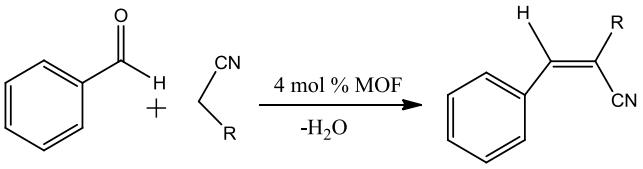

R	Conversion %
NC, CN	98
NC, O	7
NC, O, O, tBu, O	0

Scheme I.1.2. Knoevenagel Condensation reaction of benzaldehyde with active methylene compounds.

Enantioselective Catalysis: An hexagonal porous chiral MOF (POST-1) {$Zn_3(_{\mu 3}$-O)(tartrate)} is constructed from D-tartric acid derivative as linker and Zn^{2+} as inorganic node. It has some pyridyl groups connected to its backbone. It was used on the enantioselective transesterification of dinitrobenzyl acetate with a racemic mixture of 1-phenyl-2-propanol.[27]

C-C Bond formation: The organic reaction between aryl halides and arylboronic acids is known as Suzuki–Miyaura (C-C cross-coupling reaction). Some MOFs are used as catalysts in this kind of reaction, for example [Pd(2-pymo)$_2$·3H$_2$O, 2-pymo = 2-hydroxypyridimidolate]. The activity of palladium MOF catalyst has a turnover frequency (TOF) of 1230 h^{-1} at 150 °C in the Suzuki–Miyaura reaction of boronic acid with *p*-methoxybenzyl bromide and it can be reused without special treatments (Scheme I.1.3).[28]

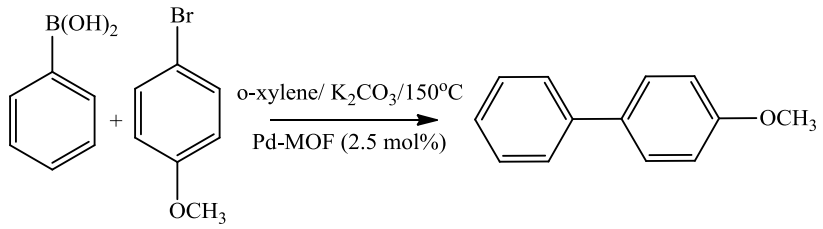

Scheme I.1.3. Suzuki–Miyaura cross coupling of of boronic acid with *p*-methoxybenzyl bromide.

It is well known that palladium is used in catalyzed Suzuki-Miyaura cross-coupling reaction of aryl halides with arylboronic acids. Recently, palladium nanoparticles (Pd NPs) supported on amino functionalized UiO-66-NH_2 were used as catalyst for Suzuki-Miyaura cross-coupling reaction giving excellent activity and able to be reused several times without any appreciable loss of activity, even after five consecutive times.[29]

Photocatalysis: Metal-organic frameworks are use on photocatalytic reactions, including hydrogen evolution, carbon dioxide reduction and degradation and transformation of organic compounds. Hydrogen evolution is the process of splitting water into hydrogen and oxygen that can be catalyzed by MOFs, being the best photocatalyst used the Zr-based MOFs UiO-66 and UiO-66(NH_2). This material catalyzes the hydrogen evolution under UV irradiation (>300 nm) and methanol as the sacrificial electron donor.[30] NH_2-MIL-125 is a photoactive MOF used in the carbon dioxide reduction under visible light.[31] The mechanism of reduction consists in the conversion of CO_2 to HCO_2^- in the presence of

acetonitrile with triethanolamine (TEOA) as the sacrificial reducing agent. $[Co(btec)_{0.5}(bimb)]_n$), $[Ni(btec)_{0.5}(bimb)(H_2O)]_n$ and $[Cd(btec)_{0.5}(bimb)_{0.5}]_n$ [btec = 1,2,4,5-benzenetetracarboxylic acid and bimb = 4,4\-bis(1-imidazolyl)biphenyl] are used in the photocatalytic degradation of organic compounds (dye X3B).[32] The results obtained by these catalysts are better than those obtained with the commercial TiO_2 (Degussa P-25) under visible light. The post-modified NH_2-MIL-125 is used on photocatalytic organic transformations, it is able to absorb 100% more photons emitted by the Xe-lamp leading to higher activity of the framework in benzyl alcohol oxidation.[33]

References

[1] J. L.C. Rowsell, O. M. Yaghi, *Microp. Mesop. Mater*., **2004**, *73*, 3-14.

[2] Z.-J. Lin, J. Lu, M. Hong, R. Cao, *Chem. Soc. Rev*., **2014**, DOI: 10.1039/C3CS60483G.

[3] F. A. A. Paz, J. Klinowski, S. M. F. Vilela, J. P. C. Tome, J. A. S. Cavaleiro, J. Rocha, *Chem. Soc. Rev.*, **2012**, *41*, 1088-1110.

[4] S. T. Meek, J. A. Greathouse, M. D. Allendorf, *Adv. Mater.*, **2011**, *23*, 249-267.

[5] a) Z. Ni, R. I. Masel, *J. Am. Chem. Soc.*, **2006**, *128*, 12394-12395., b) A. M. Joaristi, J. Juan-Alcan˜iz, P. Serra-Crespo, F. Kapteijn, J. Gascon, *Cryst. Growth Des.*, **2012**, *12*, 3489-3498.

[6] A. J. Fletcher, K. M. Thomas, M. J. Rosseinsky, *J. Solid State Chem.*, **2005**, *178*, 2491-2510.

[7] P. Horcajada, C. Serre, G. Maurin, N. A. Ramsahye, F. Balas, M. Vallet-Regi, M. Sebban, F. Taulelle, G. Ferey, *J. Am. Chem. Soc.*, **2008**, *130*, 6774-6780.

[8] P. Horcajada, C. Serre, M. Vallet-Regi, M. Sebban, F. Taulelle, G. Ferey, *Angew. Chem. Int. Ed.*, **2006**, *45*, 5974-5978.

[9] N. J. Hinks, A. C. McKinlay, B. Xiao, P. S. Wheatley, R. E. Morris, *Microp. Mesop. Mater.*, **2010**, *129*, 330-334.

[10] A. C. McKinlay, B. Xiao, D. S. Wragg, P. S. Wheatley, I. L. Megson, R. E. Morris, *J. Am. Chem. Soc.*, **2008**, *130*, 10440-10444.

[11] B. Xiao, P. S. Wheatley, X. B. Zhao, A. J. Fletcher, S. Fox, A. G. Rossi, I. L. Megson, S. Bordiga, L. Regli, K. M. Thomas, R. E. Morris, *J. Am. Chem. Soc.*, **2007**, *129*, 1203-1209.

[12] P. Horcajada, T. Chalati, C. Serre, B. Gillet, C. Sebrie, T. Baati, J. F. Eubank, E. Heurtaux, P. Clayette, C. Kreuz, J.-S. Chang, Y. K. Hwang, V. Marsaud, P.-N. Bories, L. Cynober, S. Gil, G. Frey, P. Couvreur, R. Gref, *Nat. Mater*., **2010**, *9*, 172-178.

[13] D. Britt, D. Tranchemontagne, O.M. Yaghi, *PNAS*, **2008**, *105*, 11623-11627.

[14] B. Chen, C. Liang, J. Yang, D. S. Contreras, Y. L. Clancy, E. B. Lobkovsky, O. M. Yaghi, S. Dai, *Angew. Chem., Int. Ed.*, **2006**, *45*, 1390-1393.

[15] A. Corma, H. Garcia, F. X. L. Xamena, *Chem. Rev*., **2010**, *110*, 4606-4655.

[16] J. Gascon, A. Corma, F. Kapteijn, F. L. Xamena, *ACS Catal*., **2014**, *4*, 361-378.

[17] F. L. Xamena, J. Gascon, *Metal Organic Frameworks as Heterogeneous Catalysts*, The Royal Society of Chemistry, *Cambridge*, **2013,** ISBN: 978-1-84973-572-8.

[18] D. Farrusseng, S. Aguado, C. Pinel, *Angew. Chem. Int. Ed.*, **2009**, *48*, 7502-7513.

[19] A. Dhakshinamoorthy, M. Alvaro, A. Corma, H. Garcia, *Dalton Trans.*, **2011**, *40*, 6344-6360.

[20] J. Lee, O. K. Farha, J. Roberts, K. A. Scheidt, S. T. Nguyen, J. T. Hupp, *Chem. Soc. Rev.*, **2009**, *38*, 1450-1459.

[21] J.-L. Wang, C. Wang, W. Lin, *ACS Catal.*, **2012**, *2*, 2630-2640.

[22] C. G. Silva, A. Corma and H. Garcia, *J. Mater. Chem*., **2010**, *20*, 3141-3156.

[23] L. Alaerts, E. Seguin, H. Poelman, F. Thibault-Starzyk, P. A. Jacobs, D. E. De Vos, *Chem. Eur. J.*, **2006**, *12*, 7353-7363.

[24] K. Schlichte, T. Kratzke, S. Kaskel, *Microp. Mesop. Mater*., **2004**, *73*, 81-88.

[25] P. Horcajada, S. Surble, C. Serre, D. Y. Hong, Y. K. Seo, J. S. Chang, J. M. Greneche, I. Margiolaki, G. Frey, *Chem. Commun*., **2007**, 2820-2822.

[26] S. Hasegawa, S. Horike, R. Matsuda, S. Furukawa, K. Mochizuki, Y. Kinoshita, S. Kitagawa, *J. Am. Chem. Soc*. **2007**, *129*, 2607-2614.

[27] J. S. Seo, D. Whang, H. Lee, S. I. Jun, J. Oh, Y. J. Jeon, K. Kim, *Nature*, **2000**, *404*, 982-986.

[28] F. Xamena, A. Abad, A. Corma, H. Garcia, *J. Catal*., **2007**, *250*, 294-298.

[29] R. Kardanpour, S. Tangestaninejad, V. Mirkhani, M. Moghadam, I. M. Baltork, A. R. Khosropour, F. Zadehahmadi, J. Organometallic Chem., **2014**, *761*, 127-133.

[30] S. C. Gomes, I. Luz, F. Xamena, A. Corma, H. Garcıa, *Chem. Eur. J*., **2010**, *16*, 11133-11138.

[31] Y. Fu, D. Sun, Y. Chen, R. Huang, Z. Ding, X. Fu, Z. Li, *Angew. Chem., Int. Ed.*, **2012**, *51*, 3364-3367.

[32] L. Wen, J. Zhao, K. Lv, Y. Wu, K. Deng, X. Leng, D. Li, *Cryst. Growth Design*, **2012**, *12*, 1603-1612.

[33] M. A. Nasalevich, M. G. Goesten, T. J. Savenije, F. Kapteijn, J. Gascon, *Chem. Commun.*, **2013**, *90*, 10575-10577.

Chapter 2: Post-Synthetic Modification of MOFs

- Synthesis and structure description of functional-MOFs
- Post-synthetic modification (PSM) definition
- Types of post-synthetic modification
  - (a) Post-functionalization of MOFs by non-covalent and coordinative interactions.
  - (b) Post-functionalization of MOFs by covalent bonds.
  - (c) Post-synthetic metalation of MOFs.
- References

Along this chapter we will describe: i) the synthesis and the structure of different functional MOFs used as excellent platforms for the grafting of various functional groups, ii) the post-synthetic approaches to modify and functionalize MOFs in order to introduce new properties relevant for gas sorption, catalysis, and biomedical applications, and iii) the post-synthetic metalation of metal–organic frameworks to highlight the broad scope of this technique for enhancing the performance characteristics of MOFs and to demonstrate how the post-synthetic metalation concept can be developed for future applications.

Synthesis and structure description of functional-MOFs

MOFs with amino group on their organic linkers are very important materials for post-synthetic modifications. In this part we will focuses on the synthesis and the structure of NH_2-MOFs to understand how the position of amino group interfere in the structure organisation of MOFs. We will also describe other functional group such as aldehyde group.

IRMOF-3

Isoreticular metal-organic framework (IRMOF-3) was synthesized from 2-aminoterephthalic acid (2-aminobenzene-1,4-dicarboxylic acid) and $Zn(NO_3)_2.6H_2O$ in DMF. IRMOF-3 is a highly porous, crystalline structure and the presence of non-coordinated amino groups on the benzenedicarboxylate (bdc) linker can be efficiently modified (Figure I.2.1). The lattice structure of IRMOF-3 was determined from X-ray data; it shows that Zn_4O tetrahedral subunits are linked in octahedral arrays by the terephthalate to form a porous material with channel windows of 7.4 Å. The Zn edges of the tetrahedra are bridged by six carboxylate groups forming octahedral nodes, linked one to another with the aromatic rings of the terephthalate linker resulting in a 3D cubic network.[1]

DMOF-1-NH_2

DMOF-1-NH_2 (DABCO MOF-1-NH_2) was prepared from mixture of DABCO (1,4-diazabicyclo[2.2.2]octane), 2-aminoterephthalic acid and $Zn(NO_3)_2.6H_2O$. DMOF-1-NH_2 has a channel diameter of 5.6 Å, it is a zero-dimensional-type MOF (isolated clusters) with a layered structure made of Zn-carboxylate sheets supported by DABCO pillars that weakly coordinate to the Zn paddlewheel (Figure I.2.2).[2] The single-crystal X-ray diffraction shows uncoordinate amino group. The measured BET surface area and the microporous volume of DMOF-1-NH_2 are 1320 m^2g^{-1} and 0.54 cm^3g^{-1} respectively.

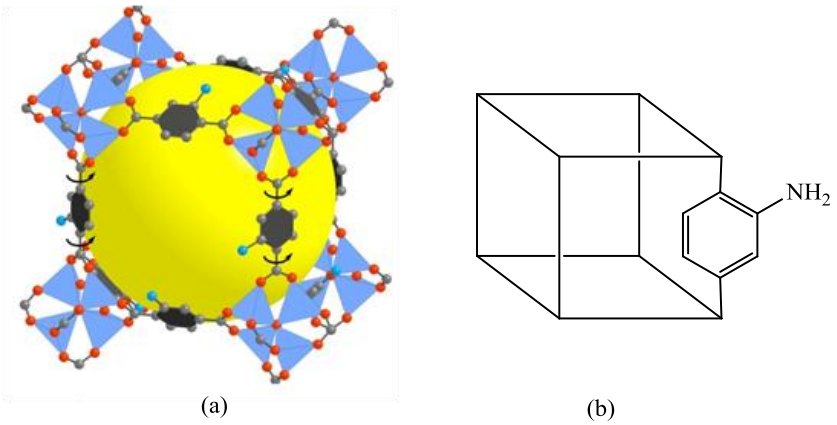

Figure I.2.1 IRMOF-3: [a] Lattice structure from X-ray data (Zn = turquoise, C = gray, N = blue, O = red; the yellow ball indicates the size of the pore openings) and [b] scaffold representation.

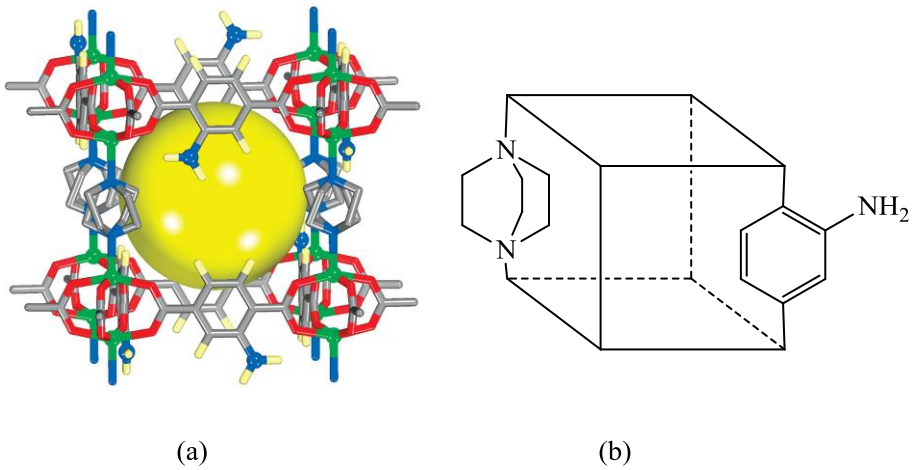

Figure I.2.2 DMOF-1–NH_2: [a] Lattice structure from X-ray data (Zn = green, C = grey, N = blue, O = red; the yellow ball indicates the size of the pore openings) and [b] scaffold representation.

UMCM-1-NH_2

UMCM-1-NH_2 is an NH_2-bdc derivative of UMCM-1 (University of Michigan Crystalline Material-1), UMCM-1-NH_2 is a highly porous MOF and consists of both NH_2-bdc and btb (btb = 4,4',4''-benzene-1,3,5-triyl-tribenzoate) linkers with Zn_4O SBUs (Figure I.2.3).[3] BET surface areas for UMCM-1-NH_2 is 3920 m^2g^{-1}.

MOF-LIC-1

The reaction of gadolinium (III) nitrate with 2-aminobenzene-1,4-dicarboxylic acid in *N*,*N*-dimethylformamide (DMF) at 120 °C produces the 3D coordination network $\{[Gd_2(NH_2\text{-bdc})_3(DMF)_4]\}_n$ (MOF-LIC-1),[4] whose building unit is depicted in Figure I.2.4.

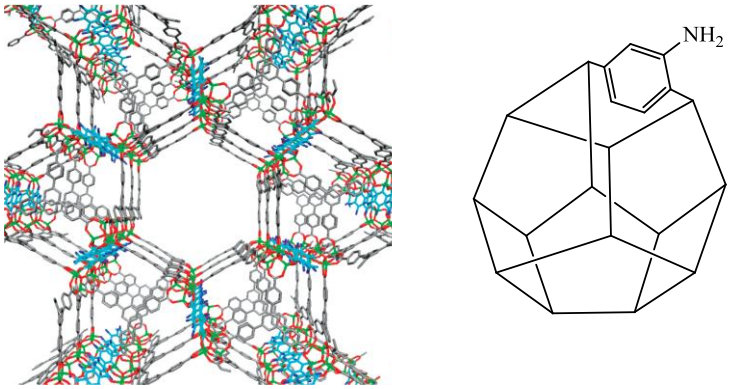

(a) (b)

Figure I.2.3 UMCM-1-NH_2: [a] Lattice structure from X-ray data and [b] scaffold representation.

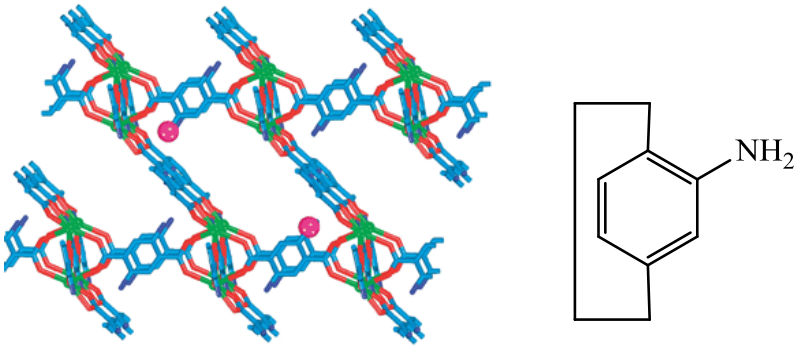

(a) (b)

Figure I.2.4 MOF-LIC-1: [a] Lattice structure from X-ray data and [b] scaffold representation.

MIL-53(Al)–NH_2

MIL-53(Al)-NH_2 was synthesized using 2-aminoterephthalic acid as linker and aluminium nitrate nonahydrate as metal source. MIL-53 is built up from $AlO_4(OH)_2$ octahedra with 1D diamond shaped pores having a free diameter of 8.6 Å (Figure I.2.5).[5]

UiO-66–NH_2

UiO-66–NH_2 was synthesized using zirconium (IV) and 2-aminoterephthalic acid. Owing to the highly oxophilic nature of zirconium (IV), the Zr_6-cluster SBU formed in these MOFs makes these materials very resistant towards various solvents and high pressures. Figure I.2.6 shows the UiO-66 framework with its Zr_6O_6 cuboctahedron SBU.[6] The BET surface area and the micropore volume are 850 m^2g^{-1}, 0.43 cm^3 g^{-1}, respectively.

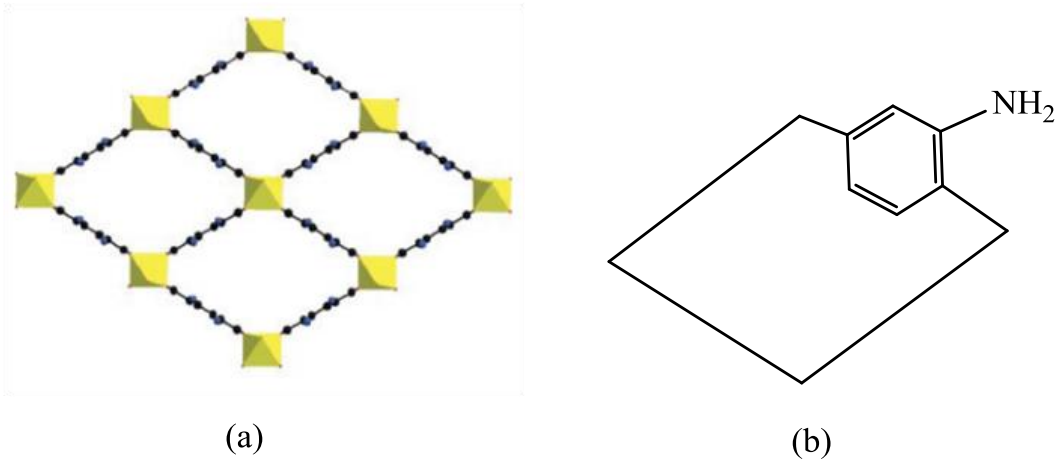

Figure I.2.5 MIL-53(Al) NH_2: [a] Lattice structure from X-ray data (Al = yellow, C = black, O = red, N = blue) and [b] scaffold representation.

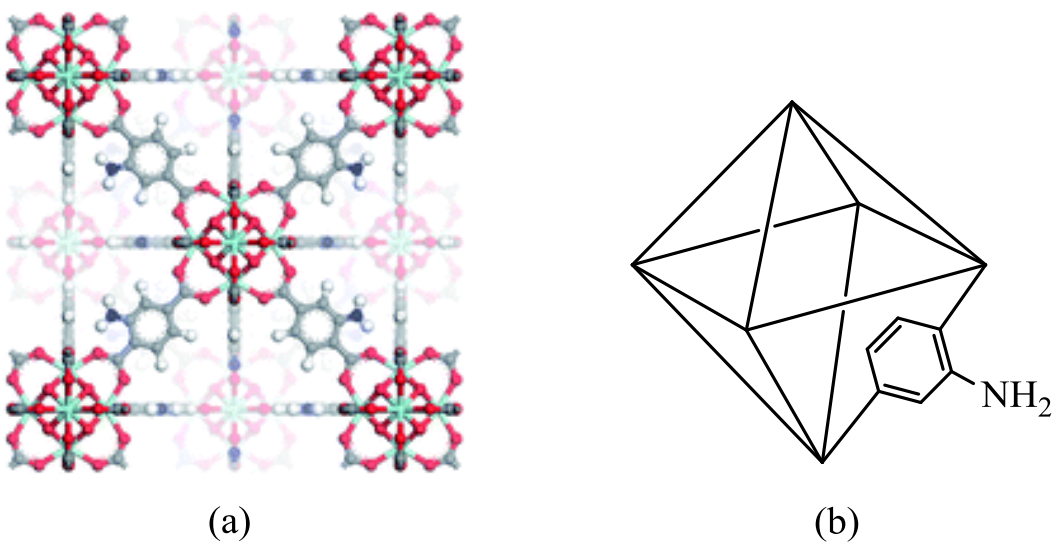

Figure I.2.6 UiO-66-NH_2: [a] Lattice structure from X-ray data and [b] scaffold representation.

MIL-101(Fe)-NH_2

MIL-101(Fe)-NH_2 has as chemical formula $[Fe_3O(solv)_3Cl(C_8H_5O_4N)_3$ (solv = H_2O, DMF]. It was prepared by treatment of $FeCl_3$•$6H_2O$ with 2-aminoterephthalic acid in DMF. Figure I.2.7 represents the lattice structure of MIL-101-NH_2 (Matériaux de l'Institut Lavoisier) which consists of trivalent metal ions (Fe^{3+}) and 2-aminoterephthalate. The resulting cubic cell volumes are huge with two types of mesoporous cages limited by pentagonal faces for the smaller and by pentagonal and hexagonal faces for the larger. After the removal of the guest molecules, the free internal diameters of the parent structure MIL-101(Fe) are close to 29 and 34 Å.[7]

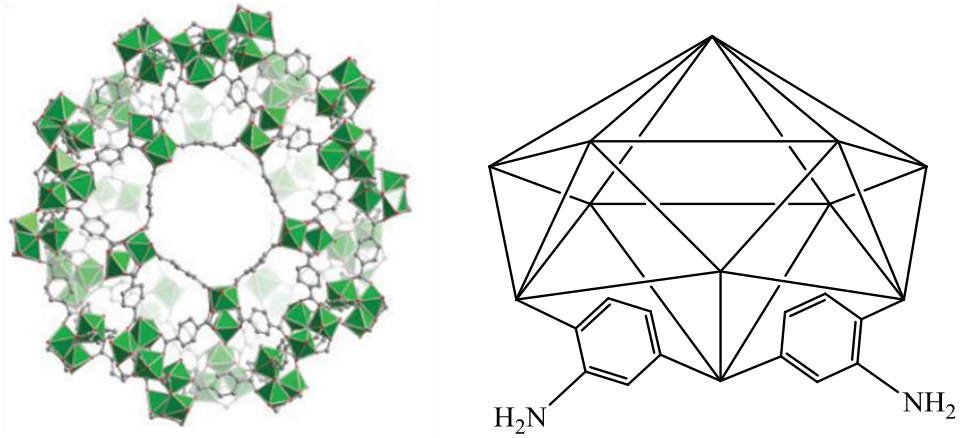

(a) (b)

Figure I.2.7 MIL-101-NH_2: [a] Lattice structure from X-ray data (Al = green, C = grey, O = red) and [b] scaffold representation.

MIL-68(In)-NH_2

MIL-68(In)-NH_2 has as chemical formula [(In(OH)($C_8H_5O_4N$)]. It was synthesized by precipitation reaction from a mixture of indium nitrate and NH_2-bdc in DMF to which a DABCO solution in DMF was added. MIL-68(In)-NH_2 framework is built up from infinite straight chains of metal-centered $InO_4(OH)_2$ octahedra connected to each other through the NH_2-bdc ligands, generating 1D channels. The octahedral units are linked together via two hydroxyl groups located in *trans*-positions, two adjacent octahedra also being connected via the carboxylate functions. These corner-sharing octahedral species MO_6 form a network of three- and six-membered windows, generating two types of channels. The diameter openings of MIL-68 parent structure are 6 Å and 17 Å, respectively, for the triangular and hexagonal rings (Figure I.2.8).[8]

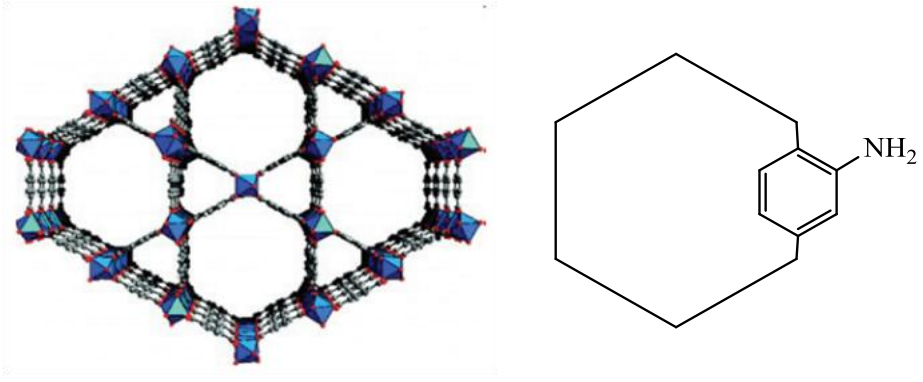

(a) (b)

Figure I.2.8 MIL-68(In)-NH_2: [a] Lattice structure from X-ray data (In = green, C = grey, O = red), and [b] scaffold representation.

NH_2-MIL-125

NH_2-MIL-125 $[Ti_8O_8(OH)_4\text{-}(C_8H_5O_4N)_6]$ was solvothermally prepared by treatment of NH_2-bdc with titanium tetraisopropoxide in a mixture of DMF and methanol, as solvent, at 150°C. NH_2-MIL-125 has a quasi-cubic tetragonal structure (Figure I.2.9) in which the atoms are substituted by cyclic octamers (SBU-8) of edge- and corner-sharing $TiO_5(OH)$ octahedra. 1,4-Benzenedicarboxylates (bdc) replace the contacts between atoms, link the octamers, and provide a 3D structure. The 3D arrangement provides two types of cages corresponding to the octahedral (12.55 Å) and tetrahedral vacancies (6.13 Å).[9] The BET surface area and the microporous volume are 1500 m^2g^{-1} and 0.65 cm^3g^{-1}, respectively.

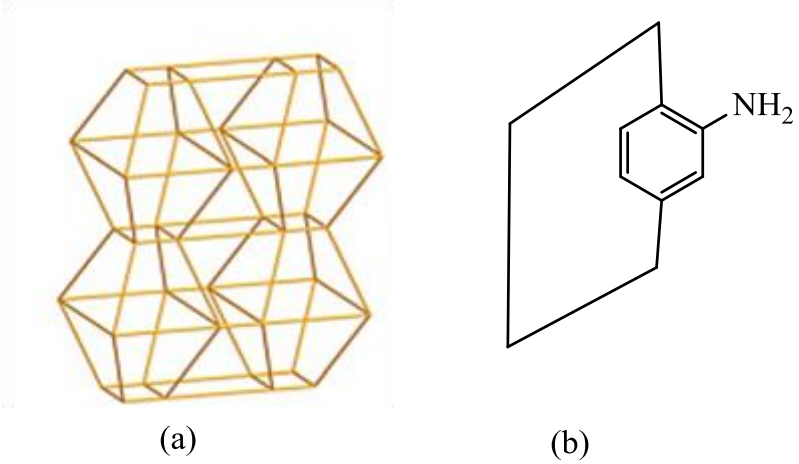

Figure I.2.9 NH_2-MIL-125**:** [a] Lattice structure from X-ray data and [b] scaffold representation.

CAU-1

CAU-1 $[Al_4(OH)_2(OCH_3)_4(C_8H_5O_4N)_3]$ was solvothermally prepared from a mixture of aluminium chloride and NH_2-bdc in MeOH. It is built up from a pseudo-body-centered-cubic arrangement of 8-ring building blocks $[Al_8(OH)_4(OCH_3)_8]^{12+}$ linked by 12 aminoterephthalate ions. The wheel shaped 8-rings are built from corner- and edge-sharing AlO_6 octahedra through hydroxide and methoxide groups. The Al(III) is coordinated to three carboxylate oxygen atoms, one hydroxide and two methoxide ions. Each wheel is connected to 12 others units by aminoterephthalate linkers with four linkers in the plane of the 8-rings as well as four above and below the ring. Hence, a 3D microporous framework is formed with two types of cages, distorted octahedra and distorted tetrahedra, with diameter of 10 Å and 4.5 Å, respectively (Figure I.2.10).[10] The BET surface area and a microporous volume of CAU-1 are 1434 m^2g^{-1} and 0.52 cm^3g^{-1}, respectively.

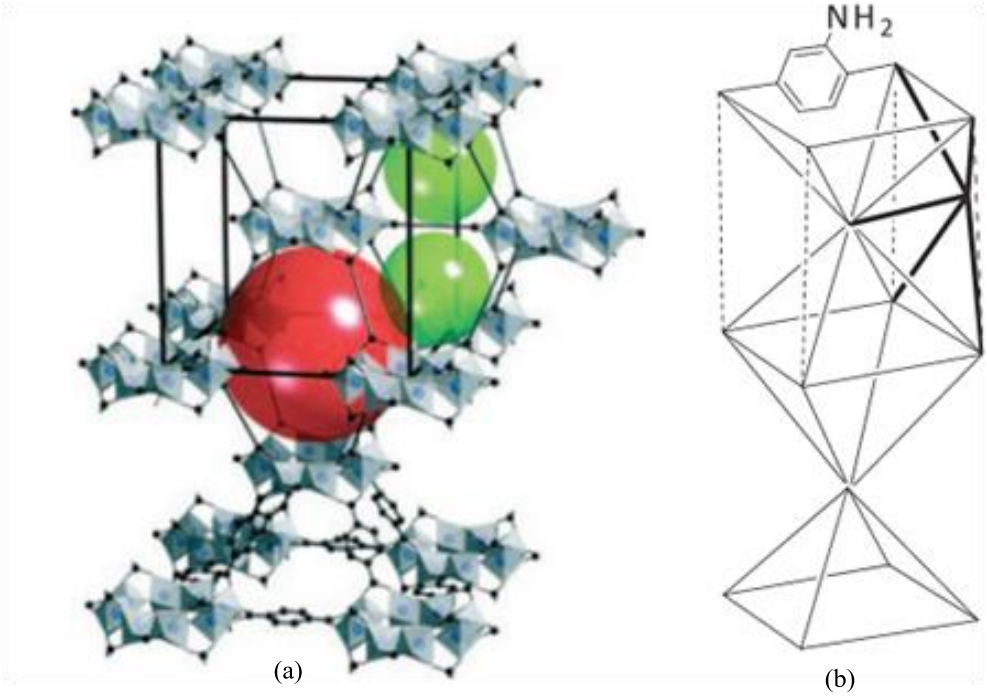

Figure I.2.10 CAU-1: [a] Lattice structure from X-ray data (Al = grey, C =black; O = blue; the red and green balls indicate the different size of the pore openings) and [b] scaffold representation.

ZIF-90

ZIFs (zeolitic imidazolate framework) are a new class of metal–organic frameworks (MOFs), which have great potential in gas adsorption and storage, molecular separation, and catalysis because of their large internal surface area and uniform pore structures. ZIF-90 was prepared with adding Zn(II) and imidazolate-2-carboxaldehyde. Figure I.2.11 represented the attached Zn(II) ion with imidazolate-2-carboxaldehyde, the lattice structure and also the scaffolds representation of ZIF-90.[11] The BET surface area and a microporous volume of CAU-1 are 1270 m^2g^{-1} and 0.58 cm^3g^{-1}, respectively.

POST-1

2D homochiral MOF (POST-1) was prepared from Zn(II) trimer SBU and an enantiopure tartrate derivative containing a pyridyl moiety (Figure I.2.12). Although all the carboxylate groups coordinate to the Zn(II) trimers within the MOF, only half of the pyridyl units are engaged in the coordinate bonding, with the other half exposed in the channels without any interaction with the framework metal ions. It was speculated that these free pyridyl groups were essential to the enantioselective catalytic activity of the MOF for the transesterification of 2,4-dinitrophenyl acetate.[12]

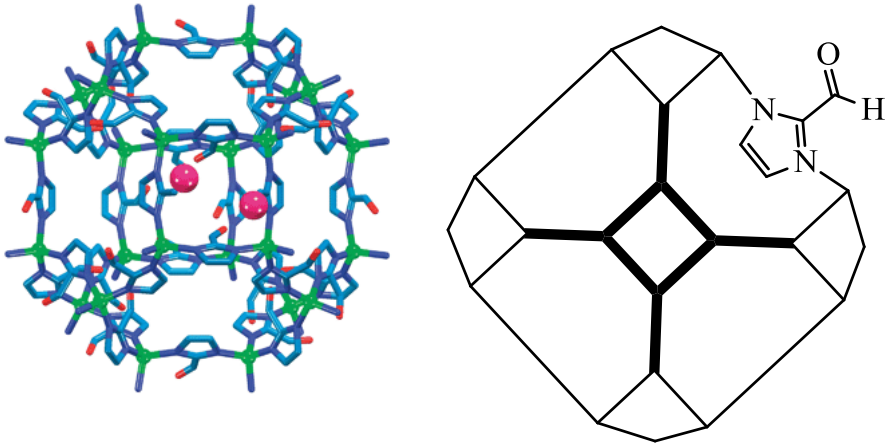

(a) (b)

Figure I.2.11 ZIF-90: [a] Lattice structure from X-ray data and [b] scaffold representation.

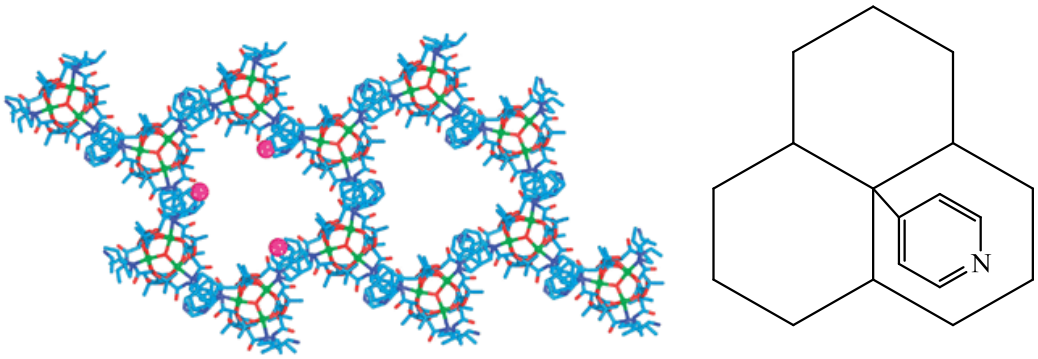

(a) (b)

Figure I.2.12 POST-1: [a] Lattice structure from X-ray data and [b] scaffold representation.

Post-synthetic modification (PSM) definition

Post-synthetic modification is a chemical modification of a MOF framework to prepare functionalized MOFs.[13-16] Figure I.2.13 shows the formation of a MOF by the reaction of a metal ion (M) with a functionalized ligand (L) to form the framework, followed by the reaction with another reagent to form a new metal-organic frameworks. The second transformation is the so called post-synthetic modification (PSM). MOFs need some requirements for the PSM process such as porosity, stability toward reaction condition and by-products and also to have functional groups. There are many advantages for PSM, for example the metal and organic linker can be functionalized without affecting the stability of the framework. PSM is also an excellent tool for preparing topologically identical, but functionally diverse frameworks.

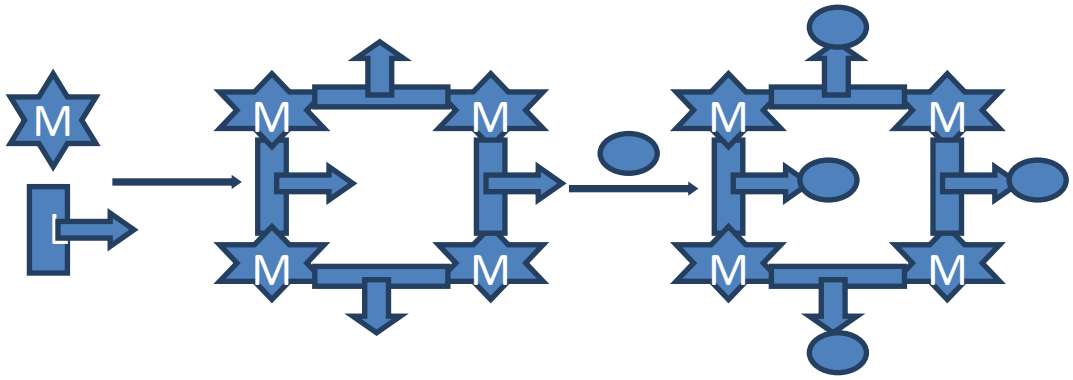

Figure I.2.13 Schematic representation for the synthesis and post-synthetic modification of MOFs.

Types of post-synthetic modification

Post-synthetic modification of MOFs are divided into three main areas: (a) non-covalent and coordinative interactions PSM, (b) covalent PSM and (c) post-synthetic metalation. We will briefly describe the characteristics of each one of them and also the modifications integrated in each one of these groups.

(a) Post-functionalization of MOFs by non-covalent and coordinative interactions:

PSM of MOFs by non-covalent interactions

PSM by non-covalent interactions is defined as the use of a reagent that forms a static bond with a component of the MOF. The most common forms of post-synthetic non-covalent modification of MOFs include guest removal, guest exchange, and ion exchange.

Guest removal

Guest removal is defined as desolvation of a coordination site on an SBU or removing a guest molecule from MOFs cavity. The 2D Ag(I)-MOF was synthesized through solvothermal treatment of Ag_2O with 1,3,5-tris(3-ethynylbenzonitrile)benzene in the presence of benzene, it can post-synthetically modified via guest removal through partially releasing of benzene guests under heating at 110 °C for 10 min (Figure I.2.14a).[17] A similar guest removal process show in 2D Co(II)-btc MOF (btc = 1,3,5-benzenetricarboxylate) through release of pyridine guests and for MIL-101 (Cr) via removal of water molecule by thermal treatment under vacuum (Figure I.2.14b).[18] This technique is very important because it produce highly activated porous MOFs and may be adsorb different other molecules that are smaller than the pore size of the MOFs.

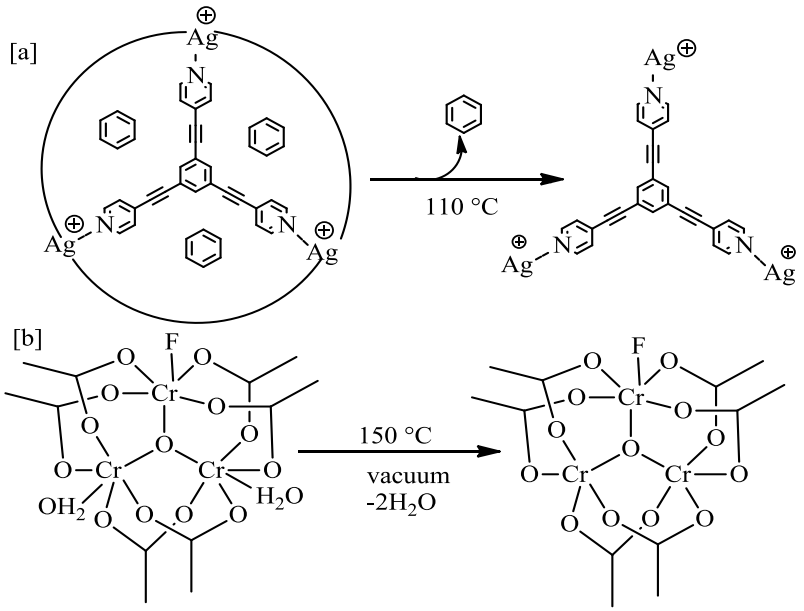

Figure I.2.14 Schematic representation for the benzene and water guest removal from Ag(I)-MOF and MIL-101 (Cr).

Guest exchange

Guest exchange is defined as the replacement of the solvent incorporated in the cavity of the MOF during its preparation by a solvent with fewer boiling points, such as the exchange of DMF molecules on IRMOF-3 with chloroform molecules. This PSM method was used for the activation of porous-MOFs by removing the volatile solvents under vacuum.[19]

Ion exchange

Another way to prepare a mixed-metal MC-MOF is through a post-synthetic modification. Some metal centres were substitute by another metal. Kim and co-workers[20] used this approach with $Cd_{1.5}(H_2O)_3[(Cd_4O)_3(L_9)_8$ and showed that this compound reversibly exchanges Cd^{2+} from the framework for Pb^{2+} without the loss of crystallinity or structural integrity (Figure I.2.15). The substitution was 98% complete after 2 hours and went to completion after 2 days in water, as witnessed by inductively coupled plasma atomic emission spectroscopy (IC-PAES), although the mixed Cd–Pb MOFs were observed using shorter reaction times. The substitution is reversible, but the exchange of lead by cadmium is slower: the ICP-AES analysis showed approximately 50% exchange of Pb^{2+} by Cd^{2+} in 1 day, with compete substitution taking 3 weeks. Post-synthetic modification was a useful strategy for preparing a variety of MOFs that would be difficult to produce otherwise, including MOFs with long hydrophobic chains, with free carboxylic acids and with non-

structural metal centers. Shultz *et al*[21] showed that post-synthetic removal of the Mn ions from the salen structures of Mn(III)SO-MOF with aqueous H_2O_2 can be used to modify its surface selectively and induce size-selective pore-based catalysis. Mn(III)SO-MOF crystals was soaked in methanol and then treated with aqueous H_2O_2 overnight. The material were placed under nitrogen and exposed to solutions containing M(II) salts (M = Cr, Co, Mn, Ni, Cu, Zn) for 24 h (Scheme I.2.1).

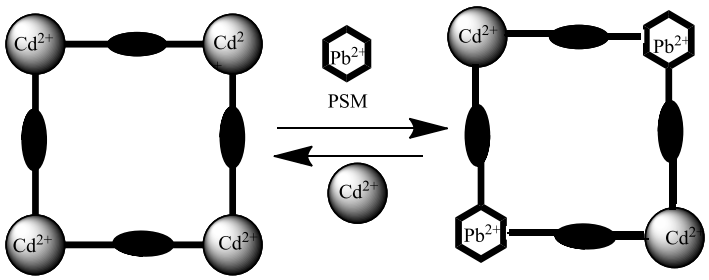

Figure I.2.15 Reversibly ion exchanges framework Cd^{2+} for Pb^{2+}.

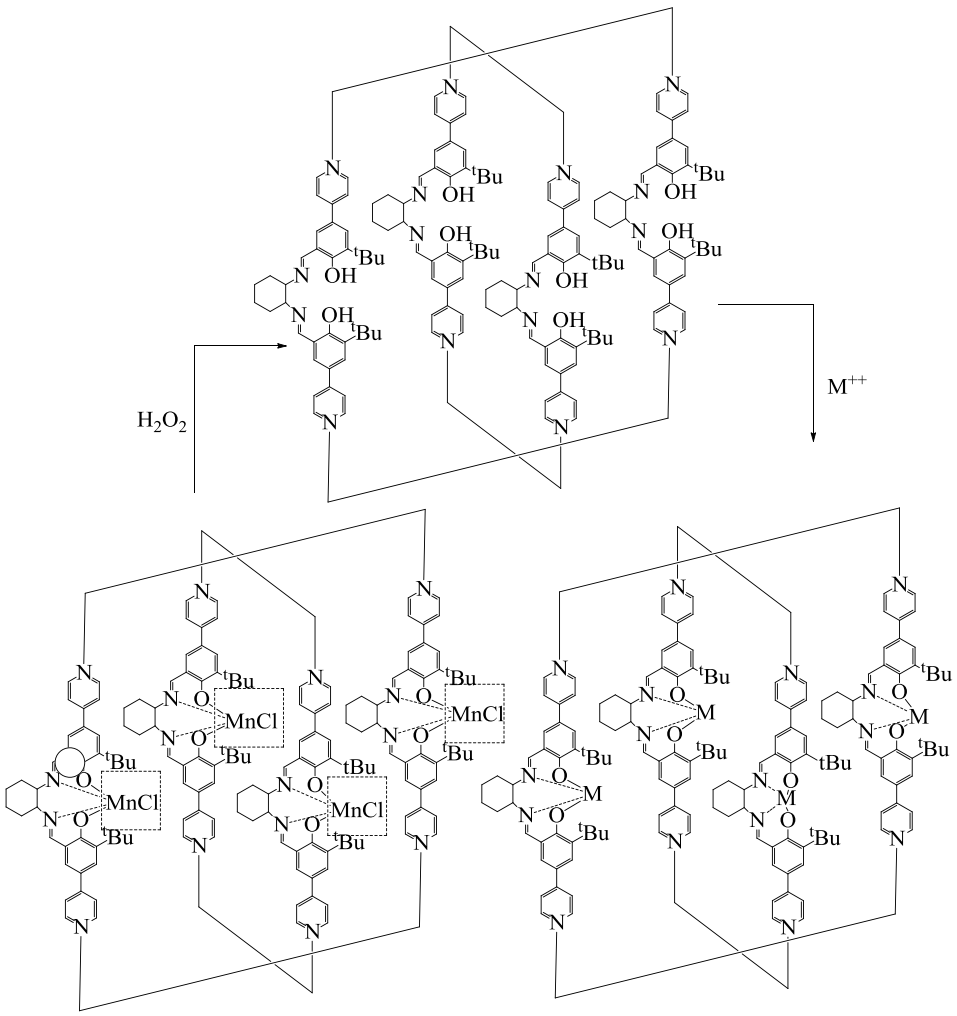

Scheme I.2.1 Removal of Mn^{3+} and exchange with another metals (M = Cr, Co, Ni, Cu, Zn).

PSM of MOFs by coordinative interactions

Thiol-functionalized MOFs was synthesized by a facile coordination-based PSM strategy. The new MOF has an important application in the Hg^{2+} adsorption from water. UMCs $[Cu_3(BTC)_2(H_2O)_3]_n$ (btc = benzene-1,3,5-tricarboxylate) was treated with dithioglycol, and the obtained thiol-functionalized MOF was treated with a Hg^{2+} solution resulted in a 99.79% removal of Hg^{2+} (Scheme I.2.2).[22]

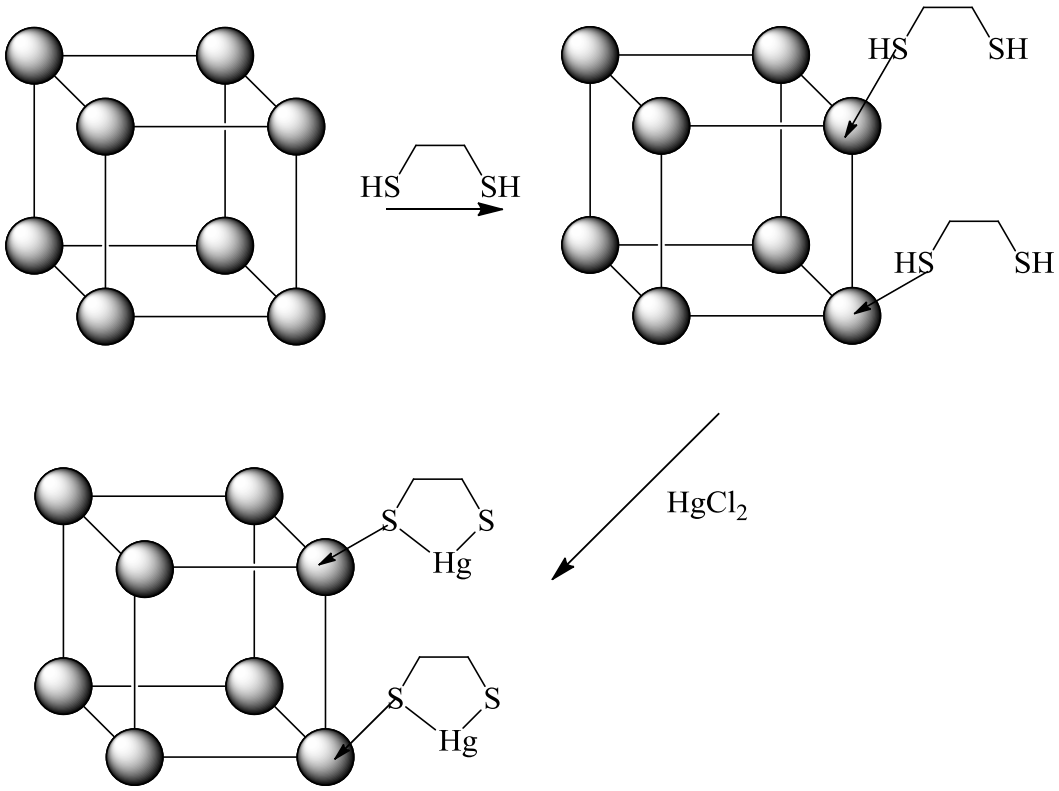

Scheme I.2.2 Thiol-functionalization of UMCs through coordination bonding and metalation with Hg^{2+} ions.

MIL-101 (Cr) has unsaturated chromium(III) centers, so it can coordinate with the amino group of dopamine in anhydrous THF at 50 °C for 24 h affording a brown catechol-bearing MOF [Dop-MIL-101 (Cr)]. The modified material was then reacted with vanadyl acetylacetonate $[VO(acac)_2]$ to afford a dark-brown vanadium modified framework [V(dop)-MIL-101 (Cr)] (Scheme I.2.3). The MIL-101-supported vanadyl catecholate moieties are active in the catalytic oxidation of thioanisole to the corresponding sulfoxide and sulfone.[23] MIL-101 (Cr) can also be post-synthetically modify with grafting of diethylenetriamine (DETA), under refluxing toluene for 8 h to afford DETA-MIL-101. The

amine functionalized MOF, DETA-MIL-101, was reacted with $PdCl_2$ in ethanol at 50 °C for 3 h to produce Pd-DETA-MIL-101 (Scheme I.2.3). The results of this study showed that DETA grafting caused a reduction in the CO_2 capture capacity, but the stronger interaction of the N species in the DETA-MIL-101 with CO_2 resulted in higher adsorption heat compared with that of MIL-101 in low pressure regions (< 15 kPa).

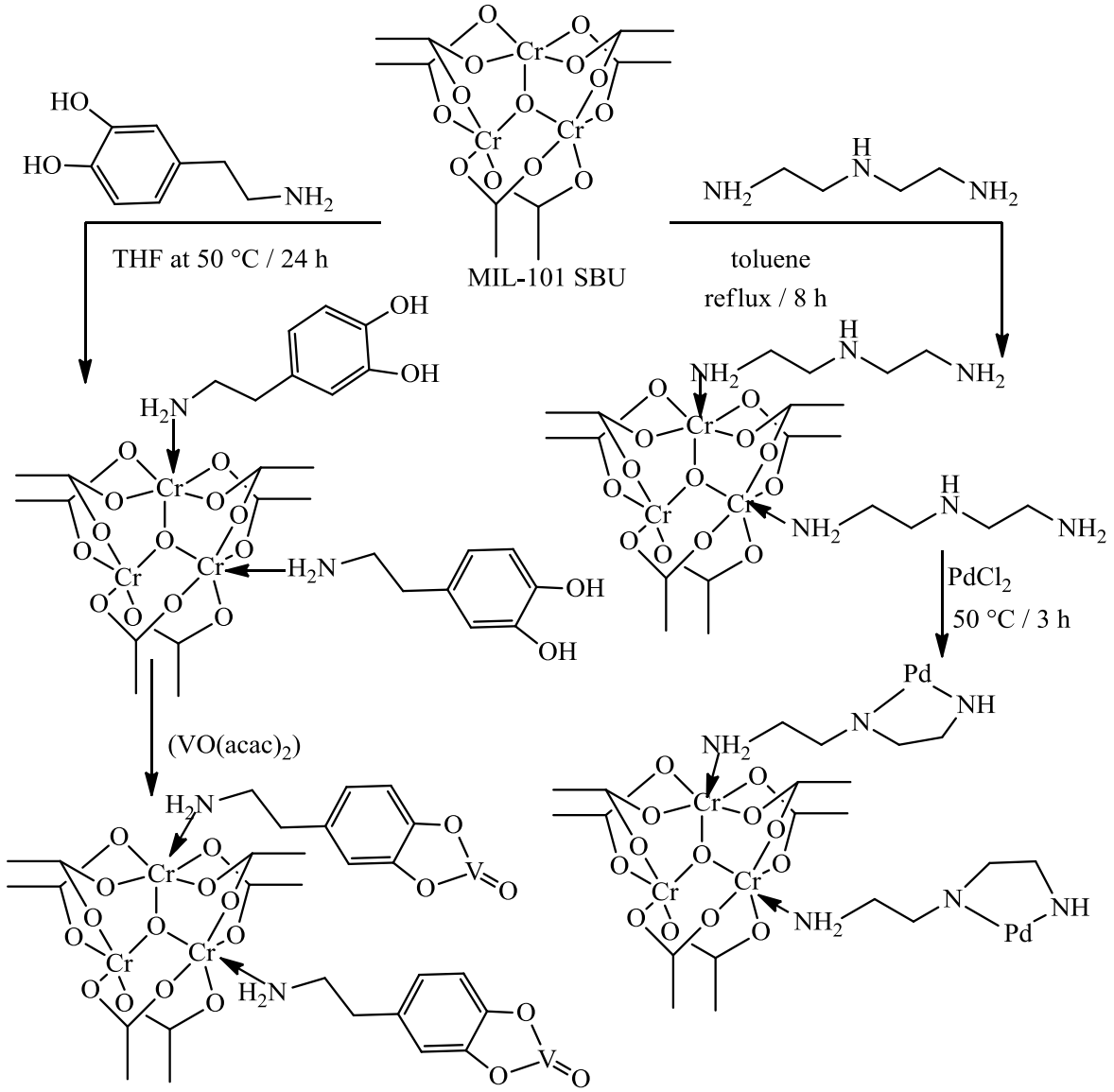

Scheme I.2.3 Post-synthetic modification of MIL-101 (Cr) with dopamine followed by coordination with vanadium (V) or modification with DETA followed by metalation with palladium (II) to create new catalysts.

DETA-MIL-101 has highly catalytic activity on Knoevenagel condensation of benzaldehyde with malononitrile under mild reaction conditions, while Pd-DETA-MIL-101 is used as a stable catalyst for the Heck reaction of the acrylic acid with iodobenzene.[24]

(b) Post-functionalization of MOFs by covalent bonds.

Covalent PSM of MOFs is the most important strategy among the different post-synthetic methods because it can introduce a broad range of functional groups into MOFs. Herein we will describe the PSM of MOFs forming covalent bonds [*N*-acylation, *O*-acylation, *N*-alkylation, conversion of amino groups into iso(thio)cyanate, azide groups, imine, hydrazone formation, reduction of the formyl group, thioether oxidation, deprotection reactions, exchange of bromo for cyano, nitration, sulfation, reduction of a nitro group, photo-induced formation of nitrenes, addition of bromine, 1,3-dipolar cycloaddition reactions of alkynes and azides].

Ring-Opening Reactions

IRMOF-3 reacts with propane-1,3-sultone and 2-methylaziridine in $CHCl_3$ at 45 ºC to produce the corresponding sulfonate and alkylamine derivatives via ring opening reactions (Scheme I.2.4). These reactions present several advantages as a route to new functionalities in MOFs. The wide variety of strained or reactive heterocycles readily available provides a range of functionalities that can be included. Such ring-opening reactions are irreversible, making it possible to use a functionalized MOF in gas adsorption, catalysis, or other application without loss of the relevant group. Finally, the groups added in this study have not proven to be readily accessible by traditional MOF synthesis (Scheme I.2.4).[25]

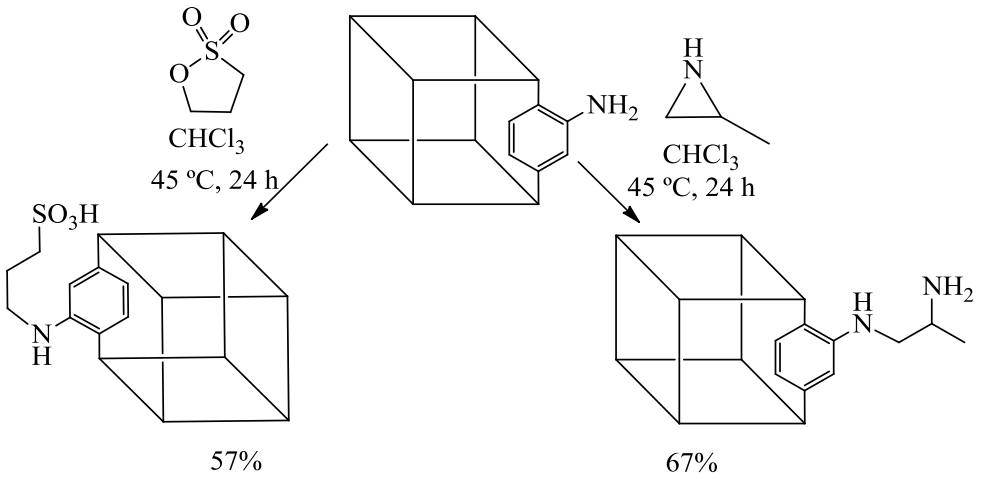

Scheme I.2.4 Reaction of IRMOF-3 with propane-1,3-sultone and 2-methylaziridine.

Both ring construction and opening reactions were done on a square paddle-wheel MOF $[Zn_2(TDC)_2L^1]$xDMF, TDC = 9,10-triptycenedicarboxylate, L^1 = 3-(but-3-enyl)-3'-methyl-

4,4'-bipyridine). Ring functionalized was performed by epoxidation of the olefinic group with dimethyldioxirane (DMDO) and the epoxide ring-opening was prepared by addition of ethyl mercaptan (Scheme I.2.5).[26]

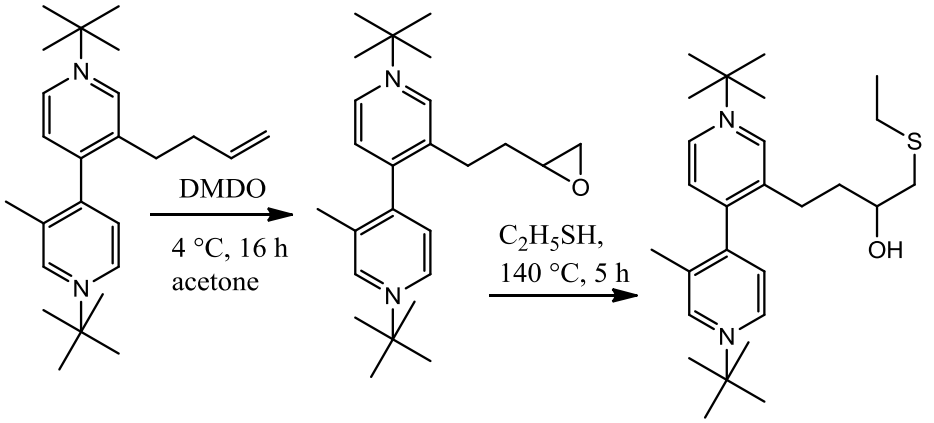

Scheme I.2.5 Two post-synthetic transformations of pyridine based-MOF: Epoxidation of an olefinic bond followed by ring opening with ethyl mercaptan.

Reactions with carboxylic anhydrides and iso(thio)cyanates

MIL-53(Al)-NH_2 was modified by treatment with acetic, succinic and maleic anhydrides which results in ~40% conversion of the amine sites to produce MOFs containing pendant carboxylate groups within the pores (Scheme I.2.6).[27]

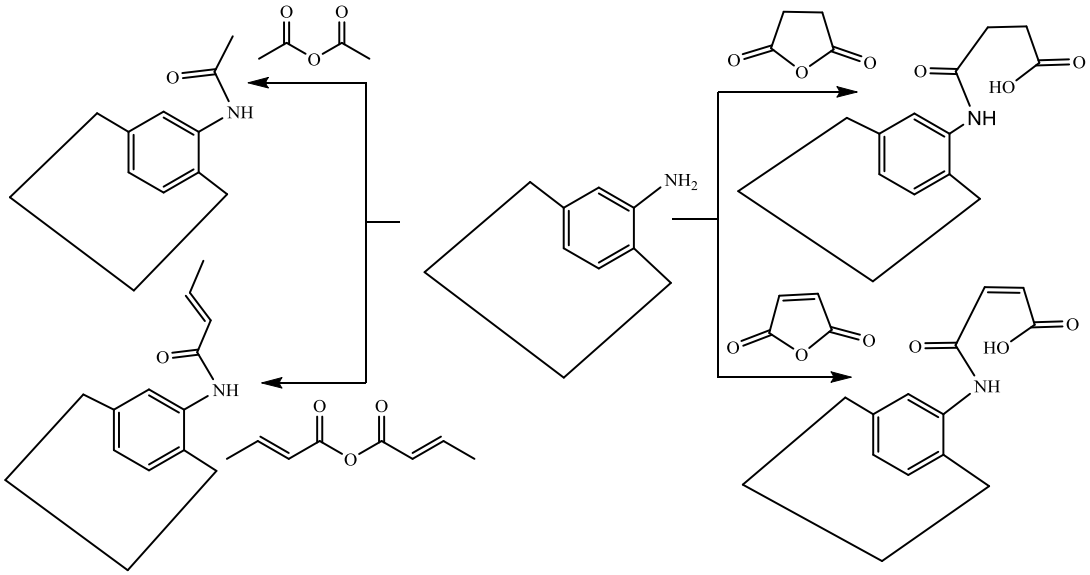

Scheme I.2.6 Reaction of MIL-53(Al)–NH_2 with alkyl anhydrides.

IRMOF-3 was modified by reaction with a series of carboxylic anhydrides. By this way, new MOF compounds with unprecedented chemical complexity were obtained (Scheme I.2.7).[27]

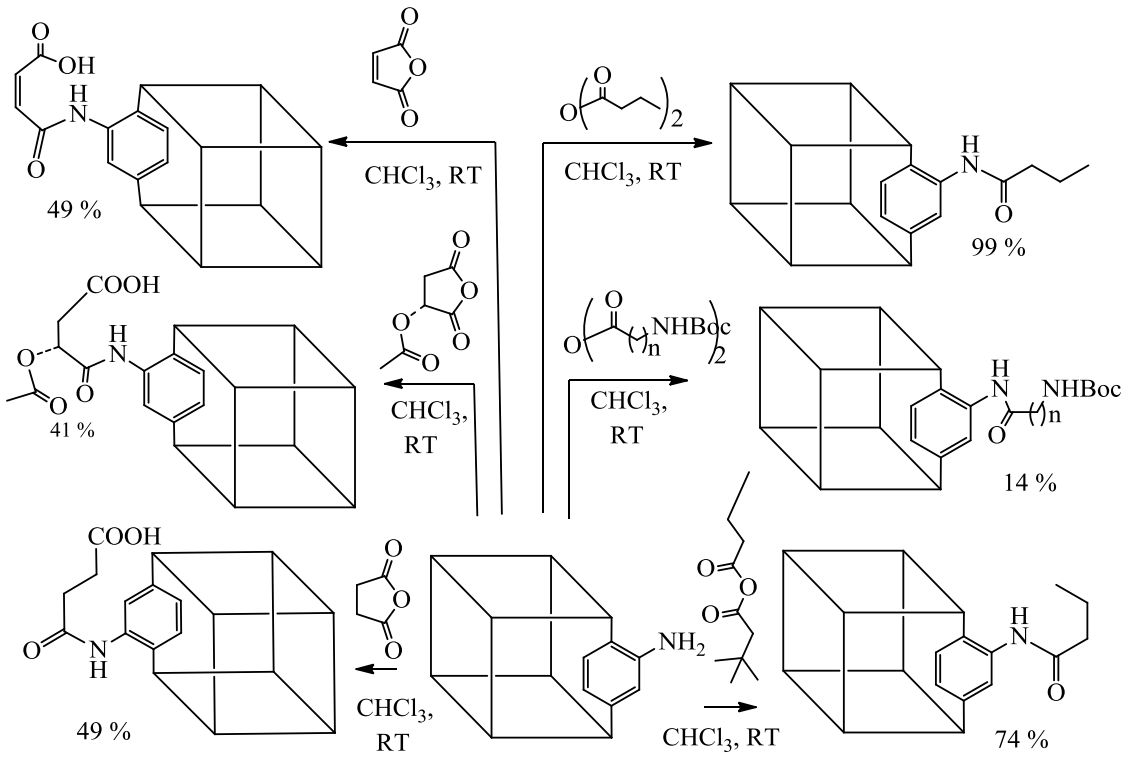

Scheme I.2.7 Post-synthetic modification of IRMOF-3 by reaction with aliphatic carboxylic anhydrides.

The covalent post-synthetic modification of UiO-66–NH_2 was explored using a series of aliphatic anhydrides to produce amide modified frameworks designated UiO-66–AM (Scheme I.2.8). The postsynthetic modification of UiO-66–NH_2 was accomplished with aliphatic and cyclic anhydrides and verified through a combination of ^{1}H NMR, IR, and ESI-MS analysis. The chemical stability of the UiO-66 framework and facile incorporation of functionalized or extended species, through reticular synthesis or post-synthetic modification, show that this class of porous solid can serve as a tunable, microporous scaffold for novel applications in separations, catalysis, and biotechnology.[28]

UHM-30 (UHM =University of Hamburg Materials) is a greenish crystalline material whose has the chemical formula of $Cu_3(NH_2btc)_2$ (NH_2btc = 2-amino-1,3,5-benzenetricarboxylate). It was prepared by solvothermal reaction of NH_2btc with $Cu(NO_3)_2.3H_2O$ in a mixture of dimethylacetamide and water. It shows good adsorption properties for a series of gases (H_2, CH_4 and CO_2). This MOF was modified with acetic anhydride affording amide functionality (Scheme I.2.9). The modification was confirmed by NMR spectroscopy, electrospray mass spectrometry (ESI-MS), N_2 physisorption, and

XRD. The presence of both ‘‘open’’ metal sites (Cu) and amino group in UHM-30 give to this MOF a great potential for use as NO storage material.[29]

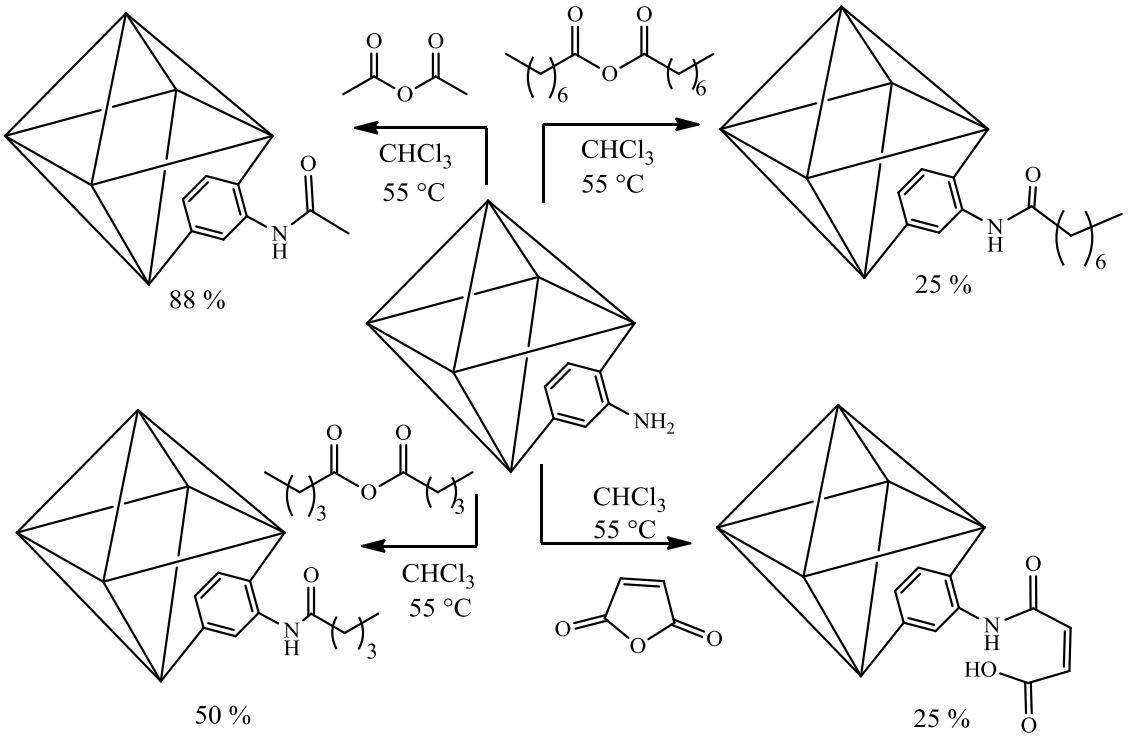

Scheme I.2.8 Reaction of UiO-66–NH_2 with aliphatic anhydrides.

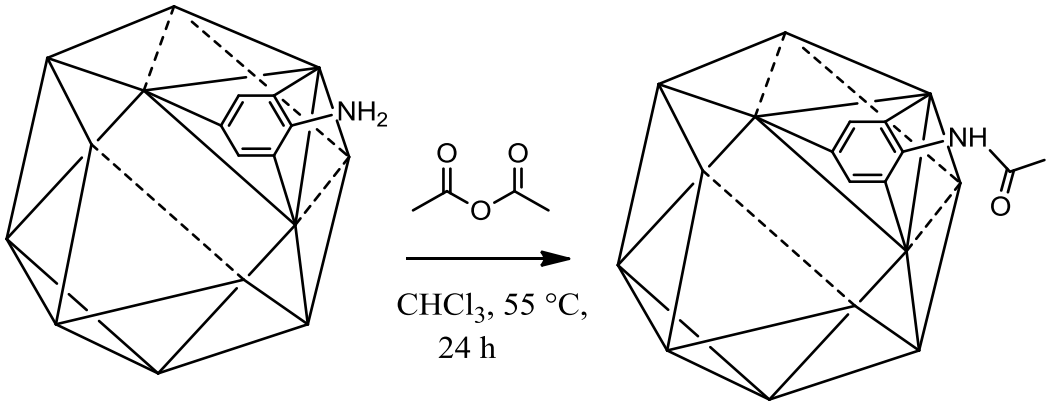

Scheme I.2.9 Reaction of MOF [$Cu_3(NH_2btc)_2$] with acetic anhydride.

To increase the hydrogen sorption of IRMOF-3, it was modified with aromatic anhydrides (benzoic anhydride) and isocyanates (phenylisocyanate) to produce amide-, urea-functionalized MOF (Scheme I.2.10). This study showed that by modification the gravimetric and volumetric uptake of the hydrogen gas was increased by 40 %. This effect is related to the binding of hydrogen with substituents introduced by PSM.[30]

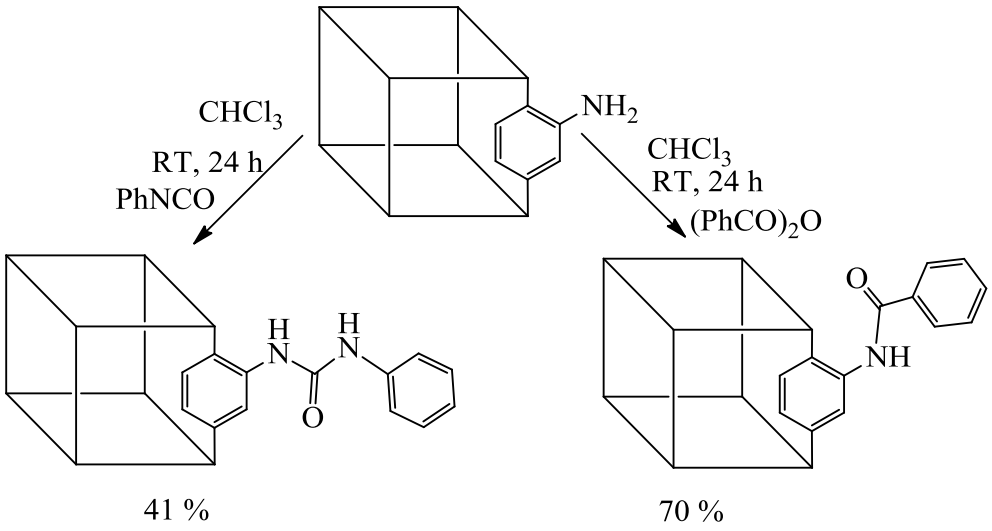

Scheme I.2.10 Reaction of IRMOF-3 with benzoic anhydride and phenylisocyanate.

UMCM-1-NH_2 was covalent post-synthetically modified with acetic, butyric, benzoic, and 4-(trifluoromethyl)benzoic anhydrides producing UMCM-1-NHCO-Me, -Pr, -Ph, and -$PhCF_3$, respectively (Scheme I.2.11). The results of study showed an enhancement on the carbon dioxide adsorption. The authors have also studied the methane adsorption and at every tested temperature, the adsorbed amounts of CH_4 were ranked: UMCM-1-NHCO-Ph > UMCM-1-NHCO-$PhCF_3$ > UMCM-1-NH_2 > UMCM-1-NHCO-Me > UMCM-1-NHCO-Pr. In contrast, CO_2 uptake was ranked as follows: UMCM-1-NHCO-Ph > UMCM-1-NHCO-$PhCF_3$> UMCM-1-NHCO-Me > UMCM-1-NHCO-Pr > UMCM-1-NH_2. This means that the aromatic electron-withdrawing groups enhanced CO_2 uptake more than the electron-donating alkyl groups.[31] MOF-LIC-1 reacted with ethylisocyanate to produce a urea derivative and with acetic acid to produce an amide functional group without any change in crystallinity of the starting MOF (Scheme I.2.12). The modified MOF can be used in heterogeneous catalysts.[32]

MIL-101(Cr)-NH_2 was covalent post-synthetically modified by treatment with 4-phenylazobenzoyl chloride and 4-(phenylazo)phenylisocyanate to produce Cr-MIL-101-amide and Cr-MIL-101-urea. By this way, it was possible to introduce a photo-switchable functional group (azo-function) into the mesoporous cages (Scheme I.2.13). In this study it was investigated the influence of the degree of functionalization on the reversible *cis/trans*-isomerization of the covalent attached azobenzene derivatives using UV/Vis spectroscopy as well as methane gas adsorption measurements.[33]

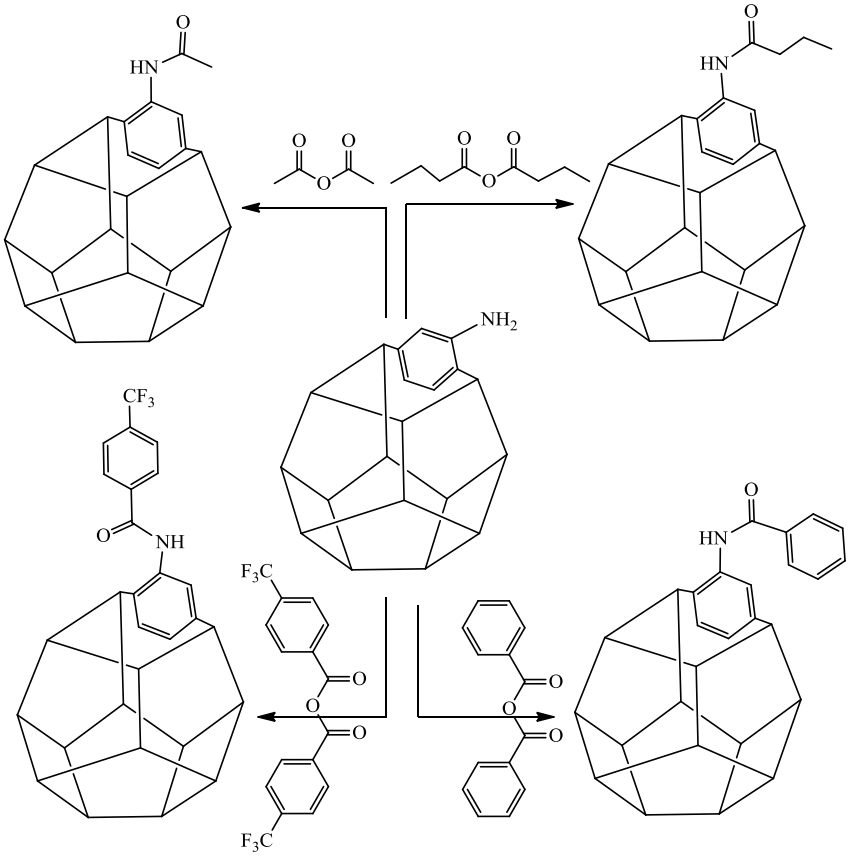

Scheme I.2.11 Reaction of UMCM-1-NH_2 with acetic anhydride, butyric anhydride, benzoic anhydride and 4-(trifluoromethyl)benzoic anhydride.

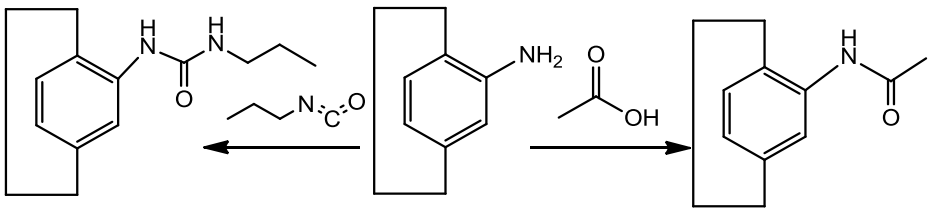

Scheme I.2.12 Reaction of MOF-LIC-1 with ethylisocyanate and with acetic acid.

The free amine groups of MIL-53(Al)–NH_2 was transformed into reactive iso(thio)cyanates using diphosgene or thiophosgene. The resulting MIL-53(Al)–NCX (X=O or S) reacts with amines and alcohols to produce (thio)urea and (thio)carbamate-bearing MILs (Scheme I.2.14).[34] Al-MIL-53-NH_2 and In-MIL-68-NH_2 was reacted with *tert*-butylnitrite (^{t}BuONO) and trimethylsilyl-azide ($TMSN_3$) to produce azido groups, and then the produced nitrene species react with carbon monoxide to yield an isocyanato-functionalized MOF. An alternative way involves the reaction of the amino-MOF with phosgene.

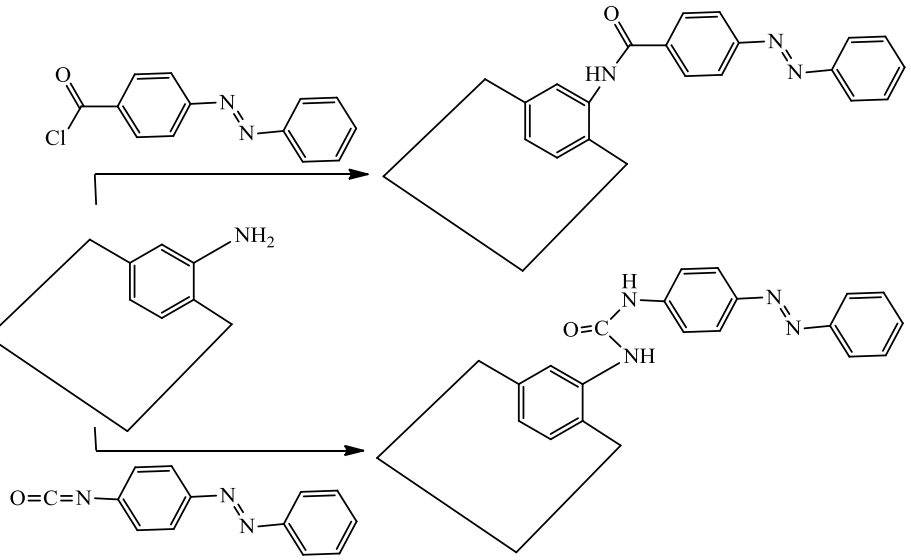

Scheme I.2.13 Reaction of Cr-MIL-101-NH_2 with *p*-phenylazobenzoyl chloride and 4-(phenyl-azo)phenylisocyanate.

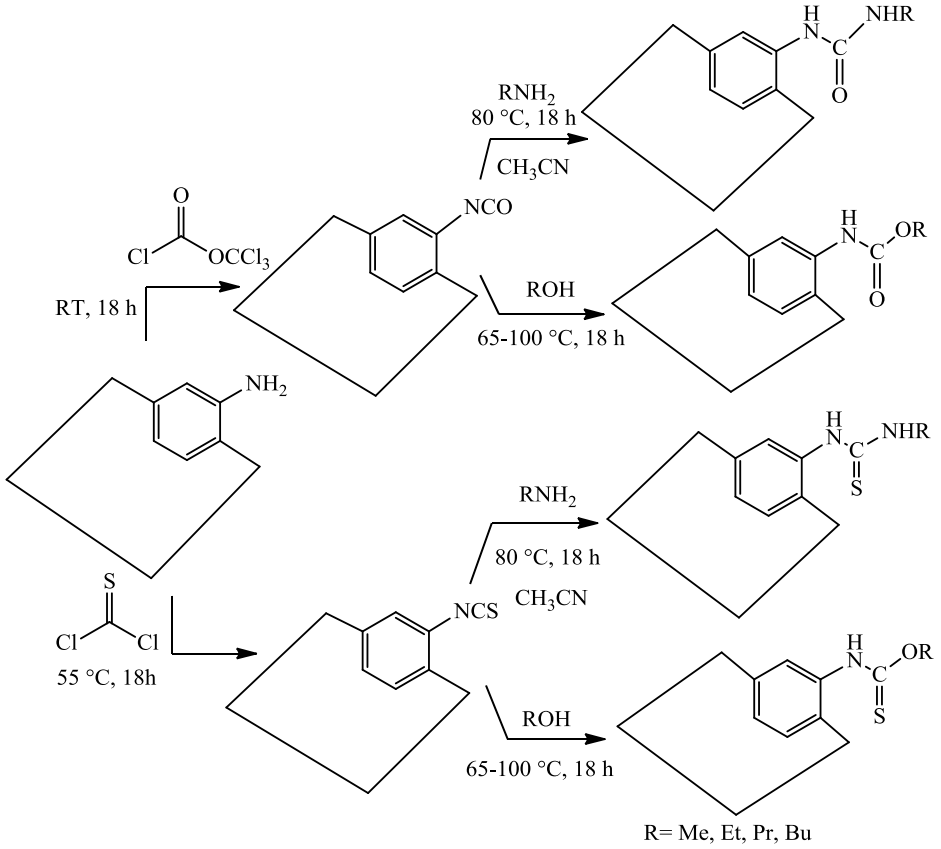

Scheme I.2.14 Reaction of MIL-53(Al)–NH_2 with phosgene or thiophosgene followed by reaction with alkyl amines and alkyl alcohols.

The urea-functionalized MOF was synthesized via condensation of amines with isocyanato-MOF (Scheme I.2.15). This study opens the door to design organometallics derivatives to be used in metal-catalyzed transformations.[35]

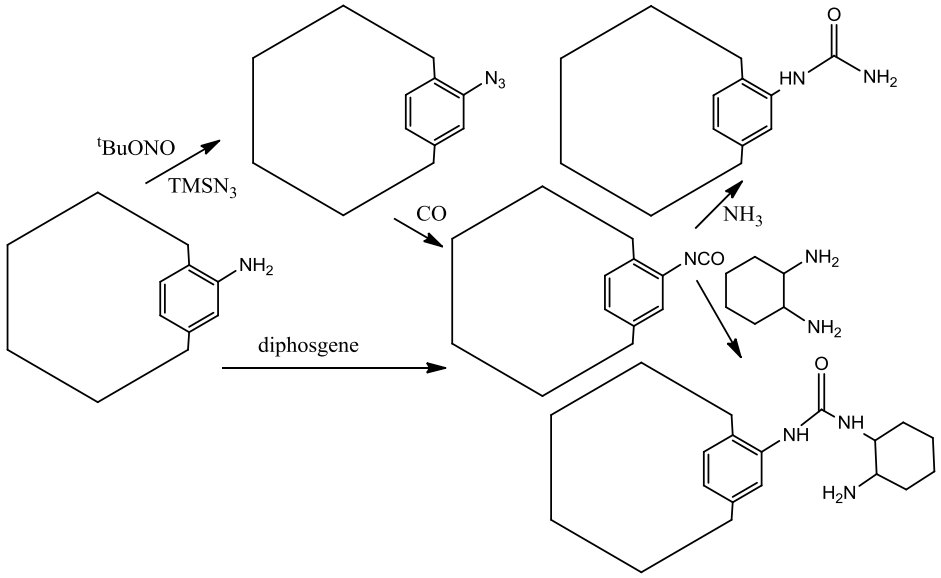

Scheme I.2.15 Converstion of the amino group into an isocyanate by two different ways, followed by the reaction with amonia and amines.

Diazeniumdiolate group formation

UMCM-1–NH_2 is an excellent candidate for NO delivery and release. UMCM-1–NH_2 was exposed to NO at room temperature for 24 hours to yield UMCM-1–NONO (Scheme I.2.16).[36]

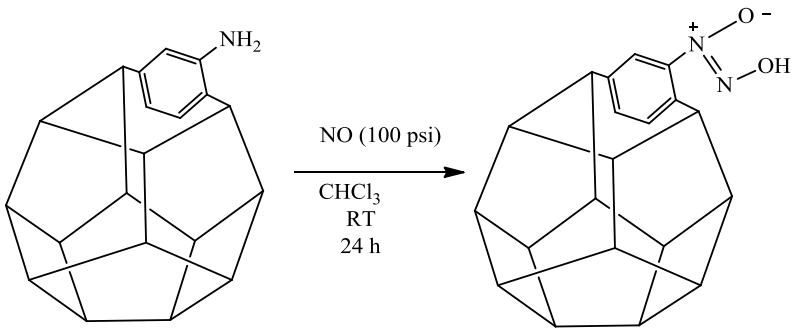

Scheme I.2.16 Reaction of UMCM-1-NH_2 with nitric oxide.

IRMOF-3 is also an excellent candidate for NO delivery and release. The amino group of IRMOF-3 react with NO at room temperature for 24 hours to yield IRMOF-3–NONO (diazeniumdiolate) (Scheme I.2.17). The NONOate functional group would not be attainable in a MOF by traditional solvothermal synthesis. More importantly, NO-release studies showed that NONOate modification is specific to MOFs containing the NH_2–bdc ligand and those large amounts of "absorbed" NO can be liberated. Overall, these results showed that covalent PSM provides an excellent avenue for the production of NO-releasing MOFs.[36]

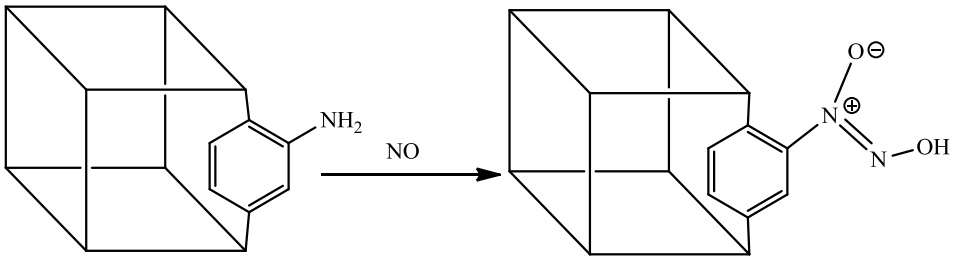

Scheme I.2.17 Reaction of IRMOF-3 with nitric oxide.

Sulfation reaction

Sulfated-functionalized MOF was obtained by adding chemically stable MIL-101(Cr) and MIL-53(Al) to a mixture of triflic anhydride and sulfuric acid. The yield of the Brønsted sulfoxy acid group attached to the backbone of MOF is up to 50% (Scheme I.2.18).

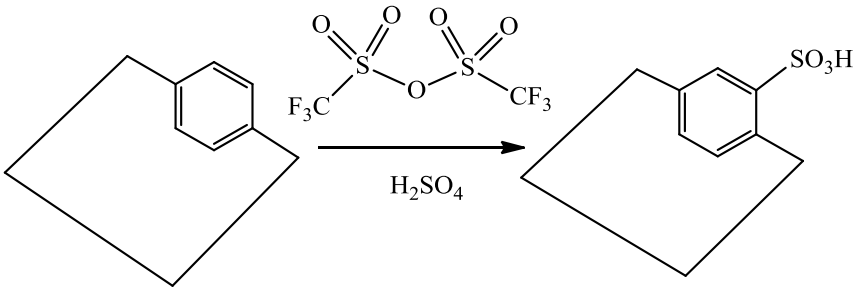

Scheme I.2.18 Reaction of MIL-101(Cr) with a mixture of triflic anhydride and sulfuric acid.

The techniques used to study the structure are solid-state NMR, XANES, and FTIR spectroscopy. Sulfated-MOF show catalytic activity similar to that of acidic polymers like Nafion display in the esterification of n-butanol with acetic acid (TOF 1 min^{-1}@ 343 K). This is not only the uses of modified material but also it is used proton conductivity. The results show high proton conductivity, because the material adsorbed water and it is acting as conductor in a continuous phase. [37]

Nitration

MIL-101(Cr) was directly modified through an electrophilic substitution reaction using nitric acid and sulfuric acid to produce the nitro-functionalized MOF MIL-101(Cr)-NO_2 (Scheme I.2.19). The studies were done to confirm that the afforded nitro-functionalized MOF can be submitted to a reduction reaction conditions. The nitro group was converted into an amino group with $SnCl_2$. Further confirmation of this transformation was done by reaction of the amino-MOF with ethyl isocyanate to yield a urea derivative.[38]

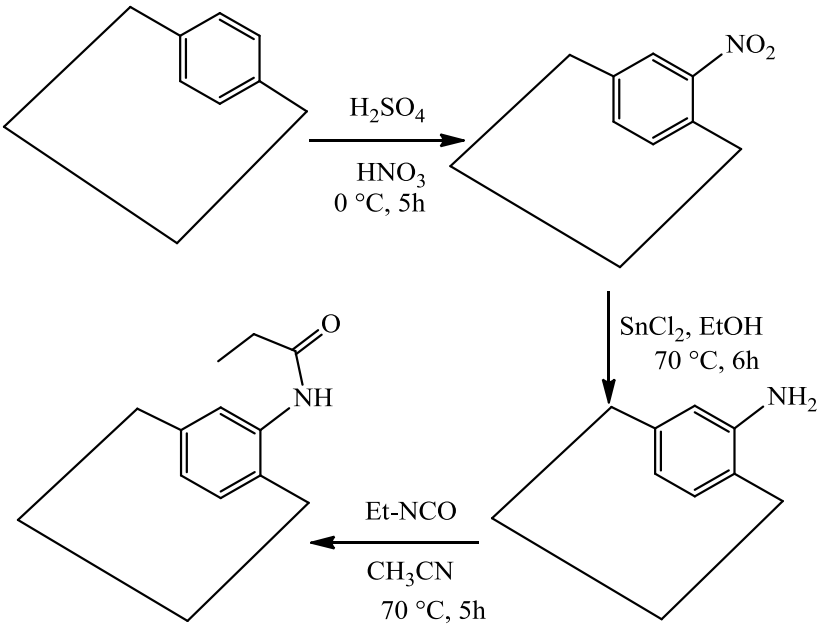

Scheme I.2.19 Reaction of MIL-101(Cr) with sulfuric acid and nitric acid, followed by reduction of the nitro group to produce Cr-MIL-101–NH_2 which further reacted ethyl isocyanate to afford a urea-functionalized MOF.

Chloromethylation

MIL-53(Al) and MIL-101(Cr) were reacted with methoxyacetyl chloride, in the presence of aluminium chloride to produce a chloromethylene-functionalized MOF. This method of chloromethylation is safe, does not destroy the framework and give high yield of the chloromethylated derivative (50%).

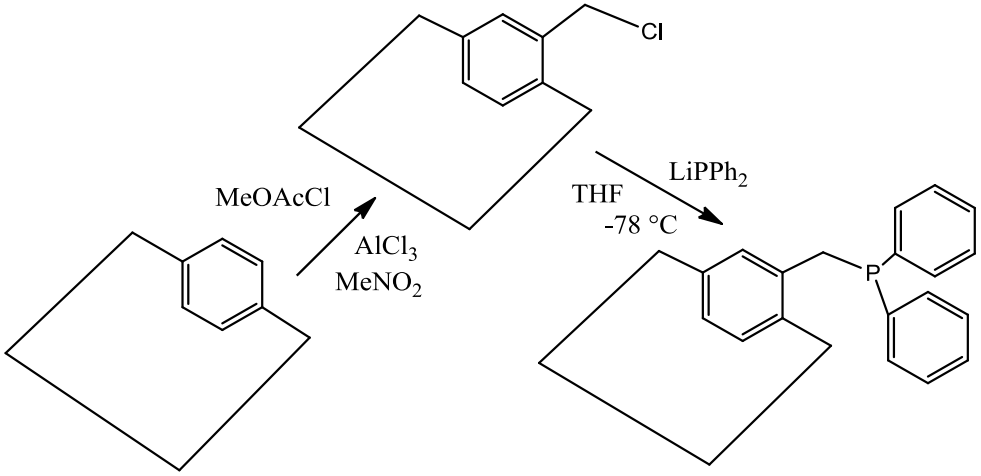

Scheme I.2.20 Chloromethylation of MIL-101(Cr) followed by the reaction with diphenylphosphine.

The confirmation of modification was done by the reaction and introduction of a diphenylphosphine moiety (PPh_2) (Scheme I.2.20).[39]

Exchange of a bromo substituent by a cyano group

Cyano-functionalized MOF (UiO-66-CN) was synthesized by microwave-assisted cyanation (CuCN) of an aryl bromide functionalized MOF (UiO-66-Br). A typical procedure consisted in the microwave irradiation (170 °C, 10 min) of a suspenstion of UiO-66-Br in *N*-methyl-2-pyrrolidone (NMP) producing UiO-66-CN in ca. 90% yield (Scheme I.2.21).[40]

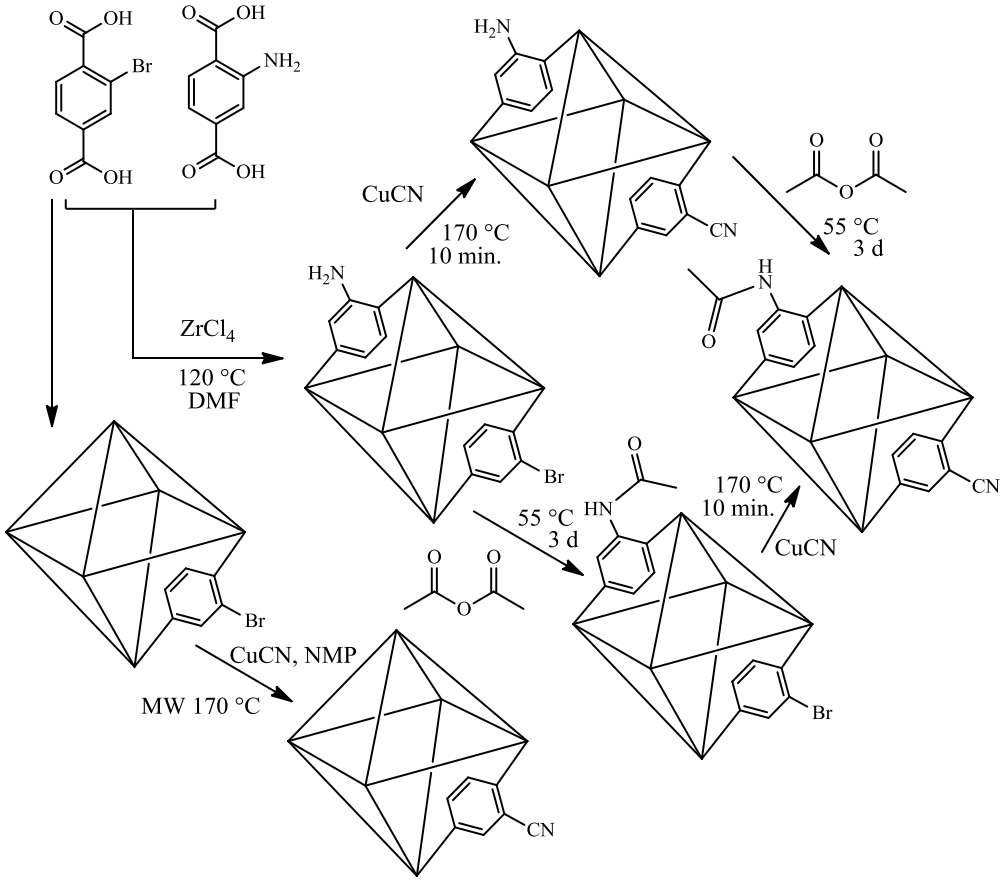

Scheme I.2.21 Synthesis and post-synthetic modification of mixed UiO-66-(Br)(NH_2).

Bifunctional UiO-66-(Br)(NH_2) was prepared by a solvothermal process, by adding 2-aminoterephthalic acid and 2-bromoterephthalic acid to $ZrCl_4$ in DMF and heating the mixture at 120°C for 24 h (Scheme I.2.21). Powder X-ray diffraction of the resulting material showed the same structure as other UiO-66 materials. UiO-66-(Br)(NH_2) was then submitted to a cyanation in the bromoaryl ring by reacting it with CuCN under microwave irradiation conditions to produce the cyano-functional MOF with 95% conversion. After that, UiO-66-(CN)(NH_2) was reacted with acetic anhydride for the amino group acylation. The final product can also be obtained performing the acylation prior to the cyanation (Scheme I.2.21).[41]

Acylation and N-alkylation

Acylation of Fe(III)-carboxylate nanoscale metal-organic frameworks (NMOFs) with ethoxysuccinato-cisplatin (ESCP) prodrug, *c*,*c*,*t*-[$PtCl_2(NH_3)_2(OEt)(O_2CCH_2CH_2CO_2H)$], in DMF at room temperature was used to provide a therapeutic payload. Similarly, the alkylation of a potential optical imaging contrast agent diaza-s-indacene (Br-BODIPY) in THF at room temperature was used to integrate it as an imaging component (Scheme I.2.22). SEM imaging showed no change in the particle size or morphology after ESCP and BODIPY loading. This material was used for delivering high payloads of imaging contrast agents and anticancer drugs.[42]

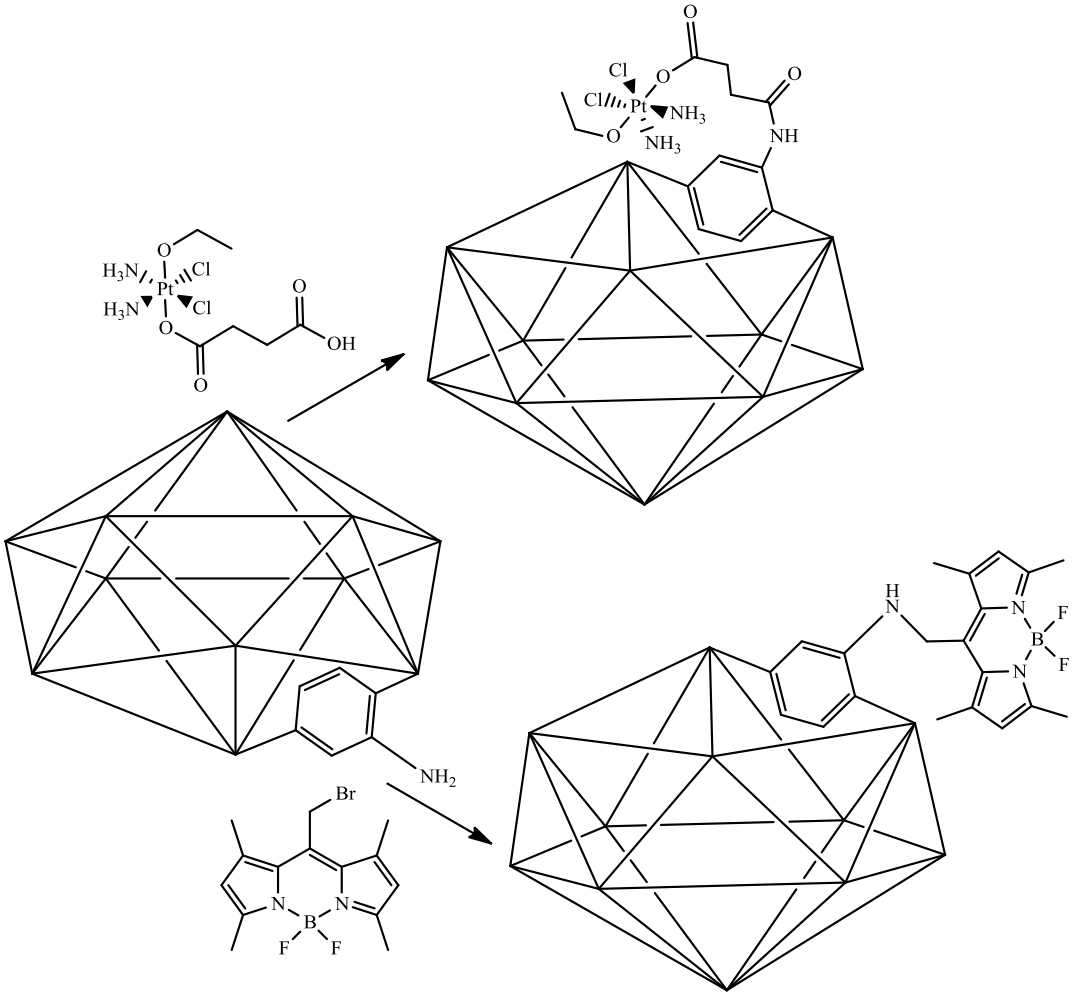

Scheme I.2.22 Reaction of MIL-101–NH_2 with cisplatin and Br-BODIPY.

The reaction of POST-1 with an excess of CH_3I at room temperature for 2 h lead to the formation of *N*-methylpyridinium ions (Scheme I.2.23). ^1H NMR and Raman spectroscopy confirms the structure and the presence of I^- counter ions.[12]

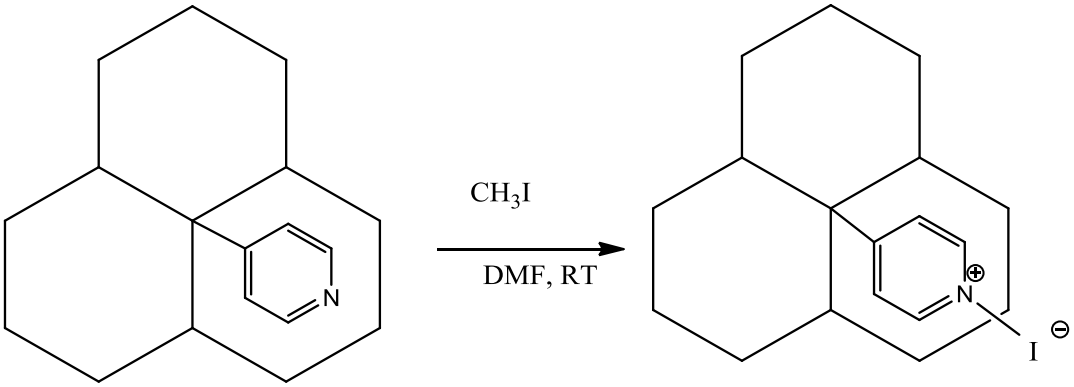

Scheme I.2.23 Alkylation of POST-1 with CH_3I.

IRMOF-3 was post-synthetically modified with cyanuric chloride in presence of triethylamine (Scheme I.2.24). X-ray diffraction confirms that the crystalline structure of MOF is maintained during the modification reaction and N_2 isotherms show the presence of micro- and meso-porosity in IRMOF-3 after modification.[43]

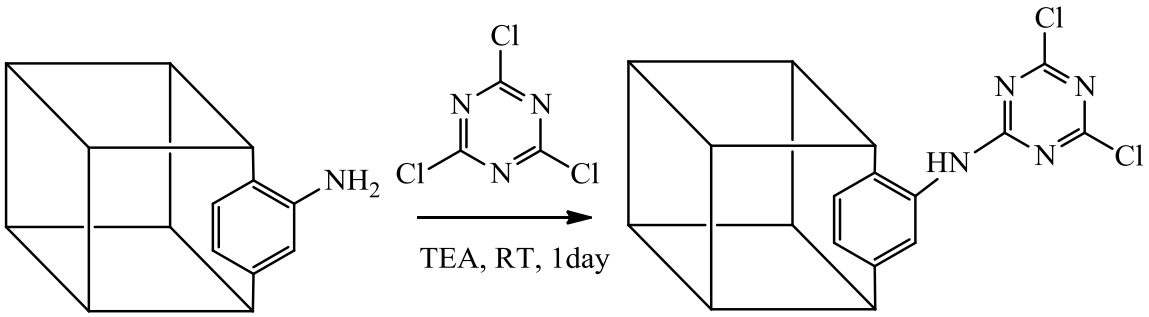

Scheme I.2.24 Reaction of IRMOF-3 with cyanuric chloride.

Thioether oxidation

Sulfur-tagged metal–organic frameworks (IRMOF-9) was synthesized by treatment of $Zn(NO_3).6H_2O$ with 4,4'-biphenyldicarboxylic acid. Oxidative post-synthetic modification was done with dimethyldioxirane (DMDO) in acetone at room temperature converting the sulfide tags to the corresponding sulfone with 23% yield (Scheme I.2.25).[44]

Hydrazone formation

A formyl-functionalized MOF was synthesized by adding 2-formylbiphenyl-4,4'-dicarboxylic acid to $Zn(NO_3)_26H_2O$ in DMF at 100 °C for 24 h. Post-synthetic modification of the tagged (formyl)metal–organic framework was done by reaction with 2,4-nitrophenylhydrazone at room temperature for a week to afford the orange-red hydrazone-functionalized MOF crystals (yield 60 %) (Scheme I.2.26).[45]

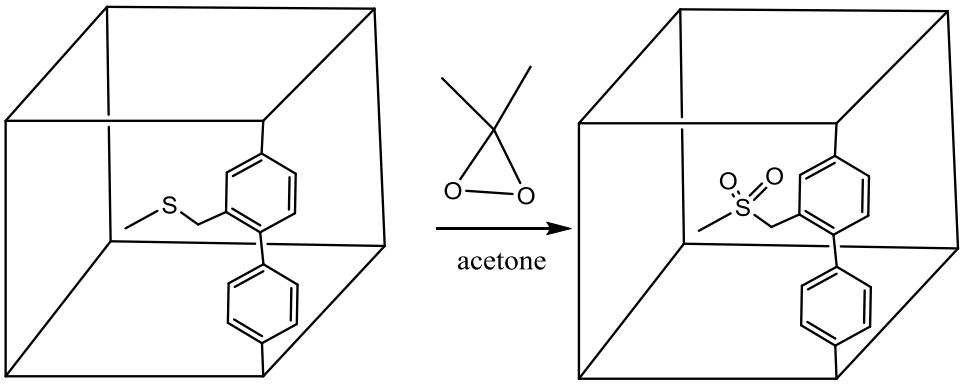

Scheme I.2.25 PSM of an IRMOF-9 analog by sulfur oxidation with dimethyldioxirane (DMDO)

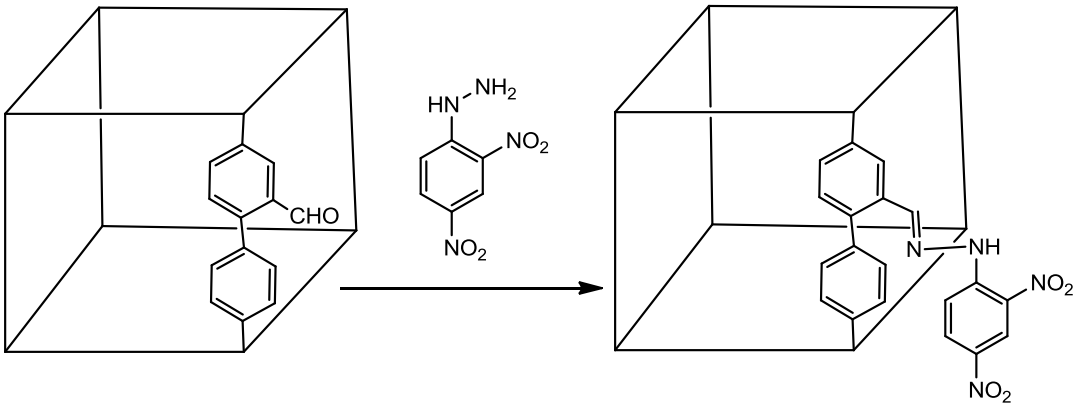

Scheme I.2.26 Post-synthetic modification of a formyl-functionalized-MOF to add a hydrazone moiety.

Thermolysis

Thermolysis is a chemical decomposition of MOFs by using heat. For example, Al-MIL-53–COOH {[Al(OH)(bdc–COOH)].0.9H_2O} was obtained under solvothermal conditions. It has high structural flexibility and large-pores obtained from the activation process of the framework consisting in the removal of water from pores. Al-MIL-53–COOH was thermally modified producing two compounds, the first compound resulted from the partial decarboxylation and the second one was an acid anhydride due to condensation of neighboring non-coordinating carboxylic acid groups of MOF (Scheme I.2.27). The nitrogen sorption measurements of this material confirm that its capacity depends strongly on the degree of decarboxylation; increasing the degree of decarboxylation increases the N_2 sorption because the pores become accessible to nitrogen. This is due to a decrease of intraframework interactions in the MOF.[46]

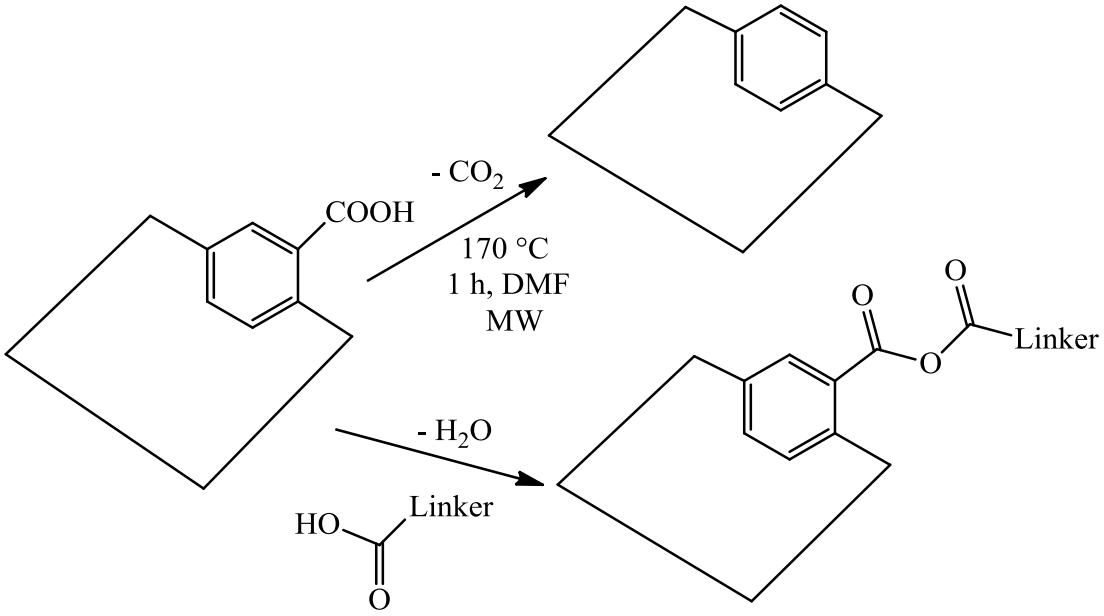

Scheme I.2.27 Effect of heat on Al-MIL-53–COOH.

An allyloxy-functionalized metal-organic framework was prepared by adding 2-(allyloxy)-[1,1'-biphenyl]-4,4'-dicarboxylic acid to $Zn(NO_3)_2.6H_2O$ in hot DMF. Single crystal analysis shows that the new MOF has a cubic structure like those of the IRMOF series. Under thermal condition, allyloxy-MOF was changed through a Claisen rearrangement (Scheme I.2.28). The pendant allyloxy tag group was rearranged and gave a free hydroxyl group at 260 °C, while at temperatures of 300 °C it gives a furan ring. This study opened the door to post-modification of the frameworks via thermal rearrangement in reagentless conditions.[47]

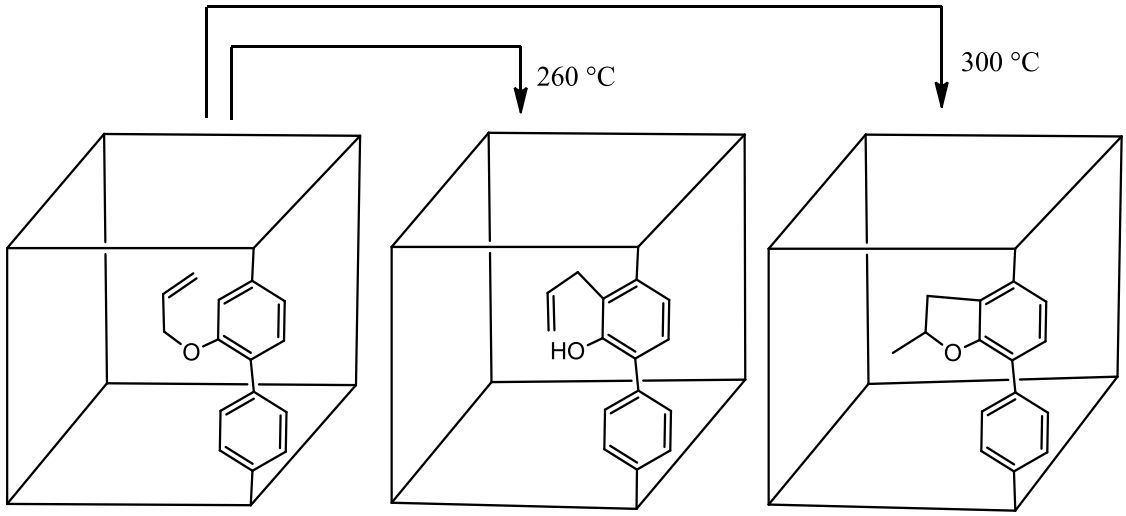

Scheme I.2.28 A reagentless thermal post-synthetic rearrangement of an allyloxy-tagged metal–organic framework.

The protected Boc-IRMOF-9 analog (BOC = *tert*-butoxycarbonyl) was thermally deprotected giving the deprotected-IRMOF-9 analog (Scheme I.2.29). The permanent pore of MOF was not changed, and the new modified material has impact on sorption properties, since the protecting group prevent the uptake of sorbates.[48]

N-Boc-proline decorated ligand was synthesised by the reaction of dimethyl 2-aminobiphenyl-4,4-dicarboxylate with *N*-Boc-L-proline. This ligand was connected with zinc ions to form IRMOF-Pro-Boc via a solvothermal reaction in presence of *N*,*N*-diethylformamide (DEF). IRMOF-Pro-Boc was thermally deprotected to afford the organocatalyst metal-organic framework (IRMOF-Pro) (Scheme I.2.30). IRMOF-Pro has catalytic activity on the asymmetric aldol reaction of acetone or cyclopentanone with 4-nitrobenzaldehyde to give 4-hydroxy-4-(4-nitrophenyl)pentan-2-one or (4-nitrophenyl) hydroxymethylcyclopentanone, but IRMOF-Pro-Boc is inactive to the aldol reactions this meaning that unprotected pyrrolidine groups are responsible for the catalytic activity.[49]

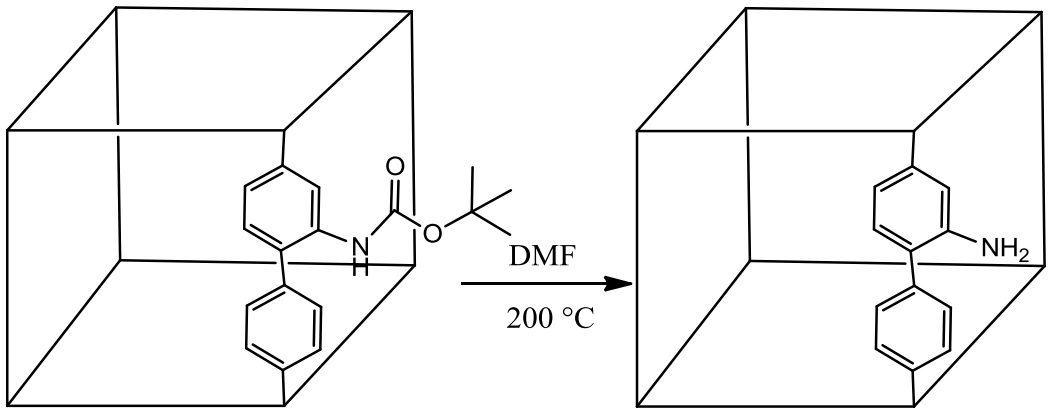

Scheme I.2.29 A thermal deprotection of a Boc-IRMOF-9 analog.

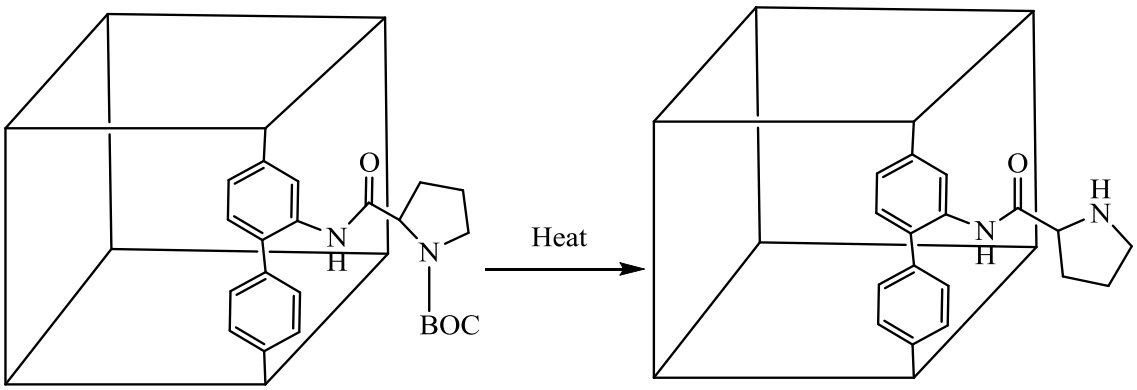

Scheme I.2.30 Thermal Boc-deprotection of an IRMOF-9 analog.

Deprotection reactions

The amino group of MIL-68-(In)-NH_2 was protected with two different coupling procedures: i) in the first one there the reaction with +*(D)*-Fmoc-Ala-OH (Ala = alanine, Fmoc = fluorenylmethyloxycarbonyl group) in presence of 4-(dimethylamino)pyridine (DMAP) and bromo-trispyrrolidinophosphonium hexafluorophosphate (PyBroP); and ii) in the second one there is the reaction with +(L)-Fmoc-Pro-OH (Pro = proline) in the presence of both PyBroP and DMAP.

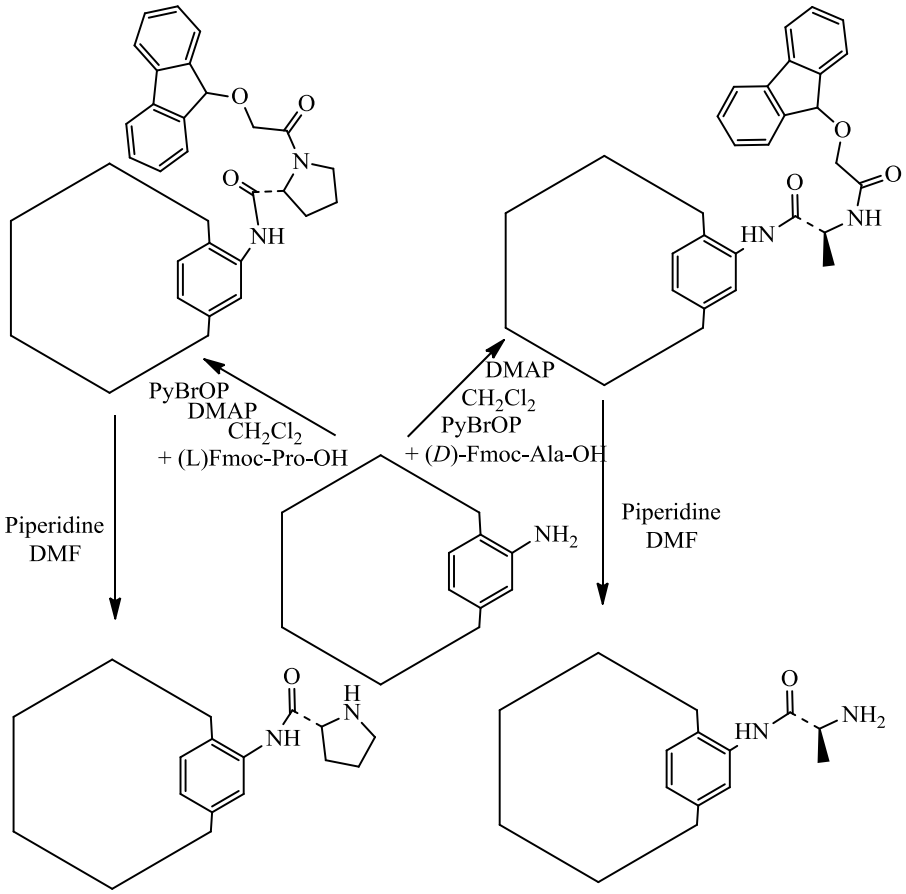

Scheme I.2.31 Anchoring chiral functional groups into the framework by a two-step MOF functionalization through peptide coupling.

These authors used PyBroP combined with DMAP (base additive) as a very efficient homogeneous coupling agent rather than the *N*,*N*'-dicyclohexylcarbodiimide (DCC), because DCC produce an insoluble solid *N*,*N*'-dicyclohexylurea (DCU) which is difficulty to separate from the parent MOF. Both of the two modified materials were subjected to a chemically-assisted deprotection using piperidine in DMF (Scheme I.2.31). This methodology offers new tend for anchoring chiral functional groups into the framework in order to obtain highly catalytically active and/or metal-coordinating moieties.[50]

Click chemistry

IRMOF-3 was modified by the reaction with pent-4-enoic anhydride to produce IRMOF-3-$(AMPent)_n$. This material has smaller pore size and steric crowding of the olefin groups but it reacted with dimethyl 1,2,4,5-tetrazine-3,6-dicarboxylate via a Diels-Alder cycloaddition reaction to produce a MOF bearing a dihydropyridazine moiety. The structure of this material was confirmed by ^{1}H NMR spectra, ESI-MS analysis and single-crystal XRD. The final IRMOF-3-AMPent-TDC is a highly crystalline material (Scheme I.2.32).[51]

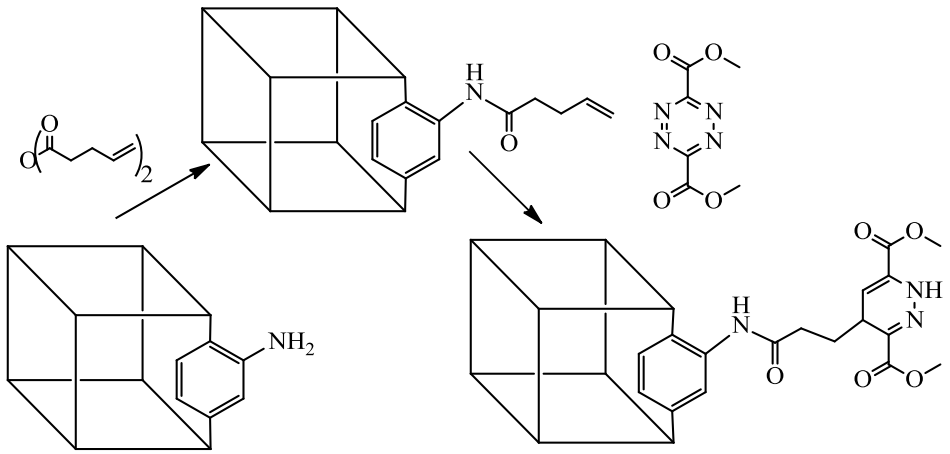

Scheme I.2.32 Reaction of IRMOF-3 with pent-4-enoic anhydride followed by a Diels-Alder cycloaddition reaction.

UMCM-1-NH_2 was also subjected to the same type of modification by reaction with pent-4-enoic anhydride to produce a functionalized MOF (UMCM-1-AMPent) with an olefin group appended in the benzene-1,4-dicarboxylate ligands. UMCM-1-AMPent reacts with dimethyl-1,2,4,5-tetrazine-3,6-dicarboxylate (TDC) via Diels-Alder cycloaddition to produce a MOF bearing a dihydropyridazine moiety (UMCM-1-AMPent-TDC). The structure was confirmed by ^{1}H NMR spectroscopy. Single-crystal X-ray diffraction indicates that it's a highly crystalline, stable and microporous material (Scheme I.2.33).[51]

The amino group of DMOF-1–NH_2 was converted into an azide by the reaction with ^{t}BuONO and $TMSN_3$. Then DMOF–N_3 was treated with an excess of phenylacetylene and $Cu(CH_3CN)_4PF_6$ to generate the 1,2,3-triazole modified DMOF, named DMOF–fun, via click chemistry with an yield of > 90% (Scheme I.2.34).[52]

The amino-functionalized MOF (DMOF) was converted into their azido-analogous, using the same transformation described above. Then through a (3+2) cycloaddition (click chemistry) reaction between the azido group and phenylacetylene or propargylamine and or both (Scheme I.2.35), a series of modified functionalized materials were produced, bearing

new basic catalytic centers (amino groups) and lipophilic groups (phenyl groups). This study also showed that the catalytic activity on the transesterification of ethyldecanoate, a fatty ester, in methanol was enhanced in the presence of the obtained PSM-MOFs.[53]

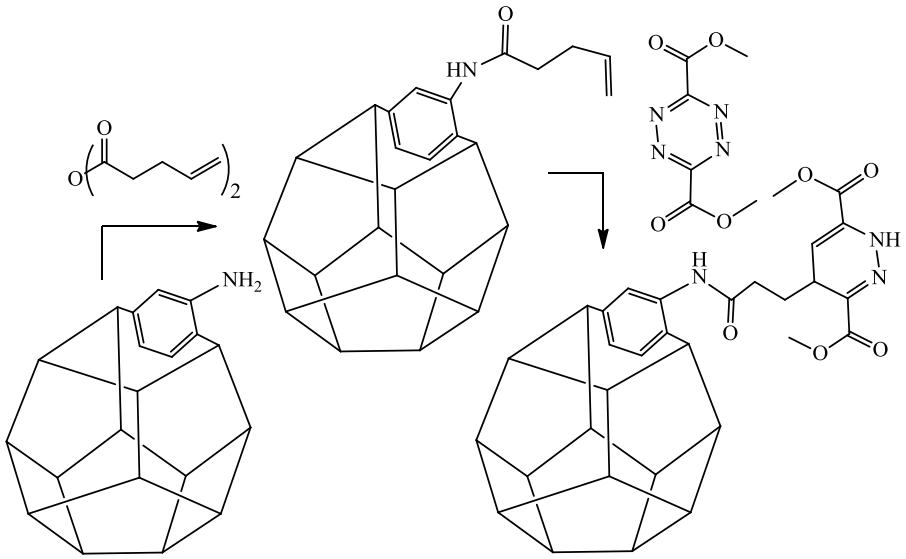

Scheme I.2.33 UMCM-1-NH_2 was modified by reaction with pent-4-enoic anhydride followed by a Diels-Alder reaction with TDC.

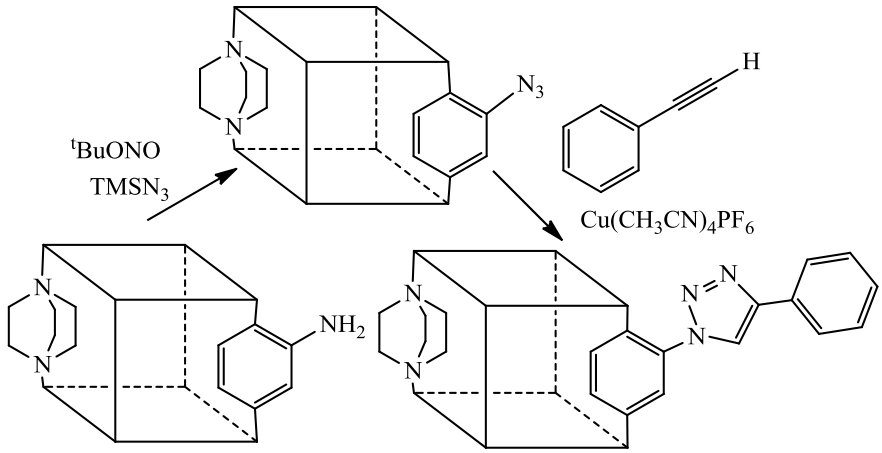

Scheme I.2.34 Synthesis of a 1,2,3-triazole MOF by PSM and using click chemistry.

MIL-68(In)-NH_2 reacted with *t*-BuONO and $TMSN_3$ in THF for one night at room temperature, to introduce the azide group. The resulting MOFs-N_3 reacted with alkynes in the presence of Cu(I)$(CH_3CN)_4PF_6$ to produce a triazole ring bearing different side chains (Scheme I.2.36). The degrees of post-modification of amino-MOFs with different alkynes was very high (90%, calculated from liquid ^{1}H NMR analysis). This study will open the way to produce porous coordination polymers with different properties (adsorption and catalysis).[54]

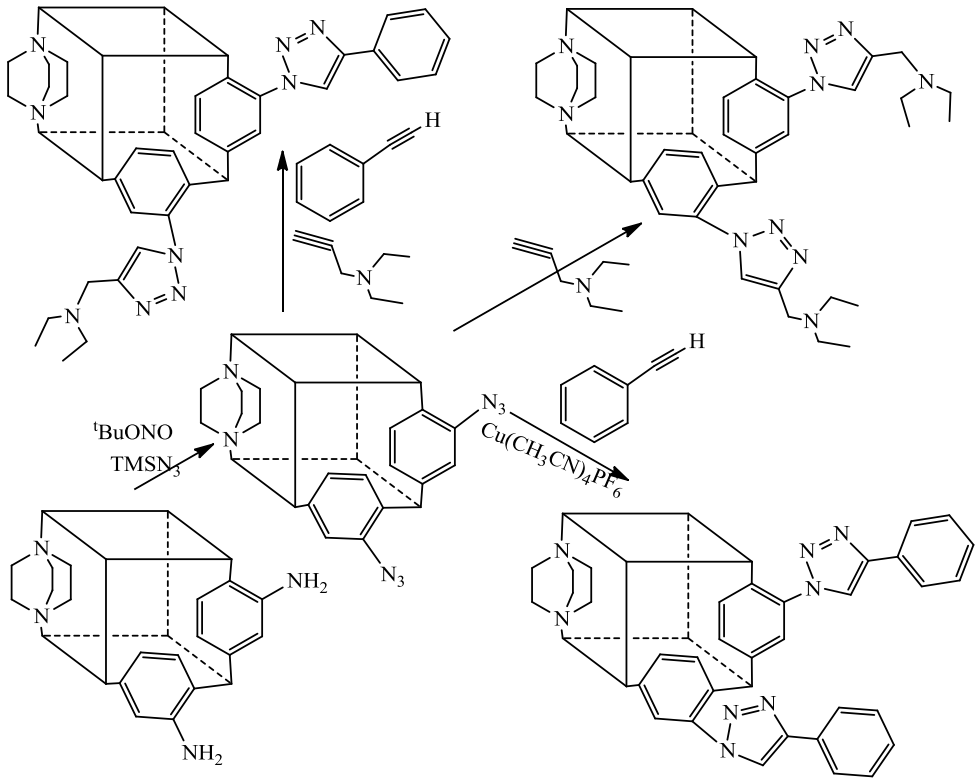

Scheme I.2.35 Studies on the DMOF post-synthetic modifications, by introduction an azide group followed by their (3+2) cycloaddition reaction.

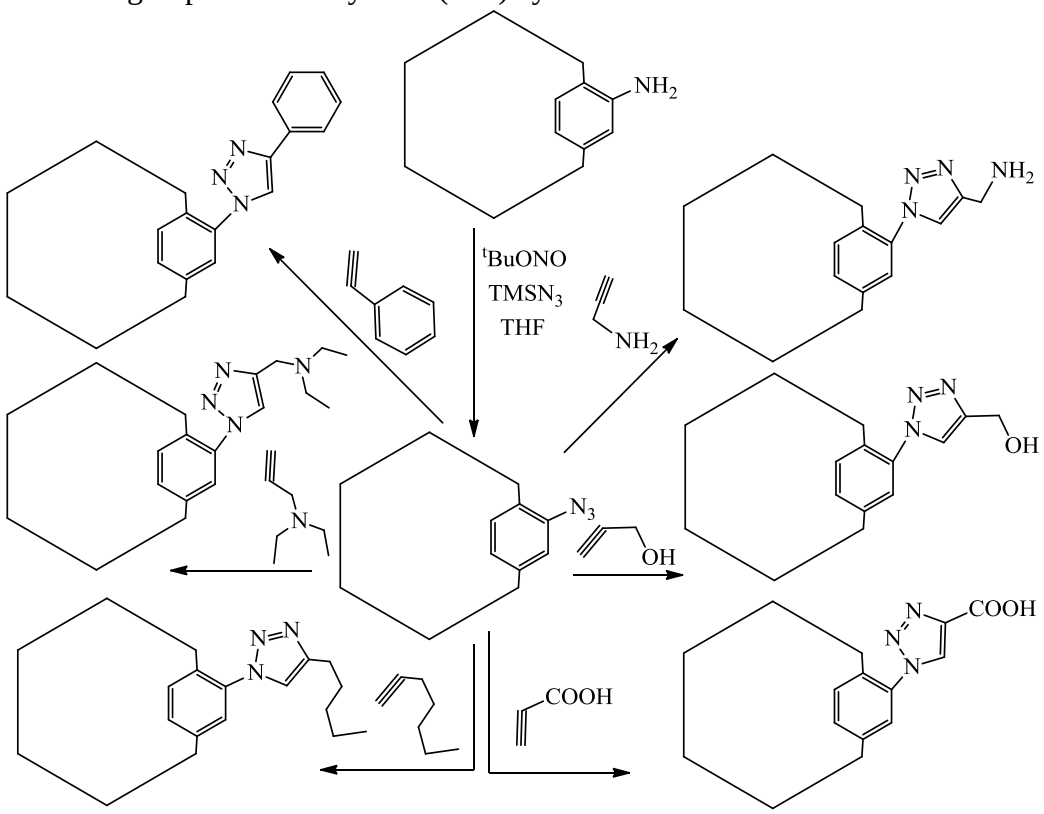

Scheme I.2.36 the reaction of MIL-68 (In)-NH_2 with *t*-BuONO and $TMSN_3$ followed by the (3+2) cycloaddition reaction with alkynes.

PIZOF-(OMe, $OCH_2C{\equiv}CH$) was designed from $Zr_6O_4(OH)_4(CO_2)_{12}$ as the nodes and the dicarboxylates $^-O_2C[PE\text{-}P(R^1,R^2)\text{-}EP]CO_2^-$ (P: phenylene, E: ethynylene; R^1 = OMe, R^2 = $OCH_2C{\equiv}CH$) as the linkers. The pendant ethyne moieties of PIZOF-(OMe, OCH2C≡CH) was reacted with 4-methylbenzyl-azide via 1,3-dipolar cycloaddition giving the expected material in 98% yield (Scheme I.2.37).

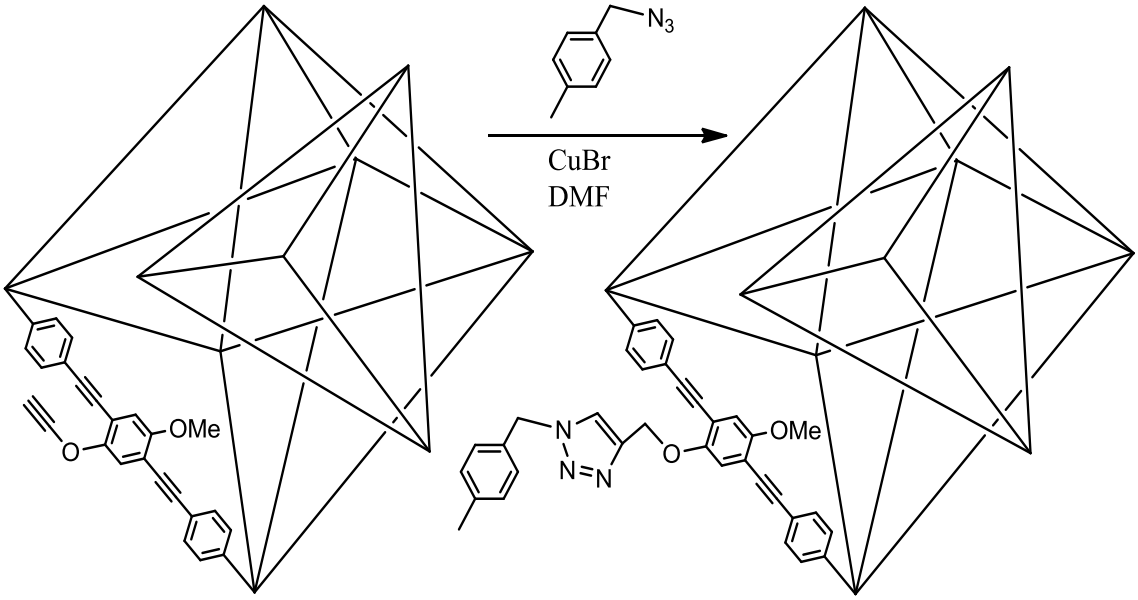

Scheme I.2.37 1,3-Dipolar cycloaddition of PIZOF(OMe,OCH2CCH) with 4-methylbenzyl azide.

Another type of MOF [PIZOF(OMe, $O(CH_2)_3$furan] was synthesised as described above but bearing a different side chain R^1 = OMe and R^2 = $O(CH_2)_3$furan. PIZOF-[OMe,$O(CH_2)_3$furan] was reacted with maleimide, *N*-methylmaleimide and *N*-phenylmaleimide to afford the corresponding Diels–Alder adducts in 98, 99, and 89 % (Scheme I.2.38). This study describes very simple techniques to determine the modification of MOFs by ^{1}H NMR spectroscopy. The modified MOFs were solubilized in DMSO-d_6 through the addition of CsF and DCl followed by the addition of K_2CO_3.[55]

The alkyne-functionalized MOF Zn-DPYI was synthesized through treatment of the mixed ligands (1-propargyloxy-3,5-phenyldicarboxylic acid and 4,4'-dipyridine) with a zinc salt ($Zn(NO_3)_2$). Zn-DPYI was reacted with L-*N*-2-azidomethylpyrrolidine (L-AMP) or D-*N*-2-azidomethylpyrrolidine (D-AMP) via 1,3-dipolar cycloaddition of alkynes with azides to produce chiral catalytic sites (Scheme I.2.39). This new material exhibited a catalytic activity on asymmetric aldol reactions.[56]

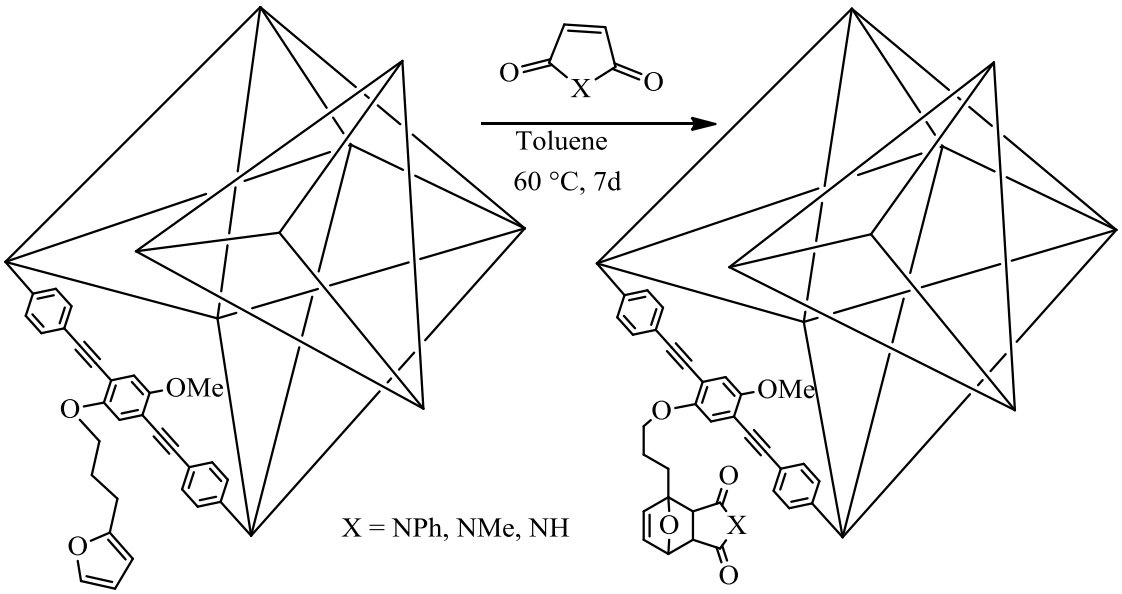

Scheme I.2.38 Diels–Alder additions of PIZOF[OMe,O(CH_2)$_3$furan] with maleimides.

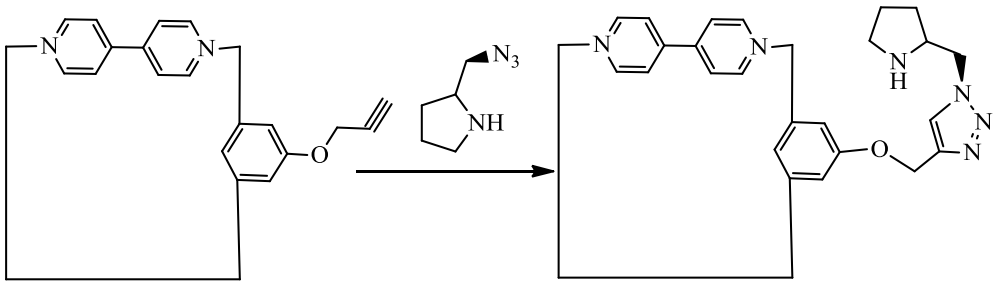

Scheme I.2.39 A (3+2) dipolar cycloaddition reaction of the alkyne-functionalized MOF Zn-DPYI with a chiral azide.

Photolysis

UMCM-1-OBnNO_2 and UMCM-1-(OBnNO_2)$_2$ were prepared by treatment of 2-[(2-nitrophenyl)methoxy]terephthalic acid (NO_2BnO-bdc) and 2,3-bis[(2-nitrophenyl) methoxy]terephthalic acid ((NO_2BnO)$_2$-bdc) separately with mixed 4,4',4''-benzene-1,3,5-triyl-tribenzoate (btb) and Zn(NO_3)$_2$6H_2O. Post-synthetic photolysis of UMCM-1-OBnNO_2 and UMCM-1-(OBnNO_2)$_2$ produce the corresponding hydroxy-functionalized MOFs (Scheme I.2.40). This study describe how UV-light can be used to remove the nitrobenzyloxy protecting groups through single-crystal-to-single-crystal (SCSC) transformation, being the aromatic linkers converted to 2-hydroxy-1,4-benzenedicarboxylate and 2,3-dihydroxy-1,4-benzenedicarboxylate.[57] Well-faceted colorless cubic crystals of MOF $Zn_4O(L1)_3$ [L1 = 2-(2-nitrophenoxy)-[1,1'-biphenyl]-4,4'-dicarboxylic acid] were synthesized by a solvothermal reaction of H_2L1 with Zn(NO_3)$_2$ in

N,*N*-diethylformamide. In $[Zn_4O(L1)_3]$ the hydroxyl group is protected by a large 2-nitrobenzyl group, which was cleaved by a photolytic process via a single-crystal-to-single-crystal procedure. The photolytic conversion of $[Zn_4O(L1)_3]$ consisted in their irradiation with a 355 nm laser light with stirring in DMF or THF. The advantage of this study is to show how one can mask an hydroxy functional groups during MOF synthesis (Scheme I.2.41).[58]

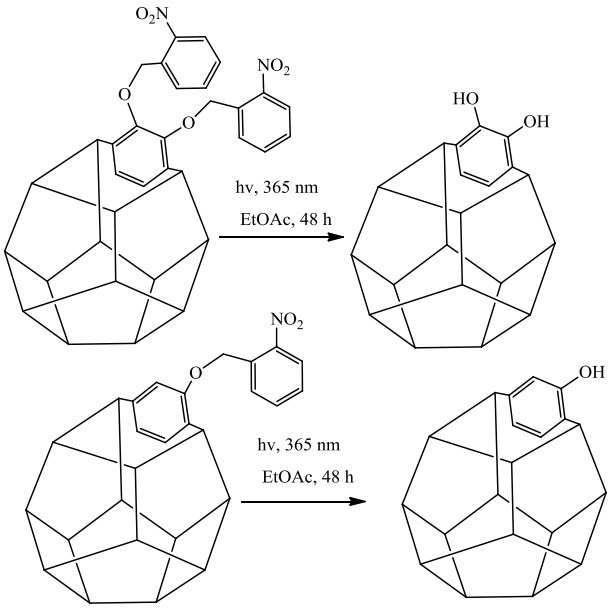

Scheme I.2.40 Post-synthetic photochemical deprotection of UMCM-1-OBnNO_2 and UMCM-1-$(OBnNO_2)_2$.

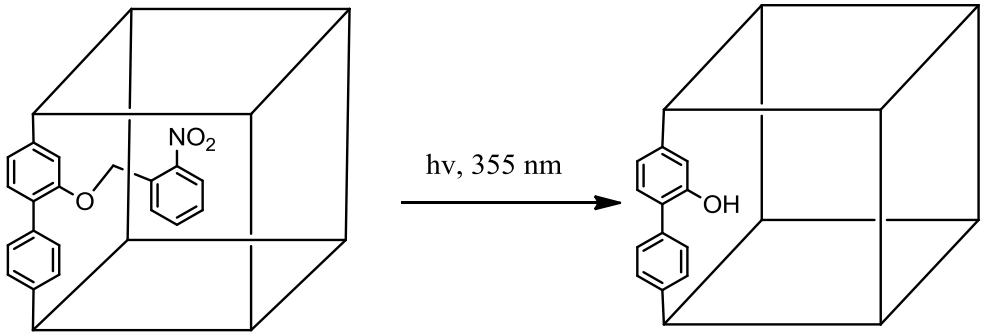

Scheme I.2.41 Photolysis of 2-nitrobenzyloxy-protected MOF to give the corresponding free hydroxyl form.

The dinuclear silver tetracarbene complexes {$[Ag_2(L1)_2](PF_6)_2$ and $[Ag_2(L2)_2](PF_6)_2$, (L1 = ethyl-*trans*-4,4'-bis(imidazolium)stilbene and L2 = n-butyl-*trans*-4,4'-bis(imidazolium) stilbene} were synthesized by adding Ag_2O to H_2-L1$(PF_6)_2$ and H_2-L2$(PF_6)_2$ in acetonitrile. The metallacycles $[Ag_2(L1)_2](PF_6)_2$ and $[Ag_2(L2)_2](PF_6)_2$ were post-synthetic modified via

a photochemical (Hg lamp, 365 nm) induced [2+2] cycloaddition reaction, in respectively DMSO-d_6 and CD_3CN as solvent, affording dinuclear *rctt*-cyclobutane−silver complexes. The olefin-functionalized Ag-MOF and cyclobutane-bridged Ag-MOF were transmetallated with [Au(THT)Cl] (THT = tetrahydrothiophene) to give the corresponding gold-MOFs (Scheme I.2.42). The modified materials were fully characterized by NMR spectroscopy and mass spectrometry.[59]

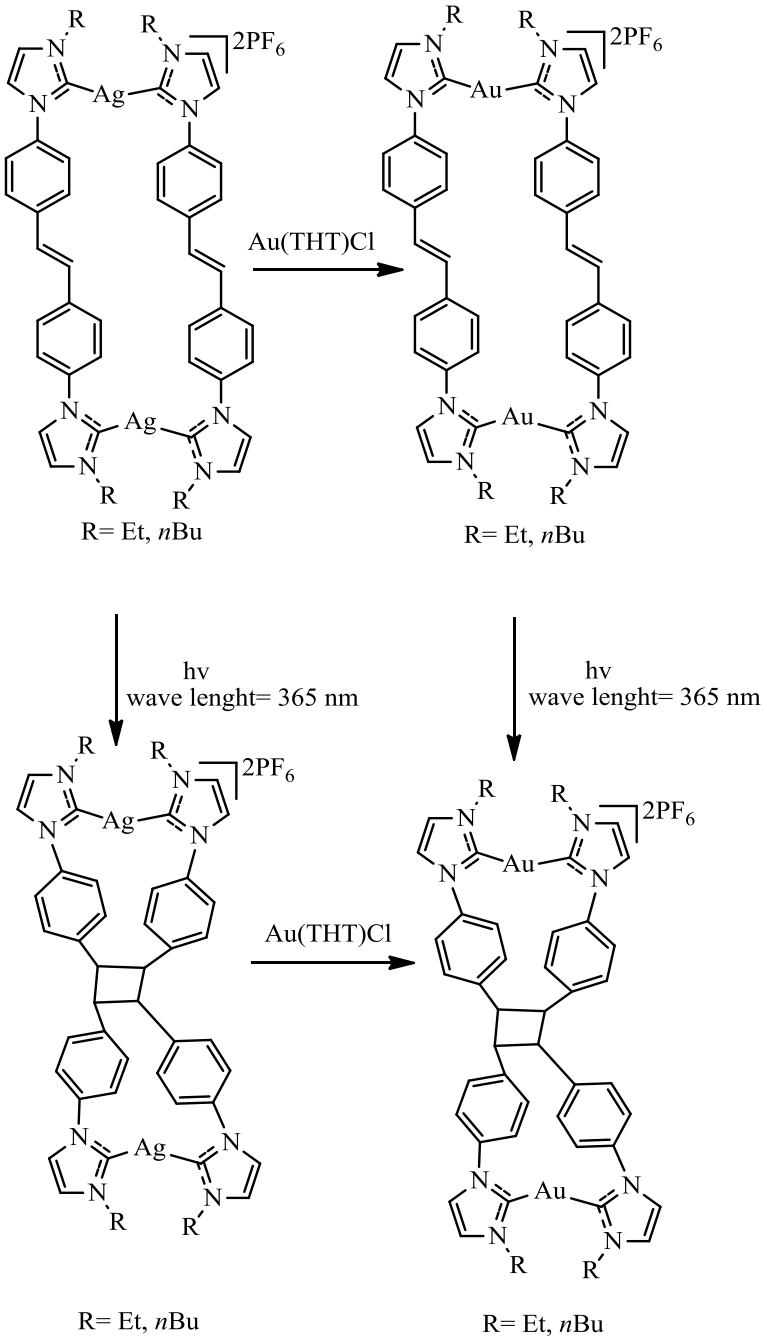

Scheme I.2.42 Photo-induced [2+2] cycloaddition reaction and transmetallation of dinuclear silver tetracarbene complexes.

Reduction reaction

Reduction process is playing an important role in producing stable functionalized MOFs. For instance IRMOF-3 was treated with different aldehyde affording the corresponding imine functionalized MOFs, this functional group is chemically unstable and much efforts were done to overcome that problem, being the reduction one of them. IRMOF-3-imine was treated with $NaBH_3CN$ in THF leading to conversion of imines into the chemically stable secondary amines (Scheme I.2.43).[60]

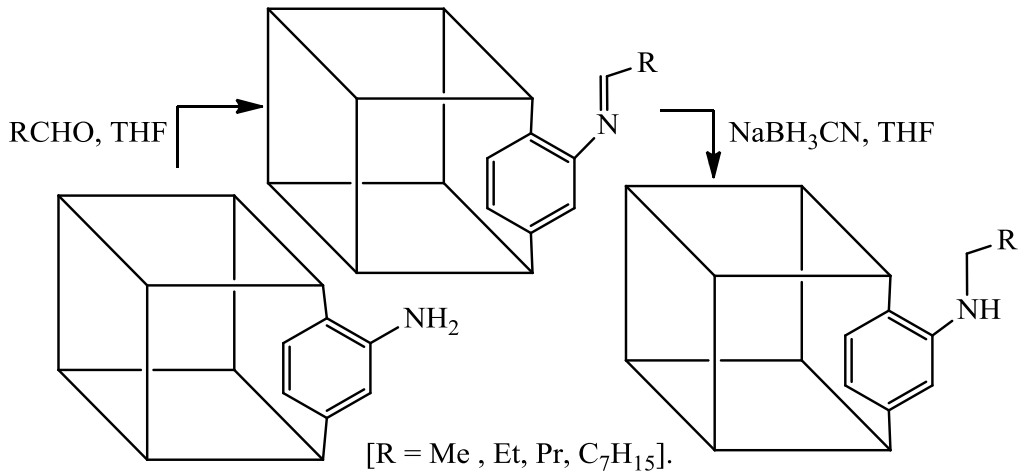

Scheme I.2.43 A two steps reductive amination of IRMOF-3.

MIL-68-(In)-NH_2 was treated with ^{t}BuONO and $TMSN_3$ in THF overnight at room temperature to give an azido-functionalized MOF, and then reacted with propargylamine in the presence of $Cu(CH_3CN)_4PF_6$ in acetonitrile affording a clicked functionalized MOFs. The presence of the nitrogen atoms on the triazolyl ring and the free terminal amino group of clicked functionalized MOFs provide a good environment for copper chelation as a *N*,*N*-donating group. The new copper-coordinated triazolyl moieties induced an azido reduction, under vacuum at 100 °C, to give the aromatic–NH_2 moieties (Scheme I.2.44). The nature and oxidation state of heterogenized copper complex was characterized by cutting-edge EPR techniques.[61] The formyl group of ZIF-90 reacts with ethanolamine via covalent modification to form an imine derivative. The formyl group was also reduced to the corresponding alcohol with $NaBH_4$ in methanol at 60 °C for 24 h (Scheme I.2.45).[62] These results were confirmed by solid-state ^{13}C CP-MAS NMR, solution ^{1}H NMR, and ESI-MS. A bisazide-functionalized MOF was synthesized by mixing zinc nitrate hexahydrate with 2,2-bis(azidomethyl)biphenyl-4,4-dicarboxylic acid.

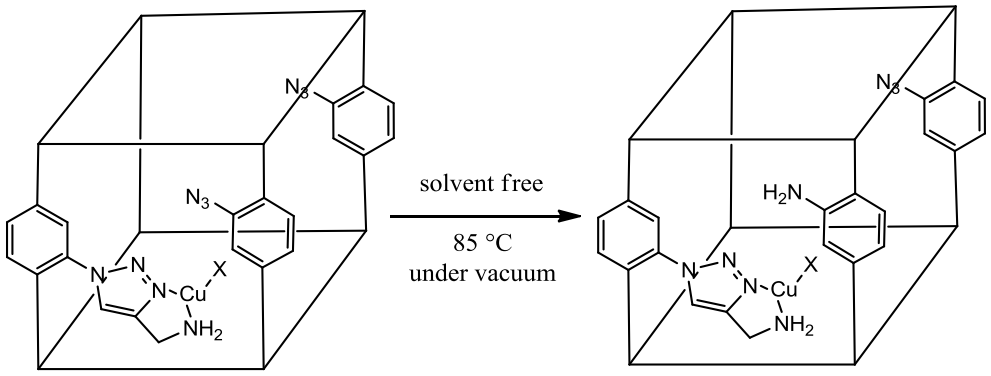

Scheme I.2.44 Copper-mediated intrareticular reduction of MOF azido functions to their amino analogues.

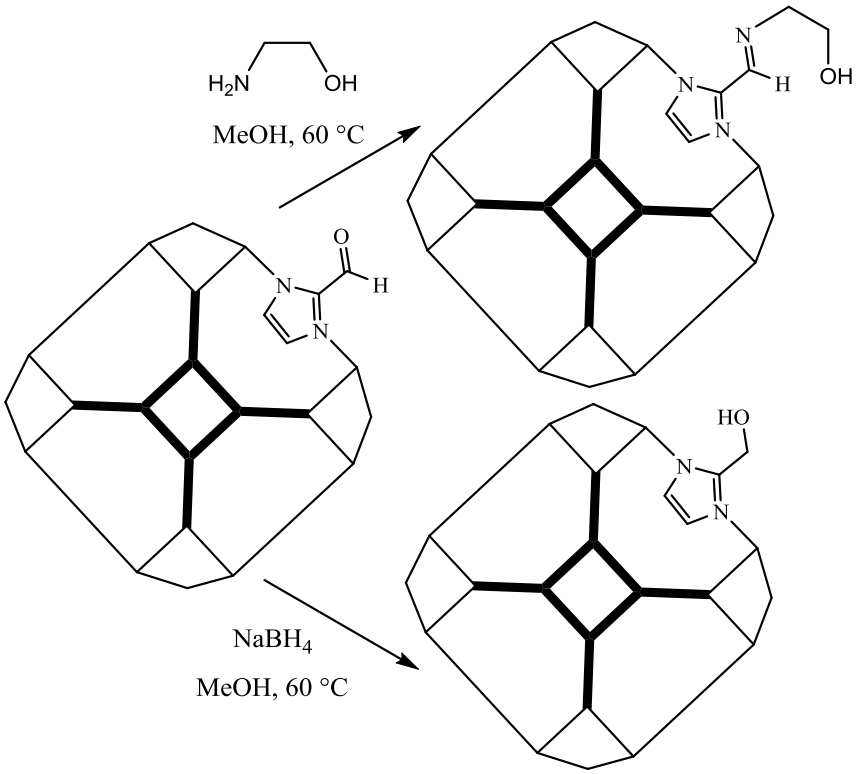

Scheme I.2.45 PSM of imidazole-2-carbaldeyde-functionalised MOF by formyl group reduction and imine formation.

Therefore since amine groups are more important for post-synthetic modification of MOFs, Nagata *et al.*[63] investigated the reduction of the highly reactive azide groups into the corresponding primary amino groups by treatment with triphenylphosphine, as a reducing agent. In order to test the reactivity of the resulting primary amine groups, further condensation reaction with a carboxyl-activated rhodamine-type compound was done and test by optical microscopy and confocal laser scanning microscope (CLSM) (Scheme I.2.46).

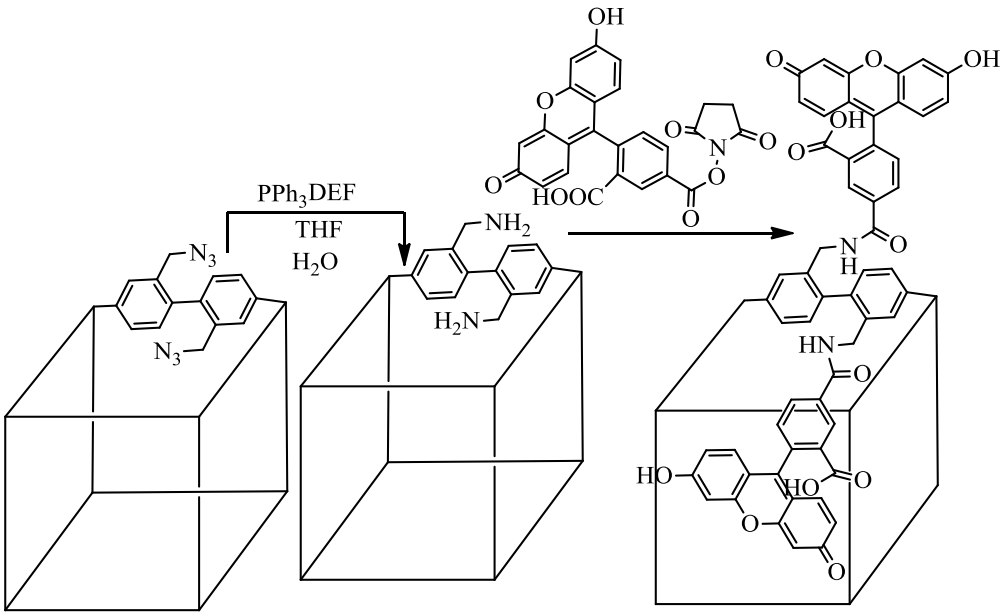

Scheme I.2.46 PSM of a bisazide-functionalised MOF by azide reduction and further reaction with a carboxyl-activated rhodamine-type compound.

Addition reactions

$\{Zn_3[(L)_2(\mu_2\text{-}OH)_2]6H_2O\}_n$ (i), (L = 2-(1-hydroxyethyl)-1*H*-benzo[*d*]imidazole-5-carboxylic acid) are a rhombus-shaped crystalline material that was synthesized by the reaction of H_2L, $Zn(NO_3)_26H_2O$, and triethylamine in an ethanol/water mixture under solvothermal conditions. It was then submitted to a tandem post-synthetic modification via thermal elimination of water at 250 °C to produce (ii) and further addition of bromine at room temperature to give (iii) (Scheme I.2.47). The modified material have dramatic effects on the absorption of gases (N_2, CO_2), solvents (H_2O, CH_3OH, C_2H_5OH, C_3H_7OH), and I_2. Considerable difference in the amount of gas or solvents was observed for the three different compounds, decreasing in the order i > ii > iii. Similarly, the difference on their luminescence properties was observed.[64] The olefin-tagged MOF $Zn_2(TDC)_2L1$ was synthesized by mixing 3-functionalized 4,4'-bipyridines (L1) with 9,10-triptycenedicarboxylic acid (TDC) and $Zn(NO_3)_26H_2O$ under microwave irradiation. It was post-synthetically modified through different organic reactions, including oxidation of the olefin side groups with osmium tetroxide (OsO_4) giving free vicinal diol functionalities, epoxidation with dimethyldioxirane (DMDO) producing epoxy-functionalized MOFs and further reaction with ethyl mercaptan, hydroboration with borane-dimethyl sulfide, addition of bromine, and reaction with ethyl mercaptan under UV-light irradiation (Scheme I.2.48).[65]

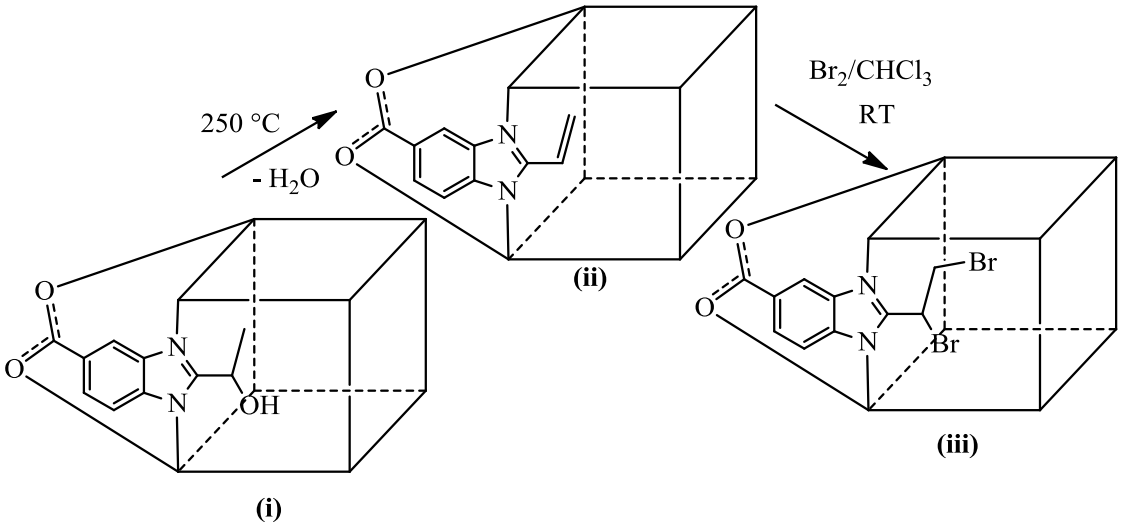

Scheme I.2.47 Tandem PSM of a 2-hydroxyethylbenzoimidazole-MOF through a thermal elimination of water and further addition of bromine to the formed vinyl groups.

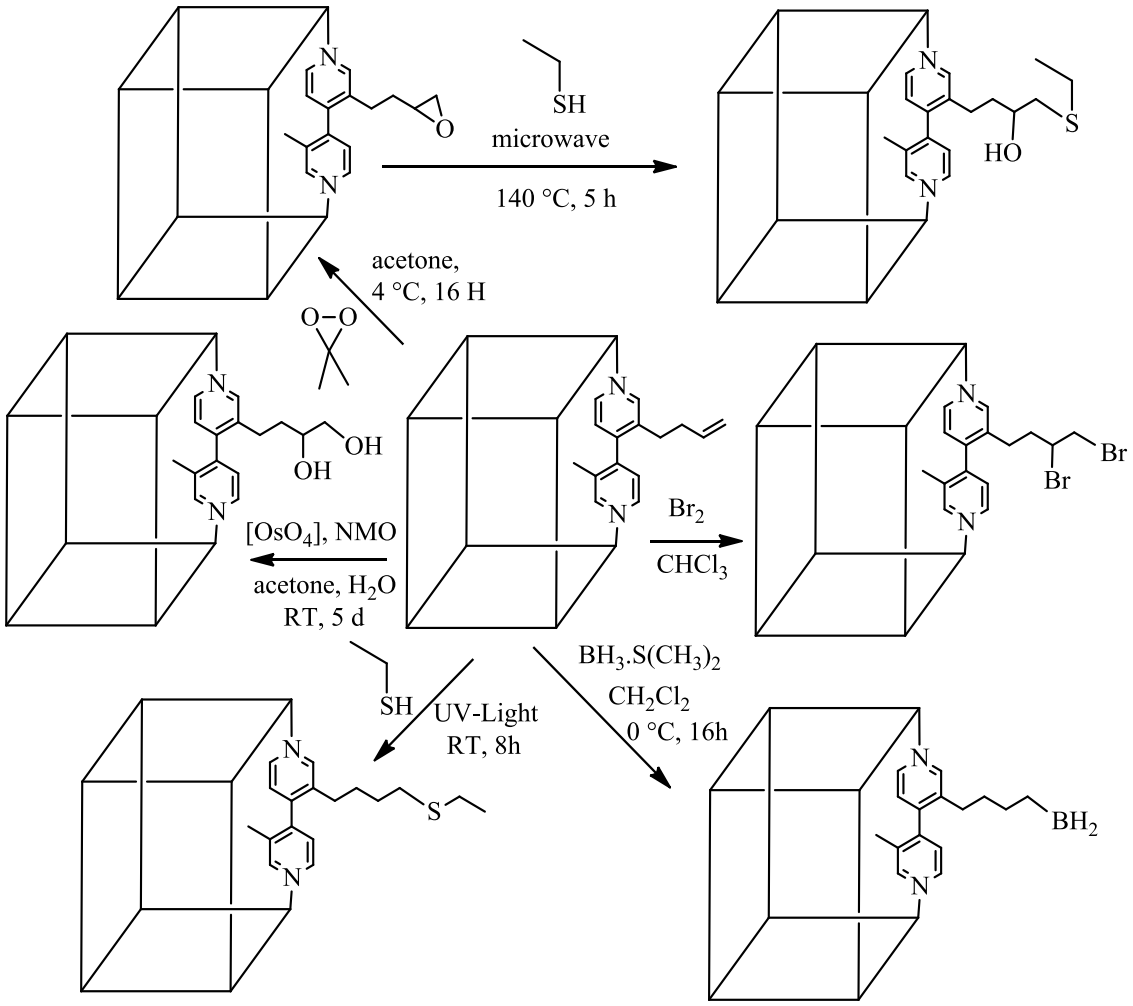

Scheme I.2.48 Several PSM of a but-3-en-functionalised MOF through addition, oxidation, epoxidation and hydroboration reactions of the C=C double bond.

Diazotization reaction

Methyl red-MIL-125 [MR-MIL-125)] was synthesized via a post-synthetic diazotization reaction. NH_2-MIL-125 was reacted with nitrosonium ion NO^+, generated *in situ* by the HCl–$NaNO_2$ at 0°C, then coupled with diethylaniline to produce MR-MIL-125 (Scheme I.2.49). The new material methyl red-MIL-125 exhibited improved light absorption properties over a wide range of the visible spectrum, and showed enhanced photocatalytic oxidation activity of benzyl alcohol under visible light illumination.[66]

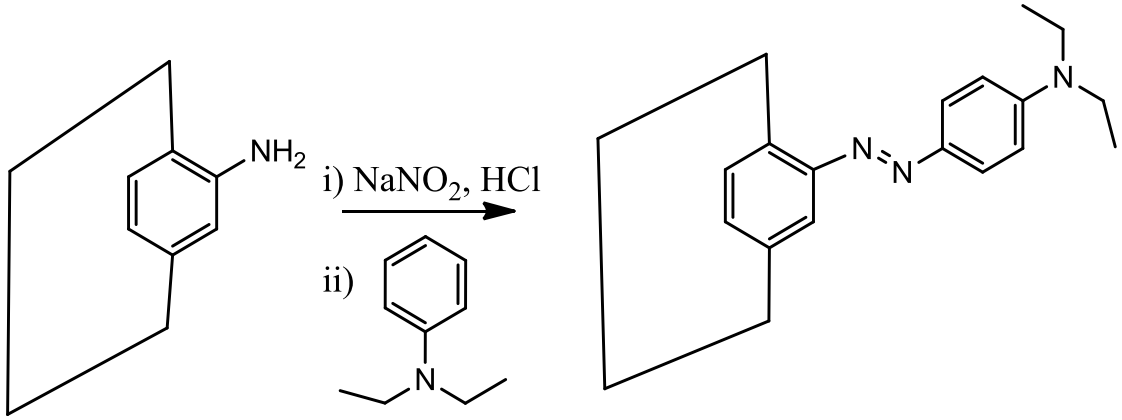

Scheme I.2.49 Diazotization reaction of NH_2-MIL-125.

MIL-101(Cr) {$[Cr_3O(F,OH)(H_2O)_2(bdc)_3]n.H_2O$, bdc = 1,4-benzenedicarboxylate} was converted to MIL-101(Cr)-NH_2 via nitration and further reduction of its nitro group. MIL-101(Cr)-NH_2 was modified via a tandem diazotization process. Because amine-tagged MOFs are not stable in acidic aqueous conditions, the diazotization route is not much reported in MOFs chemistry. MIL-101(Cr)-NH_2 is one of few chemically stable MOF even in acidic aqueous solution, allowing to be submitted to a diazotization process. The diazotization process occurred by treatment a suspension of MOF in $NaNO_2$/HCl, being the corresponding diazonium salt transformed by substitution or coupling reactions (Scheme I.2.50). One of the new modified products MIL-101(Cr)-azo showed excellent selectivity for CO_2 sorption at low pressure.[67] UiO-66-NH_2 is water-stable MOF that was modified via a diazotization process ($NaNO_2$/HCl) and then followed by coupling with 1-methylindole to form UiO-66-NQN-ind (Scheme I.2.51). UiO-66-NH_2 and UiO-66-NQN-ind are used as a broad-range fluorescent pH sensors. This study reported the pH dependent fluorescent response of UiO-66-NH_2 across the range 1 to 9. After the post-synthetic diazotization with indole groups, the range of the stability was increased to pH 12.[68]

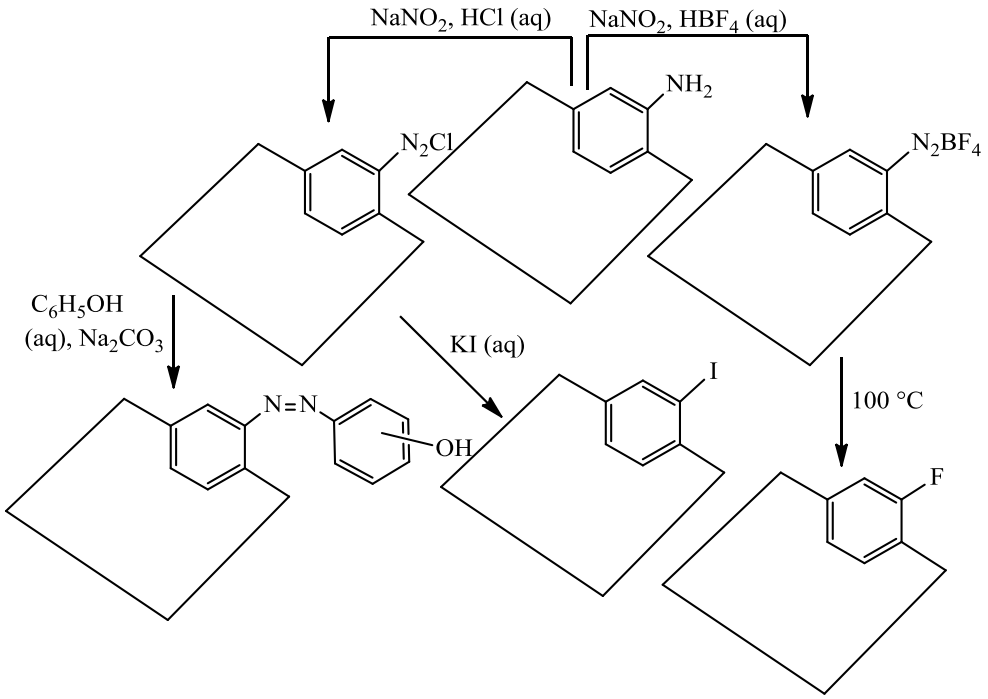

Scheme I.2.50 Diazotization process of MIL-101(Cr)-NH_2 and further reactions of the formed diazonium salts.

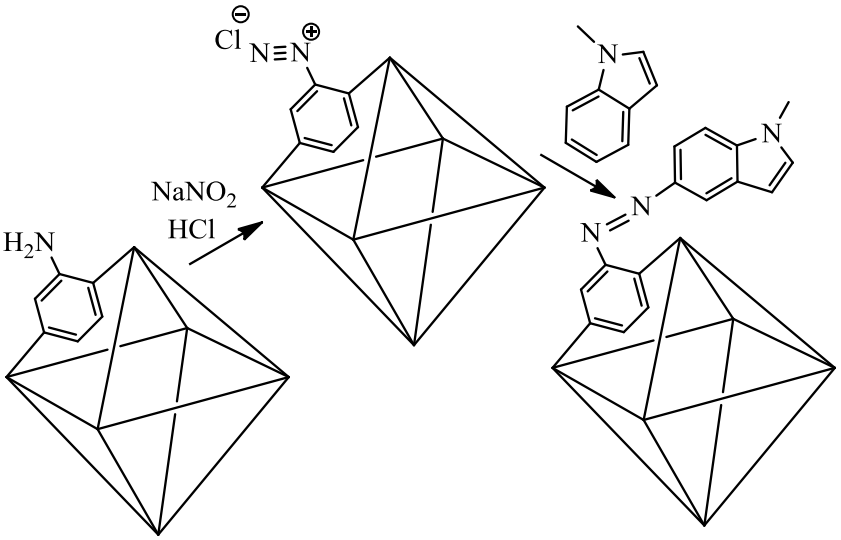

Scheme I.2.51 Diazotization reaction of UiO-66-NH_2 and further coupling with 1-methylindole.

Tandem PSM of MOFs

The term tandem modification of MOFs means that there is a series of post-synthetic modification of MOFs by reacting them sequentially with many chemical reagents. MOFs can be modified with one reagent and then subsequently modified with a second reagent on the remaining reactive sites, allowing to obtain a final product with several new moieties.

IRMOF-3 is a good example for tandem modification as shown in scheme I.2.52.[69] At first IRMOF-3 react with phenylisocyanate in chloroform at room temperature to produce 32% modified-NH_2 and the resulted modified material react with decanoic anhydride (24%), and then with 1-isocyanatoprop-1-ene (20%).

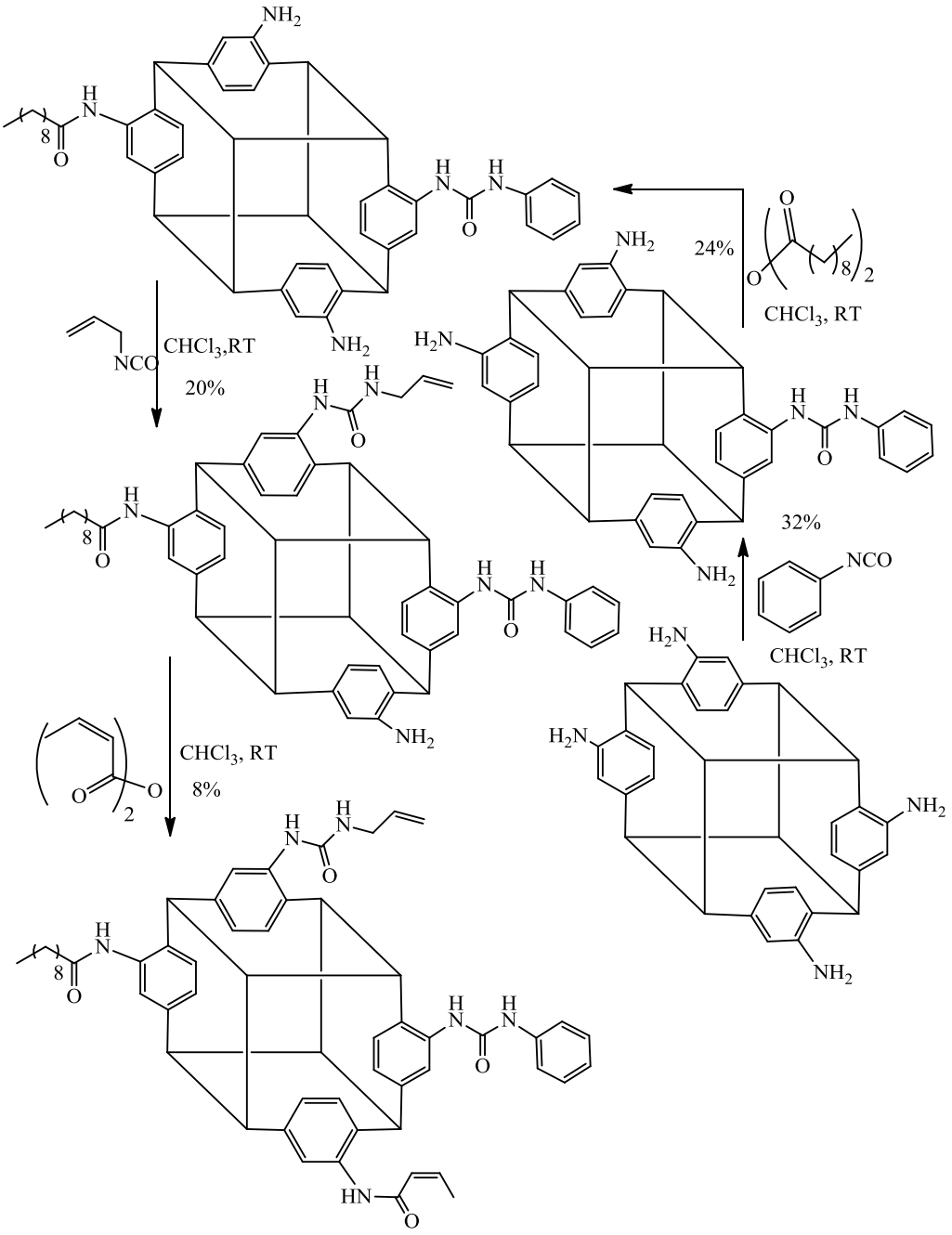

Scheme I.2.52 Tandem PSM of IRMOF-3.

The last step on this modification is the reaction with but-2-enoic anhydride (8%). The structure of modified MOFs was confirmed by ^1H NMR and the crystallinity was determined by PXRD.

(c) Post-synthetic metalation of MOFs

This part aims to introduce the reader to the general strategies that have been employed to perform post-synthetic metalation on MOFs. We provide an exhaustive survey of the literature, in which we will illustrate how post-synthetic metalation has been applied to enhance the performance characteristics of parent MOFs.

IRMOF-3 reacted with salicylaldehyde to give salicylimine-IRMOF-3. The salicylimine sites were metallated with $V(O)(acac)_2H_2O$ (acac = acetylacetonate)[70] and $NaAuCl_4$[71] to produce new catalysts for oxidation of cyclohexene with ^{t}BuOOH (40% conversion of cyclohexene in THF at 60 °C for 72h) (Scheme I.2.53).

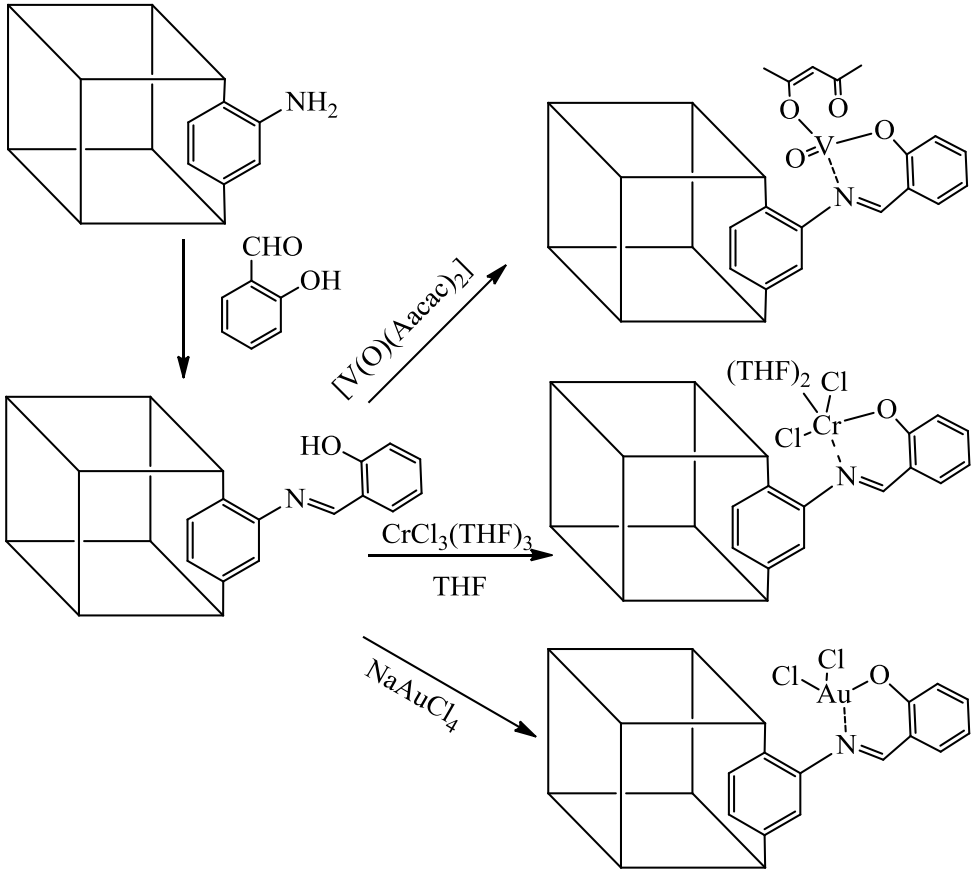

Scheme I.2.53 Reaction of IRMOF-3 with salicylaldehyde followed by metalation with vanadium, chromium and gold ions to create solid-state catalysts.

The salicylimine-IRMOF-3 was also chelated with chromium[72] to produce a new catalyst for the ethylene polymerization, which presented very good results on this transformation. The activity on the polymerization process was also increased by activation with various alkylaluminium co-catalysts. The formed polyethylenes have high molecular weights and a broad molecular weight distribution.

IRMOF-3 was reacted with glyoxal in acetonitrile at room temperature for 24 h to produce the corresponding imine-MOF. The imine-MOF was complexed with Cu(I) giving MOF-supported Cu(I) complex (Scheme I.2.54). This study shows that MOF-supported Cu(I) gives a highly efficient and recyclable catalyst for a three-component (aldehyde–alkyne–amine) coupling reaction.[73]

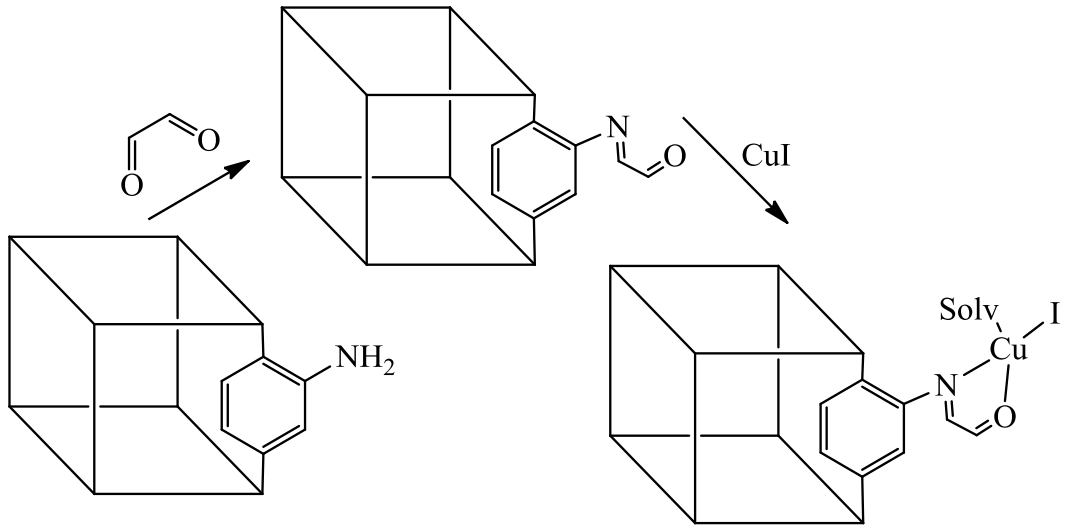

Scheme I.2.54 Reaction of IRMOF-3 with glyoxal and further metalation with copper (I).

IRMOF-3 and UiO-66-NH_2 were modified via imine-MOF functionalisation, followed by incorporation of iridium to produce chemoselective catalysts (Scheme I.2.55 and I.2.56) for the synthesis of secondary amines by a one-pot three-step cascade reaction. The results show that the iridium-supported MOF generate a diverse range of *N*-alkyl amines in good to excellent yields.[74,75]

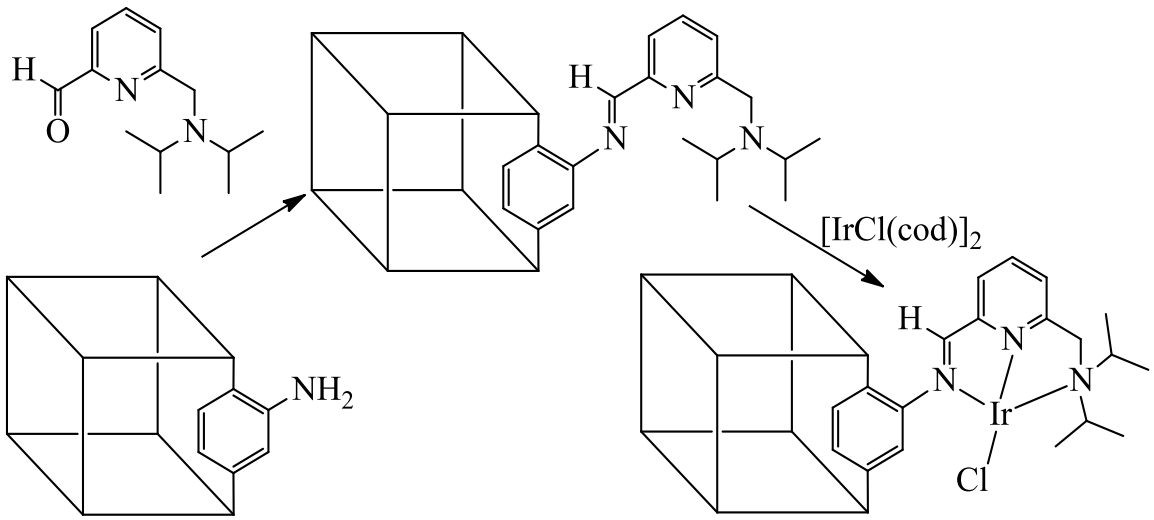

Scheme I.2.55 Functionalization of IRMOF-3 followed by metalation with iridium ions.

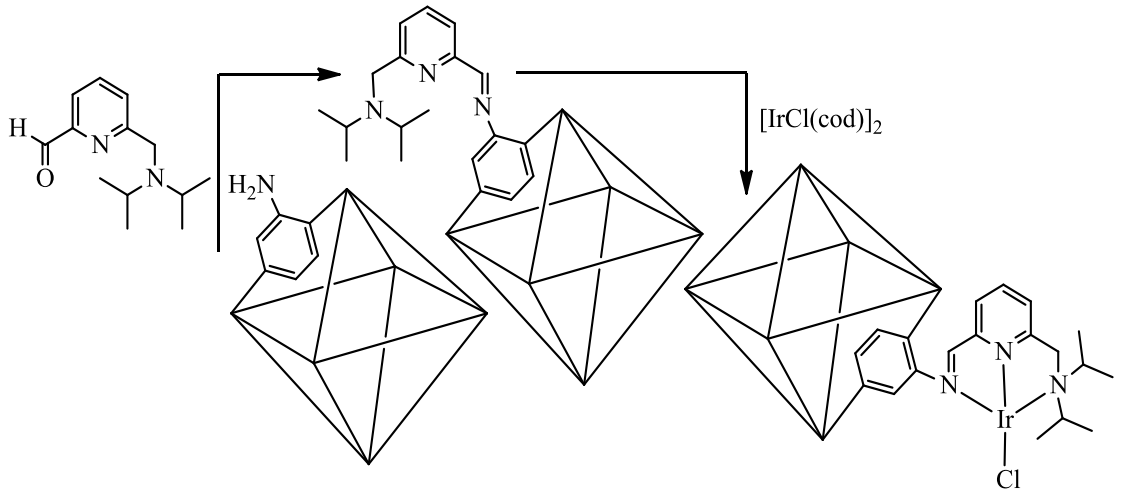

Scheme I.2.56 Functionalization of UiO-66-NH_2 followed by metalation with iridium ions.

IRMOF-3 was modified by the reaction with pyridine-2-carbaldehyde to give the functionalized IRMOF-3-PC, which was treated with CuI to generate the corresponding Cu(I)-containing catalyst material IRMOF-3-PC-CuI (Scheme I.2.57). It is used as catalyst on the synthesis of 2-aminobenzothiazoles by the reaction of 2-iodoanilines with isothiocyanates.

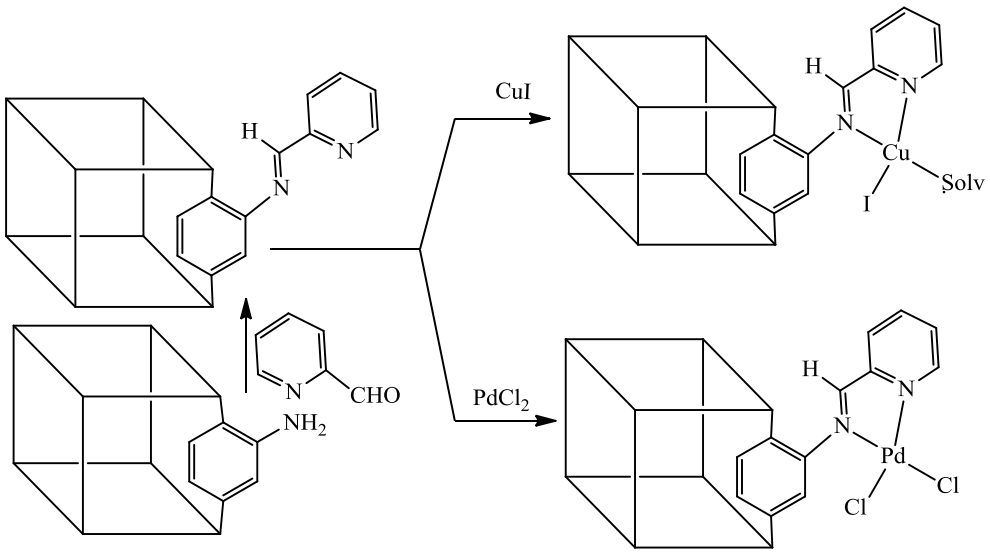

Scheme I.2.57 Reaction of IRMOF-3 with pyridine-2-carbaldehyde followed by metalation with palladium and copper ions.

The modified catalyst can be recoverable and can be reused six times without leaching and loss of activity, thus making this procedure environmentally more acceptable.[76] Similarly, IRMOF-3-PC was complexed with $PdCl_2$ in dichloromethane to give a framework with isolated Pd(II) sites.

Covalent transformation followed by metalation opens a route of incorporating metal ions into a wide range of frameworks. UMCM-1-NH_2 [$(Zn_4O)_3(bdc\text{-}NH_2)_3(btb)_4$] crystals were reacted with pyridine-2-carbaldehyde to form the covalently bound iminopyridine chelate derivative $(Zn_4O)_3$-$(bdc\text{-}C_6H_5N_2)_3(btb)_4$, which was then reacted with $PdCl_2(CH_3CN)_2$ to give the metal-complexed MOF $(Zn_4O)_3(bdc\text{-}C_6H_5N_2PdCl_2)_3$-$(btb)_4$ (Scheme I.2.58).[77]

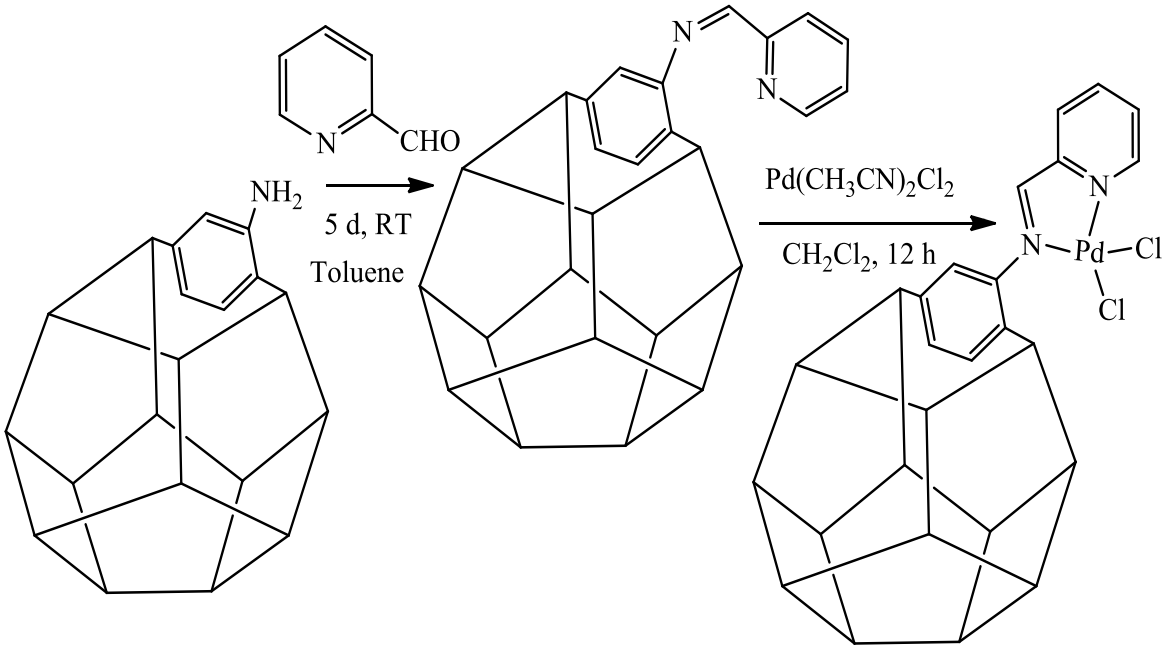

Scheme I.2.58 Reaction of UMCM-1-NH_2 with pyridine-2-carbaldehyde followed by metalation with palladium ion.

Post-synthetic modification can be used to introduce chelating sites into a MOF, these sites can be metallated with divalent or trivalent transition metals, and the resulting materials can be used as catalysts for carbon–carbon bond forming reactions. UMCM-1-NH_2 was transformed by the reaction with 3-hydroxyphthalic anhydride and pyrazine-2,3-dicarboxylic anhydride into UMCM-1-AMsal and UMCM-1-AMpz with conversions of 35% and 50%, respectively. Both modified MOFs were metallated with $Fe(acac)_3$ and $Cu(acac)_2$. The colour of the metallated MOFs was changed from pale yellow to dark red in the case of $Fe(acac)_3$ and bluish green in case of $Cu(acac)_2$. Atomic absorption analysis of UMCM-1–AMFesal and UMCM-1–AMCupz confirmed that UMCM-1–AMFesal contained 0.77 wt% of Fe^{3+} while UMCM-1–AMCupz had 1.76 wt% of Cu^{2+} (Scheme I.2.59).[78]

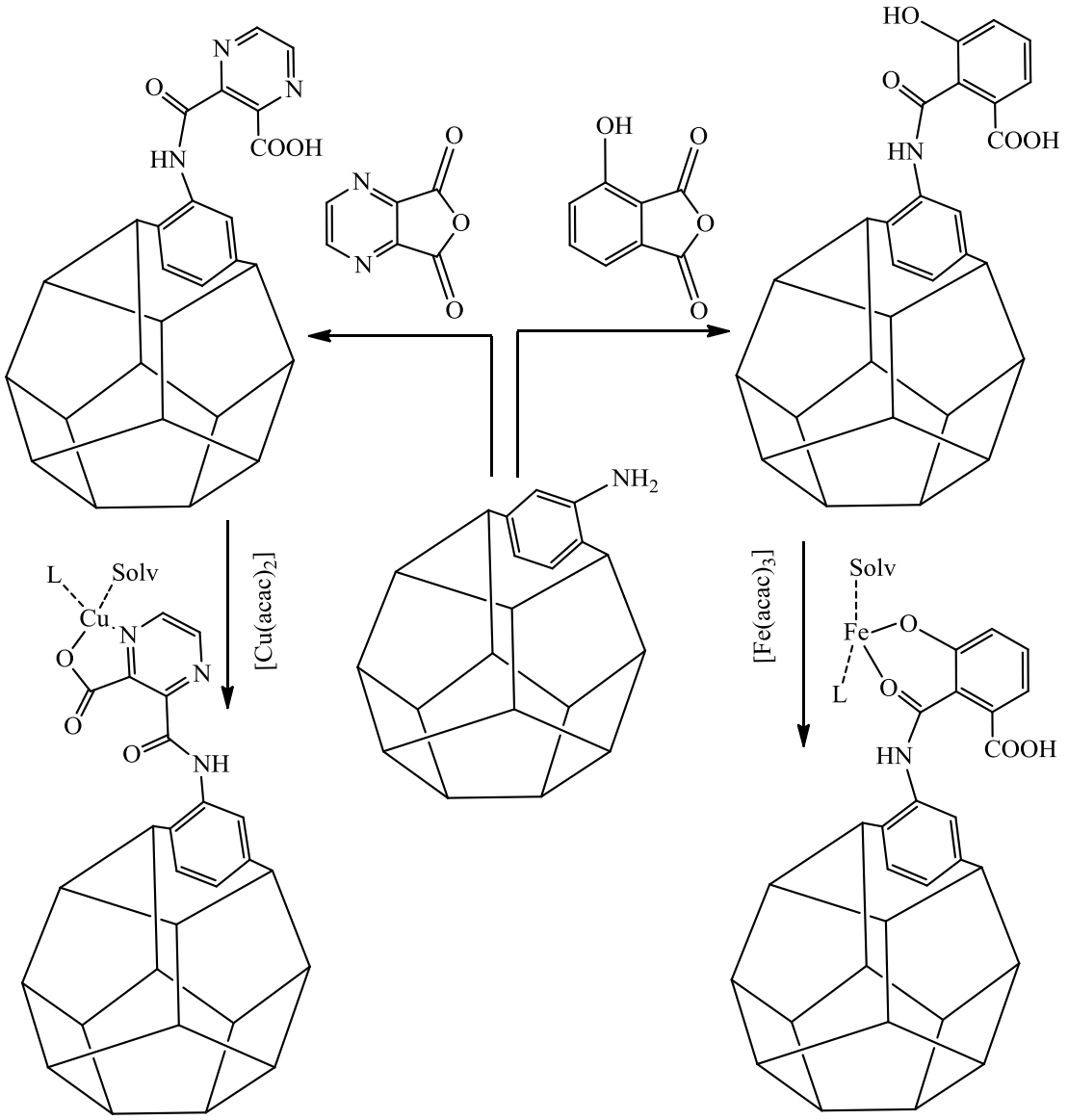

Scheme I.2.59 Reaction of UMCM-1-NH_2 with acid anhydride followed by metalation iron and copper ions.

MIL-101(Cr)-NH_2 was modified via condensation of the amino groups with ethyl chloro-oxoacetate to produce free oxamates attached to the MOF backbone. Through the coordination of Cu, Pd and Au with the oxamate ligand; a highly stable MIL-101(Cr) framework was formed (Scheme I.2.60). This study also showed that Cu-supported MOF give a good catalytic activity in 'click chemistry' catalysis (1,3-dipolar cycloaddition reactions) and multicomponent coupling reactions (propargylamine formation). The authors also showed that Pd-catalysts are very active and selective in the Suzuki–Miyaura condensation, while the the Au-catalysts showed a good performance in benzyl alcohol oxidation to benzaldehyde for at least 4 consecutive runs.[79]

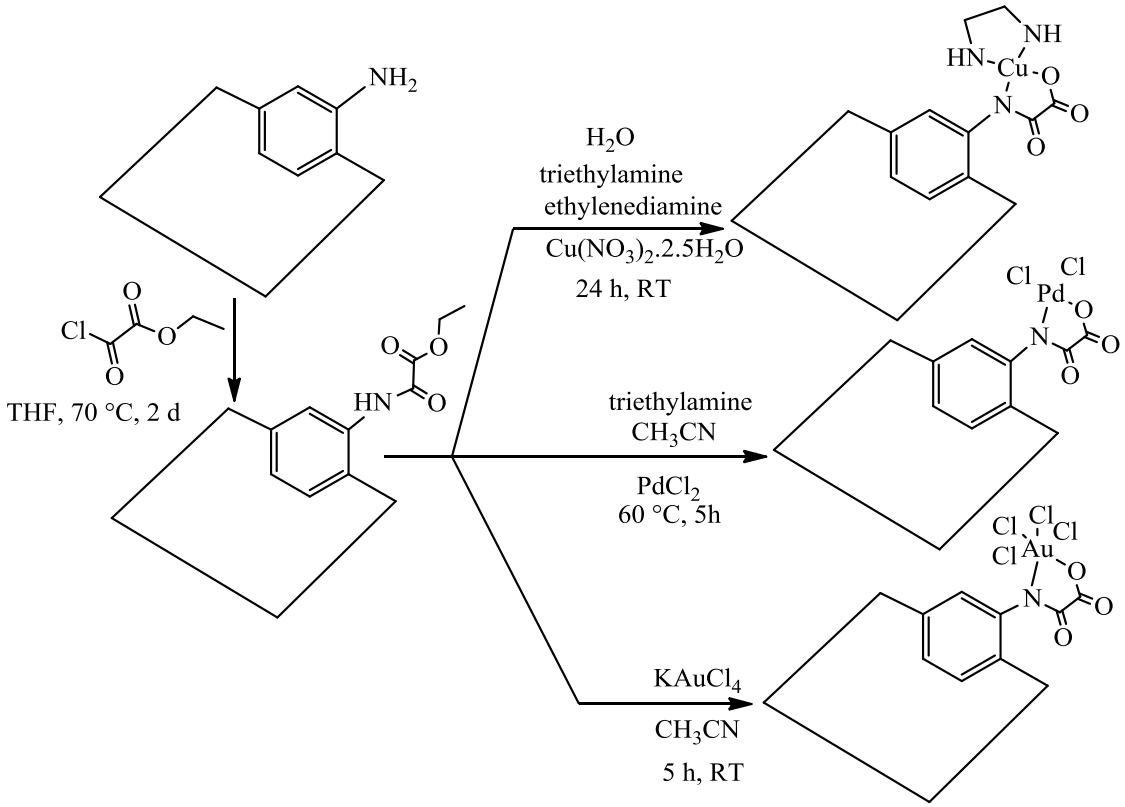

Scheme I.2.60 Reaction of MIL-101(Cr) with ethyl chlorooxoacetate and further incorporation of Cu, Pd, and Au ions.

Hydroxyl-functionalized MOF (**ii**) was obtained by deprotection of the corresponding *t*-butyloxycarbonyl-MOF (**i**) in presence of in 1,2-dichlorobenzene at 140 °C (Scheme 1.2.61) Removal of the butyloxycarbonyl group was confirmed by the ^{1}H NMR spectrum of a concentrated HCl/DMSO-d_6-digested MOF sample. Furthermore metalation with vanadium acetylacetonate was done (Scheme I.2.61). The resulting novel and catalytically active vanadyl-(monocatecholate)-MOF (**iii**) catalyze the benzylic oxidation of a large substrate such as tetralin in the presence of a bulky oxidant with minimal metal leaching in a non-coordinating solvent. These results point toward the potential of MOF as a support platform for homogeneously inaccessible coordination complexes that are competent for catalysis.[80] The diol-functionalized MOF (DO-MOF) consisted in Zn^{2+} as inorganic nodes and meso-1,2-bis(4-pyridyl)-1,2-ethanediol as the organic linker. It was post-synthetically modified by the reaction with succinic anhydride resulting in a ring opened product with free carboxylic groups. The covalent modified MOF with chelating group was exposed to a solution of $CuCl_2$ affording the corresponding Cu^{2+} complexes (Scheme I.2.62). The produced materials have a potential application on gas sorption.[81]

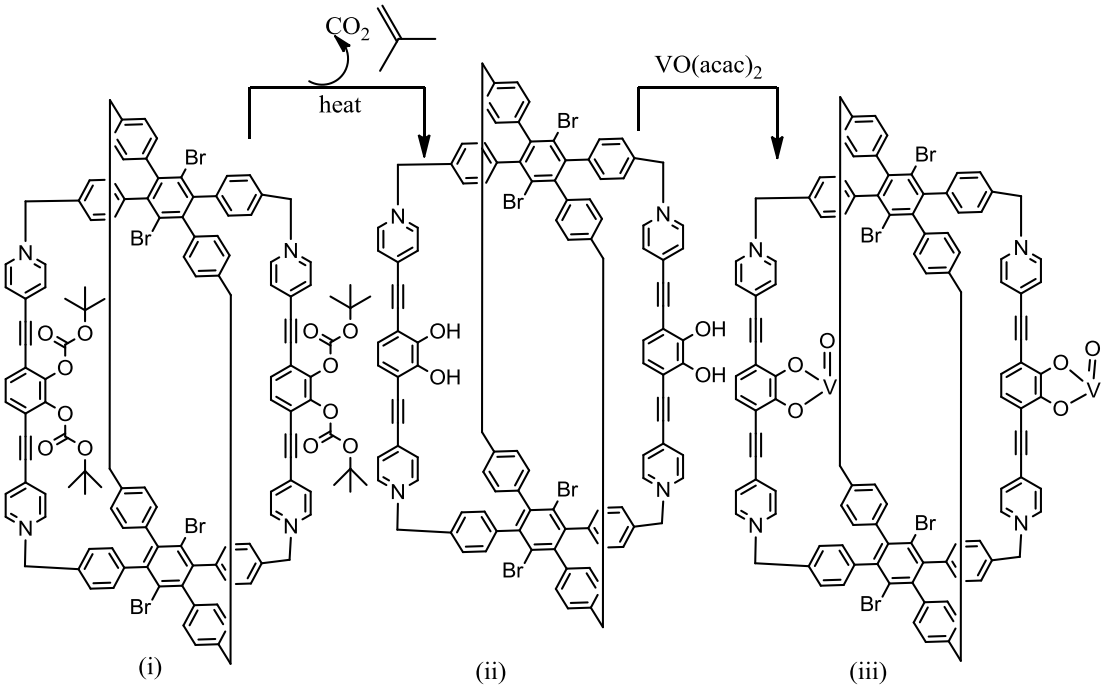

Scheme I.2.61 Post-synthetic deprotection of a *t*-butyloxycarbonyl followed by metalation with vanadium ions.

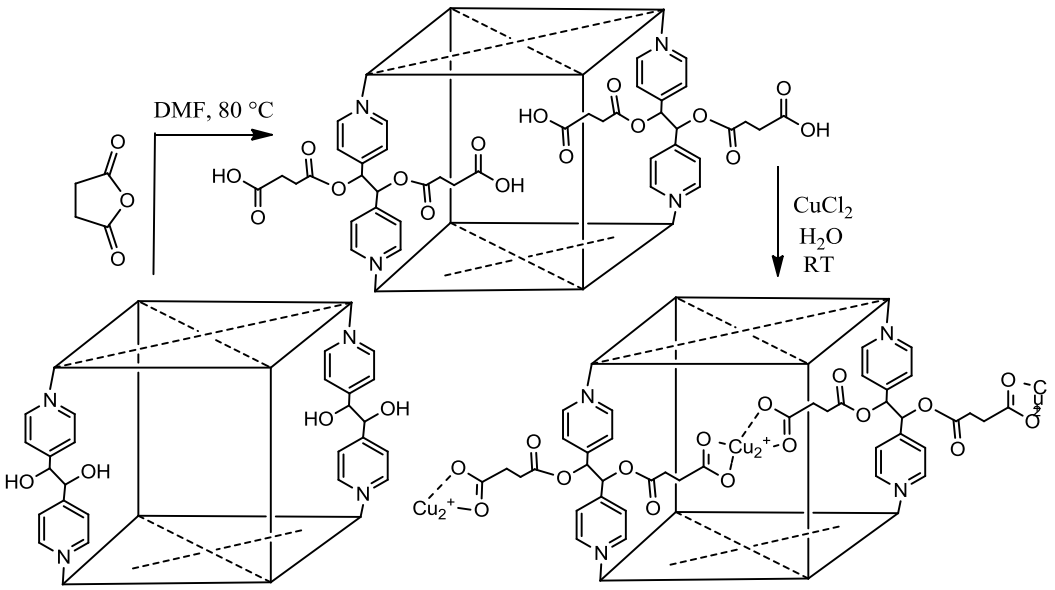

Scheme I.2.62 Reaction of the diol-functionalized MOF (DO-MOF) with succinic anhydride followed by coordination with Cu(II).

Bhattacharjee *et al*[82] prepared an IRMOF-3 containing a $Mn(acac)_2$ moiety through a one-step post-synthetic functionalization of IRMOF-3 through the reaction with manganese(II) acetylacetonate. The resulting MOF is a highly selective, reusable, and non-leaching catalyst for the epoxidation of several important alkenes (Scheme I.2.63).

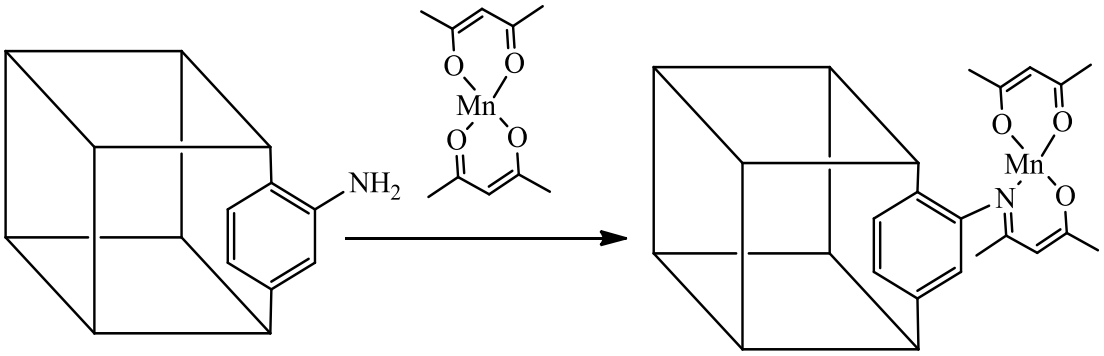

Scheme I.2.63 Reaction of IRMOF-3 with manganese(II) acetylacetonate.

IRMOF-3 was post-synthetically modified with ferrocenecarboxylic anhydride to form a ferrocenyl-MOF (redox active materials) and investigated by voltammetry in aqueous and non-aqueous media (Scheme I.2.64). The reversible electrochemical responses of functionalized MOF are observed. In aqueous media, voltammetric responses for the ferrocene oxidation exhibit rapid decay due to dissolution of the functionalised MOF framework.[83]

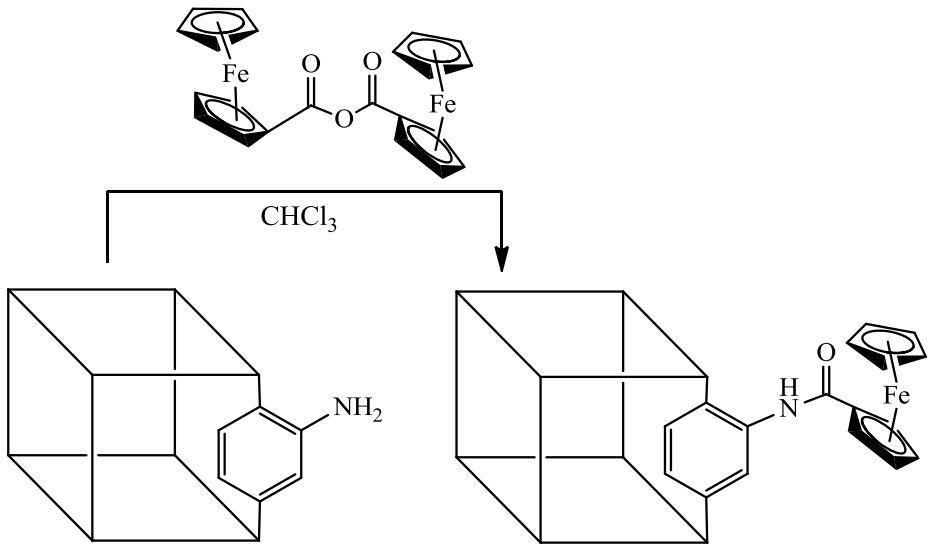

Scheme I.2.64 Post-synthetic modification of an amine-functionalized MOF to give a ferrocenyl amide-functionalized MOF.

IRMOF-16 (HCC-1) was synthesized by adding 1,4-di(4-carboxy-2-hydroxyphenyl) benzene to $Zn(NO_3)_26H_2O$. The value of BET surface area of HCC-1 is 3000 m^2/g. HCC-1 was post-synthetically modified with organic-metal precursors (isopropoxytitanatrane and tetrabenzyl titanium) giving high yield of conversion of the corresponding metallated derivatives (Scheme I.2.65).[84]

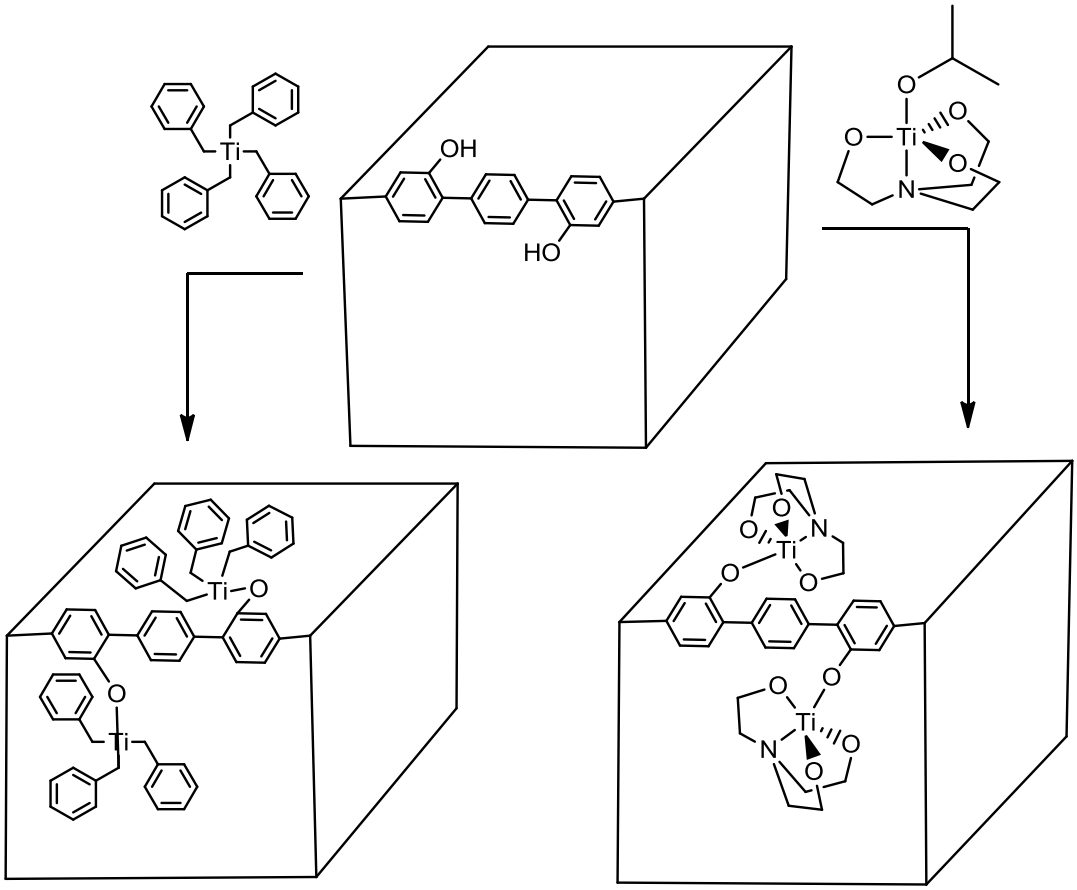

Scheme I.2.65 Reaction of HCC-1 with titanium precursors (isopropoxytitanatrane and tetrabenzyl titanium).

The solvothermal reaction of $ZrCl_4$ with 2,2'-bipyridine-5,5'-dicarboxylic acid in DMF and trifluoroacetic acid lead to form the bipyridyl-derived MOF (bpy-UiO). From X-ray results, the authors conclude that bpy-UiO have the same crystalline structure of the UIO. The post-synthetic metalation of bpy-UiO was performing by treating it with $[Ir(COD)(OMe)]_2$ in THF to produce bpy-UiO-Ir as a deep green solid or with $[Pd(CH_3CN)_4][BF_4]_2$ in DMSO to produce the bpy-UiO-Pd as a light yellow solid (Scheme I.2.66). Bpy-UiO-Ir exhibited excellent activity in the dehydrogenative borylation of aromatic C−H bonds using $B_2(pin)_2$ (pin = pinacolate) as the borylating agent.[85] MIL-47(V)-NH_2 was modified by reaction with the titanylacetylacetonate complex to afford Ti-functionalized MOF (Scheme I.2.67). The resulting material is effective and stable epoxidation catalyst. The authors showed that the Ti-supported MOF give high cyclohexene conversion compared to the non-functionalized material, because of the extra active sites (V and Ti).[86]

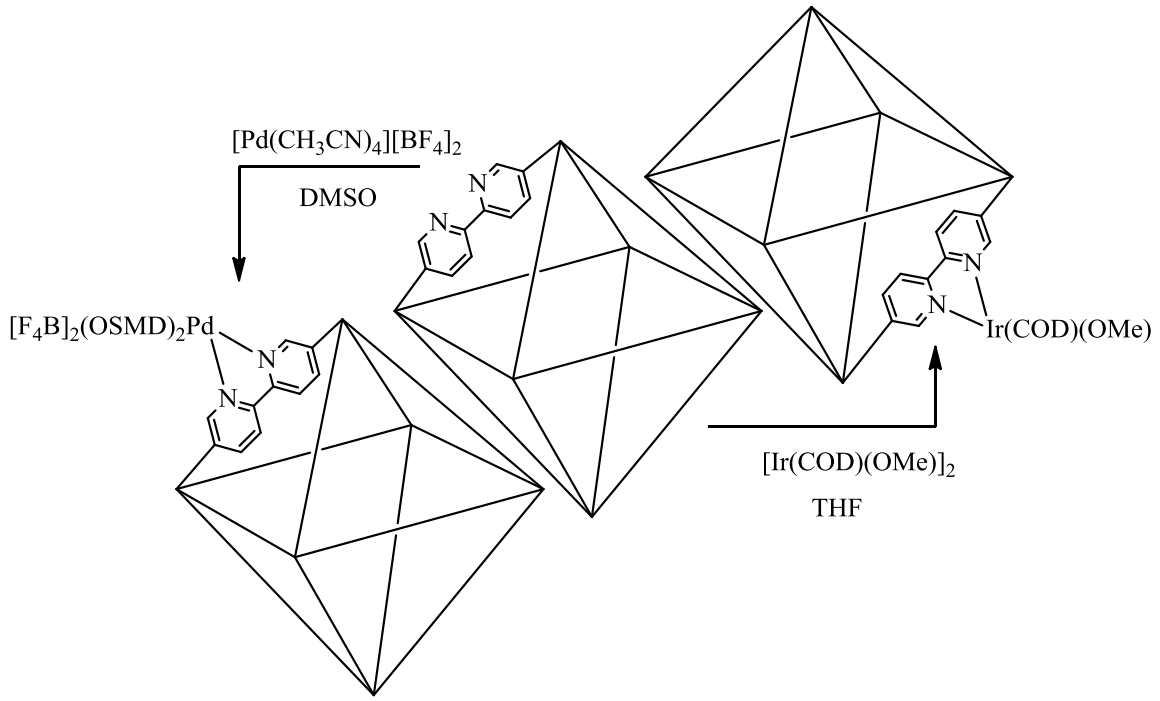

Scheme I.2.66 Direct metalation of bipyridyl-containing MOF with iridium and palladium ions.

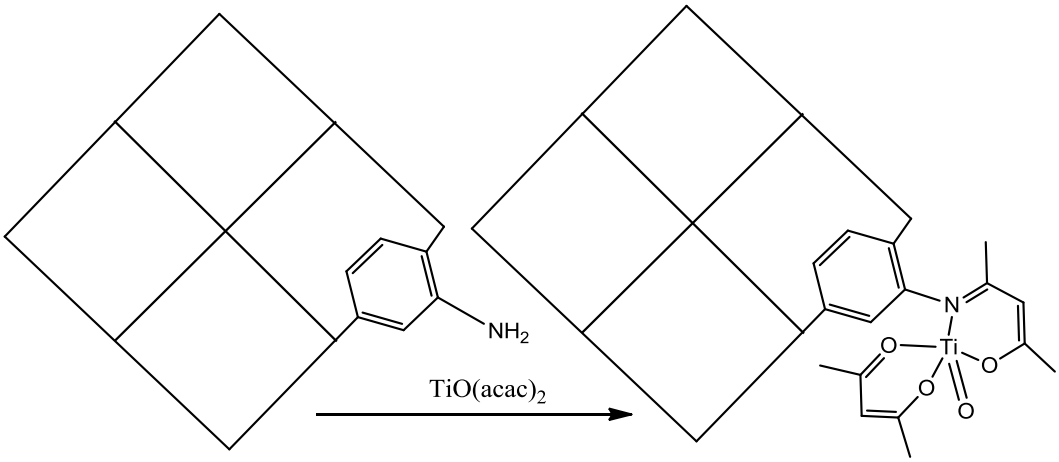

Scheme I.2.67 Reaction of MIL-47-NH_2 with titanylacetylacetonate complex.

Due to high surface area, high chemical and thermal stability of Al(OH)(bpydc) (MOF-253, bpydc 2,2'-bipyridine-5,5'-dicarboxylic acid), it was modified by the reaction with *cis*-$Pt(DMSO)_2Cl_2$ in CH_3CN (Scheme I.2.68). The modified material $Al(OH)(bpydc).0.5PtCl_2$ (MOF-253-Pt) serves as a photosensitizer and as a photocatalyst for hydrogen production. The importance of this study is due to the use of a photocatalyst without an additional use of both a co-catalyst and a photosensitizer.[87]

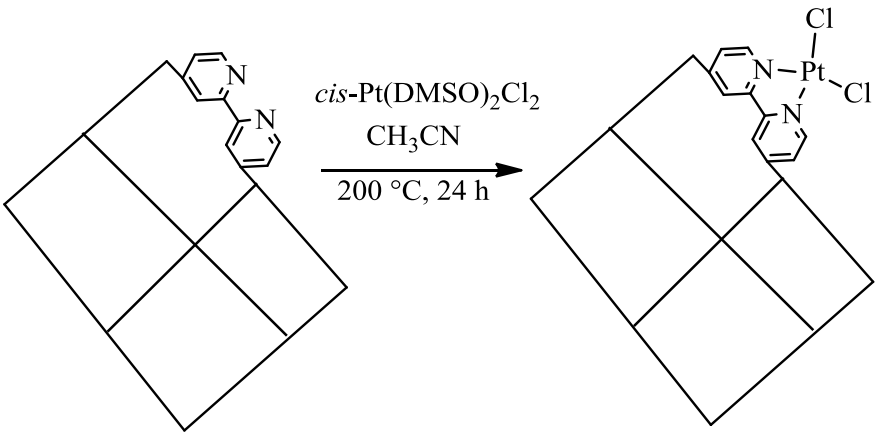

Scheme I.2.68 Direct metalation of MOF-253 with $PtCl_2$.

$[Cu_2(mand)_2(hmt)]H_2O$ (mand = mandelic acid, hmt = hexamethylenetetramine) were prepared through the reaction of copper(II) perchlorate, D/L-mandelic acid, and hexamethylenetetramine in the presence of triethylamine and ammonia. It was post-synthetically modified by the reaction with chromium(III) acetate resulting in a chiral salen oxo-chromium(III) acetate complex (Scheme I.2.69). The modified material are active and highly enantioselective in the epoxidation of *trans*-methyl cinnamate to form methyl 3-phenylglycidate, providing significantly high *ee* (>99.9%) values for methyl (*2R,3S*)-phenylglycidate at room temperature.[88]

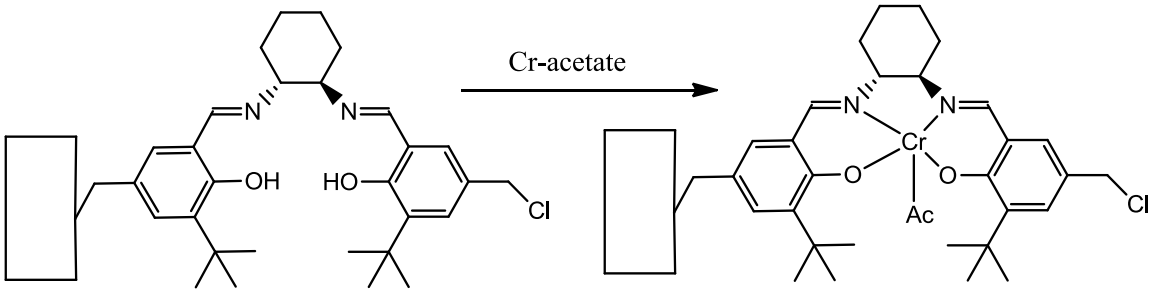

Scheme I.2.69 Direct metalation with chromium(III) acetate to form salen oxo-chromium(III) acetate complex.

Post-synthetic metalation of MIL-101(Fe)-NH_2 was occurred via a one-pot post-synthetic grafting of a nickel-based organometallic catalyst, prepared by adding nickel chloride to pyridine 2-carbaldehyde, within a MOF framework under mild conditions, preventing the interactions of the organic graft with the metal nodes and the encapsulation of metal particles (Scheme I.2.70). The modified material (Ni-supported MOF) presented a selective activity for ethylene dimerization to give the corresponding 1-butene in liquid phase.[89]

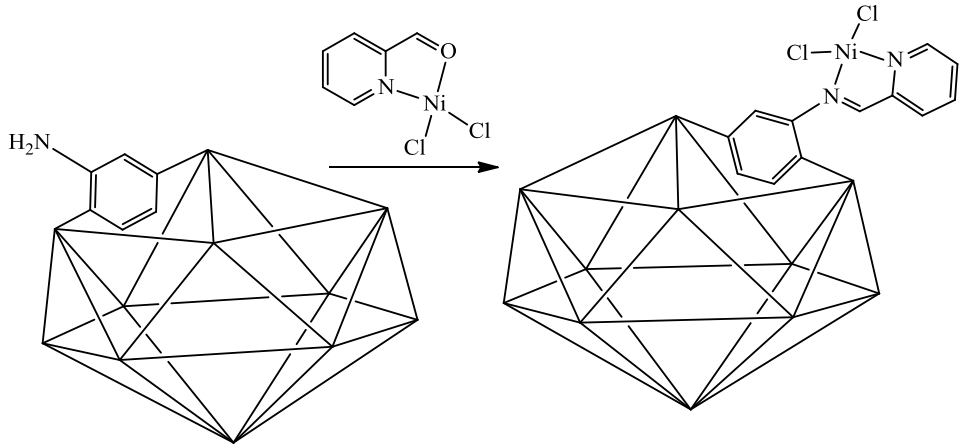

Scheme I.2.70 Direct anchored of a nickel complex within MIL-101(Fe)-NH_2.

DMOF-1-dcppy [DMOF = dabco MOF, dcppy = 6-(4-carboxyphenyl)nicotinic acid] and BMOF-1-dcppy (BMOF = 4,4'-bipyridine-MOF) were post-synthetically cyclometallated with $[Ir(COD)(OCH_3)]_2$ (COD = 1,5-cyclooctadiene) to produce MOFs bearing other organometallic species (Scheme I.2.71). The new materials are stable, efficient and reusable heterogeneous catalysts for allylic *N*-alkylation of amines.[90]

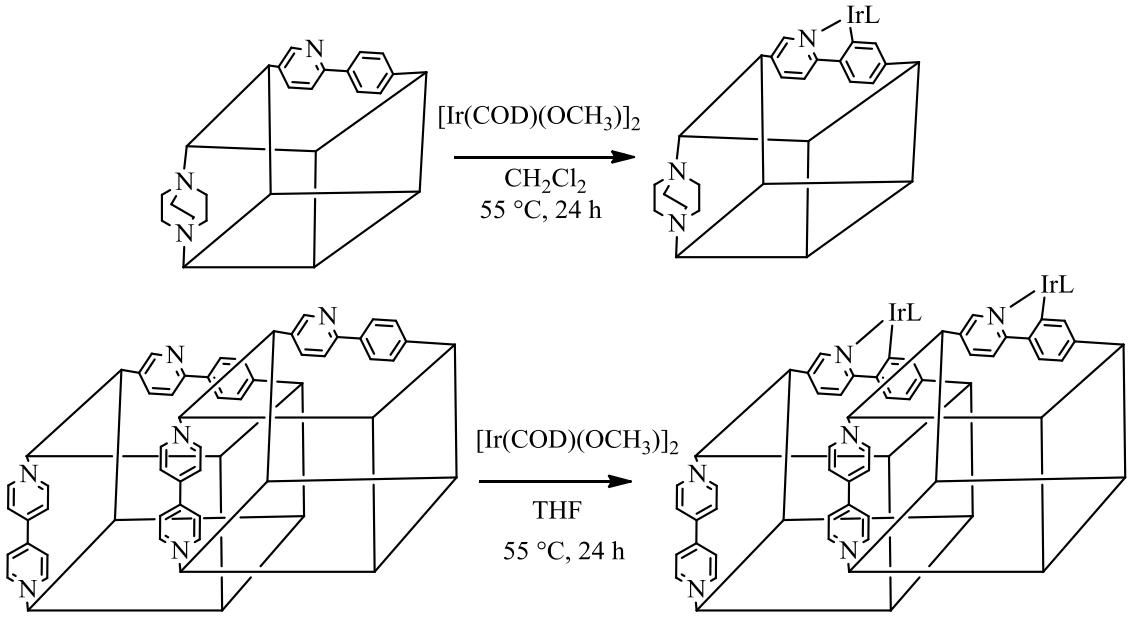

Scheme I.2.71 Post-synthetic cyclometallation of DMOF-1-dcppy and BMOF-1-dcppy with $[Ir(COD)(OCH_3)]_2$.

This new way of cyclometallation was also applied to UiO-67-dcppy through the reaction with $[Ir(COD)(OCH_3)]_2$ or $[Rh(COD)(Cl)]_2$ to afford stable a single active metal center with high catalytic activity for C–N bond forming reactions (Scheme I.2.72). This study provides a possible pathway for the site-selective modification of MOFs.[91]

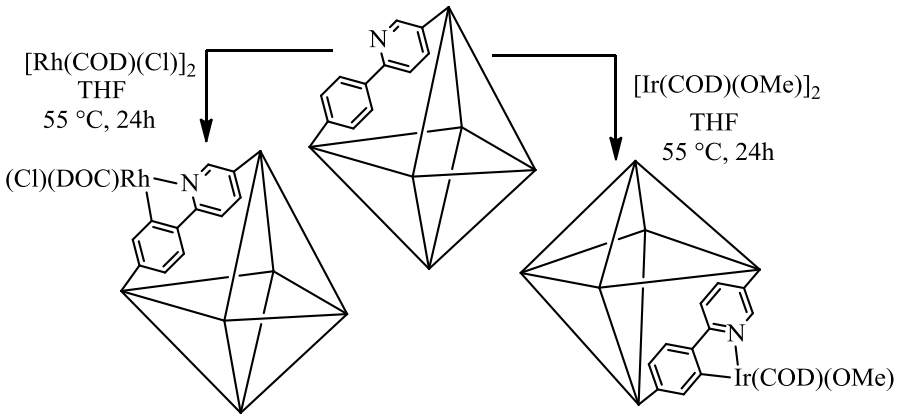

Scheme I.2.72 Post-synthetic cyclometallation of UiO-67-dcppy.

References

[1] M. Eddaoudi, J. Kim, N. Rosi, D. Vodak, J. Wachter, M. O'Keefe, O. M. Yaghi, *Science*, **2002**, *295*, 469-472.

[2] Z. Wang, K. K. Tanabe, S. M. Cohen, *Inorg. Chem.*, **2009**, *48*, 296-306.

[3] K. Koh, A. G. Wong-Foy, A. J. Matzger, *Angew. Chem. Int. Ed.*, **2008**, *47*, 677-680.

[4] J. S. Costa, P. Gamez, C. A. Black, O. Roubeau, S. J. Teat, J. Reedijk, *Eur. J. Inorg. Chem.*, **2008**, 1551-1554.

[5] S. Bauer, C. Serre, T. Devic, P. Horcajada, J. Marrot, G. Ferey, N. Stock, *Inorg. Chem.*, **2008**, *47*, 7568-7576.

[6] F. Vermoortele, R. Ameloot, A. Vimont, C. Serre, D. De Vos, *Chem. Commun.*, **2011**, *47*, 1521-1523.

[7] M. Hartmann, M. Fischer, *Microp. Mesop. Mater*., **2012**, *164*, 38-43.

[8] M. Savonnet, D. Farrusseng, PCT Appl. WO2011048284, 2011

[9] M. A. Moreira, J. C. Santos, A. F. P. Ferreira, J. M. Loureiro, F. Ragon, P. Horcajada, P. G. Yot, C. Serre, A. E. Rodrigues, *Langmuir*, **2012**, *28*, 3494-3502.

[10] P. Gamez, J. S. Costa, C. A. Black, O. Roubeau, S. J. Teat, J. Reedijk, *Eur. J. Inorg. Chem.* **2008**, 1551-1554.

[11] A. D. Burrows, C. G. Frost, M. F. Mahon, C. Richardson, *Angew. Chem., Int. Ed.*, **2008**, *47*, 8482-8486.

[12] J. S. Seo, D. Whang, H. Lee, S. I. Jun, J. Oh, Y. J. Jeon, K. Kim, *Nature*, **2000**, *404*, 982-986.

[13] V. Valtchev, G. Majano,S. Mintova, J. Perez-Ramırez, *Chem. Soc. Rev.*, **2013**,*42*, 263-290.

[14] S. M. Cohen, *Chem. Rev*., **2012**, *112*, 970-1000.

[15] Z. Wang, S. M. Cohen, *Chem. Soc. Rev*., **2009**, *38*, 1315-1329.

[16] K. K. Tanabe, S. M. Cohen, *Chem. Soc. Rev*., **2011**, *40*, 498-519.

[17] D. Venkataraman, G. B. Gardner, S. Lee, J. S. Moore, *J. Am. Chem. Soc*., **1995**, *17*, 11600-11601.

[18] a) O. M. Yaghi, G. M. Li, H. L. Li, *Nature*, **1995**, *378*, 703-706., b) Y. K. Hwang, D.-Y. Hong, J.-S. Chang, H. Seo, M. Yoon, J. Kim, S. H. Jhung, C. Serre, G. Férey, *Appl. Catal. A*, **2009**, *358*, 249-253.

[19] J. L. C. Rowsell, O. M. Yaghi, *J. Am. Chem. Soc.*, **2006**, *128*, 1304-1315.

[20] S. Das, H. Kim, K. Kim, *J. Am. Chem. Soc*., **2009**, *131*, 3814-3815.

[21] A. M. Shultz, A. A. Sarjeant, O. K. Farha, J. T. Hupp, S. T. Nguyen, *J. Am. Chem. Soc.* **2011**, *133*, 13252-13255.

[22] F. Ke, L. G. Qiu, Y. P. Yuan, F. M. Peng, X. Jiang, A. J. Xie, Y.-H. Shen, J. F. Zhu, *J. Hazardous Mater.*, **2011,** *196*, 36-43.

[23] H. G. T. Nguyen, M. H. Weston, O.K. Farha, J.T. Hupp, S. T. Nguyen, *Cryst. Eng. Comm.*, **2012**, *14*, 4115-4118.

[24] S.-N. Kim, S.-T. Yang, J. Kim, J.-E. Park, W.-S. Ahn, *Cryst. Eng. Comm*., **2012**, *14*, 4142-4147.

[25] D. Britt, C. Lee, F. J. Uribe-Romo, H. Furukawa, O.M. Yaghi, *Inorg. Chem*., **2010**, *49*, 6387-6389.

[26] K. Hindelang, S. I. Vagin, C.Anger, B. Rieger, *Chem. Commun*., **2012**, *48*, 2888-2890.

[27] S. J. Garibay, Z. Wang, K. K. Tanabe, S. M. Cohen, *Inorg. Chem*., **2009**, *48*, 7341-7349.

[28] S. J. Garibay, S. M. Cohen, *Chem. Commun*., **2010**, *46*, 7700-7702.

[29] K. Peikert, F. Hoffmann, M. Froba, *Chem. Commun*., **2012**, *48*, 11196-11198.

[30] Z. Wang, K. K. Tanabe, Seth M. Cohen, *Chem. Eur. J*., **2010**, *16*, 212-217.

[31] N. Ko, J. Kim, *Bull. Korean Chem. Soc*., **2011**, *32*, 2705-2710.

[32] J. S. Costa, P. Gamez, C.A. Black, O. Roubeau, S. J. Teat, J. Reedijk, *Eur. J. Inorg. Chem.*, **2008**, 1551-1554.

[33] A. Modrow, D. Zargarani, R. Herges, N. Stock, *Dalton. Trans*., **2012**, *41*, 8690.

[34] C. Volkringer, S. M. Cohen, *Angew. Chem. Int. Ed*., **2010**, *49*, 4644-4648

[35] T. Lescouet, J. G. Vitillo, S. Bordiga, J. Canivet, D. Farrusseng, *Dalton Trans.*, **2013**, *42*, 8249-8258.

[36] J. G. Nguyen, K. K. Tanabe, S. M. Cohen, *Cryst. Eng. Comm*., **2010**, *12*, 2335-2338.

[37] M. G. Goesten, J. Juan-Alcañiz, E. V. Ramos-Fernandez, K. B. S. S. Gupta, E. Stavitski, H. Bekkum, J. Gascon, F. Kapteijn, *J. Catal.*, **2011**, *281*, 177-187.

[38] S. Bernt, V. Guillerm, C. Serre, N. Stock, *Chem. Commun*., **2011**, *47*, 2838-2840.

[39] M. G. Goesten, K. B. S. S. Gupta, E. V. Ramos-Fernandez, H. Khajavi, J. Gascon, F. Kapteijn, *Cryst. Eng. Comm*., **2012**, *14*, 4109-4111.

[40] M. Kim, S. J. Garibay, S.M. Cohen, *Inorg. Chem*., **2011**, *50*, 729-731.

[41] M. Kim, J. F. Cahill, K. A. Prather, S. M. Cohen, *Chem. Commun*., **2011**, *47*, 7629-7631.

[42] K. M. L. Taylor-Pashow, J. D. Rocca, Z. Xie, S. Tran, W. Lin, *J. Am. Chem. Soc*., **2009**, *131*, 14261-14263.

[43] Y. Yoo, H.-K. Jeong, *Chem. Eng. J*., **2012**, *181–182*, 740-745.

[44] A. D. Burrows, C. G. Frost, M. F. Mahon, C. Richardson, *Chem. Commun*., **2009**, 4218-4220.

[45] A. D. Burrows, C. G. Frost, M. F. Mahon, C. Richardson, *Angew. Chem*., **2008**, *120*, 8610-8614.

[46] N. Reimer, B. Gil, B. Marszalek, N. Stock, *Cryst. Eng. Comm*., **2012**, *14*, 4119-4125.

[47] A. D. Burrows, S. O. Hunter, M. F. Mahon, C. Richardson, *Chem. Commun*., **2013**, *49*, 990-992.

[48] A. S. Gupta, R. K. Deshpande, L. Liu, G. I. N. Waterhouse, S.G. Telfer, *Cryst. Eng. Comm*, **2012**, *14*, 5701-5704.

[49] D. J. Lun, G. I. N. Waterhouse, S. G. Telfer, *J. Am. Chem. Soc*., **2011**, *133*, 5806-5809.

[50] J. Canivet, S. Aguado, G. Bergeret, D. Farrusseng, *Chem. Commun*., **2011**, *47*, 11650-11652.

[51] C. Chen, C. A. Allen, S. M. Cohen, *Inorg. Chem*., **2011**, *50*, 10534-10536.

[52] M. Savonnet, D. Bazer-Bachi, N. Bats, J. Perez-Pellitero, E. Jeanneau,V. Lecocq, C. Pinel, D. Farrusseng, *J. Am. Chem. Soc*., **2010**, *132*, 4518-4519.

[53] M. Savonnet, A. Camarata, J. Canivet, D. Bazer-Bachi, N. Bats, V. Lecocq, C. Pinel, D. Farrusseng, *Dalton Trans.*, **2012**, *41*, 3945-3948.

[54] M. Savonnet, E. Kockrick,A.Camarata, D. Bazer-Bachi, N. Bats,V. Lecocq, C. Pinel, D. Farrusseng, *New J. Chem*., **2011**, *35*, 1892-1897.

[55] P. Roy, A. Schaate, P. Behrens, A. Godt, *Chem. Eur. J.*, **2012**, *18*, 6979-6985.

[56] W. Zhu, C. He, P. Wu, X. Wu, C. Duan, *Dalton Trans*., **2012**, *41*, 3072-3077.

[57] K. K. Tanabe, C. A. Allen, S. M. Cohen, *Angew. Chem. Int. Ed*., **2010**, *49*, 9730-9733.

[58] R. K. Deshpande, G. I. N. Waterhouse, G. B. Jameson, S. G. Telfer, *Chem. Commun*., **2012**, *48*, 1574-1576.

[59] Y. F. Han, G. X. Jin, F. E. Hahn, *J. Am. Chem. Soc.*, **2013**, *135*, 9263-9266.

[60] A. D. Burrows, L. L. Keenan, *Cryst. Eng. Comm*., **2012**, *14*, 4112-4114.

[61] M. Savonnet, J. Canivet, S. Gambarelli, L. Dubois, D. Bazer-Bachi, V. Lecocq, N. Bats, D. Farrusseng, *Cryst. Eng. Comm*., **2012**, *14*, 4105-4108.

[62] W. Morris, C. J. Doonan, H. Furukawa, R. Banerjee, O. M. Yaghi, *J. Am. Chem. Soc*., **2008**, *130*, 12626-12627.

[63] S. Nagata, H. Sato, K. Sugikawa, K. Kokado, K. Sada, *Cryst. Eng. Comm*., **2012**, *14*, 4137-4141.

[64] F. Sun, Z. Yin, Q.-Q. Wang, D. Sun, M.H. Zeng, M. Kurmoo, *Angew. Chem*., **2013**, *125*, 4636-4641.

[65] K. Hindelang, A. Kronast, S. I. Vagin, B. Rieger, *Chem. Eur. J.*, **2013**, *19*, 8244-8252.

[66] M. A. Nasalevich, M. G. Goesten, T. J. Savenije, F. Kapteijn, J. Gascon, *Chem. Commun.*, **2013**, *49*, 10575-10577.

[67] D. Jiang, L. L. Keenan, A. D. Burrows, K. J. Edler, *Chem. Commun*., **2012**, *48*, 12053-12055.

[68] J. Aguilera-Sigalat, D. Bradshaw, *Chem. Commun*., **2014**, *50*, 4711-4713.

[69] Z. Wang, S. M. Cohen, *Angew. Chem. Int. Ed*., **2008**, *47*, 4699-4702.

[70] X. Zhang, F. X. L. Xamena, A. Corma, *J. Catal*., **2009**, *265*, 155-160.

[71] M. J. Ingleson, J. P. Barrio, J. B. Guilbaud, Y. Z. Khimyak, M. J. Rosseinsky, *Chem. Commun.*, **2008**, 2680-2682.

[72] B. Liu, S. Jie, Z. Bu, B. G. Li, *J. Mol. Catal. A: Chem.*, **2014**, *387*, 63-68.

[73] J. Yang, P. Li, L. Wang, *Catal. Comm.*, **2012**, *27*, 58-62.

[74] M. Pintado-Sierra, A. M. Rasero-Almansa, A. Corma, M. Iglesias, F. Sánchez., *J. Catal*., **2013**, *299*, 137-145.

[75] A. M. Rasero-Almansa, A. Corma, M. Iglesias, F. Sanchez, *ChemCatChem*, **2013**, *5*, 3092-3100.

[76] J. Liu, X. Zhang, J. Yang, L. Wang, *Appl. Organometal. Chem.*, **2014**, *28*, 198-203.

[77] C. J. Doonan, W. Morris, H. Furukawa, O. M. Yaghi, *J. Am. Chem. Soc*. **2009**, *131*, 9492-9493.

[78] K. K. Tanabe, S. M. Cohen, *Angew. Chem. Int. Ed*., **2009**, *48*, 7424-7427.

[79] J. Juan-Alcañiz, J. Ferrando-Soria, I. Luz, P. Serra-Crespo, E. Skupien, V. P. Santos, E. Pardo, F. X. L. Xamena, F. Kapteijn, J. Gascon, *J. Catal.*, **2013**, *307*, 295-304.

[80] H. G. T. Nguyen, M.H. Weston, A. A. Sarjeant, D. M. Gardner, Z. An, R. Carmieli, M. R. Wasielewski, O. K. Farha, J. T. Hupp, S. T. Nguyen, *Cryst. Growth Des*., **2013**, *13*, 3528-3534.

[81] T. Gadzikwa, O. K. Farha, K. L. Mulfort, J. T. Hupp, S. T. Nguyen, *Chem. Commun.*, **2009**, 3720-3722.

[82] S. Bhattacharjee, D.A. Yang, W. S. Ahn, *Chem. Commun*., **2011**, *47*, 3637-3639.

[83] J. E. Halls, A. Hernan-Gomez, A. D. Burrows, F. Marken, *Dalton Trans*., **2012**, *41*, 1475-1480.

[84] J. Kim, D. O. Kim, D. W. Kim, J. Park, M. S. Jung, *Inorg. Chim. Acta*, **2012**, *390*, 22-25.

[85] K. Manna, T. Zhang, W. Lin, *J. Am. Chem. Soc*., **2014**, *136*, 6566-6569.

[86] K. Leus, G. Vanhaelewyn, T. Bogaerts, Y.-Y. Liu, D. Esquivel, F. Callens, G.B. Marind, V. V. Speybroeck, H. Vrielinck, P. V. D. Voort, *Catal. Today*, **2013**, *208*, 97-105.

[87] T. Zhou, Y. Du, A. Borgna, J. Hong, Y. Wang, J. Han, W. Zhang, R. Xu, *Energy Environ. Sci*., **2013**, *6*, 3229-3234.

[88] N. Candu, M. Tudorache, M. Florea, E. Ilyes, F. Vasiliu, I. Mercioniu, S. M. Coman, I. Haiduc, M. Andruh, V. I. Parvulescu, *Chem.PlusChem.*, **2013**, *78*, 443-450.

[89] J. Canivet, S. Aguado, Y. Schuurman, D. Farrusseng, *J. Am. Chem. Soc.*, **2013**, 135, 4195-4198.

[90] P. V. Dau, S. M. Cohen, *Chem. Commun*., **2013**, *49*, 6128-6130.

[91] P. V. Dau, M. Kim, S. M. Cohen, *Chem. Sci*., **2013**, *4*, 601-605.

Part II: Synthesis and Post-Synthetic Modification

Chapter II.1: Designing Near-Infrared and Visible Light Emitters by Post-Synthetic Modification of Ln^{3+}-IRMOF-3

- Introduction
- Post-Synthetic Modification of IRMOF-3
- Ln^{3+} coordination to PSM-terminated IRMOF-3
- Photoluminescence properties
- Magnetic properties
- References

Introduction

Porous metal-organic frameworks (MOFs) or porous coordination polymers are crystalline materials consisting of metal ions bridged by organic linkers and exhibiting microporosity reminiscent of zeolites.[1] MOFs have been synthesized using different methods (hydrothermal, solvothermal, mechanochemical and sonochemical syntheses and microwave-assisted synthesis).[2] Due to their high surface areas and interesting topological structures, MOFs have potential for being used in gas storage and purification, catalysis, chemical sensing, and biotechnology.[3]

Yaghi and co-workers prepared functionalized MOFs bearing a variety of chemical moieties (*e.g.*, NH_2, Br, CH_3) via a 'pre-synthetic' approach, *i.e.*, by functionalization of the linkers prior to the MOFs synthesis.[4] Since this method has some limitations [reactivity and polarity properties of the functional groups in the organic linker is a challenging for the MOF synthesis, because the groups may be not compatible with the MOF synthetic conditions (*e.g.*, chemical or thermal instability, insolubility, steric bulk, etc.), an alternative route for obtaining functionalized MOFs was proposed by Cohen *et al.*, the so-called post-synthetic modification (PSM),[5] which encompasses the chemical transformation of the linker present in the synthesized MOFs. PSM allows controlling the type and number of functional groups incorporated into the framework to an extent that is often not possible by direct synthesis. Both the metal and organic components may be changed and functionalized, without compromising the overall stability of the framework, permitting the preparation of topologically-identical, though functionally-diverse, frameworks. The use of PSM has some requirements, MOFs must: i) be sufficiently porous to admit the organic reagents; ii) have chemically-modifiable functional groups; iii) be stable in the reaction media, and iv) be stable to any of the formed by-products.

Lanthanide complexes have many important applications, *e.g.*, in cellular imaging, fluoroimmunoassays, lasers, magnetic resonance imaging, light emitting diodes (LEDs) and optical fibers.[6] Eu^{3+} and Tb^{3+} ions are of particular interest due to their visible long-live emission and strong photoluminescence properties.[7] Near-infrared (NIR) light-emitters Nd^{3+}, Yb^{3+} and Er^{3+} have potential applications in luminescence bioassays, laser systems and optical amplification.[8] The synthesis of Ln-based MOFs is, at present, a very active field of research,[9] particularly in view of the possibility of combining microporosity and light emission and fabricating sensor devices for small molecules,[10] anions,[11] cations,[12]

gases and vapors,[13] temperature,[14] etc. Other applications for Ln-MOFs encompass light-emitting devices,[15] multimodal imaging[16] and drug delivery.[17]

Our objectives are i) design and tuning of NIR hybrid materials via covalent post-synthetic modification of IRMOF-3 followed by the complexation of Nd^{3+}, hosted in the nanochannels, by pendant protruding ligands (*e.g.*, *β*–diketonates: pentane-2,4-dione (AC) and 3-(2-hydroxyphenyl)-3-oxopropanal (OL)), ii) extend the study to two other types of PSM modification, *viz.* the reaction of IRMOF-3 with ethyl oxalyl monochloride (EOC) and ethyl acetoacetate (EAA), followed by complexation with Ln^{3+}, resulting in NIR (Nd^{3+}) and visible-light (Eu^{3+}, Tb^{3+}) emitters, iii) further extend the study to engineering lanthanide-optical center in IRMOF-3 via Michael addition of amines onto α,β -unsaturated carbonyl compounds (methyl vinyl ketone), nucleophilic substitution with diethyl (ethoxymethylene)malonate and/or chloroacetic acid, and nucleophilic addition onto glyoxylic acid. The novel PSM route produced active chelating site, which opening the door to the coordinated with lanthanide for optical applications.

Our method may be applied to other porous MOFs, and is particularly suited for engineering multifunctional materials combining the properties of both, the framework metals and linkers, and the pendant ligands and Ln^{3+} ions.

Post-Synthetic Modification of IRMOF-3

This part describe the post-synthetic modification of IRMOF-3 and the characterization of the structure using powder X-ray diffraction (PXRD), solid state NMR, liquid state NMR, CHN analysis and IR spectroscopy.

IRMOF-3-AC

IRMOF-3-AC was obtained by reacting IRMOF-3 with an excess of pentane-2,4-dione in toluene for one day in a closed vessel at 60 °C (scheme II.1.1). Single crystal X-ray analysis of modified IRMOF-3 yielded good solutions for bdc ligands and the Zn_4O SBUs (SBU = secondary building unit). The new substituents of the linker, however, could not be resolved by single crystal X-ray analysis of the modified IRMOF-3, presumably due to disorder over the four positions of the bdc ligand.[18,19] The crystals were, then, digested in a mixture of d_6-DMSO (500 μL) and DCl (100 μL, 35% DCl) for solution NMR analysis, to confirm the modification of the bdc ligand.

The modified crystals were also characterized by powder XRD, which indicated that the integrity and crystallinity of the framework were not affected (Figure A1). The degree of conversion of the amine groups was ascertained by ^{1}H NMR analysis of the acid-digested modified IRMOF-3-AC. Because the imine group is unstable in acidic medium,[20] this digestion decomposes the MOF, releasing the modified linker. A 46% conversion was calculated from the intensity (area) ratio of the resonances given by pentane-2,4-dione and 2-aminoterephthalic acid in the case of IRMOF-3-AC. This transformation was also confirmed by solid-state ^{13}C CP/MAS NMR (Figure II.1.1, A13), with the resonances at 20.3 and 29.9 (methyl groups) 100.2 (vinylic CH), 151.3 (=CNH) and 195.5 (C=O) ppm being assigned to the pentane-2,4-dione moiety.

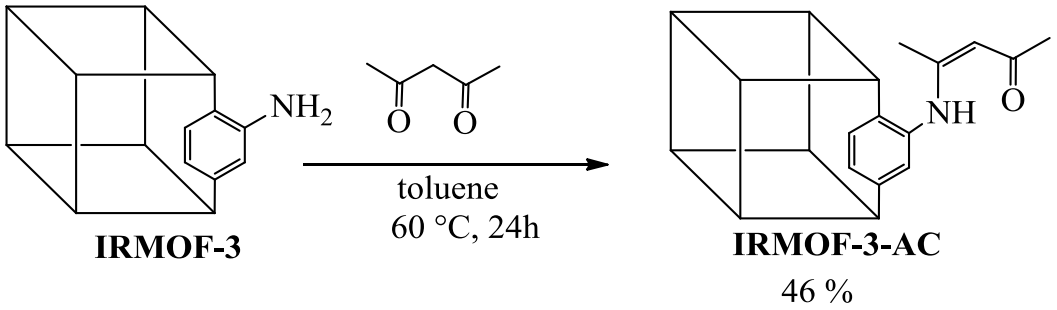

Scheme II.1.1 Post-synthetic modification of IRMOF-3 with pentane-2,4-dione.

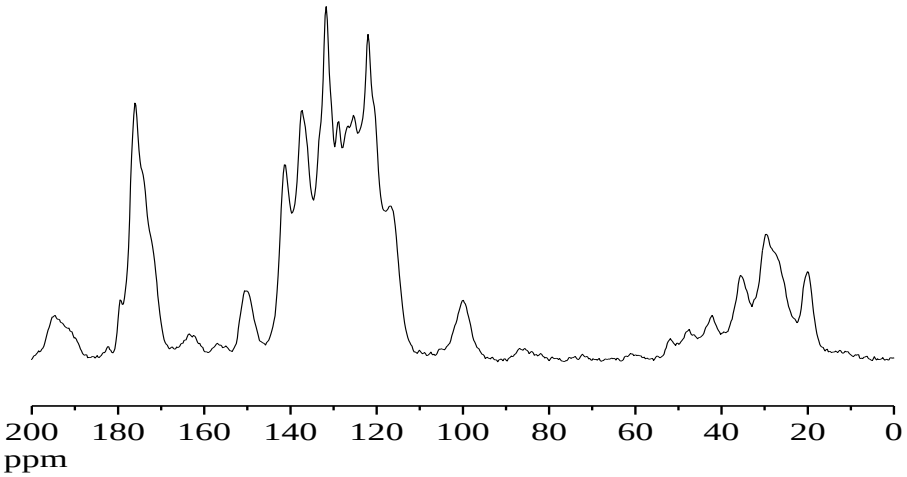

Figure II.1.1 Solid-state ^{13}C CP/MAS NMR spectra of IRMOF-3-AC.

The FTIR spectra of IRMOF-3-AC show intense bands at 1620 and 1578 cm^{-1} due to the carboxylate and phenyl ring vibrations, and at 1384 cm^{-1}, ascribed to the bending vibration of C-CH_3 (Figure A65). CHN analysis (Table A1) and NMR spectroscopy allow formulating IRMOF-3-AC as $[Zn_4O(C_{13}H_{11}NO_5)_{1.38}(C_8H_5NO_4)_{1.62}]$.

IRMOF-3-OL

The reaction of IRMOF-3 with 3-(2-hydroxyphenyl)-3-oxopropanal in refluxing chloroform for 48h gave IRMOF-3-OL (scheme II.1.2). IRMOF-3 and IRMOF-3-OL was characterized by X-ray powder diffraction as shown in Figure A2, the results show well-resolved identical peaks, indicating that the original MOF framework structure was not change after the post-synthetic reaction (high phase purity and high crystalline).

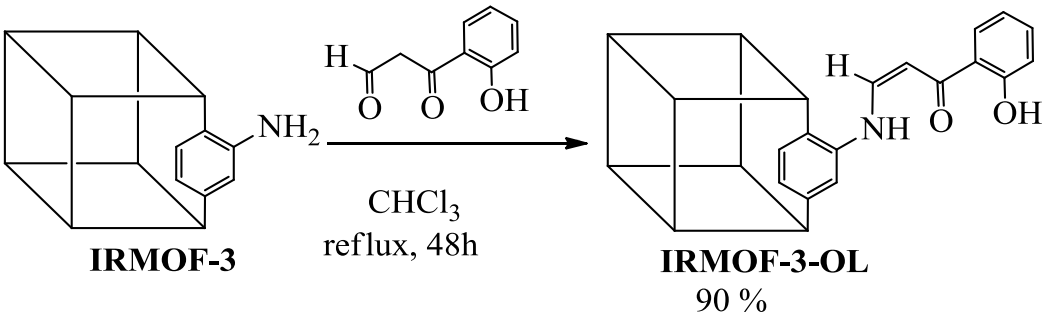

Scheme II.1.2 Post-synthetic modification of IRMOF-3 with 3-(2-hydroxyphenyl)-3-oxopropanal.

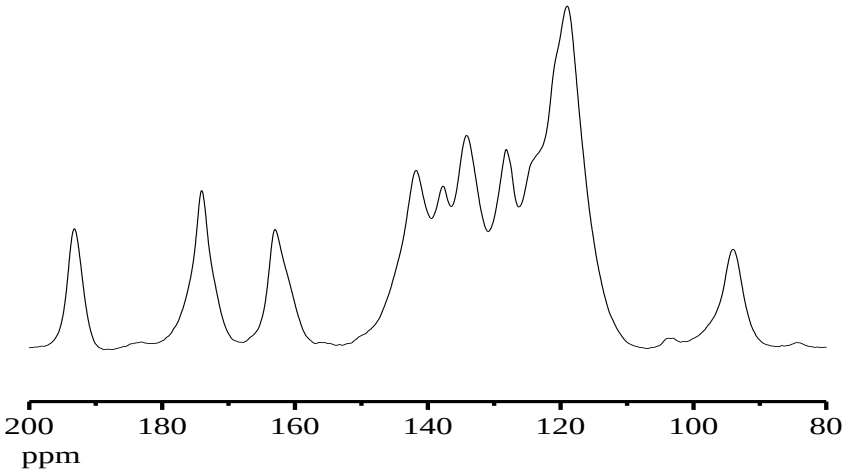

Figure II.1.2 Solid-state ^{13}C CP/MAS NMR spectra of IRMOF-3-OL.

The solution ^{1}H NMR of this compound after decomposition with DCl-D_2O-DMSO-d_6 revealed the degree of conversion of the IRMOF-3-OL amine groups to be 90% (Figures A14 and A15). This spectrum exhibits all the proton resonances of the modified MOF (Figures A14 and A15), namely those of the *α,β*-unsaturated system at 6.30 and 8.08 ppm (the *J* coupling constant of this vinylic system, 8.3 Hz, indicates a *cis*-configuration). Again, ^{13}C CP-MAS NMR, (Figure II.1.2, A16) confirmed the modification, namely by the typical resonances of the new substituent of the linker at 94.4 (vinylic CH), 163.3

(aromatic C-OH), 193.2 (C=O) ppm, as well as the resonance of the linker carboxylates at 174.2 (COO) ppm. The FTIR spectra exhibit intense carboxylate and phenyl ring bands in the region 1616 – 1578 cm^{-1}. In addition, the –OH bending appears at 1234 cm^{-1} (Figure A66). CHN analysis (Table A1) and NMR spectroscopy yield for IRMOF-3-OL the formula $[Zn_4O(C_{17}H_{11}NO_6)_{2.7}(C_8H_5NO_4)_{0.3}]$.

IRMOF-3-EOC

Recently, the oxamate route was used as a multilateral post-functionalization for metal (Cu, Pd, and Au) incorporation in MIL-101(Cr). The modified materials were applied in catalysis (click chemistry catalysis and multicomponent coupling reactions).[21] Mixing IRMOF-3 with a solution of EOC and triethylamine (TEA) in chloroform for 48 h at 40°C affords IRMOF-3-EOC (scheme II.1.3) (TEA is added to scavenge the formed HCl and to prevent the dissolution of IRMOF-3).

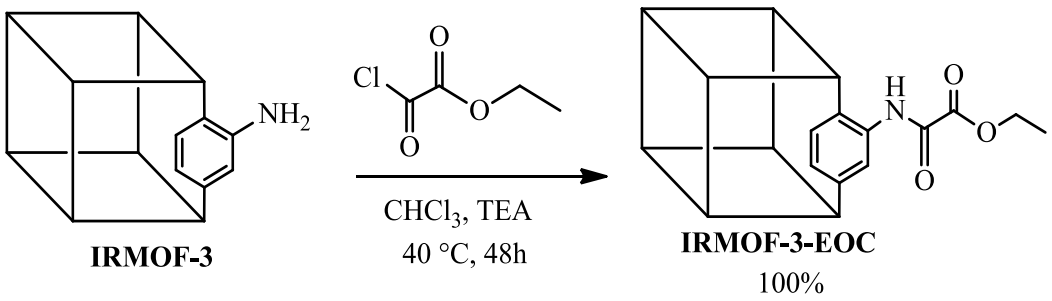

Scheme II.1.3 Post-synthetic modification of IRMOF-3 with ethyloxolylchloride.

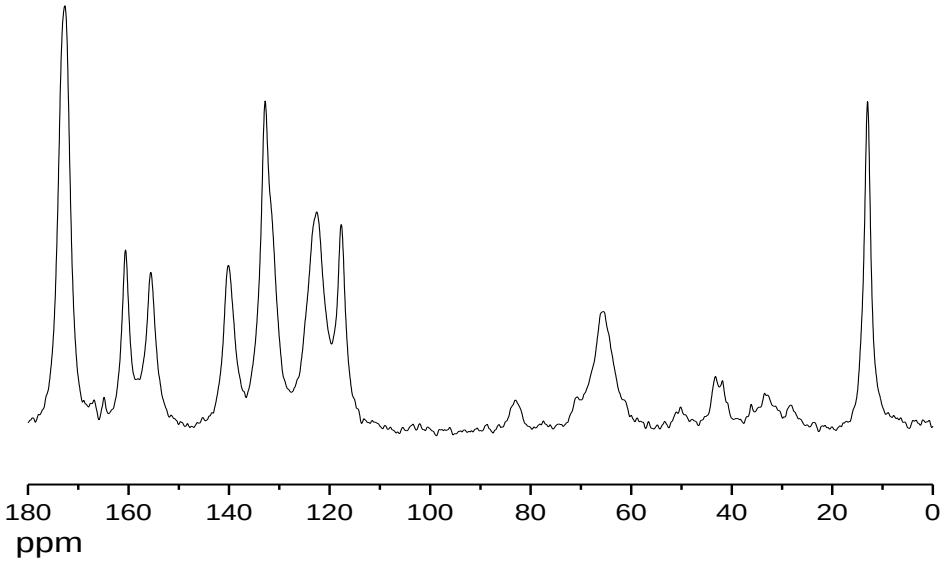

Figure II.1.3 Solid-state ^{13}C CP/MAS NMR spectra of IRMOF-3- EOC.

The solid-state ^{13}C CP/MAS NMR spectrum of IRMOF-3-EOC further confirms PSM, exhibiting resonances at δ 13.2 and 61.1 ppm given by the ethyl group and peaks at δ 157.3, 161.2 and 173.5 ppm assigned to the carbonyl groups (Figure II.1.3, A20). The ^{1}H NMR spectrum of the digested crystals with diluted DCl (100 µL, 35% DCl) in D_6-DMSO shows a 100 % degree of conversion of the amine groups. Signals at δ 1.35 (t, *J* 7.3 Hz), 4.35 (q, *J* 7.3 Hz), 7.77 (dd, *J* 1.6 and 8.2 Hz), 8.11 (d, *J* 8.2 Hz), 9.11 (d, *J* 1.6 Hz) ppm were assigned to the ethyl group and aromatic protons of the modified MOF (Figure A17-A19). Powder X-ray diffraction (PXRD) indicates that the structural integrity of IRMOF-3-EOC is preserved (Figure A2).

The Fourier transform infrared (FTIR) spectra of IRMOF-3-EOC show intense bands in the region 1623 and 1583 cm^{-1} due to the stretching vibrations of chelated carboxylates and phenyl ring; a band at 1685 cm^{-1} attributed to the stretching vibration of the free C=O; a band at 3372 cm^{-1} ascribed to the amine proton; and bands at 3100, 2832 and 2649, 1371 cm^{-1} due to the stretching and bending vibrations of CH_2 and C-CH_3 (Figure A67). CHN analysis (Table A2) and NMR confirm the chemical formula of IRMOF-3-EOC to be $[Zn_4O(C_{12}H_9NO_7)_3]$.

IRMOF-3-EAA

IRMOF-3-EAA was prepared by a dropwise addition of EAA to IRMOF-3 dispersed in toluene at 80°C for 24 h (scheme II.1.4). PXRD indicates that the structure of IRMOF-3-EAA is not affected by modification (Figure A5). The degree of transformation (65%) was calculated from solution ^{1}H NMR spectrum by digested modified crystals with diluted DCl in D_6-DMSO (Figure A21). The characteristic ^{1}H NMR resonances of the methyl, methylene and ethyl moieties appear at δ 1.18 (t, 3H, *J* 7.3 Hz), 2.15 (s, 3H), 3.45 (br s, 2H), 4.10 (q, 2H, *J* 7.3 Hz), and the hydrolysed aromatic ring at δ 6.99 (dd, 1H, *J* 1.6 and 8.2 Hz), 7.33 (d, 1H, *J* 8.2 Hz), 7.78 (d, 1H, *J* 1.6 Hz) (Figure A21). Solid-state ^{13}C CP/MAS NMR (Figure II.1.4, A22) confirms PSM, exhibiting resonances at δ 13.8, 29.7 (CH_3), 49.7 (CH_2), 61.3 (CH_2 from the ethyl group), 118.7, 125.8, 132.9 (aromatic ring) 150.8 (C=N) and 175.6 ppm (C=O).

The FTIR spectrum shows an intense band at 1579 cm^{-1} due to the stretching vibrations of carboxylate of the framework, and a new band at 1708 cm^{-1} because the modified MOF has a free carbonyl group (Figure A68).

The chemical formula of IRMOF-3-EAA was confirmed by CHN analysis (Table A2) and NMR to be $[Zn_4O(C_{14}H_{13}NO_6)_{1.95}(C_8H_5NO_4)_{1.05}]$.

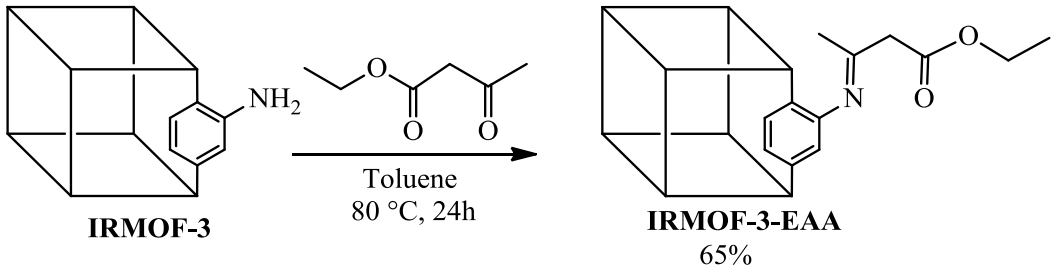

Scheme II.1.4 Post-synthetic modification of IRMOF-3 with ethylacetoacetate.

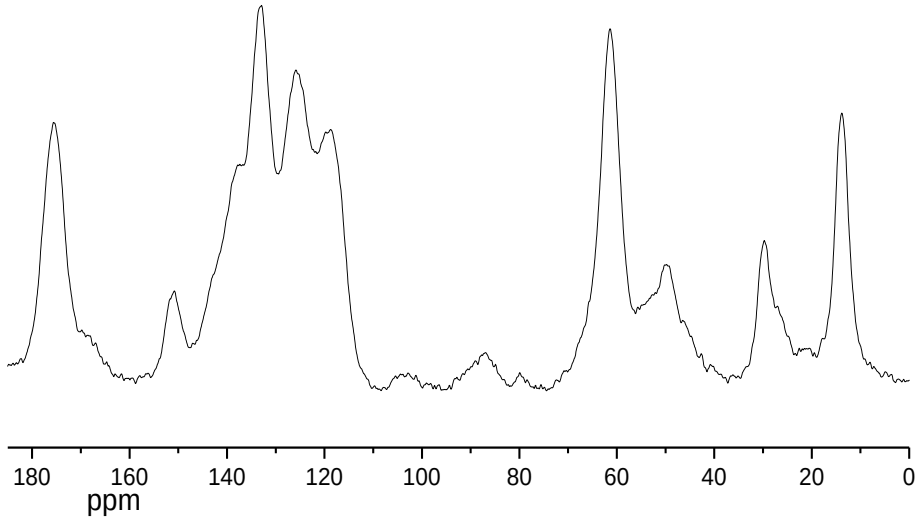

Figure II.1.4 Solid state ^{13}C CP/MAS NMR spectrum of IRMOF-3-EAA.

IRMOF-3-CA

IRMOF-3-CA resulted from the reaction of IRMOF-3 with 2-chloroacetic acid in chloroform in presence of tri ethyl amine (TEA) for 48 h at room temperature (scheme II.1.5). TEA is added to scavenge the formed HCl and to prevent the dissolution of IRMOF-3-CA. The ^1H NMR spectrum of IRMOF-3-CA shows signals at δ 7.45 (dd, J 1.6 and 8.2 Hz), 7.80 (d, J 1.6 Hz) and 7.95 (d, J 8.2 Hz) ppm due to the aromatic CH atoms (Figure II.1.5). The methylene group of IRMOF-3-CA appears as a singlet at δ 4.28 ppm (Figure A23 and A24). ^1H NMR shows that the conversion of the amine group was *ca.* 100 % since only signals from the modified structure were observed.

The ^{13}C NMR spectrum of IRMOF-3-CA shows signals at δ 43.2 (CH_2), 113.1, 115.3, 117.2, 131.4, 135.7 (aromatic carbons), 150.1 ($C_{aromatic}$-N), 167.2, 168.1 and 169.5 (carboxylates) ppm (Figure A25).

To ensure that the modification occurs within the crystals (and not just on their external surface), the solid-state ^{13}C CP/MAS NMR spectrum was measured and it displays resonances (δ 44.2, 117.9, 133.1, 137.9, 149.6, 173.0 and 176.8 ppm; Figure A26) similar to those seen in the solution-state spectrum.

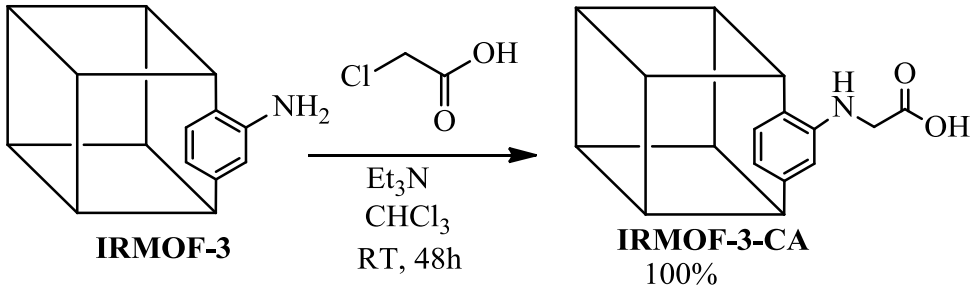

Scheme II.1.5 Post-synthetic modification of IRMOF-3 with 2-chloroacetic.

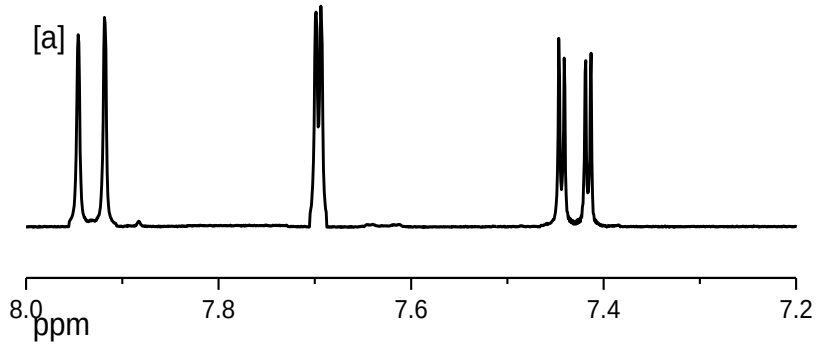

Figure II.1.5 Aromatic region of the ^{1}H NMR spectrum of IRMOF-3-CA after dissolving in DCl..

The Fourier transform infrared spectrum of IRMOF-3-CA shows intense bands in the region 1578-1616 cm^{-1}, due to the carboxylates, and at 2968, 2878 and 1438 cm^{-1}, assigned to the stretching and bending vibrations of the CH_2 group (Figure A69). CHN analysis confirms the chemical formula $[Zn_4O(C_{10}H_7NO_6)_3(C_6H_{15}N)_2]$ (Table A3).

IRMOF-3-GL

IRMOF-3-CL resulted from the reaction of IRMOF-3 with glyoxylic acid in acetonitrile for 48 h at room temperature (scheme II.1.6). The ^{1}H NMR spectrum of IRMOF-3-GL show signals at δ 7.42 (dd, *J* 1.6 and 8.2 Hz), 7.65 (d, *J* 1.6 Hz) and 7.92 (d, *J* 8.2 Hz) ppm due to the aromatic protons of the modified material and signals at δ 7.25, 7.56 and 7.96 ppm due to the aromatic protons of the unmodified material (Figure II.1.6).

The spectrum of IRMOF-3-GL shows a new peak at 5.31 ppm, which is assigned to the methynic proton of the NH-C*H*(OH)-COOH moiety. A 75% conversion of the amine group was calculated by comparing the integration of the signals from the modified material with the sum of both the modified and unmodified IRMOF-3 aromatic signals (Figures II.1.6, A27, A28). The ^{13}C NMR spectrum of IRMOF-3-GL shows signals at δ 84.1 (CH-OH), 115.3, 118.2, 120.1, 130.5, 135.4 (aromatic carbons), 145.2 ($C_{aromatic}$-N), 167.3, 168.4 and 169.5 (carboxylates) ppm for the modified MOF and signals at δ = 113.1, 119.3, 132.5, 136.2 (aromatic carbons), 148.4 ($C_{aromatic}$-N), 166.2 and 167.5 (carboxylates) ppm for the unmodified MOF (Figure A29). Solid-state ^{13}C CP/MAS NMR shows also the expected main signals (δ 86.0, 159.5, 167.7, 173.0-176.6 ppm) (Figure A30).

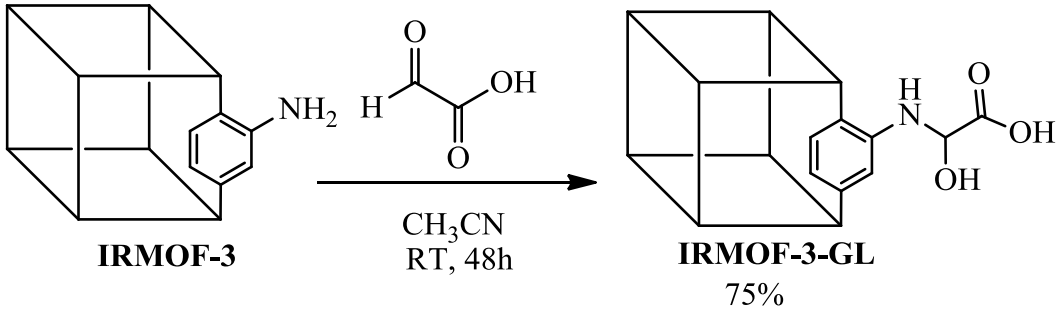

Scheme II.1.6 Post-synthetic modification of IRMOF-3 with gycoxalic acid.

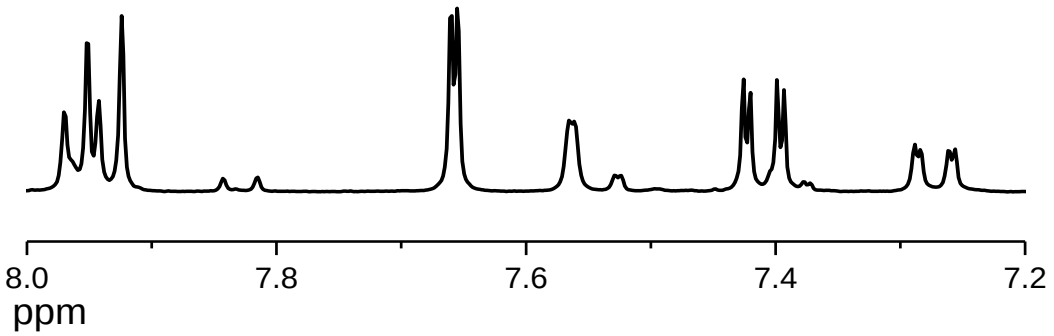

Figure II.1.6 ^{1}H NMR Spectra (aromatic region) recorded in DMSO-d_6 after dissolving the modified MOF in DCl of IRMOF-3-GL, (aliphatic signals are not shown, see A27 for details).

The successful linker modification may also be followed by infrafred spectroscopy, namely by the strong absorptions of the carboxylate groups at *ca.* 1627 cm^{-1} (asymmetric stretch) and 1392 cm^{-1} (symmetric stretch), and that at 1578 cm^{-1} due to phenyl ring vibrations. In addition, the –OH bending band appears at 1234 cm^{-1} (Figure A70).

^{1}HNMR, FTIR, EDX and CHN analysis (table A3) confirms the chemical formula: $[Zn_4O(C_{10}H_7NO_7)_{2.25}(C_8H_5NO_4)_{0.75}]$.

The available spectroscopic evidence shows that the reaction of glyoxylic acid with the MOF-amino group affords a structure resulting from the addition of the amino group to the aldehyde carbonyl group [Ar-NH-CH(OH)-CO_2H]. However, the elimination of water leading the imine group does not occur.

IRMOF-3-GL-R

A pseudo-reductive amination of IRMOF-3-GL was performed using sodium triacetoxyborohydride to afford IRMOF-3-GL-R (scheme II.1.7). The ^{1}H NMR spectrum shows some changes in signals and the aromatic protons of the modified material appear at δ 7.45 (dd, J=1.6 and 8.2 Hz), 7.69 (d, J= 1.6 Hz) and 7.94 (d, J=8.2 Hz) ppm (Figure II.1.7). The most important change is the disappearance of the signal at δ 5.31 ppm and appearance of a new resonance at δ 4.28 ppm, assigned to the methylene proton of the NH-CH_2-COOH moiety (Figure II.1.7, A31 and A32). This data indicates that the addition of triacetoxyborohydride favours the elimination of water and the formation of an imine, which is reduced to the correspondent amine (Scheme II.1.8).

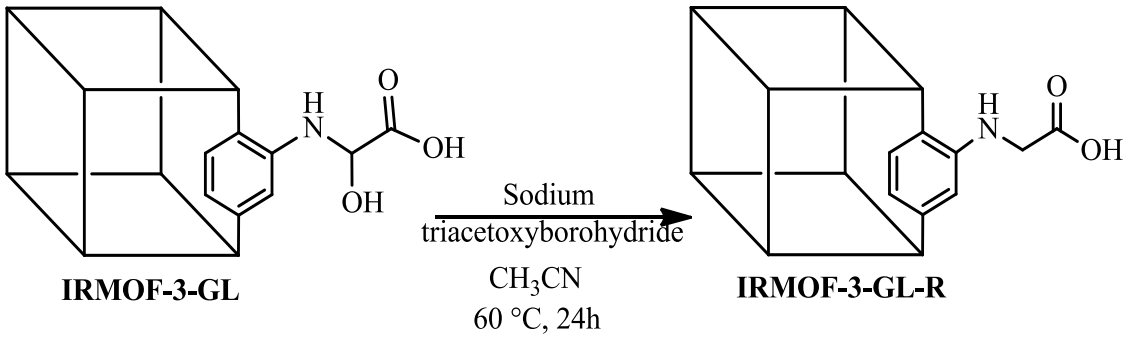

Scheme II.1.7 Post-synthetic modification of IRMOF-3-GL with sodium triacetoxyborohydride.

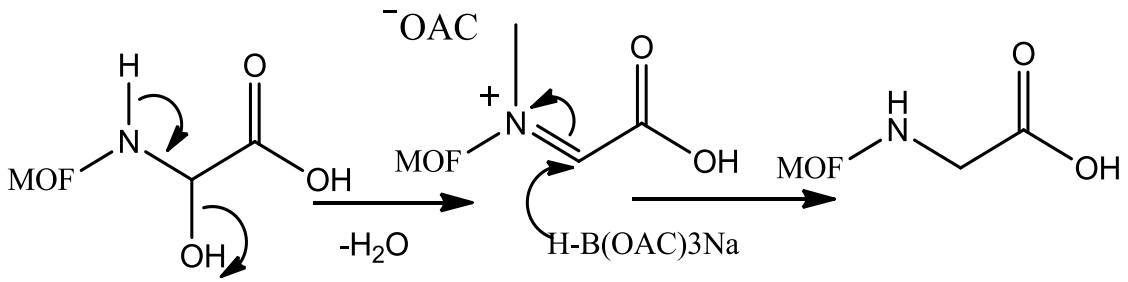

Scheme II.1.8 Reductive amination mechanism using sodium triacetoxyborohydride.

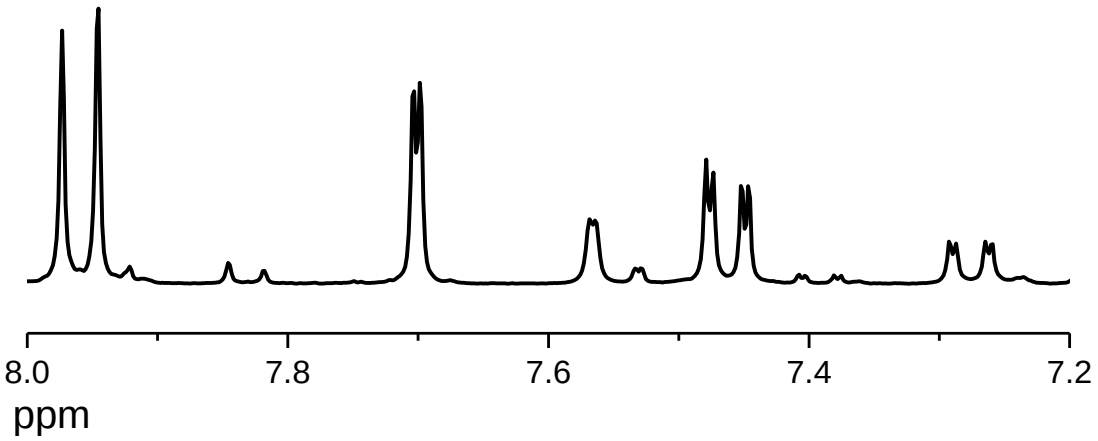

Figure II.1.7 ^{1}H NMR spectra (aromatic region) recorded in DMSO-d_6 after dissolving the modified MOF in DCl of IRMOF-3-GL-R (aliphatic signals are not shown, see A31 for details).

IRMOF-3-EM

Appending diethyl methylenemalonate to IRMOF-3 was accomplished in a 80 % yield by the reaction of the MOF-amino group with diethyl (ethoxymethylene)malonate in dry toluene at 80 °C, for 24 h (Scheme II.1.9, II.1.10).

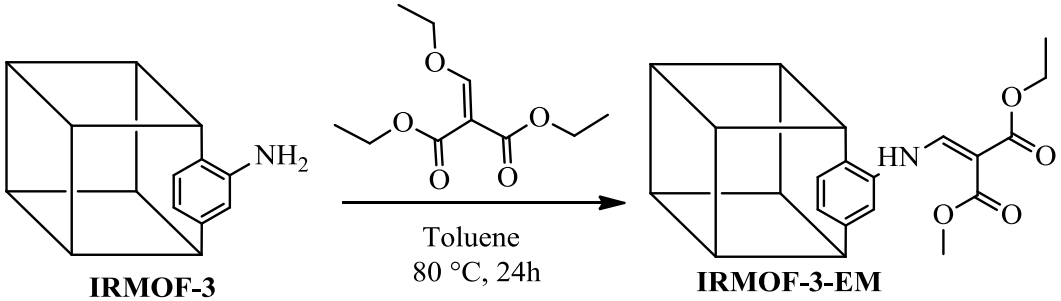

Scheme II.1.9 Post-synthetic modification of IRMOF-3 with diethyl(ethoxymethylene)malonate.

The ^{1}H NMR spectrum (Figures A33-A35) confirms that diethyl (ethoxymethylene)malonate in indeed linked to IRMOF-3 via a tandem Michael addition-elimination process (Scheme II.1.10). The ^{1}H resonances of IRMOF-3-EM appear at δ 1.21 and 1.24 (t, 3H, *J* 7.1 Hz, CH_3), 4.13 and 4.20 (q, 2H, *J* 7.1 Hz, CH_2), assigned to the protons of the inequivalent ethyl group, 7.64 (dd, 1H, *J* 8.2 and 1.3 Hz), 7.86 (d, 1H, *J* 1.3 Hz), 8.02 (d, 1H, *J* 8.2 Hz), attributed to the aromatic protons, 8.39 (s, 1H, olefinic-H). ^{13}C NMR also confirms the presence of IRMOF-3 bearing a diethyl methylenemalonate group: δ 14.4 (CH_3), 60.1 (CH_2), 96.6 (quaternary olefinic carbon), 114.3, 116.5, 120.5, 131.7,

136.1, 141.2 (aromatic carbons and olefinic CH), 148.5 ($C_{aromatic}$-N), 165.7, 167.7 and 168.8 (carboxylates) (Figure A36). All the ^{1}H and ^{13}C assignments were based on 2D NMR techniques [HMBC (Figures A37-39) and HSQC (Figures A40, 41)].

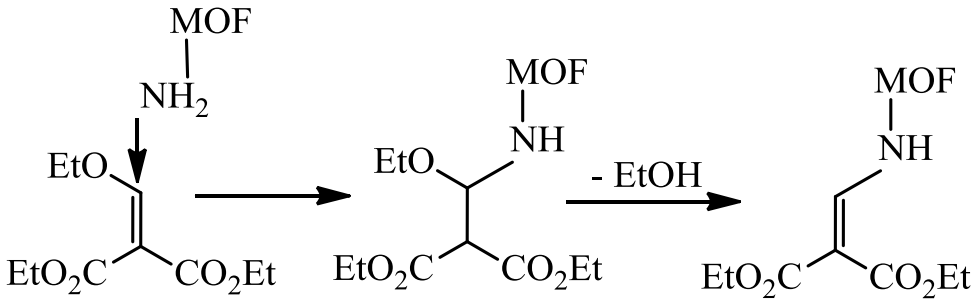

Scheme II.1.10 Reaction mechanism of IRMOF-3 with diethyl (ethoxymethylene)-malonate.

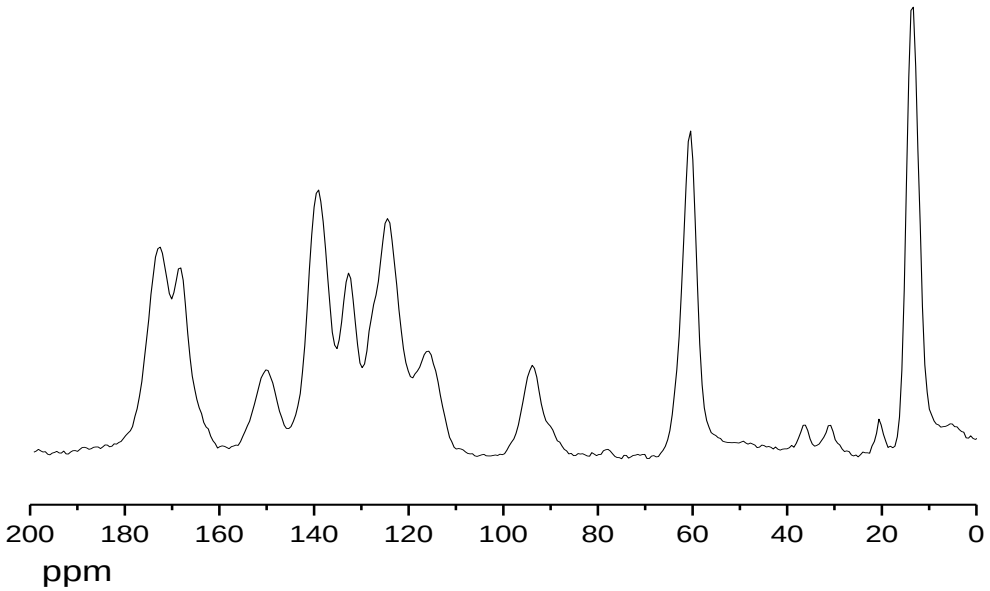

Figure II.1.8 ^{13}C CP/MAS spectrum of IRMOF-3-EM.

The solid-state ^{13}C CP/MAS NMR spectrum of IRMOF-3-EM further confirms the post-synthetic modification, exhibiting resonances at δ 13.2 and 61.1 ppm due to the ethyl group, and at δ 157.3, 161.2 and 173.5 ppm assigned to the carboxylates (Figure II.1.8).

The Fourier transform infrared spectrum of IRMOF-3-EM shows intense bands in the region 1623 and 1583 cm^{-1} due to the stretching vibrations of chelated carboxylates and of the phenyl ring, a band at 1685 cm^{-1} attributed to the stretching vibration of the free carboxylate, a band at 3372 cm^{-1} ascribed to the amine proton, and bands at 3100, 2832 and 2649, 1371 cm^{-1} due to the stretching and bending vibrations of CH_2 and C-CH_3 (Figure A71).

All data obtained from solid state NMR, solution state, FTIR, EDS and CHN analysis (Table A4) confirms the chemical formula $[Zn_4O(C_{16}H_{15}NO_8)_{2.4}(C_8H_5NO_4)_{0.6}]$.

IRMOF-3-MVK

Solid–gas and solid–vapour reactions have been studied since the end of the 19th century.[36] More recently these reactions have been applied extensively to organic,[37-41] organometallic[42-45] and metal–organic[46-50] compounds. Such studies have shown that not only dry-medium reactions are possible in a wide range of cases, but also that diverse crystalline forms that are not accessible from solution may be produced when macroscopic solvation is avoided. Finally, they represent a practicable alternative for 'greener' and cheaper industrial processes. Post-synthetic methods aimed at constructing C–N bonds have been intensively studied, in particular the Michael addition of amines to α,β-unsaturated carbonyl compounds. We have devised a synthetic method for the preparation of ketone-terminated IRMOF-3 via the reaction of methyl vinyl ketone vapour with the dry crystals of IRMOF-3 (scheme II.1.11).

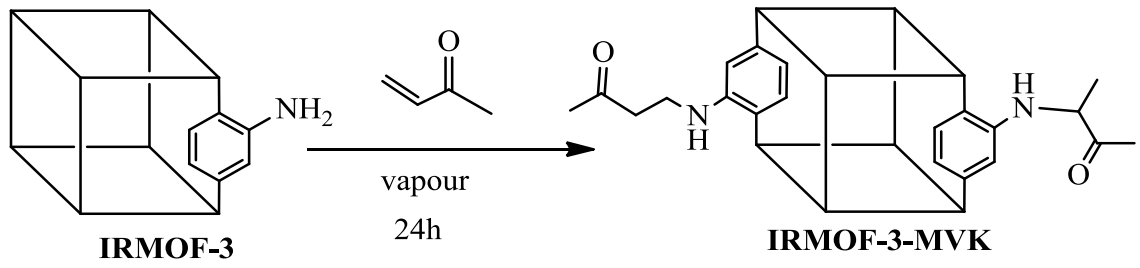

Scheme II.1.11 Post-synthetic modification of IRMOF-3 with methyl vinyl ketone.

We realised we are in the presence of two post-synthetic modifications of IRMOF-3 in a 1:1 proportion: i) a Michael addition of the MOF-amino group to the methyl vinyl ketone, appending a 3-oxobutyl group, and ii) the formation of a product resulting from the addition to the α-position of the methyl vinyl ketone. This may be due to the formation of a π complex between the double bond of the methyl ketone and the metal ions of the MOF, favouring the α-addition (Scheme II.1.12). To confirm the successful formation of the covalently functionalized IRMOF-3-MVK, a wide range of NMR spectra were measured, namely ^{1}H NMR (Figures A42-45), ^{13}C NMR (Figure A46), ^{13}C CP/MAS (Figure II.1.9), HSQC (Figures A47-49), HMBC (Figures A50-53), and 2D COSY (Figures A54-56).

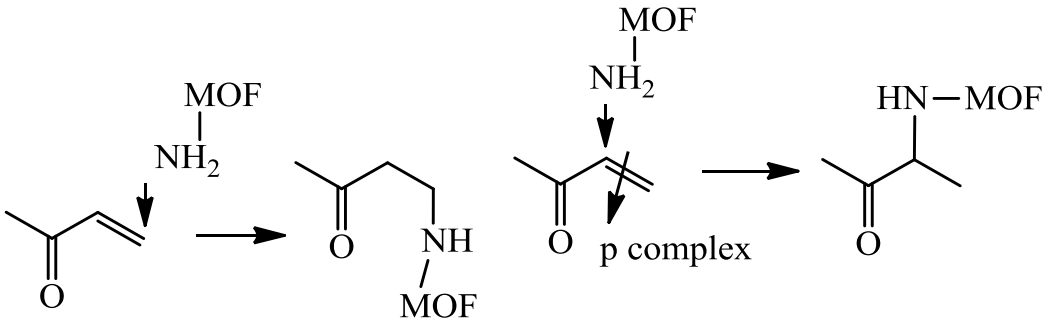

Scheme II.1.12 Reaction mechanism of IRMOF-3 with methyl vinyl ketone.

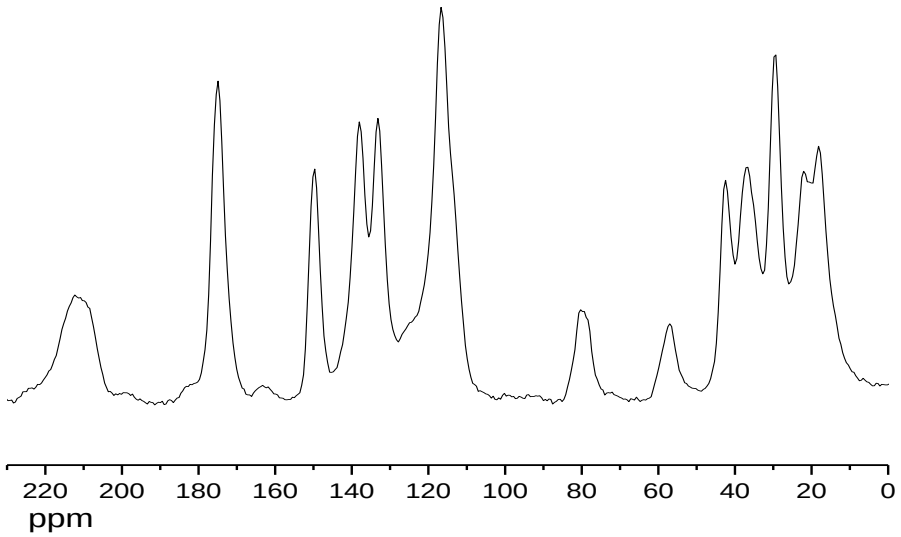

Figure II.1.9 ^{13}C CP/MAS spectrum of IRMOF-3-MVK.

The structure resulting from the Michael addition to methyl vinyl ketone is supported by the ^{1}H NMR resonances at δ 2.08 (s, 3H, CH_3), 2.76 (t, 2H, *J* 6.4 Hz, CH_2CO) and 3.35 (t, 2H, *J* 6.4 Hz, CH_2NH), assigned to the aliphatic moiety, and those at 7.02 (d, 1H, *J* 1.4 Hz), 7.07 (dd, 1H, *J* 8.2 and 1.4 Hz), 7.83 (d, 1H, *J* 8.2 Hz) due to the aromatic protons, and the carbon resonances at δ 30.5 (CH_3), 37.5 (CH_2NH) and 42.4 (CH_2CO), 112.8, 114.3, 115.4, 132.7, 136.2 (aromatic carbons), 150.5 ($C_{aromatic}$-N), 167.7 and 169.8 (carboxylates), 208.6 (ketone). The structure resulting from the α-addition of the amino-IRMOF-3 to methyl vinyl ketone is confirmed by the ^{1}H resonances at δ 1.31 (d, 3H, *J* 7.1 Hz, CH_3), 2.52 (s, 3H, $COC\underline{H}_3$), 4.33 (quart, 1H, *J* 7.1 Hz, $C\underline{H}CH_3$), 7.16 (dd, 1H, *J* 8.3 and 1.5 Hz), 7.21 (d, 1H, *J* 1.5 Hz), 7.81 (d, 1H, *J* 8.3 Hz) and the 13C resonances at δ 17.7 (CH_3), 37.2 (CH_3), 57.0 ($C\underline{H}CH_3$), 112.3, 113.9, 117.7, 132.3, 135.7 (aromatic carbons), 148.7 ($C_{aromatic}$-N), 167.8 and 169.1 (carboxylates), 211.3 (ketone). The solid-state ^{13}C

CP/MAS NMR spectrum of IRMOF-3-MVK further confirms the post-synthetic modification, as shown in figure II.1.8. The HMBC spectrum unequivocally proves the presence of the described two structures, mainly the connectivity of the $C\underline{H}_2NH$ with the $C_{aromatic}$-N (150.5 ppm) in the case of the Michael adduct and of $C\underline{H}CH_3$ with the $C_{aromatic}$-N (148.7 ppm) in the case of the α–addition (Figure II.1.10).

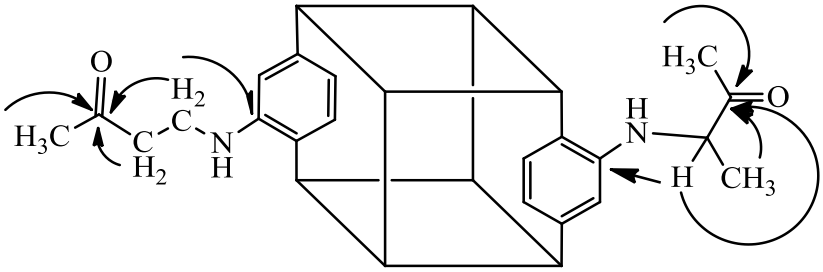

IRMOF-3-MVK

Figure II.1.10 Main connectivities observed in the HMBC spectrum.

The Fourier transform infrared spectrum (Figure A72) presents characteristic intense bands in the region 1623-1583 cm^{-1} due to the stretching vibrations of chelated carboxylates and phenyl ring, a band at 1706 cm^{-1} attributed to the stretching vibration of the free C=O. CHN analysis (Table A4) confirms the chemical formula $[Zn_4O(C_{12}H_{11}NO_5)_{1.38}(C_{12}H_{11}NO_5)_{0.9}(C_8H_5NO_4)_{0.72}]$.

Ln^{3+} coordination to PSM-terminated IRMOF-3

In this part the PSM-terminated IRMOF-3 was post-synthetically coordinated with lanthanide metal center (Eu^{3+}, Tb^{3+} or Nd^{3+}) to create light emitters material.

Ln-IRMOF-3-OL and Ln-IRMOF-3-AC

IRMOF-3-OL-Nd was prepared by mixing an ethanolic solution of $NdCl_3.6H_2O$ with IRMOF-3-OL dispersed in chloroform; the mixture was allowed to stand at room temperature for 3 days. Mixed Nd^{3+} and Y^{3+} samples were prepared by introducing $YCl_3 \cdot 6H_2O$ and $NdCl_3 \cdot 6H_2O$ (95:5 wt%) in the ethanol solution. For IRMOF-3-AC, the solid was dispersed in toluene and $NdCl_3 \cdot 6H_2O$ was dissolved in DMSO (scheme II.1.13). The integrity of the framework after Ln^{3+} complexation was confirmed by powder X-Ray diffraction (Figure A1-3). Scanning electron microscopy and optical microscopy show that the final Ln-bearing materials and the parent IRMOF-3 have the same habit (cubes, Figure

A57).

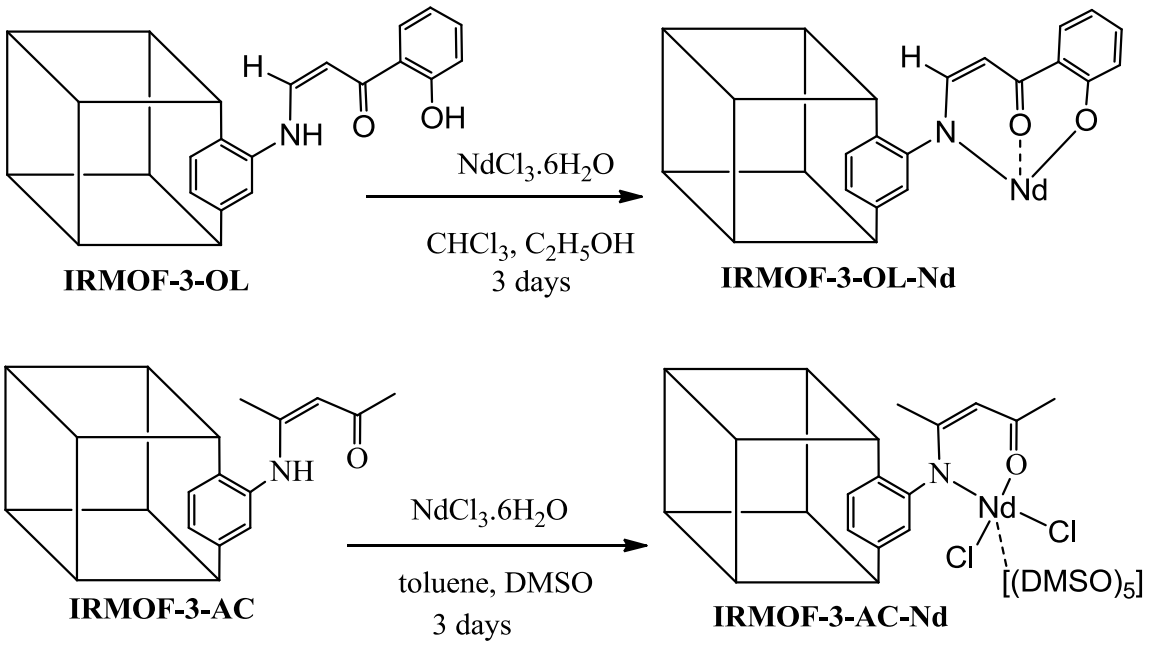

Scheme II.1.13 Post-synthetic metalation of IRMOF-3-AC and IRMOF-3-OL with neodymium ions.

The presence of neodymium (and yttrium) and the composition of the materials were ascertained by EDS, energy dispersive X-ray spectroscopy (Table A1). CHN analysis and EDS yield the formula: Nd-IRMOF-3-AC $[Zn_4O(C_{23}H_{40}NO_{10}S_5NdCl_2)_{1.38}(C_8H_5NO_4)_{1.62}]$; Nd-IRMOF-3-OL $[Zn_4O(C_{17}H_9NO_6)_{2.7}Nd_{0.9}(C_8H_5NO_4)_{0.3}]$; Nd-Y-IRMOF-3-OL $[Zn_4O(C_{17}H_9NO_6)_{2.7}Nd_{0.05}Y_{0.85}(C_8H_5NO_4)_{0.3}]$. The exact coordination spheres of the Ln^{3+} ions are still under scrutiny. Elemental analysis and FTIR suggest that in IRMOF-3-OL the Ln^{3+} ions are coordinated by three pendant organic moieties of the modified framework aromatic ring (Figure A66), while in IRMOF-3-AC the metal is coordinated to a single organic moeiety and five DMSO molecules (Figure A65).

Ln-IRMOF-3-EOC

The pendant groups of the modified IRMOF-3 were used to coordinate the light-emitter lanthanide (Nd^{3+}, Eu^{3+}, Tb^{3+}). A solution of $LnCl_3{\cdot}6H_2O$ (Nd, Eu, Tb) in ethanol was added to IRMOF-3-EOC dispersed in chloroform and allowed to stand at room temperature for 3 days (scheme II.1.14). The structural integrity of the samples after lanthanide incorporation is shown by powder X-ray diffraction (Figure A4 reveals only a small broadening of some reflections). The cubic crystal habit of all materials was confirmed by optical and scanning

electron microscopy (Figure A58-60).

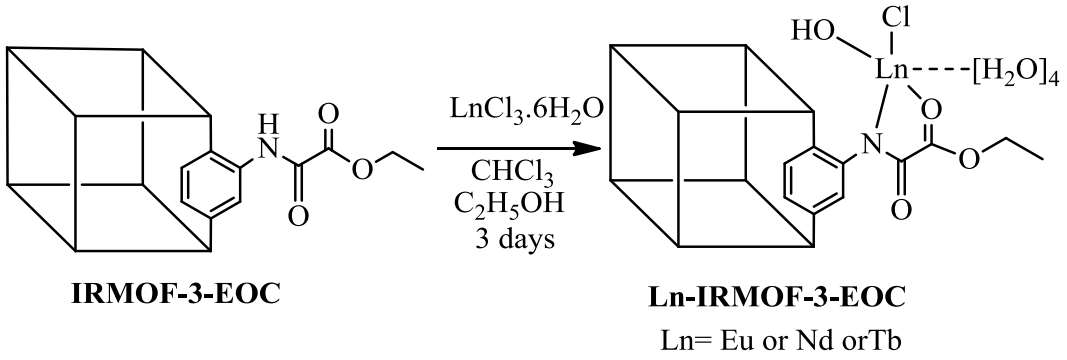

IRMOF-3-EOC **Ln-IRMOF-3-EOC**

Ln= Eu or Nd orTb

Scheme II.1.14 Post-synthetic metalation of IRMOF-3-EOC with lanthanide.

Energy dispersive X-ray spectroscopy analysis confirms the lanthanide incorporation (10 crystals measured per sample). Elemental analysis (Table A2) affords the chemical formula of the modified MOFs (Ln-IRMOF-3-EOC; Ln = Nd^{3+}, Eu^{3+}, Tb^{3+}): Nd-IRMOF-3-EOC [$Zn_4O(C_{12}H_{17}NO_{12}NdCl)_3$]; Eu-IRMOF-3-EOC [$Zn_4O(C_{12}H_{17}NO_{12}EuCl)_3$]; Tb-IRMOF-3-EOC [$Zn_4O(C_{12}H_{17}NO_{12}TbCl)_3$].

The nature of the coordination sphere of Ln^{3+} ions was ascertained from several techniques indicating for the metal a coordination number of 8. Energy dispersive X-ray spectroscopy analysis yields one chloride ion per Ln^{3+} ion (Table A2). FTIR is very informative, upon complexation (Figures II.1.11b and A68): (i) carbonyl band shifts from 1779 cm^{-1} (free carbonyl) to 1641 cm^{-1}; (ii) bands at 678 and 412 cm^{-1} are attributed to, respectively, Ln-N and Ln-O stretching vibrations;[36,37] (iii) band at 3573 cm^{-1} is assigned to Ln-OH (shifted from the usual free OH stretching at 3650-3590 cm^{-1}), while the band at 3477 cm^{-1} is attributed to Ln-OH_2 (iv) CH_3 and CH_2 bands appear at 3100, 2832 and 2649, 1371 cm^{-1}, suggesting successful chelation without hydrolysis of the ester. Thirdly, photoluminescence spectroscopy (see below) indicates the presence of 4 water molecules and one hydroxyl group per Eu^{3+} ion. Although the experimental spectroscopic evidence and chemical analysis data elucidate the nature of the Ln^{3+} coordination sphere in Ln-IRMOF-3-EOC, it is of interest to confirm it by DFT calculations. For this purpose, the MOF was replaced by a deprotonated ethyl 2-oxo-2-(phenylamino)acetate anion, coordinated to an La^{+} cation (via the amino nitrogen and the acetate carbonyl) surrounded by four H_2O molecules, one Cl^{-} and one OH^{-} anion. Following geometry optimization of several models (with distinct initial conformations) and simulation of the corresponding infrared spectra, the model whose FTIR spectrum best matched the experimental (Figure

II.1.11) one was considered representative of the real Ln^{3+} coordination (Figure II.1.12, top). The La^{3+} cation is simultaneously coordinated to four water molecules, one Cl^- and one hydroxyl as well as to the deprotonated amine nitrogen and the oxo- oxygen from the EOC fragment.

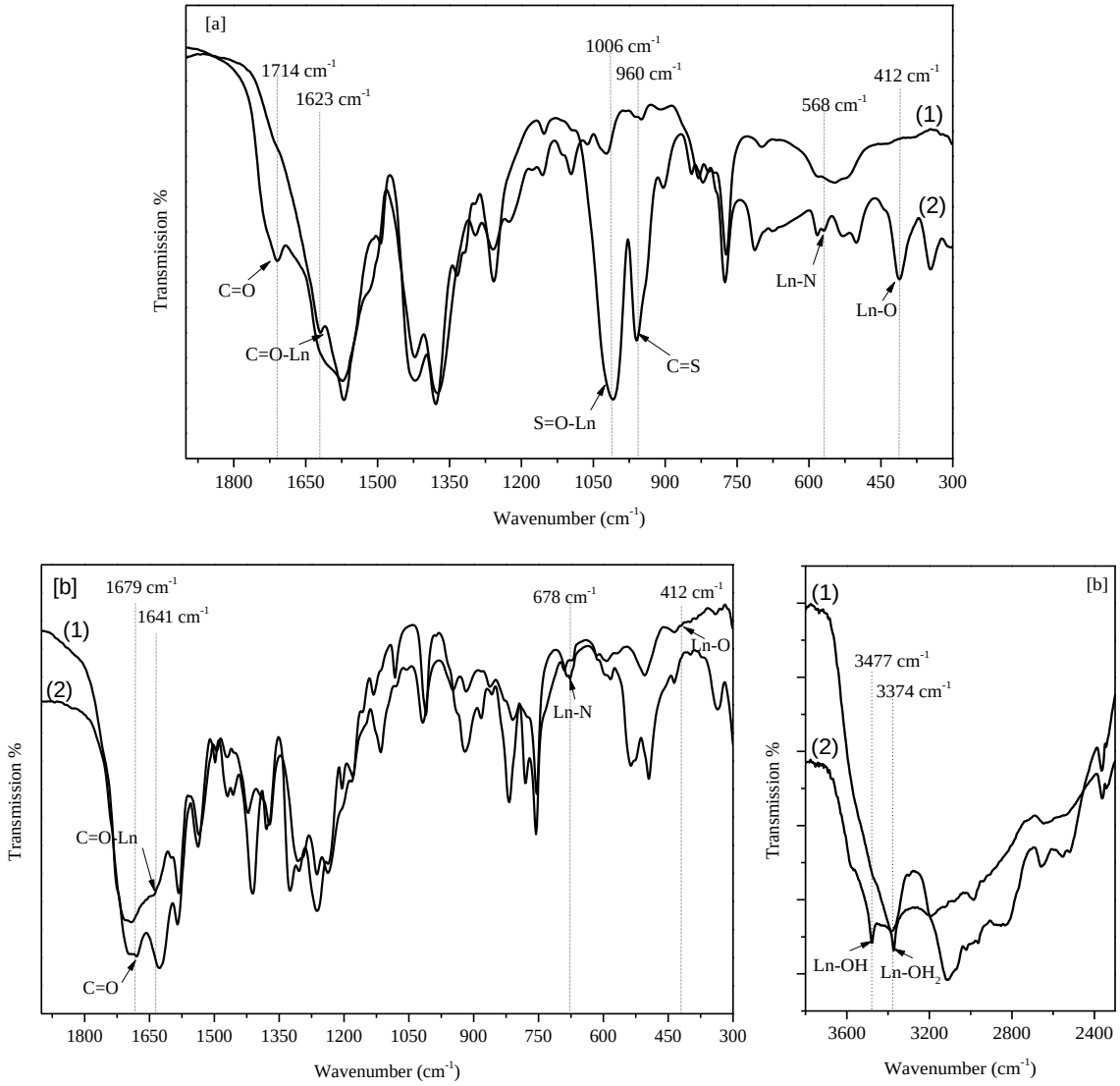

Figure II.1.11 FTIR spectra of a) IRMOF-3-EAA (1) and Tb-IRMOF-3-EAA (2), b) IRMOF-3-EOC (1) and Tb-IRMOF-3-EOC (2).

The La-OH_2 distances, ranging from 2.655 to 2.695 A°, are slightly longer than similar crystallographic distances (*ca.* 2.3-2.4 A°), which can be ascribed to an electron delocalization among the water and hydroxyl moieties, building up a network of hydrogen-bonds, leading to an efficient charge delocalization among water oxygens and, consequently, to weaker Eu-O interactions and longer Eu-O distances. The Eu-O distance involving the hydroxyl group is slightly shorter (2.452 A°) and adequately reflects a

stronger Eu-O interaction due to a more localized electron density on that oxygen.

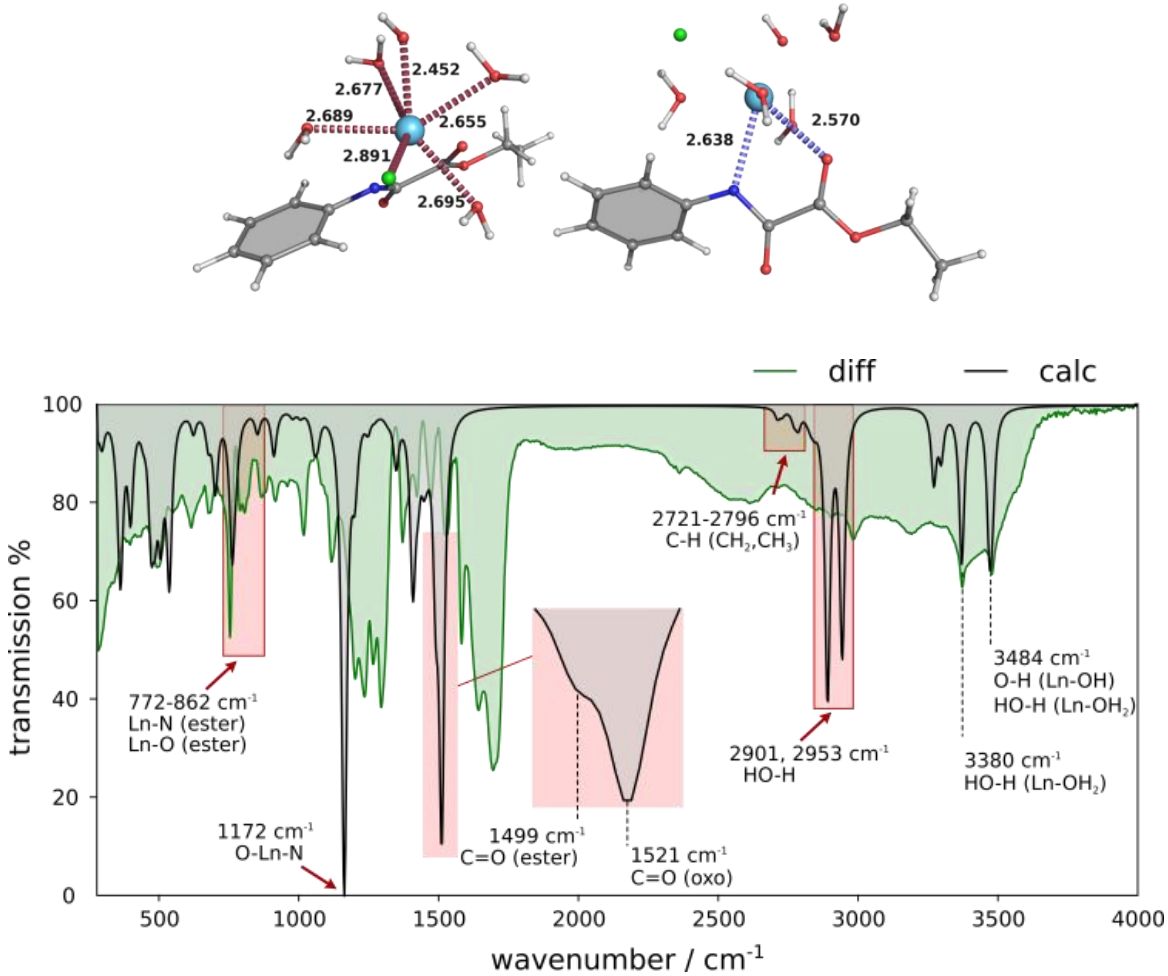

Figure II.1.12 (top) Geometry-optimized model used in the calculation of the vibration frequencies shown in (b), highlighting the Ln^{3+} coordination to the ethyl 2-oxo-2-(phenylamino)acetate anion (blue dashes) and H_2O, OH^- and Cl^- ligands (red dashes); (bottom) simulated IR spectrum (black) versus the difference between the Ln-IRMOF-3-EOC and IRMOF spectra (green); and assignment of the main vibration frequencies supporting the proposed Ln^{3+} coordination sphere.

Consider the simulated FTIR spectrum and the spectrum difference between the Ln-IRMOF-3-EOC and IRMOF spectra (Figure II.1.12, bottom). Outstanding features of the simulated spectrum are the peaks at 3380 and 3484 cm^{-1}, which closely match the experimental bands at 3374 and 3477 cm^{-1}, respectively. The former is entirely assigned to the O-H stretching of H_2O, whereas the latter is ascribed to the O-H stretching of the Ln^{3+} coordinated H_2O (3 modes) and OH^- (1 mode) species, indicating that the hydroxyl group is coordinated to the metal. Calculations reveal a peak at 1521 cm^{-1} due to C=O elongation of the oxo fragment, with a shoulder at 1499 cm^{-1} also due to the C=O elongation of the

ester. The band at 1172 cm^{-1} has contributions from two distinct modes containing O-Ln-N bending vibrations. Four vibration modes between 785 and 862 cm^{-1} are mainly ascribed to Ln-O_{ester} and Ln-N_{amine} elongations. Vibration modes at 2721 - 2796 cm^{-1} are essentially due to the C-H stretching of the CH_3 and CH_2 groups. The two major peaks at 2901 and 2953 cm^{-1} are due to parallel and anti-parallel H-O_{water} elongation involving the protons H-bonded to the hydroxyl group, respectively. Finally, it is noted that the presented model does not describe the spatial confinement imposed by the MOF framework, therefore largely influencing the intensities of the vibration modes.

Ln- IRMOF-3-EAA

Lanthanide incorporation was performed using $LnCl_3{\cdot}6H_2O$ (Nd, Eu, Tb) dissolved in DMSO as precursor and IRMOF-3-EAA dispersed in toluene to drive complex coordination (scheme II.1.15). Powder X-ray diffraction shows that the Ln-bearing materials preserve their integrity (Figure A5). All materials exhibit a cubic crystal habit from SEM analysis (Figures A58-60). The following chemical formulae were obtained:

Nd-IRMOF-3-EAA $[Zn_4O(C_{20}H_{30}NO_9S_3NdCl_2)_{1.95}(C_8H_5NO_4)_{1.05}]$;

Eu-IRMOF-3-EAA $[Zn_4O(C_{20}H_{30}NO_9S_3EuCl_2)_{1.95}(C_8H_5NO_4)_{1.05}]$;

Tb-IRMOF-3-EAA $[Zn_4O(C_{20}H_{30}NO_9S_3TbCl_2)_{1.95}\ (C_8H_5NO_4)_{1.05}]$.

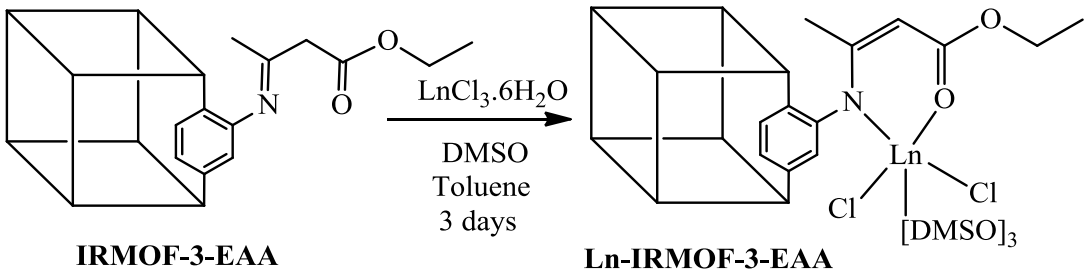

IRMOF-3-EAA **Ln-IRMOF-3-EAA**

Ln= Eu or Nd or Tb

Scheme II.1.15 Post-synthetic metalation of IRMOF-3-EAA with lanthanide.

The following evidence indicates for Ln^{3+} a coordination number of 7. Energy dispersive X-ray spectroscopy analysis gives a 2:1 Cl-to-Ln molar ratio and reveals the presence of 3 DMSO molecules. The FTIR evidence is clear, upon complexation: (Figures II.1.11a and A68): (i) carbonyl band shifts from 1714 (free carbonyl) to 1623 cm^{-1}; (ii) bands at 1006 and 960 cm^{-1} are due to, respectively, S-O and C-S stretching of coordinated DMSO.[38] ;

(iii) bands at 568 and 412 cm^{-1} are attributed to, respectively, Ln-N and Ln-O stretching vibrations.[39]

Ln^{3+}-IRMOF-3-CA

The pendant groups of the modified IRMOF-3 were used to coordinate Nd^{3+} and Eu^{3+}. To a solution of $NdCl_3.6H_2O$ or $EuCl_3.6H_2O$ in ethanol was added to IRMOF-3-CA dispersed in chloroform and the resulting mixtures were allowed to stand at room temperature for 3 days (Scheme II.1.16).

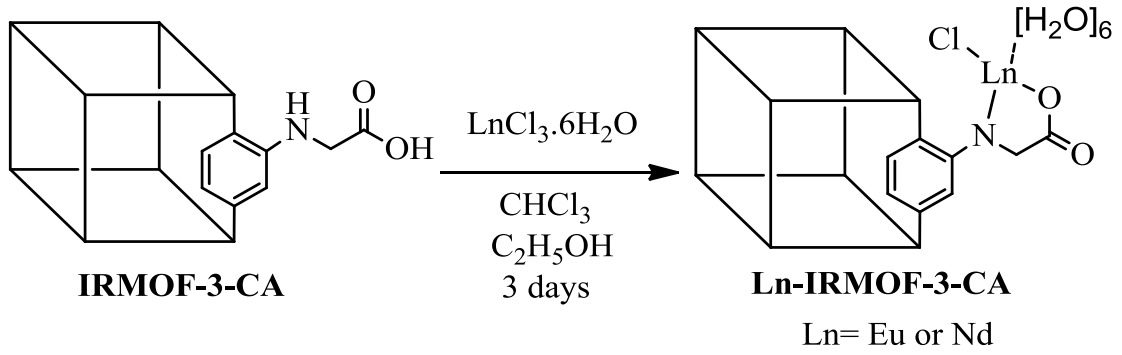

Scheme II.1.16 Post-synthetic metalation of IRMOF-3-CA with lanthanide

Powder X-ray diffraction showed that the framework and crystallinity of the MOFs were preserved upon Ln chelation (Figure A6). The crystal morphology of Ln^{3+}-IRMOF-3-CA, and Ln^{3+}-IRMOF-3-Gl was determined by scanning electron microscopy and optical microscopy (Figures A61, A62). As observed for previous IRMOF-3 samples, these materials exhibit a cubic habit. The presence of Ln ions and the composition of the materials were determined by energy dispersive X-ray spectroscopy analysis of 10 crystals (Tables A3).

The comparison of the infrared spectra of Nd-IRMOF-3-CA, Eu-IRMOF-3-CA and IRMOF-3-CA show significant differences. The CH_2 group of IRMOF-3-CA displays two intense bands at 2984, 3031 cm^{-1} corresponding to the symmetric and asymmetric stretching modes, but only one in Ln-IRMOF-3-CA 2984 cm^{-1}; the pair of bands assigned to ring CH modes at 3062 and 3078 cm^{-1} are replaced by a broad and mostly symmetrical single band at 3075 cm^{-1}. The C=O stretching vibration appearing as a shoulder in IRMOF-3-CA at 1683 cm^{-1} is shifted to lower (60 cm^{-1}) wavenumbers in the complexes indicating the participation of carboxylates in the chelation of Ln^{3+}. New bands are found in the spectra of Nd-IRMOF-3-CA at 582 and 487 cm^{-1} and assigned to Ln–OCO and Ln–N

stretching vibrations (Figure A69). Therefore, it is concluded that IRMOF-3-CA coordinates with Ln^{3+} ions via its deprotonated carboxylated and the amino groups.

EDS analysis showed that the percentage of Zn^{2+} to Ln^{3+} was 4:3 and the percentage of Ln^{3+} to Cl was 1:1. CHN analysis, FTIR and EDS confirm the chemical formula of Ln-IRMOF-3-CA as $[Zn_4O(C_{10}H_5NO_6LnCl.\ 6H_2O)_3$, Ln= Eu or Nd].

Ln^{3+}-IRMOF-3-GL

IRMOF-3-GL was dispersed in acetonitrile and ethanolic solution of $NdCl_3.6H_2O$ or $EuCl_3.6H_2O$ was added. The resulting mixtures were allowed to stand at room temperature for 3 days (Scheme II.1.17).

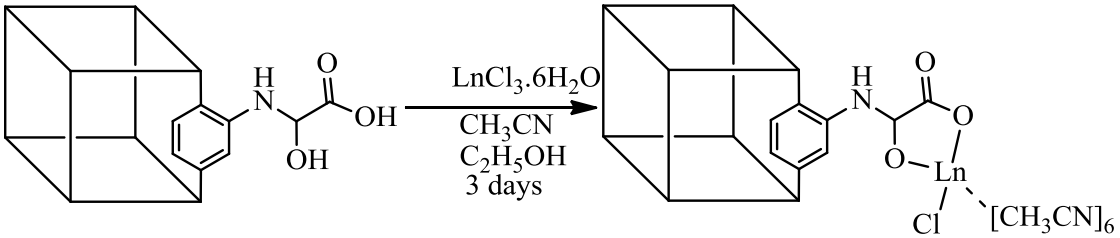

IRMOF-3-GL **Ln-IRMOF-3-GL**
Ln= Eu or Nd

Scheme II.1.17 Post-synthetic metalation of IRMOF-3-GL with lanthanide.

The FTIR spectra of IRMOF-3-GL and Ln-IRMOF-3-GL forms are similar, with small intensity variations in a few bands. The FTIR spectra are dominated by the strong absorptions of the carboxylate groups, around 1620 cm^{-1} (asymmetric stretch) and 1392 cm^{-1} (symmetric stretch). In addition, the intensity reduction of the broad band centered at ca. 1250 cm^{-1} is consistent with a change in the –OH bending mode. A new band is found in the spectra of Ln-IRMOF-3-GL at 385 cm^{-} assigned to (Ln–N) stretching vibrations (Figure A70). Energy dispersive X-ray analysis gives a ratio Zn^{2+} to Nd^{3+} of 4:2.25 and together with CHN analysis confirms the chemical formula $[Zn_4O(C_{22}H_{23}N_7O_7LnCl)_{2.25}(C_8H_5NO_4)_{0.75}]$.

Ln^{3+}-IRMOF-3-EM

As most β-diketonates may coordinate Ln ions forming stable complexes, the terminated β-diketonate IRMOF-3-EM was mixed with $LnCl_3.6H_2O$, in DMSO (Scheme II.1.18). Because MOFs functionalization to is partial, the amount of malonate moieties and Ln-β-

diketonate complex anions is too low to allow observation of their characteristic Fourier transform infrared bands (Figure A71).

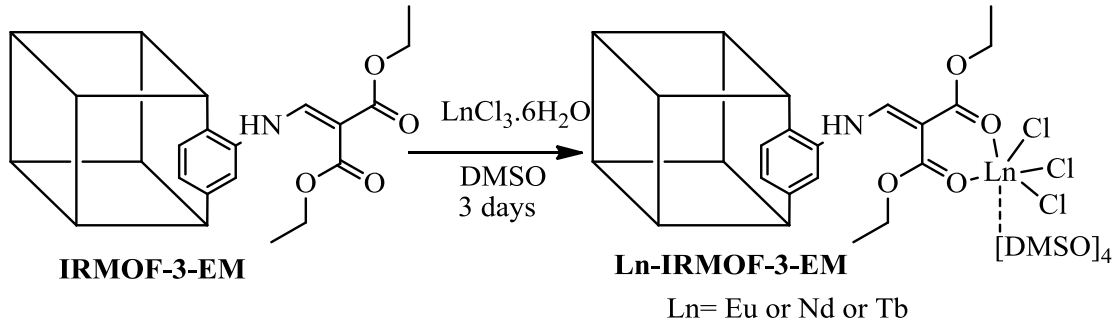

Scheme II.1.18 Post-synthetic metalation of IRMOF-3-EM with lanthanide

Fortunately, the successful attachment of Ln^{3+} ions to MOF backbones is strongly supported by the symmetrical vibration of two C=O links in the resonating structure of the coordinated β-diketonate ligands around 1535 cm^{-1}, which is similar to peak in the spectrum of the modified IRMOF-3-EM. Energy dispersive X-ray spectroscopy provides positive evidence for the successful functionalization of MOF with Ln^{3+} ions (Table A4) and together with CHN analysis confirms the chemical formula of:
Eu-IRMOF-3-EM to be $[Zn_4O(C_{37}H_{64}N_8O_{15}Eu)_{2.4}(C_8H_5NO_4)_{0.6}]$ and that of
Nd-IRMOF-3-EM $[Zn_4O(C_{37}H_{64}N_8O_{15}Nd)_{2.4}(C_8H_5NO_4)_{0.6}]$.

Ln^{3+}-IRMOF-3-MVK

A solution of $LnCl_3.6H_2O$ [Ln= Eu, Nd] in DMSO was added dropwise at room temperature to IRMOF-3-MVK (scheme II.1.19).

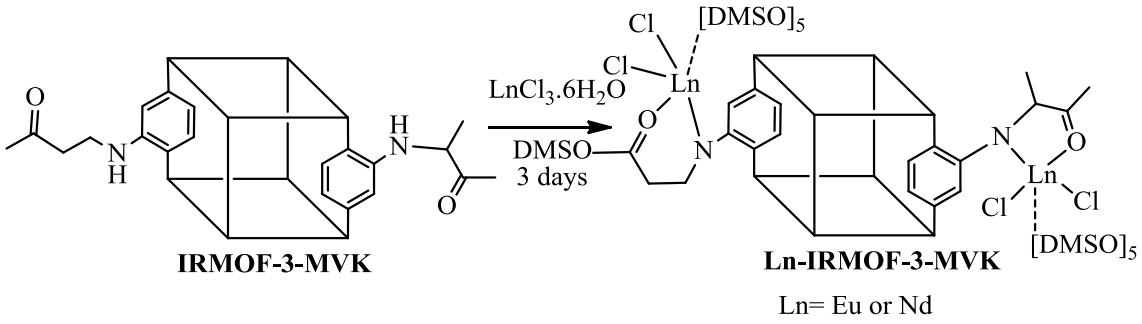

Scheme II.1.19 Post-synthetic metalation of IRMOF-3-MVK with lanthanide

Infraed spectroscopy confirms the successful Ln chelation (Figure A72): the spectrum of Ln-IRMOF-3-MVK shows the characteristic symmetric and asymmetric stretching vibrations from the deprotonated carboxylic acids at 1313 and 1580 cm^{-1}, respectively.

The band of the aromatic benzene vibration appears at 1512 cm^{-1}.

The large bands at 1006 and 960 cm^{-1} are due to, respectively, S-O and C-S stretching of the coordinated DMSO. Additional evidence for this chelation reaction was obtained by energy dispersive X-ray spectroscopy and CHN analysis, confirming the chemical formula of Eu-IRMOF-3-MVK:

$[Zn_4O(C_{22}H_{40}NS_5O_{10}EuCl_2)_{1.38}(C_{22}H_{40}NS_5O_{10}EuCl_2)_{0.9}(C_8H_5NO_4)_{0.72}]$

and that of Nd-IRMOF-3-MVK:

$[Zn_4O(C_{22}H_{40}NS_5O_{10}NdCl_2)_{1.38}(C_{22}H_{40}NS_5O_{10}NdCl_2)_{0.9}(C_8H_5NO_4)_{0.72}]$.

Photoluminescence Properties

In this part we will describe the solid state photoluminescence properties of MOF materials after and before coordinate with lanthanide metal ions. The importance of this part is offer many results to generate light emitting MOF. Also it offers how post-synthetic metalation strategies can tunable light emission for luminescent materials.

IRMOF-3 and IRMOF-3-PSM (PSM= AC, OL, EAA, EOC, MVK, EM, CA, GL)

Few publications are available on the photoluminescence properties of materials obtained by post modification.[41] In contrast, PSM has been much more explored in the field of catalysis.[42] The direct excitation of Ln^{3+} results, in general, in weak emission spectra because of the low molar absorptivity of these lanthanide ions. Chelation with organic moieties containing π-systems promotes the absorption and transfer of energy from the ligands to the metal ('antenna effect'), boosting the Ln^{3+} emission.[43] The solid-state luminescence of IRMOF-3, IRMOF-3-AC, IRMOF-3-OL, IRMOF-3-EOC, IRMOF-3-EAA, IRMOF-3-CA, IRMOF-3-GL, IRMOF-3-MVK, and IRMOF-3-EM) was investigated at room temperature and is now discussed.

The emission spectra (Figure II.1.13) of IRMOF-3, IRMOF-3-AC, IRMOF-3-OL, IRMOF-3-EOC, IRMOF-3-EAA, IRMOF-3-CA, IRMOF-3-GL, IRMOF-3-MVK and IRMOF-3-EM exhibit a broad blue band peaking at, respectively, 450, 465, 470, 570, 467, 485, 460, 479 and 480 nm, and assigned to π–π* and/or n–π* transitions within the aromatic ligands.[44] For IRMOF-3-AC, IRMOF-3-OL, IRMOF-3-EOC, IRMOF-3-EAA, IRMOF-3-CA, IRMOF-3-GL, IRMOF-3-MVK and IRMOF-3-EM, the emission band is red-shifted relatively to IRMOF-3, due to the presence of the pendant β–diketonates groups. Figure A76 shows the corresponding excitation spectra.

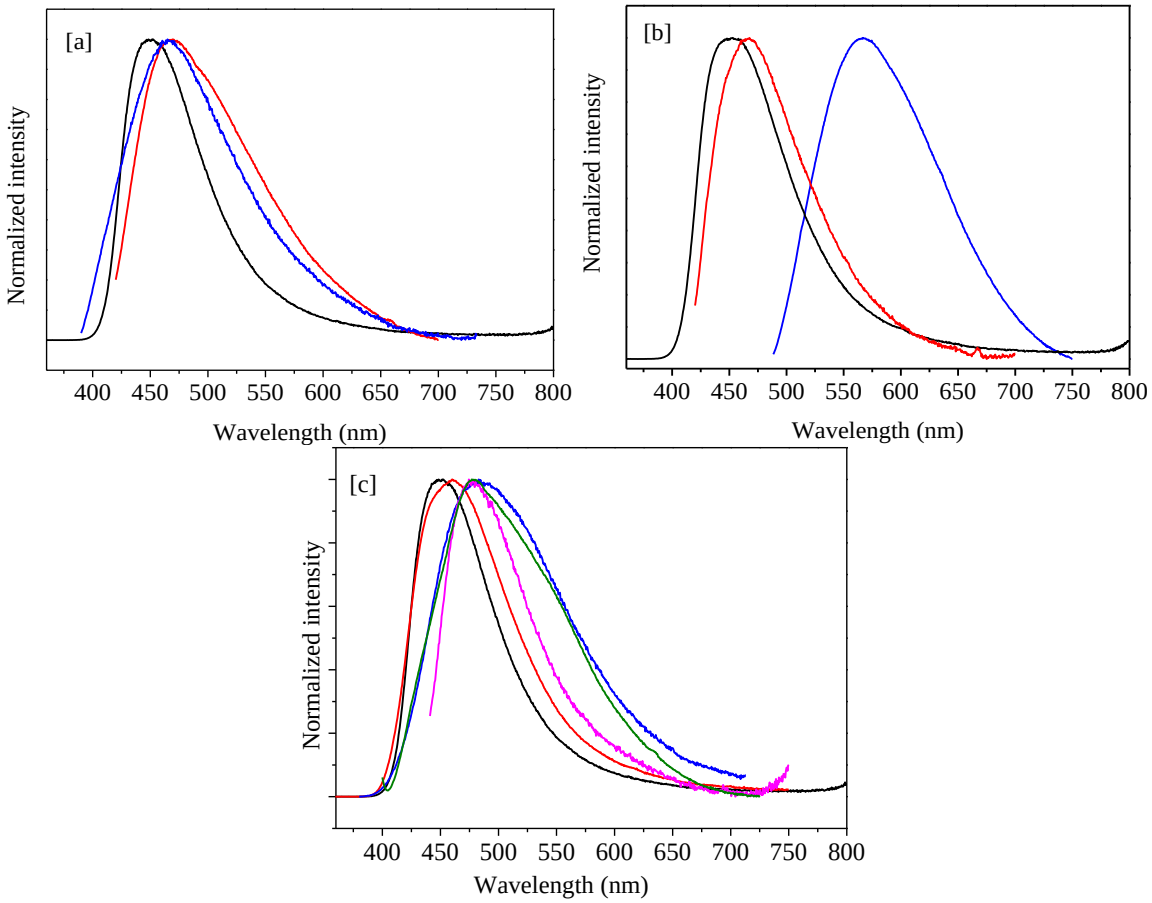

Figure II.1.13 Room temperature emission spectra of [a] IRMOF-3 (black) at 280 nm, IRMOF-3-EAA (red) at 400 and IRMOF-3-EOC (blue) at 370 nm, [b] IRMOF-3 (black) excited at 280 nm, IRMOF-3-AC (red) excited at 405 nm, IRMOF-3-OL (blue) excited at 465 nm, [c] IRMOF-3 (black) at 280 nm, IRMOF-3-GL (blue) at 280 nm, IRMOF-3-CA (red) at 280 nm, IRMOF-3-MVK (purple) at 421 nm and IRMOF-3-EM (green) at 385 nm.

Neodymium compounds: Nd-IRMOF-3-PSM

Nd-IRMOF-3-AC, Nd-IRMOF-3-OL and Nd-Y-IRMOF-3-OL

In the visible spectral range, the emission spectra of the Nd^{3+}-containing samples consist of a broad band ascribed to the hybrid host (since it is also seen in the undoped samples, Figure A75). A very similar broad band has been reported for Nd^{3+}-complexes of β–diketonates also bearing aromatic ligands, and assigned to π–π^* and/or n-π^* transitions. This broad band overlaps with a series of narrow self-absorptions assigned to intra-$4f^3$ transitions, indicating radiative host-to-Nd^{3+} energy transfer (previously observed for other organic-inorganic hybrid materials, and dubbed 'inner filter' effect). For Nd-IRMOF-3-OL and Nd-Y-IRMOF-3-OL the emission band is red-shifted relatively to Nd-IRMOF-3-AC, presumably due to the presence of an additional aromatic ring in the former materials.

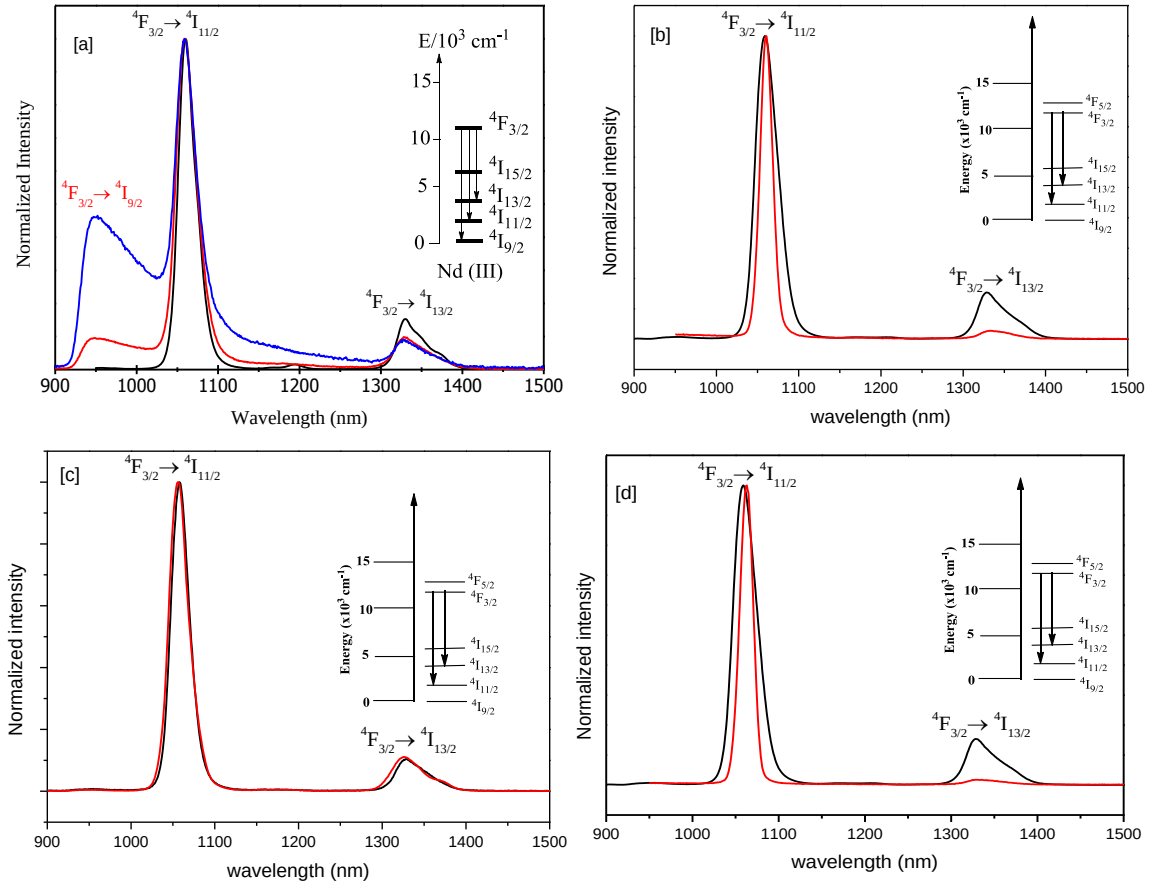

Figure II.1.14 Room-temperature NIR emission of [a] Nd-IRMOF-3-AC (black line), Nd-IRMOF-3-OL (red) and Nd-Y-IRMOF-3-OL (blue) excited at 395 nm, [b] Nd-IRMOF-3-EAA (black line) excited at 400 nm and Nd-IRMOF-3-EOC (red) excited at 525 nm, [c] Nd-IRMOF-3-MVK (black) at 395 nm, Nd-IRMOF-3-EM (red) at 378 nm, [d] Nd-IRMOF-3-CA (black) at 365 nm and Nd-IRMOF-3-GL (red) at 527 nm. The inset depicts part of the energy level diagramme of Nd^{3+} ions. The $^4F_{3/2}$ energy level is populated via the ligands excited states.

Importantly, all Nd^{3+}-containing MOFs show a $^4F_{3/2}\rightarrow {}^4I_{9/2,11/2,13/2}$ NIR emission (Figure II.1.14), excited via both the hybrid host and intra-4f^3 lines (Figure II.1.14). No significant changes are observed in the energy and full-width-at-half-maximum of the lines of the different materials, despite the presence of a broad emission overlapping the $^4F_{3/2}\rightarrow {}^4I_{9/2}$ transition and ascribed to the framework in the Nd-IRMOF-3-OL and Nd-Y-IRMOF-3-OL. The lifetime of the $^4F_{3/2}$ level is smaller than 10 μs (the detection limit of our setup). Nd-IRMOF-3-EOC and Nd-IRMOF-3-EAA display two sets of emission bands in the NIR region, 1064 nm ($^4F_{3/2}\rightarrow {}^4I_{11/2}$) and 1330 nm ($^4F_{3/2}\rightarrow {}^4I_{13/2}$), characteristic of the Nd^{3+} ion (Figure II.1.14)

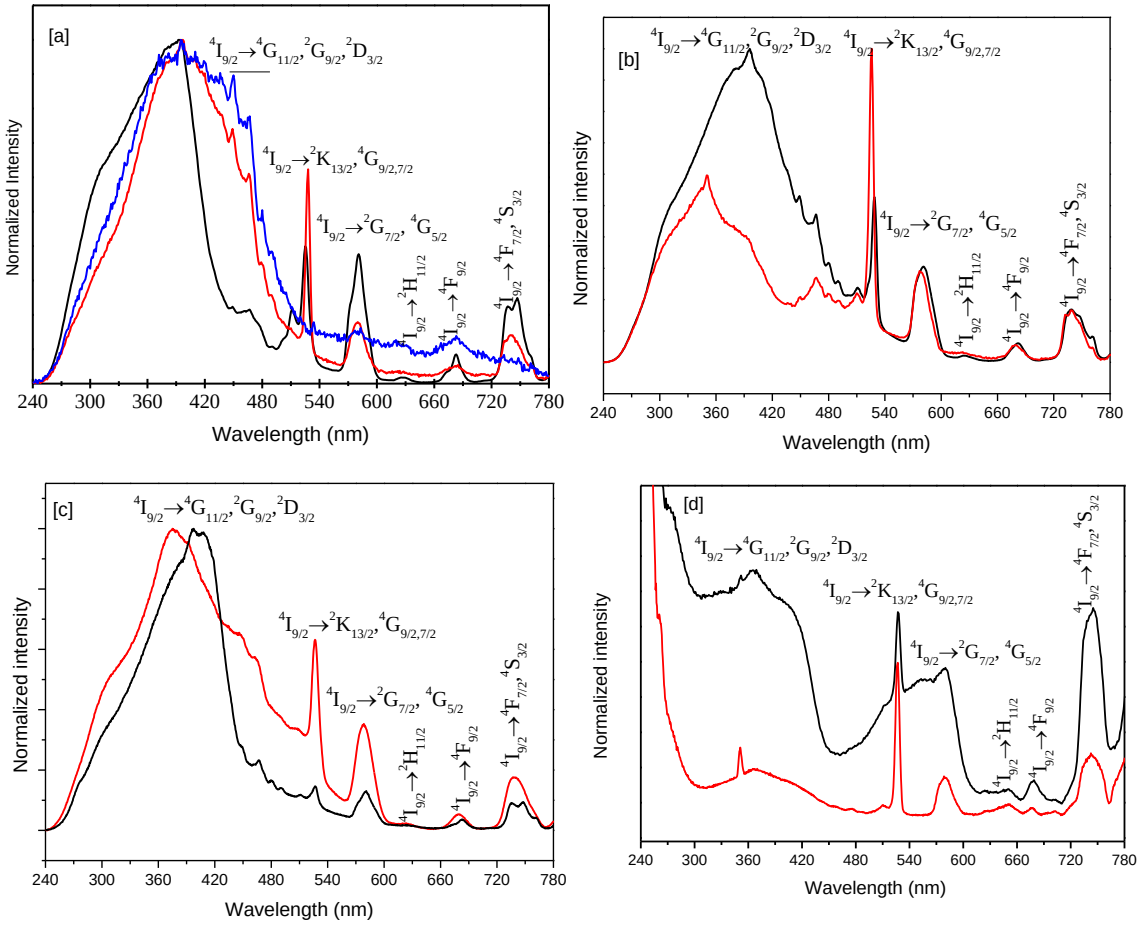

Figure II.1.15 Excitation spectra of [a] Nd-IRMOF-3-AC (black), Nd-IRMOF-3-OL (red) and Nd-Y-IRMOF-3-OL (blue) monitored at 1064 nm, [b] Nd-IRMOF-3-EAA (black) and Nd-IRMOF-3-EOC (red) monitored at 1060 nm, [c] Nd-IRMOF-3-MVK (black), Nd-IRMOF-3-EM (red) monitored at 1060 nm, [d] Nd-IRMOF-3-CA (black) monitored at 1064 nm and Nd-IRMOF-3-GL (red) monitored at 1060 nm.

The corresponding excitation spectra (Figure II.1.15) display a broad band ascribed to the ligands overlapping a series of narrow intra-$4f^3$ lines. The relative intensity of the broad emission is higher for Nd-IRMOF-3-EAA indicating that the sensitisation process is more effective in this case. Nevertheless, NIR emission is discerned exciting both the hybrid host or intra-4f lines pointing out that they the two modified MOFs are good matrices to absorb energy and transfer it to the Nd^{3+} ion. Furthermore both materials also emit in the visible range. The emission broad band overlaps with three self-absorptions assigned to intra-$4f^3$ transitions, indicating radiative host-to-Nd^{3+} energy transfer (previously observed for other organic–inorganic hybrid materials, and dubbed 'inner filter' effects).[45]

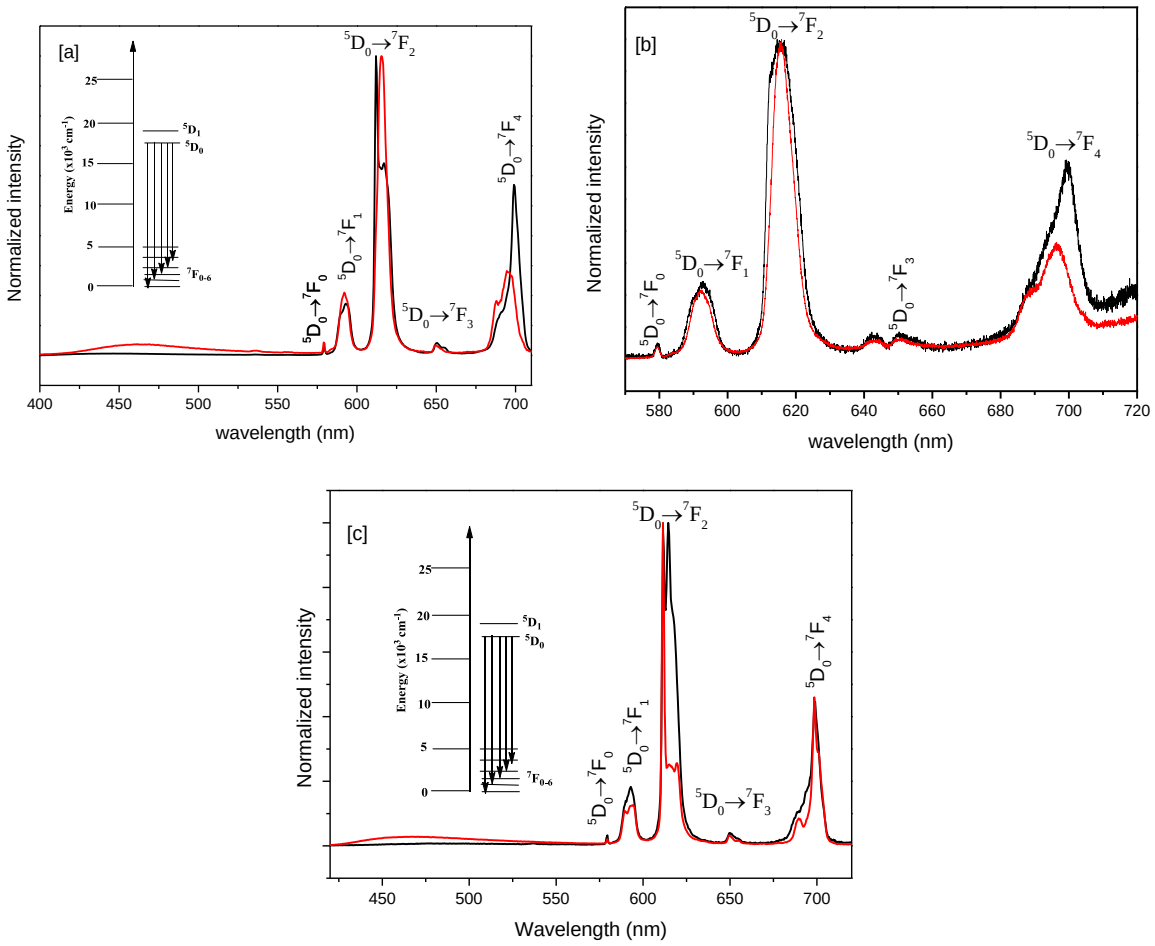

Figure II.1.16 Room-temperature emission of [a] Eu-IRMOF-3-EAA (black) excited at 370 nm and Eu-IRMOF-3-EOC (red) excited at 320 nm, [b] High-resolution of Eu-IRMOF-3-GL (red) and Eu-IRMOF-3-CA (black), [c] Eu-IRMOF-3-MVK (black) at 365 nm, and Eu-IRMOF-3-EM (red) at 365 nm. The inset depicts part of the energy level diagram of Eu^{3+} ions. The $^5D_0$ energy level is populated via the excited states of the ligands.

Europium compounds: Eu-IRMOF-3-PSM

[Eu-IRMOF-3-EOC, Eu-IRMOF-3-EEA, Eu-IRMOF-3-GL, Eu-IRMOF-3-CA, Eu-IRMOF-3-MVK and Eu-IRMOF-3-EM]

The emission spectra of Eu-IRMOF-3-PSM do not show the characteristic emission from IRMOF-3-PSM indicating an efficient energy transfer from these matrices to the Eu^{3+} ions that pumps up light emission. The typical transitions of the Eu^{3+} ion peaking at 579, 592, 616, 651 and 698 nm, ascribed to the $^5D_0\rightarrow{}^7F_0$, $^5D_0\rightarrow{}^7F_1$, $^5D_0\rightarrow{}^7F_2$, $^5D_0\rightarrow{}^7F_3$ and $^5D_0\rightarrow{}^7F_4$ transitions, respectively, are observed in Figure II.1.16. The corresponding excitation spectra of Eu-IRMOF-3-PSM are shows in Figure II.1.17.

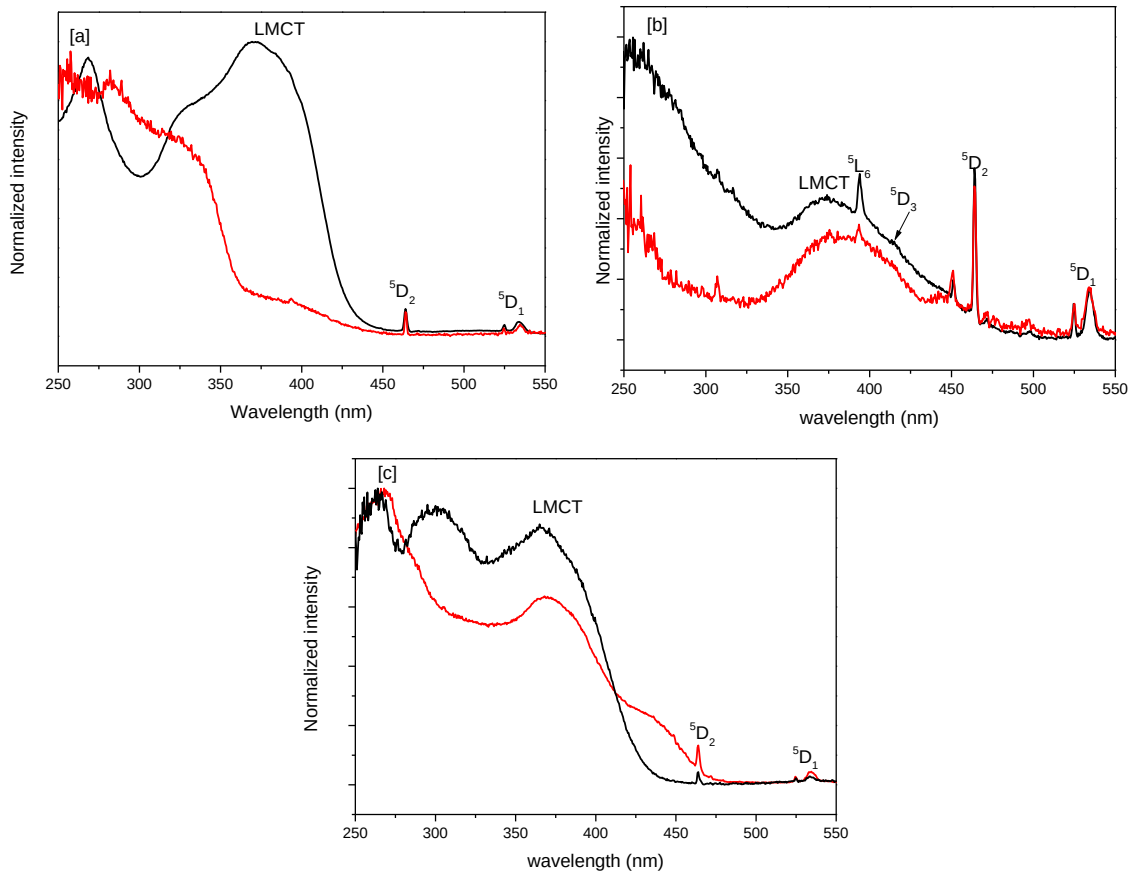

Figure II.1.17 Room temperature (300K) excitation spectra of [a] Eu-IRMOF-3-EAA (black) at 280 nm, Eu-IRMOF-3-EOC (red) at 400 nm, [b] Eu-IRMOF-3-CA(black) and Eu-IRMOF-3-GL (red) at 615 nm, [c] Eu-IRMOF-3-MVK (black) and Eu-IRMOF-3-EM (red) at 612 nm.

Terbium compounds: Tb-IRMOF-3-PSM

[Tb-IRMOF-3-EOC and Tb-IRMOF-3-EEA]

Tb-IRMOF-3-PSM emit green light when excited at 296-370 nm, giving a typical Tb^{3+} emission spectra (Figure II.1.18b). The narrow and strong peaks at 490, 545, 582, and 620 nm are ascribed to the characteristic emissions of Tb^{3+} corresponding to electronic transitions from the excited state $^5D_4$ to the multiplets ^7F_J (J = 6–3), respectively. For Tb-IRMOF-3-EAA a band is seen at 450 nm and attributed to the emission of IRMOF-3-EAA and IRMOF-3-CM. The absence of IRMOF-3-PSM emission of other samples suggests that the ligands-to-metal energy transfer is much more efficient that in Tb-IRMOF-3-EAA. The corresponding excitation spectra of Tb-IRMOF-3-PSM are shows in Figure II.1.18a.

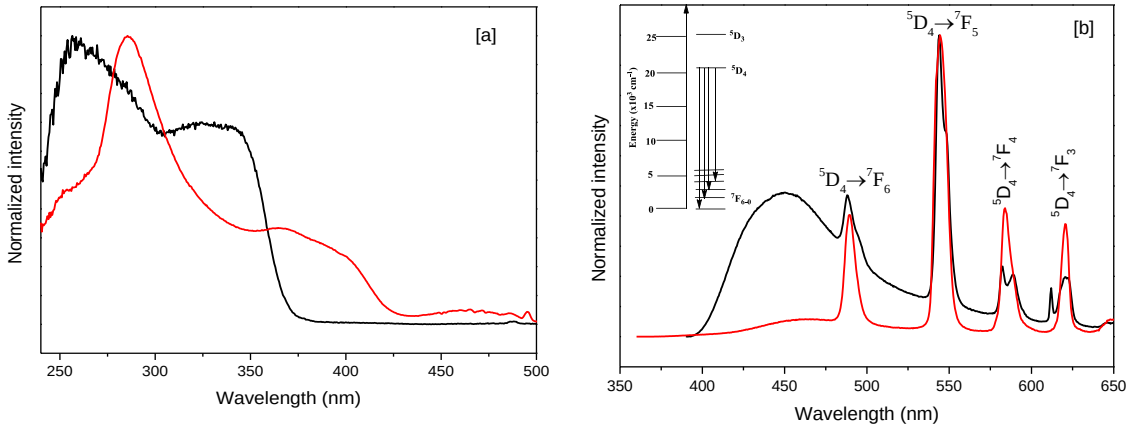

Figure II.1.18 [a] Excitation spectra of Tb-IRMOF-3-EAA (black) and Tb-IRMOF-3-EOC (red) at 545 nm.; [b] Room temperature (300K) emission of Tb-IRMOF-3-EAA (black) at 370 nm and Tb-IRMOF-3-EOC (red) at 345 nm. The inset depicts part of the energy level diagram of Tb^{3+} ions. The $^5D_4$ energy level is populated via the ligands excited states.

Calculation of water molecule from photoluminescence results

The high-energy vibrational modes of the ligands in the Eu^{3+} coordination sphere may deactivate the $^5D_0$ excited state, leading to emission quenching by nonradiative paths. In particular, the OH oscillators are so effective in this deactivation that the $^5D_0$ excited-state lifetime may be related with the number of water molecules, n_w, in the first Eu^{3+} coordination shell. Indeed, n_w may be obtained from the difference between the decay time values measured in H_2O and D_2O: [46]

$$n_W = 1.11\,[(1/\tau_{H2O}) - (1/\tau_{D2O}) - 0.31 + 0.45 n_{OH}] \qquad (1)$$

where $\tau(H_2O)$ and $\tau(D_2O)$ are the decay times, in milliseconds, in water and in D_2O, respectively, and n_{OH} is the number of hydroxyl OH oscillators in the first coordination sphere of Eu^{3+}.

Table II.1.1 $^5D_0$ or $^5D_4$ lifetime values and absolute emission quantum yields (ϕ) obtained under distinct excitation wavelengths (λ_{ex}, nm).

Sample	λ_{ex}	λ_{em}	τ (ms)	ϕ
Eu-IRMOF-3-EAA	270	612	0.318±0.004	<0.01
	325	612	0.279±0.028	<0.01
	370	612	0.304±0.002	<0.01
Eu-IRMOF-3-EOC	280	612	0.281±0.008	<0.01
	320	612	0.272±0.009	<0.01
Tb-IRMOF-3-EAA	285	544	0.081±0.002	<0.01
	370	544	0.021±0.001	<0.01
Tb-IRMOF-3-EOC	260	545	0.562±0.004	0.02
	345	545	0.511±0.004	0.01

In Equation 1, $\tau(D_2O)$ may be replaced by the purely radiative decay (τ_{rad}) calculated from the experimental emission spectrum.[47] The value obtained experimentally for the decay time (at the same excitation wavelength of the abovementioned emission spectrum, 320 nm), $\tau_{exp}=0.272\times10^{-3}$ s (Table II.1.1) is also used substituting $\tau(H_2O)$, and Equation 1 may thus be used to calculate n_w. Assuming $n_{OH}=1$, the values obtained for Eu-IRMOF-3-EOC are $\tau_{rad}=2.081\times10^{-3}$ s and $n_w=3.7\pm0.1$. Considering the τ_{rad} and τ_{exp} values indicated above, the emission quantum efficiency of the $^5D_0$ level (q) is calculated by:

$$q = \tau_{exp}/\tau_{rad} \qquad (2)$$

yielding q=0.13.

The $^5D_0$ quantum efficiency is the upper limit of the emission quantum yield (η),[31] according to $\eta=kq$, where the rate k includes all processes involved in the efficiency of light absorption by the sensitizer, the energy transfer to the emitting state, and the decay rates populating the emitting state.[48] In the present case, the low quantum yield (Table II.1.1) $k<0.07$ indicates an inefficient process of light absorption and energy transfer from the IRMOF-3-EOC lattice to the Eu^{3+} ions.

Magnetic properties

The magnetic properties of all compounds were investigated in the temperature range 1.8 – 300 K. The magnetic behaviours and moment values are consistent with that expected for the rare-earth ions present in the structure in the amount evaluated by chemical analysis. Eu(III), Nd(III) and Tb(III) ions exhibit an orbitally degenerate ^{2S+1}L ground state. The degeneracy of the terms are removed by spin –orbit coupling leading to $^{2S+1}L_J$ states that can split further due to Stark-effect induced by the crystal field.[49] The rare-earth magnetic behaviour thus depends on these splitting's and on the thermal population of the resulting states.[50] The energy of the excited states is given by $E(J) = \lambda J(J+1)/2$, taking the ground state as the origin, were λ holds for the spin-orbit coupling. Excepted for Eu(III) and Sm(III), the first excited state is located far above the ground state, which is thus the only state populated even at room temperature. In the single ion approximation, the magnetic susceptibility is then derived from the general expression:[50b,c, 51]

$$\chi(J) = \frac{N\mu_B^2 g_J^2 J(J+1)}{3kT} + \frac{2N\mu_B^2 (g_J - 1)(g_J - 2)}{3\lambda} \qquad (3)$$

The Zeeman factor is given by:

$$g_J = \frac{3}{2} + \frac{[S(S+1) - L(L+1)]}{2J(J+1)}$$

Experimentally, the χT product of isolated rare-earth ions decreases when lowering the temperature due to depopulation of the Stark levels. Expressions of the molar magnetic susceptibility have been derived by considering a splitting (Δ) of the m_J levels in an axial crystal field. Such expressions were used for a rough estimation of the splitting value in our compounds (see appendixes Information). In the case of the Eu(III) ions (and Sm(III) as well), the separation between the ground state and the first excited state is small. Hence, the first excited state is thermally populated and has to be involved in the expression of the magnetic susceptibility as a function of temperature.

Europium compounds: Eu-IRMOF-3-EAA and Eu-IRMOF-3-EOC

Regarding the Eu(III) derivatives, Eu-IRMOF-3-EAA and Eu-IRMOF-3-EOC, the ground term ^{7}F is split by spin-orbit coupling into seven states, ^7F_J, with J = 0 – 6. In that case, λ is small and the first excited states are thermally populated. Using eq. 3, the molar magnetic susceptibility may then be expressed by:[50a, 51, 52]

$$x = \frac{\sum_{J=0}^{6} (2J+1) x(J) \exp\left(\frac{-\lambda J(J+1)}{2kT}\right)}{\sum_{J=0}^{6} (2J+1) \exp\left(\frac{-\lambda J(J+1)}{2kT}\right)} = \qquad (4)$$

$$\left(\frac{N\mu_B^2}{3kTx}\right) \frac{24 + \left(\frac{27x}{2} - \frac{3}{2}\right)e^{-x} + \left(\frac{135x}{2} - \frac{5}{2}\right)e^{-3x} + \left(189x - \frac{7}{2}\right)e^{-6x} + \left(405x - \frac{9}{2}\right)e^{-10x} + \left(\frac{1485x}{2} - \frac{11}{2}\right)e^{-15x} + \left(\frac{2457x}{2} - \frac{13}{2}\right)e^{-21x}}{1 + 3e^{-x} + 5e^{-3x} + 7e^{-6x} + 9e^{-10x} + 11e^{-15x} + 13e^{-21x}}$$

$$\text{with } x = \frac{\lambda}{kT} .$$

The $^7F_0$ ground state is non magnetic but the thermal population of the 6 excited states leads to a non-zero and thermally-dependent magnetic moment.

The experimental thermal variation of χ is plotted in Figure II.1.19 for both compounds. When lowering the temperature, the magnetic susceptibility of Eu-IRMOF-3-EAA and Eu-IRMOF-3-EOC increases regularly from 0.0045 – 0.005 emu/Eu mol at 300 K to a plateau at 0.0058-0.0065 emu/Eu mol around 75 K. The overall behaviour is reminiscent of previous works found in the literature.[50a, 51-53] Such behaviour is consistent with the eq. 4 which allowed a fairly good fit of the experimental data in the range 100 K – 50 K with the values of λ presented in Table A6.

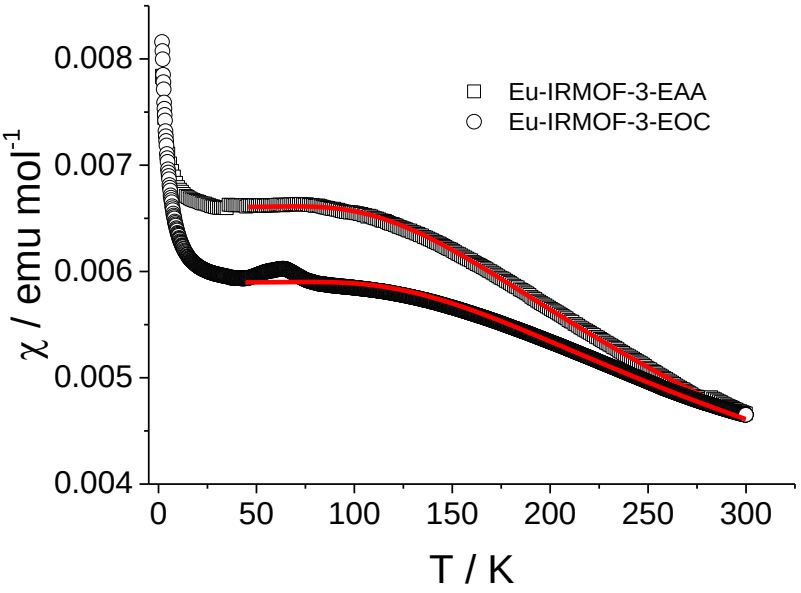

Figure II.1.19 Thermal variation of the magnetic susceptibility and χT product of **Eu-**IRMOF-3-EAA (squares) and Eu-IRMOF-3-EOC (circles). The full lines correspond to the best fit to the analytical expression given in the text. (The small hump around 60 K observed in the Eu-IRMOF-3-EOC data corresponds to residual paramagnetic oxygen present in the sample tube.)

Accordingly, the χT vs. T plot in figure II.1.20 indicates a constant decrease in the range 300 K – 1.8 K. The low temperature variation is linear and the χT product tends to zero in agreement with the occurrence of a non-magnetic ground state, $^7F_0$. The susceptibility at low temperature, χ_{LT}, is not zero due to a coupling with the closest level $^7F_1$. It leads to the limiting value given by the Caro-Porsche equation:[50a, 54]

$$\chi_{LT} = \frac{8N\beta^2}{\lambda} = 2.086/\lambda \qquad (5)$$

where λ is the energy difference between the two sublevels.

The spin-orbit coupling value of Eu-IRMOF-3-EAA and Eu-IRMOF-3-EOC was thus also evaluated from the linear fit of the low temperature χT vs T plots in figure II.1.19. The λ values refined from the magnetic data were compared with the value deduced from the photoluminescence data. The difference between the $^5D_0 \rightarrow {}^7F_1$ transition and the $^5D_0 \rightarrow {}^7F_0$ transition leads to $\lambda = 379$ cm^{-1} which is consistent with the magnetic findings of 310-350 cm^{-1} given in Table A6. These values are also of the order of magnitude of other Eu(II) coordination compounds.[50a, 52, 53, 55]

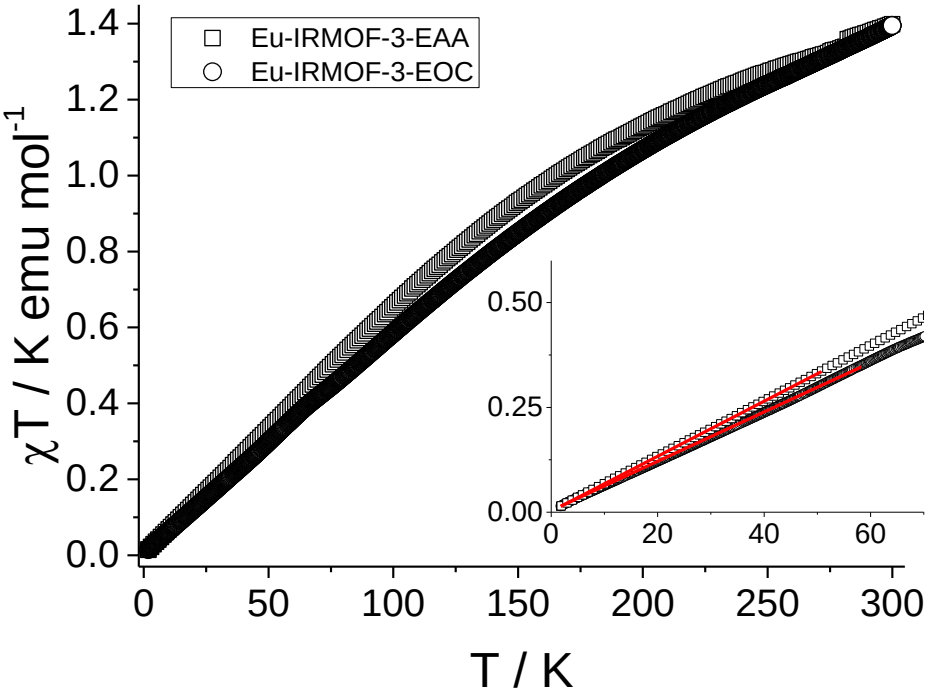

Figure II.1.20 Thermal variation of the χT product of of Eu-IRMOF-3-EAA (squares) and Eu-IRMOF-3-EOC (circles). Inset is a zoom of the low temperature region showing the linear fit of the data (see eq. 5 and text).

Neodymium compounds: Nd-IRMOF-3-EAA and **Nd-IRMOF-3-EOC**

The temperature variation of the magnetic susceptibility and magnetization *vs.* field curves at 1.8 K of the neodymium compounds is displayed in Figure A78. The two compounds exhibit a regular increase of the magnetic susceptibility when lowering the temperature and the usual decrease of the χT product from *ca.* 1.8 emu K per Nd mol at 300 K to 0.7 emu K per Nd mol at 1.8 K. Such behavior is typical of isolated Nd(III) coordination compounds.[49, 50, 53a,b, 55a,c,d, 56]

For Nd(III) ions, the spin-orbit coupling, λ, is very large and the Zeeman factor $g_J = 8/11$ which leads to $\chi T = 1.64$ emu K mol^{-1}.

The experimental χT values at 300 K is slightly higher than expected for the free ion which could arise from the cumulative effects of crystal field variation, chemical analysis and diamagnetic corrections errors.

The steep decrease of the χT product is explained by the effect of crystal field splitting of the $^4I_{9/2}$ ground state into five Kramers doublets. Considering that these doublets are equally populated at 300 K leads to the expression of χT given in Supplementary Information.[39d] When lowering the temperature, the states of higher energy are gradually depopulated. Then the χT product approaches the value of 0.7 emu K mol^{-1} (scaled to 1 Nd ion) corresponding to the lowest doublet only.[50a] The value of the zero-field splitting parameter Δ was estimated by fitting the experimental data (see Table A6).

The fit to the theoretical free-ion expression of χT=*f*(T) is rather good between 50 K and 300 K. The slight discrepancy with the free-ion model is due to a deviation from axial symmetry as expected for a heptahedral sphere of coordination. Such distortion could influence the zero-field splitting. The low-temperature magnetization *vs.* field curves confirms the paramagnetic behaviours of Nd-IRMOF-3-EAA and Nd-IRMOF-3-EOC.

Terbium compounds: Tb-IRMOF-3-EAA and Tb-IRMOF-3-EOC

The temperature variation of the magnetic susceptibility and magnetization *vs.* field curves at 1.8 K of the terbium compounds is displayed in Figure A78. The cases of Tb(III) and Nd(III) ions are qualitatively similar. As expected, Tb-IRMOF-3-EAA exhibits a regular decrease of the χT product.[55d, 57] The crystal field splitting of the m_J levels was evaluated by using the expression of the magnetic susceptibility of the free ion. The analytical model fits well the data in the range 20 K 300 K and the refined value of Δ is comparable with those found in the literature.[55d] More surprisingly, when lowering the temperature, the χT product of Tb-IRMOF-3-EOC increases from 9.1 K emu mol^{-1} at 300 K to a smoothed broad maximum of 10.6 K emu mol^{-1} around 30 K before dropping to 7 K emu mol^{-1} at 2 K. This behavior is reminiscent of that observed in a chain compound in which the lanthanide ions are in an extremely distorted eight-coordinated environment.[57] This increase of the moment was attributed to ferromagnetic dipolar coupling between Tb(III) ions which counteracts the effect of the depopulation of the Stark states. This interpretation would imply that Tb(III) ions are quite near of each other in the present Tb-IRMOF-3-EOC.

References

[1]a) O. M. Yaghi, G. Li, H. Li, *Nature* **1995**, *378*, 703-706; b) O. M. Yaghi, H. Li, *J. Am. Chem. Soc*. **1995**, *117*, 10401-10402.

[2] N. Stock, S. Biswas, *Chem. Rev*. **2012**, *112*, 933-969.

[3] a) A. Shigematsu, T. Yamada, H. Kitagawa, *J. Am. Chem. Soc.* **2012**, *134*, 13145-13147; b) M. M. Wanderley, C. Wang, C.-D. Wu, W. Lin, *J. Am. Chem. Soc.* **2012**, *134*, 9050-9053; c) Y. He, S. Xiang, B. Chen, *J. Am. Chem. Soc.* **2011**, *133*, 14570-14573; d) S. Motoyama, R. Makiura, O. Sakata, H. Kitagawa, *J. Am. Chem. Soc*. **2011**, *133*, 5640-5643; e) G. Akiyama, R. Matsuda, H. Sato, M. Takata, S. Kitagawa, *Adv. Mater.* **2011**, *23*, 3294-3297; f) R. J. Kuppler, D. J. Timmons, Q.-R. Fang, J.-R. Li, T. A. Makal, M. D. Young, D. Yuan, D. Zhao, W. Zhuang, H.-C. Zhou, *Coord. Chem. Rev.* **2009**, *253*, 3042–3066; g) L. Ma, A. Jin, Z. Xie, W. Lin, *Angew. Chem. Int. Ed.* **2009**, *48*, 9905-9908; h) J. Lee, O. K. Farha, J. Roberts, K. A. Scheidt, S. T. Nguyen, J. T. Hupp, *Chem. Soc. Rev.* **2009**, *38*, 1450-1459; i) P. Küsgens, M. Rose, I. Senkovska, H. Fröde, A. Henschel, S. Siegle, S. Kaskel, *Microporous Mesoporous Mater.* **2009**, *120*, 325-330; j) S. K. Ghosh, S. Bureekaew, S. Kitagawa, *Angew. Chem. Int. Ed.* **2008**, *47*, 3403-3406; k) S. Ma, H.-C. Zhou, *J. Am. Chem. Soc.* **2006**, *128*, 11734-11735.

[4] H. Deng, C. J. Doonan, H. Furukawa, R. B. Ferreira, J. Towne, C. B. Knobler, B. Wang, O. M. Yaghi, *Science* **2010**, *327*, 846-850.

[5] a) S. M. Cohen, *Chem. Rev.* **2012**, *112*, 970-1000; b) K. K. Tanabe and S. M. Cohen, *Chem. Soc. Rev.* **2011**, *40*, 498-519; c) S. M. Cohen, *Chem. Sci*. **2010**, *1*, 32-36; d) Z. Wang, S. M. Cohen, *Chem. Soc. Rev.* **2009**, *38*, 1315-1329.

[6] a) X.-Q. Song, W.-K. Dong, Y.-J. Zhang, W.-S. Liu, *Luminescence* **2010**, *25*, 328-335; b) S. Biju, M. L. P. Reddy, A. H. Cowley, K. V. Vasudevan, *Crystal Growth Design*. **2009**, *9*, 3562-3569; c) C. M. G. Santos, A. J. Harte, S. J. Quinn, T. Gunnlaugsson, *Coord. Chem. Rev*. **2008**, *252*, 2512-2527; d) Y. Huang, B. Yan, M. J. Shao, *Solid State Chem.* **2008**, *181*, 2935-2940; e) X.-D. Zhu, J. Lu, X.-J. Li, S.-Y. Gao, G.-L. Li, F.-X. Xiao, R. Cao, *Crystal Growth Design* **2008**, *8*, 1897-1901; f) J. Kido and Y. Okamoto, *Chem. Rev*. **2002**, *102*, 2357-2368.

[7] a) A. Bettencourt-Dias, *Dalton Trans*. **2007**, 2229-2241; b) G.-L. Law, K.-L. Wong, X. Zhou, W.-T. Wong, P.-A. Tanner, *Inorg. Chem*. **2005**, *44*, 4142-4144; c) G.-H. Cui, J.-

R. Li, R.-H. Zhang, X.-H. Bu, *J. Mol. Struct.* **2005**, *740*, 187191.

[8] a) M. D. Ward, *Coord. Chem. Rev*. **2007**, *251*, 1663-1677; b) T. C. Shehee, R. E. Sykora, K. M. Ok, P. S. Halasymani, T. E. Albrecht-Schmitt, *Inorg. Chem.* **2003**, *42*, 457-462.

[9] a) Y. Cui, Y. Yue, G. Qian, and B. Chen, *Chem. Rev*. **2012**, *112*, 1126-1162; b) J. Rocha, L. D. Carlos, F. A. A. Paz, D. Ananias, *Chem. Soc. Rev*. **2011**, *40*, 926-940; c) M. D. Allendorf, C. A. Bauer, R. K. Bhaktaa, R. J. T. Houk, *Chem. Soc. Rev*. **2009**, *38*, 1330-1352.

[10] a) B. Chen, Y. Yang, F. Zapata, G. Lin, G. Qian, E. B. Lobkovsky, *Adv. Mater.* **2007**, *19*, 1693-1696; b) Y. Bai, G.-J. He, Y.-G. Zhao, C.-Y. Duan, D.-B. Dang, Q.-J. Meng, *Chem. Commun.* **2006**, 1530-1532; c) E. Y. Lee, S. Y. Jang, M. P. Suh, *J. Am. Chem. Soc.* **2005**, *127*, 6374-6381.

[11] a) B. Chen, L. Wang, F. Zapata, G. Qian, E. B. Lobkovsky, *J. Am. Chem. Soc.* **2008**, *130*, 6718-6719; b) K. L. Wong, G. L. Law, Y. Y. Yang, W. T. Wong, *Adv. Mater.* **2006**, *18*, 1051-1054.

[12] a) B. Zhao, X.-Y. Chen, Z. Chen, W. Shi, P. Cheng, S.-P. Yan, D.-Z. Liao, *Chem. Commun.* **2009**, 3113-3115; b) X.-Q. Zhao, B. Zhao, W. Shi, P. Cheng, *Cryst. Eng. Comm.* **2009**, *11*, 1261-1269; c) B. Zhao, X.-Y. Chen, P. Cheng, D.-Z. Liao, S.-P. Yan, Z.-H. Jiang, *J. Am. Chem. Soc.* **2004**, *126*, 15394-15395; d) W. Liu, T. Jiao, Y. Li, Q. Liu, M. Tan, H. Wang, L. Wang, *J. Am. Chem. Soc.* **2004**, *126*, 2280-2281.

[13] a) J. An, C. M. Shade, D. A. Chengelis-Czegan, S. p. Petoud, N. L. Rosi, *J. Am. Chem. Soc.* **2011**, *133*, 1220-1223; b) B. V. Harbuzaru, A. Corma, F. Rey, P. Atienzar, J. L. Jordá, H. Garcia, D. Ananias, L. D. Carlos, J. Rocha, *Angew. Chem., Int. Ed.* **2008**, *47*, 1080-1083.

[14] A. Cadiau, C. D. S. Brites, P. M. F. J. Costa, R. A. S. Ferreira, J. Rocha, L. D. Carlos, *ACS Nano* **2013**, *7*, 7213-7218.

[15] a) K. A. White, D. A. Chengelis, M. Zeller, S. J. Geib, J. Szakos, S. Petoud, N. L. Rosi, *Chem. Commun.* **2009**, 4506-4508; b) K. A. White, D. A. Chengelis, K. A. Gogick, J. Stehman, N. L. Rosi, S. Petoud, *J. Am. Chem. Soc.* **2009**, *131*, 18069-18071; c) B. Chen, Y. Yang, F. Zapata, G. Qian, Y. Luo, J. Zhang, E. B. Lobkovsky, *Inorg. Chem.* **2006**, *45*, 8882-8886.

[16] a) W. Lin, W. J. Rieter, K. M. L. Taylor, *Angew. Chem., Int. Ed.* **2009**, *48*, 650-658; b)

K. M. L. Taylor, A. Jin, W. Lin, *Angew. Chem., Int. Ed.* **2008**, *47*, 7722-7725; c) W. J. Rieter, K. M. L. Taylor, W. Lin, *J. Am. Chem. Soc.* **2007**, *129*, 9852-9853; d) W. J. Rieter, Taylor, H. An, W. Lin, W. Lin, J. *Am. Chem. Soc.* **2006**, *128*, 9024-9025.

[17] K. M. L. Taylor-Pashow, J. D. Rocca, Z. Xie, S. Tran, W. Lin, *J. Am. Chem. Soc.* **2009**, *131*, 14261-14263.

[18] M. Eddaoudi, J. Kim, N. Rosi, D. Vodak, J. Wachter, M. O'Keeffe and O.M. Yaghi, *Science*, **2002**, *295*, 469-472.

[19] J. S. Costa, P. Gamez, C. A. Black, O. Roubeau, S. J. Teat and J. Reedijk, *Eur. J. Inorg. Chem.*, **2008**, 1551-1554.

[20] M. Servalli, M. Ranocchiari and J. A. Van Bokhoven, *Chem. Commun*., **2012**, *48*, 1904-1906.

[21] G. Pellizzari,*Gazz. Chim. Ital*., **1884**, *18*, 14-362.

[22] D. Braga, F. Grepioni, L. Maini, K. Rubini, M. Polito, R. Brescello, L. Cotarca, M. T. Duarte, V. Andre and M. F. M. Piedade,*New J.Chem.*, **2008**, *32*, 1788-1795.

[23] G. Kaupp, inOrganic Solid State Reactions, ed. F. Toda, Springer, Berlin, Heidelberg, **2005**, vol. 254, pp. 130-131.

[24] G. Kaupp, J. Schmeyers and J. Boy, *Chem. Eur. J*., **1998**, *4*, 2467-2474.

[25] K. Tanaka, D. Fujimoto, T. Oeser, H. Irngartinger and F. Toda, *Chem. Commun*., **2000**, 413-414.

[26] K. Tanaka and F. Toda, *Chem. Rev.*, **2000**, *100*, 1025-1074.

[27] M. Albrecht, M. Lutz, A. L. Spek and G. van Koten, *Nature*, **2000**,*406*, 970-974.

[28] M. Albrecht, R. A. Gossage, M. Lutz, A. L. Spek and G. van Koten, *Chem. Eur. J*., **2000**, *6*, 1431-1445.

[29] G. Kaupp, M. R. Naimi-Jamal, L. Maini, F. Grepioni and D. Braga, *CrystEngComm*, **2003**, *5*, 474–479.

[30] D. Braga, F. Grepioni, M. Polito, M. R. Chierotti, S. Ellena and R. Gobetto, *Organometallics*, **2006**, *25*, 4627-4633.

[31] C. J. Adams, H. M. Colquhoun, P. C. Crawford, M. Lusi and A. G. Orpen, *Angew. Chem., Int. Ed.*, **2007**, *46*, 1124-1128.

[32] C. J. Adams, M. F. Haddow, M. Lusi and A. G. Orpen, *Proc. Natl. Acad. Sci. U. S. A*., **2010**, *107*, 16033-16038.

[33] C. J. Adams, M. A. Kurawa, M. Lusi and A. G. Orpen, *CrystEngComm*, **2008**, *10*,

1790-1795.

[34] G. Mı´nguez Espallargas, M. Hippler, A. J. Florence, P. Fernandes, J. van de Streek, M. Brunelli, W. I. F. David, K. Shankland and L. Brammer, *J. Am. Chem. Soc.*, **2007**, *129*, 15606-15614.

[35] G. Mı´nguez Espallargas, J. van de Streek, P. Fernandes, A. J. Florence, M. Brunelli, K. Shankland and L. Brammer, *Angew. Chem., Int. Ed.*, **2010**, *49*, 8892-8896.

[36] Tai, X.; Wang, H., Sun, X. *Spectroscopy Lett.*, **2005**, *38*,497-504.

[37] Vinodkumar, C.R.; Radhakrishnan, P.K. *Synth.React.Inorg.Met.-Org.Chem.* **1997**, *27*, 1365-1372.

[38] Forel, M. R. ; Tranquille, M. *Spectrochim. Acta, Part A*, **1970**, *26*,1023-1034.

[39] Tang, C.; Tang, R.; Tang, C. and Zeng, Z. *Bull.KoreanChem.Soc.* **2010**, *31*, 1283-1288

[40] J. Juan-Alcañiz, J. Ferrando-Soria, I. Luz, P. Serra-Crespo, E. Skupien, V. P. Santos, E. Pardo, F. X. L. Xamena, F. Kapteijn, J. Gascon, *J. Catal*. **2013**, *307*, 295-304.

[41] a) J. Cao, Y. Gao, Y. Wang, C. Du and Z. Liu, *Chem. Commun*. **2013**, *49*, 6897-6899; b) Y.-Y. Liu, R. Decadt, T. Bogaerts, K. Hemelsoet, A. Kaczmarek, D. Poelm, M. Waroquier, V. V. Speybroeck, R. V. Deun, and P. V. D. Voort, *J. Phys. Chem. C* **2013**, *117*, 11302-11310.

[42] a) T. Zhou,Y. Du,A. Borgna, J. Hong,Y. Wang, J. Han,W. Zhanga and R. Xu, *Energy Environ. Sci*. **2013**, *6*, 3229-3234; b) A. M. Rasero-Almansa, A. Corma, M. Iglesias, F. Sanchez, *Chem.Cat.Chem.* **2013**, *5*, 3092-3100; c) K. Leus, G. Vanhaelewyn, T. Bogaerts, Y.-Y. Liu, D. Esquivel, F. Callens, G. B. Marind, V. V. Speybroeck, H. Vrielinck, P.V. D. Voort, *Catal. Today* **2013**, *208*, 97-105; d) J. Canivet, S. Aguado, Y. Schuurman, and D. Farrusseng, *J. Am. Chem. Soc.* **2013**, *135*, 4195-4198; e) P. V. Dau, S. M. Cohen, *Chem. Commun.* **2013**, *49*, 6128-6130; f) P.V. Dau, M. Kim, S. M. Cohen, *Chem. Sci*. **2013**, *4*, 601-605; g) M. Pintado-Sierraa, A.M. Rasero-Almansa, A. Corma, M. Iglesias, F. Sánchez, *J. Catal*. **2013**, *299*, 137-145; h) D. Saha, R. Sen, T. Maity, S. Koner, *Langmuir* **2013**, *29*, 3140-3151; i) J. E. Halls, A. Hernan-Gaomez, A. D. Burrows, F. Marken, *Dalton Trans.* **2012**, *41*, 1475; j) S.-N. Kim, S.-T. Yang, J. Kim, J.-E. Park, W.-S. Ahn, *CrystEngComm* **2012**, *14*, 4142-4147; k) J. Yang, P. Li, L.Wang, *Catal. Commun*. **2012**, *27*, 58-62; l) H. G. T. Nguyen, M. H. Weston, O. K. Farha, J. T. Hupp, S. B. T. Nguyen, *CrystEngComm* **2012**, *14*, 4115-4118; m) S. Bhattacharjee, D.-A. Yang, W.-S. Ahn, *Chem. Commun*. **2011**, *47*, 3637-3639; n) A.

Corma, M. Iglesias, F. X. L. Xamena, F. Sanchez, *Chem. Eur. J.* **2010**, *16*, 9789-9795; o) E.D. Bloch, D.Britt, C. Lee, C. J. Doonan, F. J. Uribe-Romo, H. Furukawa, J. R. Long, O. M. Yaghi, *J. Am. Chem. Soc*. **2010**, *132*, 14382–14384; p) C. J. Doonan, W. Morris, H. Furukawa, O.M. Yaghi, *J. Am. Chem. Soc*. **2009**, *131*, 9492-9493; q) K. K. Tanabe, S. M. Cohen, *Angew. Chem. Int. Ed*. **2009**, *48*, 7424-7427; r) M. J. Ingleson, J. P. Barrio, J.-B. Guilbaud, Y. Z. Khimyak, M. J. Rosseinsky, *Chem. Commun.* **2008**, 2680-2682.

[43] N. Sabbatini, M. Guardigli, J.-M.Lehn, *Coord. Chem. Rev.* **1993**, *123*, 201-228.

[44] G. Zucchi, *Int. J. Inorg. Chem*. **2011**, *2011*, article ID 918435.

[45] a) M. C. Gonçalves, N. J. O. Silva, V. de Zea Bermudez, R. A. S. Ferreira, L. D. Carlos, K. Dahmouche, C. V. Santilli, D Ostrovskii, I. C. Correia Vilela and A. F. Craievich, *J. Phys. Chem. B* **2005**, *109*, 20093-20104; b) C. Molina, R. A. S. Ferreira, G. Poirier, L. Fu, S. J. L. Ribeiro, Y. Messsaddeq L. D. Carlos, *J. Phys. Chem. C* **2008**, *112*, 19346-19352.

[46] Supkowski, R. M.; Horrocks, W. D., *Jr. Inorg. Chim. Acta*, **2002**, *340*, 44-48.

[47] Carlos, L. D.; Ferreira, R. A. S.; de Zea Bermudez, V.; Ribeiro, S. J. L. *Adv. Mater.* **2009**, *21*, 509.

[48] Eliseeva, S.V.; Bünzli, J.C.; *Chem. Soc. Rev*., **2010**, *39*, 189-227.

[49] Carlin, R. L. *Magneto-Chemistry, Springer-Verlag, Berlin* **1986.**

[50] a) Andruh, M.; Bakalbassis, E.; Kahn, O.; Trombe, J. C. and Porcher, P. *Inorg. Chem.* **1993**, *32*, 1616; b) Casey, A. T. and Mitra, S. *Theory and Applications of Molecular Paramagnetism, Boudreaux, E.A., Mulay, L.N. Eds. John Wiley, New York* **1976**, 135; c) Casey, A. T. *Theory and Applications of Molecular Paramagnetism, Boudreaux, E.A., Mulay, L.N. Eds. John Wiley, New York* **1976**, 27.

[51] a) Kahn, O. *Molecular Magnetism, VCH, Weinheim* **1993**; b) Van Vleck J. H. and Frank, A. *Phys. Rev.* **1929**, *34*, 1494; c) Van Vleck J. H. and Frank, A. *Phys. Rev.* **1929**, *34*, 1625.

[52] Hernadez-Molina, M.; Lorenzo-Luis, P.; Ruiz-Perez, C.; Lopez, T.; Martin, I. R.; Anderson, K. M.; Orpen, A. G.; Bocanegra, E. H.; Lloret F. and Julve, M. *J. Chem. Soc., Dalton Trans.* **2002**, 3462.

[53] a) Han, Y.; Li, X.; Li, L.; Ma, C.; Shen, Z.; Song Y.and You, X. *Inorg. Chem.* **2010**, *49*, 10781; b) Van der Horst, M. G.; Van Albada, G. A.; Ion, R.-M.; Mutikainen, I.;

Turpeinen, U.; Tanase S. and Reedijk, J. *Eur. J. Inorg. Chem.* **2008**, 2170; c) Wang, X.-J.; Cen, Z.-M.; Ni, Q.-L.; Jiang, X.-F.; Lian, H.-C.; Gui, L.-C.; Zuo H.-H. and Wang, Z.-Y. *Cryst. Growth Des.* **2010**, *10*, 2960; d) Wu, M.-F.; Wang, M.-S.; Guo, S.-P.; Zheng, F.-K.; Chen, H.-F.; Jiang, X.-M.; Liu, G.-N.; Guo G.-C. and Huang, J.-S. *Cryst. Growth Des.* **2011**, *11*, 372.

[54] a) Ofelt, G. S. *J. Chem. Phys.* **1963**, *38*, 2171; b) Huang, J.-S.; Loriers, J.; Porcher, P.; Teste de Sagey G. and Caro, P. *J. Chem. Phys.* **1984**, *80*, 6204; c) Caro P. and Porcher, P. *J. Magn. Magn. Mater*. **1986**, *58*, 61.

[55] a) Kalinovskaya, I.; Tkachenko, I.; Mirochnik, A.; Karasev V. and Kavun, V. *Russ. J. Phys. Chem. A, Focus on Chemistry* **2010**, *84*, 1452; b) Sun, M.-L.; Zhang, J.; Lin, Q.-P.; Yin, P.-X. and Yao, Y.-G. *Inorg. Chem.* **2010**, *49*, 9257; c) Lhoste, J.; Perez-Campos, A.; Henry, N.; Loiseau, T.; Rabu P. and Abraham, F. *Dalton Transactions* **2011**, *40*, 9136-9144; d) Cepeda, J.; Balda, R.; Beobide, G.; Castillo, O.; Fernández, J.; Luque, A.; Pérez-Yáñez S. and Román, P. *Inorganic Chemistry* **2012**, *51*, 7875-7888.

[56] An, H.; Han Z. and Xu, T. *Inorg. Chem.* **2010**, *49*, 11403.

[57] Wang, Y.; Li, X.-L.; Wang, T.-W.; Song Y. and You, X.-Z. *Inorganic Chemistry* **2009**, *49*, 969-976.

Chapter II.2: Enhanced photocatalytic activity of MIL-125 by Post-Synthetic Modification with Cr(III) and Ag nanoparticles

- Introduction
- Preparation and Post Synthetic Modification of Materials
- Doping with Chromium
- Doping with Silver
- Photocatalysis
- References

Introduction

Porous coordination polymers, also known as metal-organic frameworks (MOFs), are hybrid materials consisting of organic linkers bridging metal clusters,[1] having very high surface areas up to 5200 m^2g^{-1}, and a variety of chemical functionalities.[2] MOFs have potential application in the absorption and separation of gas molecules (such as CO_2, N_2, CH_4, and H_2),[3] microelectronics,[4] sensing,[5] ion conductivity,[6] optics,[7] pollutant sequestration,[8] drug delivery,[9] contrast agents,[10] micromotors,[11] bioreactors[12] and catalysis.[13]

An outstanding feature of nanoporous MOFs is that the chemical makeup of the channel walls may be adjusted by post-synthetic modification (PSM) of the organic linkers.[14] In this way, new organic functionalities and metal cations may be introduced enabling or improving gas sorption,[15] catalytic activity[16] or light emission,[17] among others.[18-20] A particularly convenient and much studied route for PSM is based on the reaction of the amino groups of MOFs linkers with incoming reactants.[14]

Recent research suggests that MOFs hold considerable potential as a new class of photocatalysts (*e.g.*, for hydrogen evolution,[21] carbon dioxide reduction,[22] and degradation[23] and transformation of organic compounds).[24] A case in point, NH_2-MIL-125 is a highly porous MOF with chemical formula $[Ti_8O_8(OH)_4(bdc\text{-}NH_2)_6]$ (bdc^{2-} = 1,4-benzene dicarboxylate) containing cyclic octamers of TiO_2 octahedra, and being photochromic due to the reduction of Ti(IV) to Ti(III) under UV irradiation.[25] Two other examples of Ti(IV)-bearing porous MOFs are know, MIL-91[26] and NTU-9,[27] the latter exhibiting a p-type semiconductor behavior and visible-light photo-response.

Anatase, a crystalline form of titanium dioxide, is a well-known semiconductor photocatalyst suffering from certain limitations, such as low efficiency and a narrow light response range, absorbing only ultraviolet (UV) light, which accounts for less than 5% of solar radiation, due to a large band gap (3.2 eV). Efforts made to overcome these drawbacks via band gap engineering are not entirely satisfactory.[28,29] In this context, NH_2-MIL-125 comprising 'TiO_2 fragments' offers the possibility of overcoming the band gap limitations of inorganic TiO_2. Indeed, although the MIL-125 band gap lies in the UV region, at *ca.* 3.6 eV/345 nm, replacement of the bdc ligand by monoaminated bdc^{2-}, 2-amino-1,4-benzenedicarboxylate, reduces the band gap to *ca.* 2.6 eV/475 nm.[30]

This effect is due to the nitrogen 2p electrons donation of the aromatic linking unit, resulting in a red-shifted band above the valence-band edge of MIL-125.[29] PSM of NH_2-MIL-125 by a diazotization reaction[28b] causes a further reduction of the band gap to *ca.* 1.93 eV/565 nm. This material (known as methyl red-MIL-125) exhibits improved light absorption over a wide range of the visible spectrum, showing an enhanced photocatalytic oxidation activity under visible light. In contrast, the study of Smalley *et al*[28a] on PSM of NH_2-MIL-125 by an amidation reaction shows that this modification significantly reduces or switches off the photocatalytic properties of the resulting MOF even when only 40–50% of the amine groups are modified.

It is well known that embedding transition metal ions, such as iron, nickel, copper, manganese, cobalt and chromium, into the TiO_2 inorganic lattice introduces additional energy levels within the band gap extending the absorption of light from the UV to the visible region, thus improving the material's photoresponse.[31] Because NH_2-MIL-125 comprises 'TiO_2 fragments', we reasoned that doping it with such transition metal might just do the same. To test this new concept, we have used PSM via the reaction of the amino group of NH_2-MIL-125 with acetylacetone, subsequently introducing Cr by complexation. Here, we show that this new material, named Cr-MIL-125-AC, extends the light absorption to the visible and improves the photocatalytic performance under solar light irradiation. On the other hand, the doping of MIL-125 with Ag nanoparticles is shown to be an alternative way of improving the photocatalytic activity of the materials because the latter are able to accept the photogenerated electrons in MIL-125, thus avoiding electron-hole recombination. Both, the Cr- and Ag-bearing materials are quite stable under photocatalytic conditions, with negligible amounts of the metals leaching out into solution.

We note that PSM of MOFs involving complexation (doping) of transition metals such as chromium, or silver has not been used before in the design of photocatalysts. PSM presents advantages over direct MOFs synthesis because, for a given framework type, the coordination sphere of *e.g.,* Cr may be changed without the need for preparing a new framework, thus allowing the optimization of the catalytic centers. Moreover, the exact nature and distribution of the catalytic sites in other photocatalysts, such as doped titanium oxides, is often not clear and depends much on the way the materials are prepared and processed, while the range of possible metal loadings is also limited.

Preparation and Post-Synthetic Modification of Materials

NH_2-MIL-125 was prepared according to the method reported previously,[27] by adding 2-aminoterephthalic acid to titanium isopropoxide in a DMF–MeOH solvent mixture. NH_2-MIL-125 was post-synthesis modified following a solid-vapour reaction: dry NH_2-MIL-125 was exposed to acetylacetone vapour (Figure A80) for 24 hours under the laboratory's oxygen atmosphere, the resulting powder was washed several times with dry ethanol to remove unreacted acetylacetone and then dried in air. Unexpectedly MIL-125-AC-1 has been obtained (Scheme II.2.1).

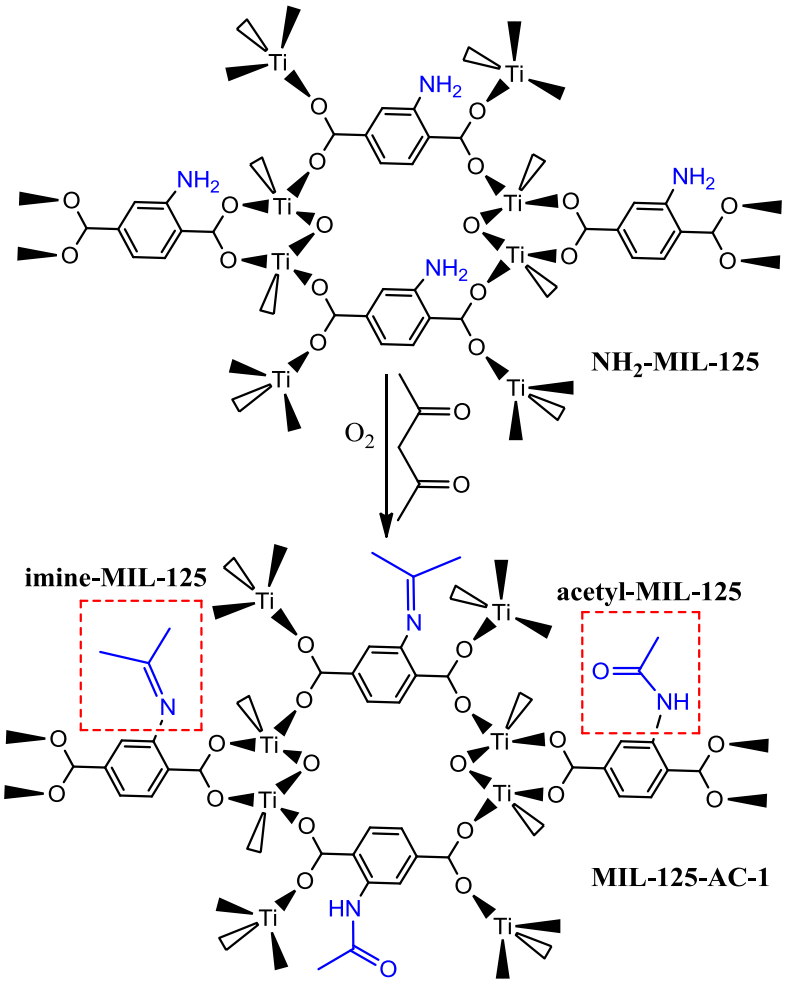

Scheme II.2.1 PSM reaction of NH_2-MIL-125 with vapour of acetylacetone under a normal oxygen atmosphere.

The powder XRD patterns of NH_2-MIL-125 and MIL-125-AC-1 are similar (Figure II.2.1a, II.2.1b), thus showing that the structural integrity was preserved upon PSM. MIL-125-AC-1 was digested by sonication in DCl–DMSO-d_6 and analysed by liquid-state ^{1}H NMR (Figure II.2.2, II.2.3).

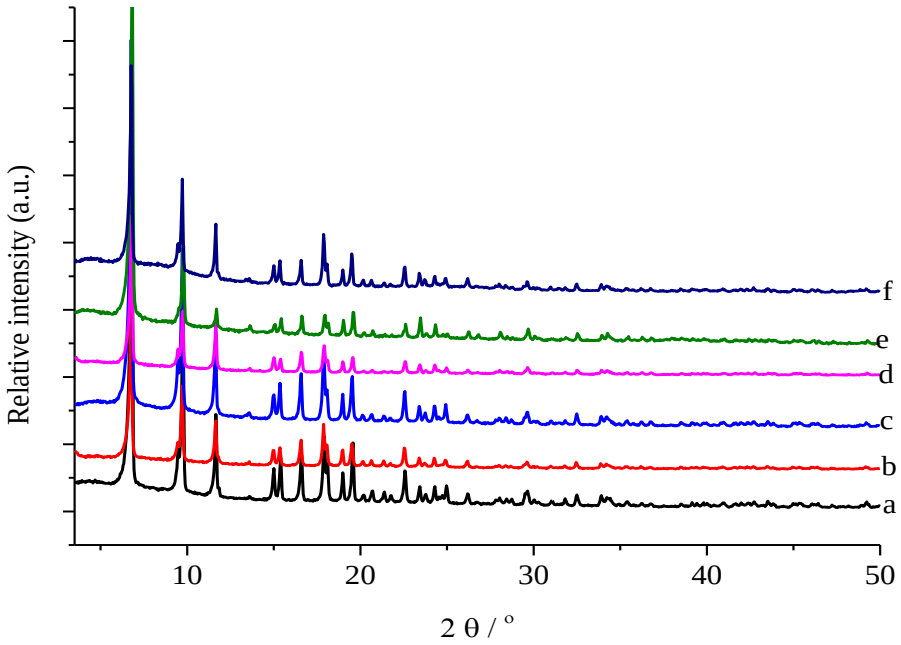

Figure II.2.1 Powder XRD patterns of a) NH_2-MIL-125, b) MIL-125-AC-1, c) MIL-125-AC-2, d) Cr-MIL-125-AC, e) Ag-MIL-125-AC and f) Ag-MIL-125-AC after 5 cycles of photocatalytic reaction.

Acetylacetone decomposed to acetic acid and acetone on the surface of NH_2-MIL-125 by reaction with atmospheric oxygen. The acetic acid participate in the acetylation reaction of the amino group of NH_2-MIL-125 yielding acetyl-MIL-125. The NH_2-MIL-125 also reacted with the formed acetone forming imine-MIL-125 (Scheme II.2.1). The ^{1}H NMR spectrum shows the tandem modification of NH_2-MIL-125 and, thus, two modified structures were found. Structure-1 (acetyl-MIL-125) originate resonances at δ 2.15 (s, 3H), assigned to the protons resonance of the acetyl methyl group, 7.70 (dd, 1H, *J* 8.3 and 1.3 Hz), 8.07 (d, 1H, *J* 8.3 Hz), 8.97 (d, 1H, *J* 1.3 Hz), confirming the aromatic ring modification (proton *ortho* to the amide group strongly deshielded). Structure-2 (imine-MIL-125) present proton resonances at δ 1.94 (s, 6H), due to the two methyl groups produced upon reaction with acetone, 7.33 (dd, 1H, *J* 8.3 and 1.3 Hz), 7.63 (d, 1H, *J* 1.3 Hz), 7.89 (d, 1H, *J* 8.3 Hz) for the aromatic ring. ^{1}H NMR quantitative analysis revealed 100% PSM of NH_2-MIL-125, being the amounts of acetyl-MIL-125 and imine-MIL-125 47% and 53%, respectively. Solid-state ^{13}C CP-MAS NMR of MIL-125-AC-1 gave the expected sp^3 CH_3 (δ 24.0) and sp^2 C=O (δ 170.1) peaks (Figure II.2.4). ^{1}H NMR and elemental analysis suggested the chemical formula of MIL-125-AC-1 to be $[Ti_8O_8(OH)_4(C_{10}H_7NO_5)_{2.82}(C_{11}H_9NO_4)_{3.18}]$ (Table A5).

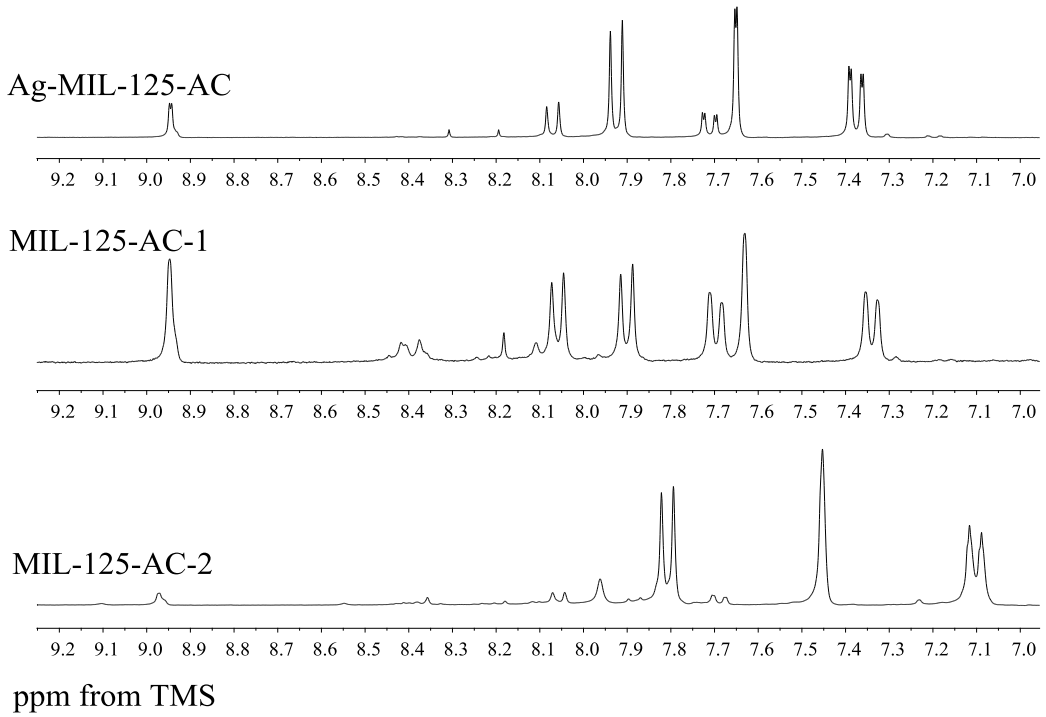

Figure II.2.2 ^{1}H NMR spectra of aromatic region of MIL-125-AC-2, MIL-125-AC-1 and Ag-MIL-125-AC.

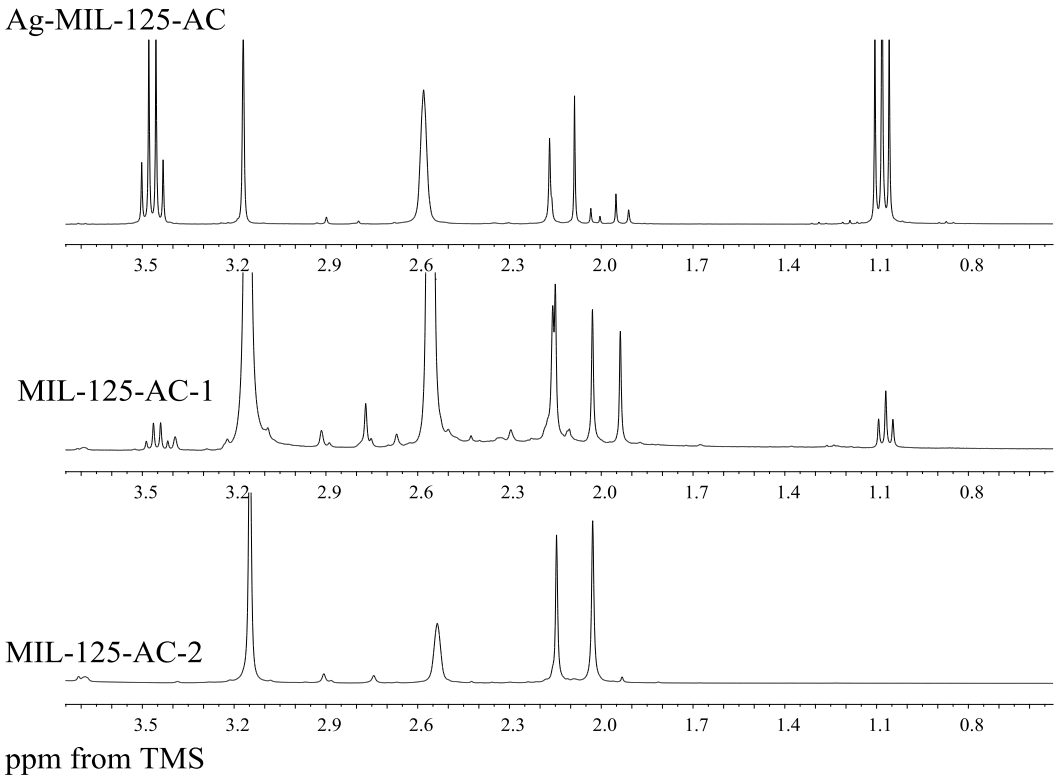

Figure II.2.3 ^{1}H NMR spectra of aliphatic region of MIL-125-AC-2, MIL-125-AC-1 and Ag-MIL-125-AC.

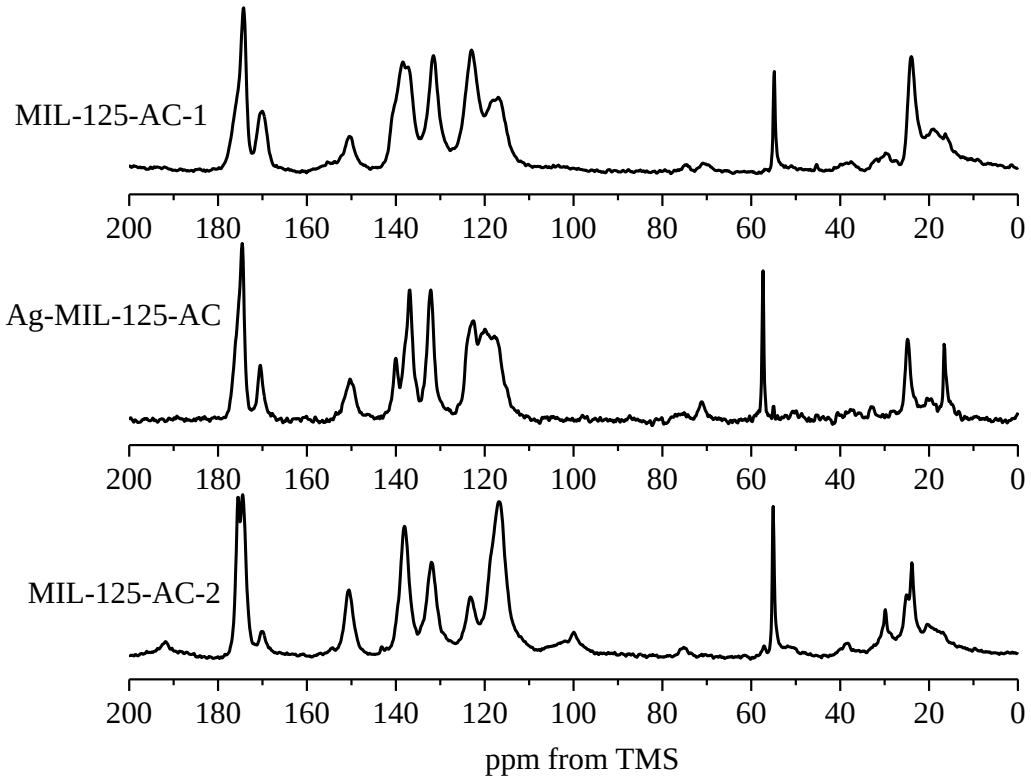

Figure II.2.4 ^{13}C CP-MAS NMR spectra of MIL-125-AC-2, MIL-125-AC-1 and Ag-MIL-125-AC.

Although these results on the decomposition of acetylacetone to acetic acid and acetone are intriguing our aim was to prepare a MOF material bearing the acetylacetone moiety able to chelate Cr. Thus, the experimental conditions were changed and NH_2-MIL-125 was exposed to acetylacetone vapours, for 24 hours, under nitrogen (rather then oxygen), affording MIL-125-AC-2 (Scheme II.2.2). The powdered product was washed five times with dry ethanol and dried in air.

Again, powder X-ray diffraction confirmed the integrity of the framework (Figure II.2.1c). ^{1}H NMR and ^{13}C CP-MAS were carried out to confirm the modification. Comparing with the reaction carried out under the laboratory oxygen atmosphere, in this reaction under a nitrogen atmosphere there was a decrease in the degradation of acetylacetone to acetic acid (only a small amount of acetyl-MIL-125 were observed) and a high yield of the modified acetylacetone moiety (AcAc-MIL-125) was identified Scheme II.2.2). The ^{1}H NMR spectra of the digested MIL-125-AC-2 (dissolved in DCl-DMSO-d_6) indicated ca. 70% of the product resulting from the direct reaction of the MOF-amino group with the acetylacetone (AcAc-MIL-125), 12% of acetyl-MIL-125 and 18% of unmodified NH_2-MIL-125 (Figure II.2.2, II.2.3).

Resonances at 7.09, 7.45, and 7.80 ppm are ascribed to the aromatic protons of the starting material NH_2-MIL-125, and the signals at 2.03, 2.15, 5.69 ppm to the acetylacetone molecule indicate some hydrolysis of acetylacetone moiety. ^{1}H NMR provides evidence for the presence of acetyl-MIL-125, although in smaller amounts.

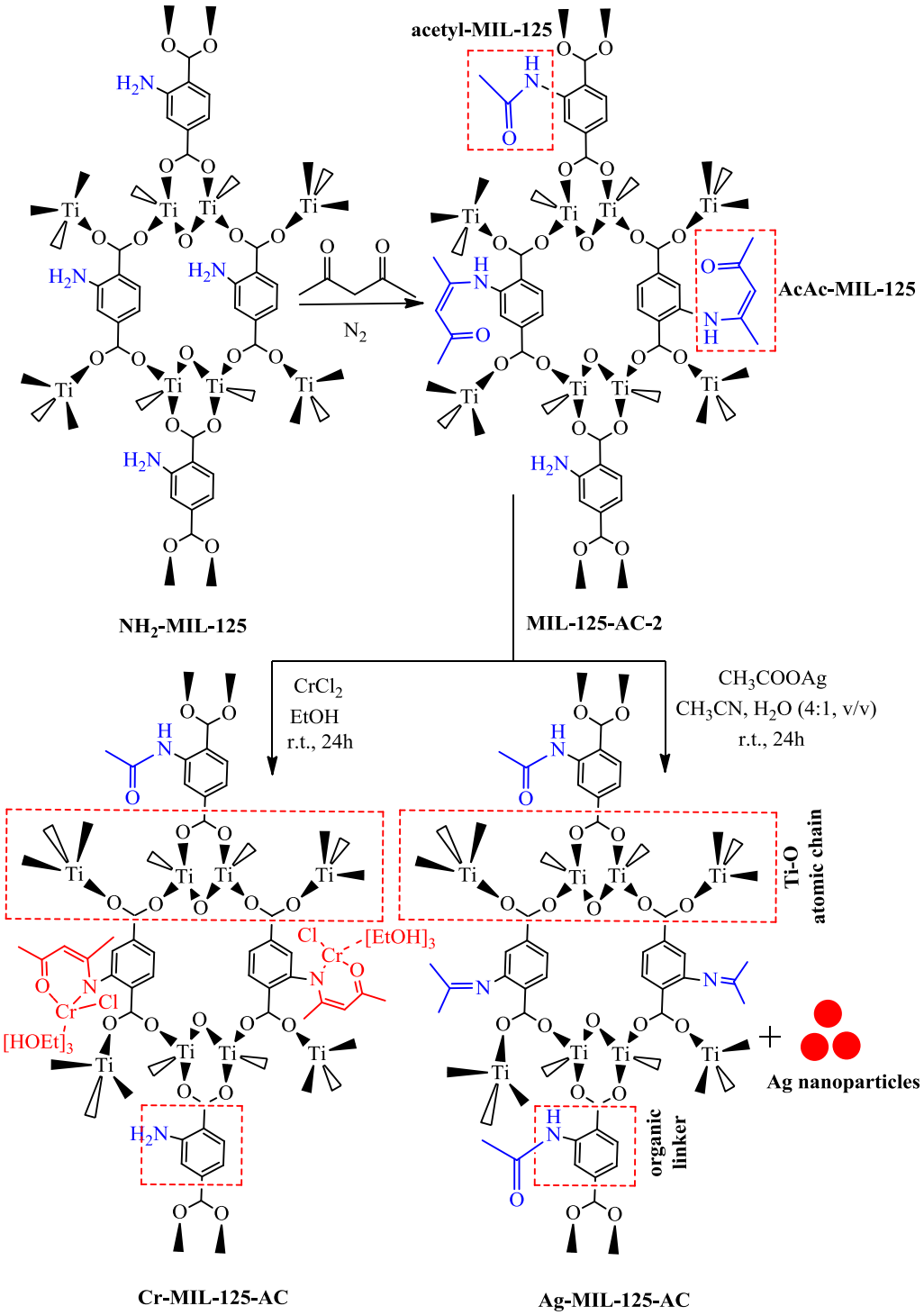

Scheme II.2.2 Post-synthetic covalent modifications of NH_2-MIL-125 with vapour of acetylacetone under N_2 and then coordinated to chromium.

The ^{13}C CP-MAS NMR spectrum of NH_2-MIL-125 exhibits resonances at 116.6, 119.0, 132.0, 137.8 and 151.2 ppm given by different aromatic sp^2 carbons and two peaks at 174.9 and 175.8 ppm assigned to the carbonyl groups of 2-aminoterephthalic acid. Additional signals confirmed the incomplete removal of both the solvent DMF (30.7 and 163.3 ppm) and methanol (55.1 ppm) used in the synthesis of the material (Figure A11). After functionalization, MIL-125-AC-2 displayed new peaks at 25.1 and 29.9 ppm due to the acetylacetonate methyl groups, and at 99.9 and 191.8 ppm assigned to, respectively, the acetylacetonate C=C and C=O groups (Figure 2). Moreover, several peaks are observed in the aromatic region (116.8, 123.2, 138.0, 150.5 ppm) and at 174.5 and 175.5 ppm, being these ascribed to the carbonyl groups of 2-aminoterephthalic acid. The peaks at 23.8 and 170.2 ppm are attributed respectively to the methyl and amide group of acetyl-MIL-125.

The Fourier transform infrared (FTIR) spectra of MIL-125-AC-2 (Figure II.2.5 and A73) display the same characteristic vibrations of parent MOF (NH_2-MIL-125). Bands at 1510–1450 cm^{-1} are assigned to aromatic ring stretch, 1225–950 cm^{-1} to aromatic C-H in plane bend, and 900–670 cm^{-1} to the aromatic C-H out of plane bend. Intense bands are also seen at 1463–1415 cm^{-1} and 1616–1597 cm^{-1}, ascribed to the symmetric and asymmetric -CO_2 stretching vibrations. The band at 1660 cm^{-1} is attributed to DMF carbonyl group. Upon PSM, the following bands appear:[28a,32-34] at 1683 cm^{-1} a shoulder attributed to the amide carbonyl stretch; at 1018 cm^{-1} a C-CO-C wagging; at 1299 cm^{-1} due to symmetric N–C=C–C and C=O stretch which is strongly coupled to δ_{NH}; while the bands at 1050 cm^{-1} and 1100 cm^{-1} (C-NH_2) disappeared. The following chemical formula for MIL-125-AC-2 was confirmed by all previous analysis and also by elemental analysis (Table A5): $[Ti_8O_8(OH)_4(C_{13}H_{11}NO_5)_{4.2}(C_{10}H_7NO_5)_{0.72}(C_8H_5NO_4)_{1.08}]$.

Doping with Chromium

The next synthesis step was the reaction of MIL-125-AC-2 with $CrCl_2$ (in dry ethanol under nitrogen, for 12 h at room temperature) affording Cr-MIL-125-AC. The composition of Cr-MIL-125-AC was determined by combined conventional elemental and EDS analysis (Table A5) and its formula is $[Ti_8O_8(OH)_4(C_{19}H_{28}NO_8CrCl)_{4.2}(C_{10}H_7NO_5)_{0.72}(C_8H_5NO_4)_{1.08}]$. ICP-AES analysis reveals the same Cr content, within experimental error. Powder X-ray diffraction pattern of the final material (Figure II.2.1d) confirmed the framework integrity.

Although TEM images of MIL-125-AC-2 and Cr-MIL-125-AC (Figure II.2.6b) show that introduction of chromium induces the formation of some defects, the crystal habit remains essentially unchanged. FTIR spectra of the final materials show the same bands as MIL-125-AC-2, although some of them (571, 1338 cm^{-1}) with a slightly decreased intensity and a small shift in another one (from 1488 to 1500 cm^{-1}) (Figure II.2.5).

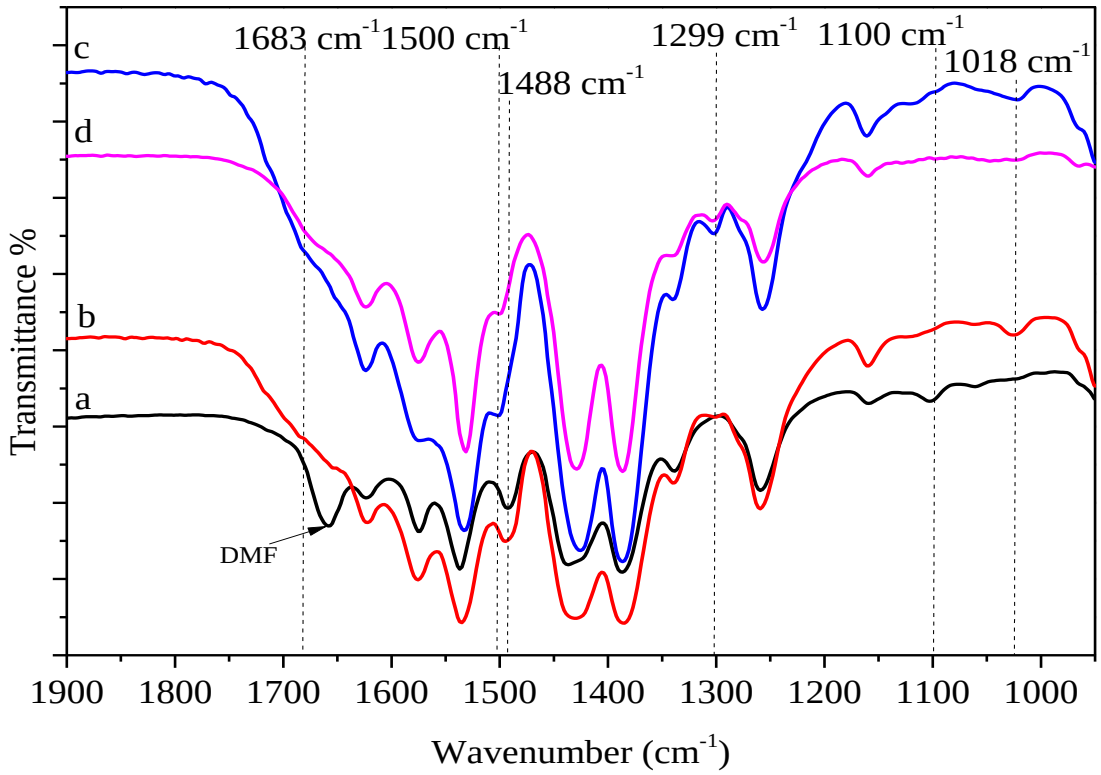

Figure II.2.5 FTIR spectrum of: a) NH_2-MIL-125; b) MIL-125-AC-2; c) Cr-MIL-125-AC; and d) Ag-MIL-125-AC.

The diffuse reflectance solid-state UV-Vis spectra of MIL-125 materials are shown in Figure II.2.7. The UV region shows broad absorptions at 262, 298 and 387 nm due to d → π*(aryl) transitions.[35] In the visible region, MIL-125-AC exhibits a broad tail extending from *ca.* 500 to 900 nm. Cr-MIL-125-AC, in turn, displays enhanced absorption between 420 and 520 nm and a new band centred at *ca.* 610 nm assigned to d → d transitions.[36] Considering Figure A74, the optical band gap of NH_2-MIL-125 is 2.58 eV (480 nm) (Table II.2.1), according with previous studies,[30] while for MIL-125-AC-2 and Cr-MIL-125-AC is, respectively, 2.51 (494 nm) and 2.21 (561 nm). The specific surface area (SSA) of Cr-MIL-125-AC is 1074 m^2/g, while pore volume is 0.2719 cm^3/g. For Ag-MIL-125-AC, SSA is 977 m^2/g and pore volume is 0.1744 cm^3/g.

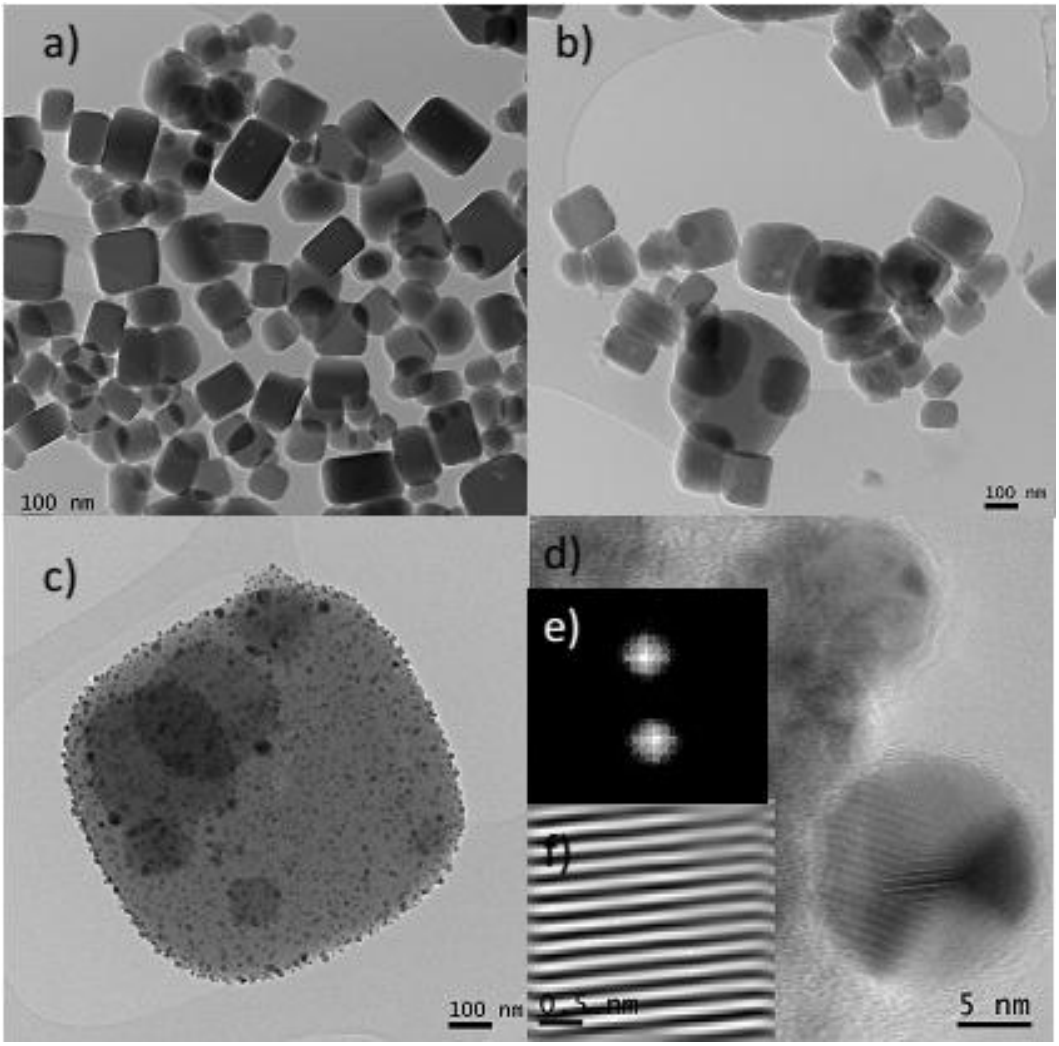

Figure II.2.6 TEM images of: a) MIL-125-AC-2 nanoplatelets; b) Cr-MIL-125-AC nanoplatelets; and c) Ag-MIL-125-AC nanoplatelets; d) HRTEM of a part of the platelet, Ag-MIL-125-AC. Fourier analysis of the image in Fig. d): (e) masked power spectrum, and (f) back Fourier transform.

X-ray photoelectron spectroscopy of Cr-MIL-125-AC consists of two Cr peaks at 587.5 and 577.7 eV corresponding to $2p_{1/2}$ and $2p_{3/2}$ energy levels, respectively (Figure II.2.8). These values indicate the presence of Cr(III) because they compare very well with the binding energies of both $Cr(NO_3)_3$ ($2p_{1/2}$ 587 eV and $2p_{3/2}$ 577.3 eV) and Cr-bearing MOF, UiO-66-CrCAT ($2p_{1/2}$ 587 eV and $2p_{3/2}$ 577.2 eV).[37] Because Cr(II) readily oxidizes to Cr(III) in the presence of oxygen the presence of the latter is not surprising. However, one cannot discard the presence of small amounts of other Cr oxidation states in Cr-MIL-125-AC. The specific surface area (SSA) of the prepared samples was evaluated by the Brunauer–Emmett–Teller (BET) method using N_2 as the adsorbate gas (Figure A83). As expected, pore volume decreases upon functionalization.

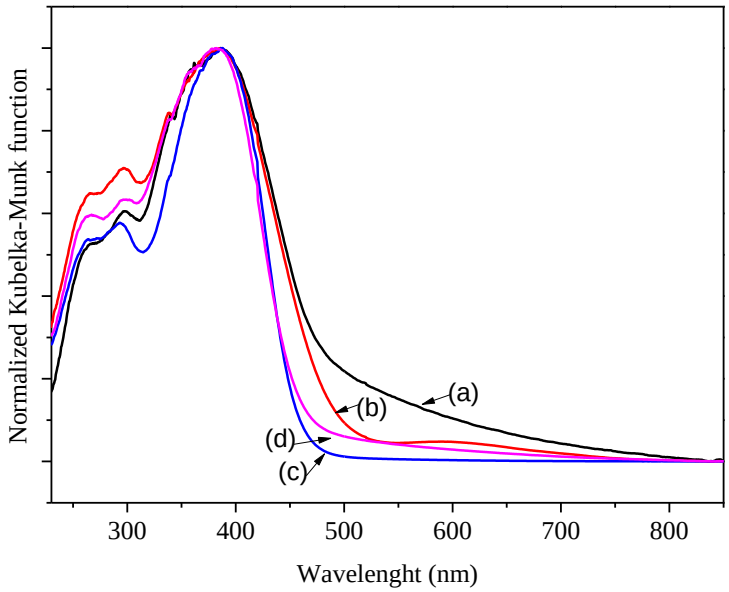

Figure II.2.7 Diffuse reflectance UV−vis spectra of: a) Ag-MIL-125-AC; b) Cr-MIL-125-AC; c) NH_2-MIL-125 and d) MIL-125-AC.

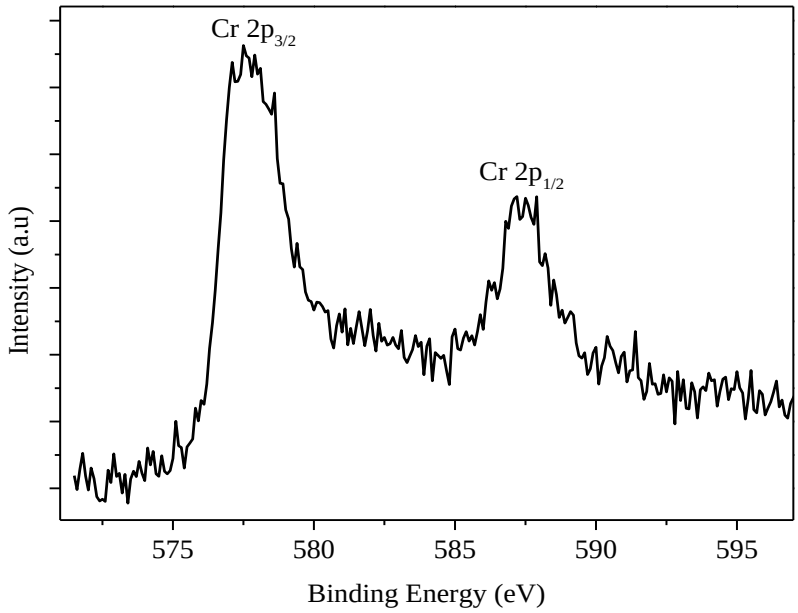

.

Figure II.2.8 The high resolution XPS spectrum of Cr2p for Cr-MIL-125-AC.

Doping with Silver

In an alternative synthesis, MIL-125-AC-2 was reacted with CH_3COOAg (in a 4:1 mixture of acetonitrile and water, at room temperature for 24 hours) affording Ag-MIL-125-AC. The powder X-ray diffraction pattern of the final material (Figure II.2.1e) confirmed, again, the framework integrity.

Surprisingly, TEM revealed the widespread formation of Ag nanoparticles, mostly having 5-10 nm in size, although some larger particles up to *ca.* 50 nm were also observed (Figure II.2.6). Lattice fringe spacing measurements (0.23 nm corresponding to the (111) plane) confirm that these are indeed silver nanoparticles. XRD did not show the reflections of silver metal presumably because most particles are very small. Careful examination reveals that nanoparticles appear both decorating the external surface and embedded within the crystals (Figure II.2.6).

We resorted to NMR to rationalize the formation of the Ag nanoparticles. The ^{1}H NMR spectrum of Ag-MIL-125-AC is very similar to the spectrum of MIL-125-AC-1 with small difference on the intensity of certain resonances (Figure II.2.2 and II.2.3). Also the ^{1}H NMR spectrum of Ag-MIL-125-AC is completely different from that of MIL-125-AC-2. This indicates that after formation of the Ag-acetylacetone complex it was decomposed into Ag nanoparticles and free acetone (Scheme II.2.3).

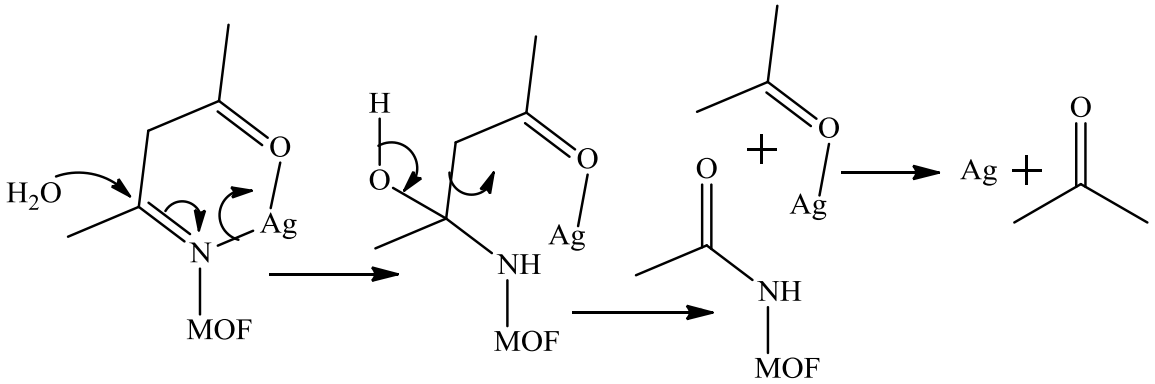

Scheme II.2.3 formation mechanism of silver nanoparticles

This is also confirmed via the ^{13}C solid state NMR spectrum of Ag-MIL-125-AC, in which the acetylacetone bands are absent (Figure II.2.4).

The UV-Vis spectrum of Ag-MIL-125-AC displays considerably more intensity in the visible region than the spectra of the other materials (Figure II.2.7). This material shows a red shift of the absorption edge, relatively to the other materials, attributed to the plasmon Ag resonance absorption.[38] The optical band gap shifts from 2.58 eV (480 nm) in NH_2-MIL-125 to 2.09 eV (593 nm) in Ag-MIL-AC (Table II.2.1). More detailed information concerning the elemental and chemical state of Ag-MIL-125-AC was also achieved by analyzing X-ray photoelectron spectroscopy (XPS).

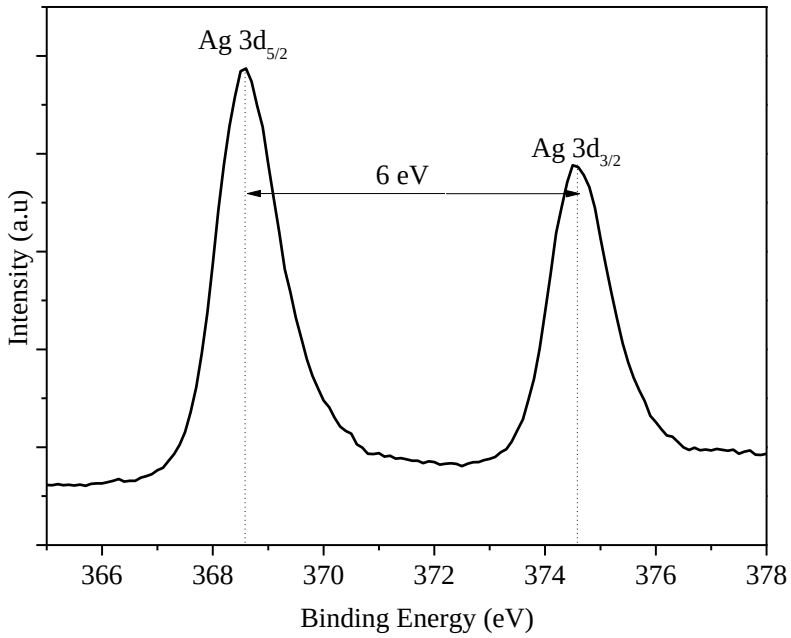

Figure II.2.9 The high resolution XPS spectrum of Ag 3d for Ag-MIL-125-AC.

The fully scanned spectrum was shown in Figure A 82. Figure II.2.9 is the high-resolution X-ray photoelectron spectrum of the Ag3d region for Ag-MIL-125-AC. It consists of two individual peaks located at ca. 368.6 eV, and ca. 374.6 eV, which assigned to Ag $3d_{5/2}$ and Ag $3d_{3/2}$ binding energies, respectively (compared with bulk Ag (368.3 eV for Ag $3d_{5/2}$, and 374.3 eV for Ag $3d_{3/2}$).[39] The splitting of the Ag3d doublet is 6 eV, So, the Ag is present as Ag^0.[40]

Photocatalysis

MIL-125 materials were next tested as photocatalysts in the decomposition of methylene blue. In order to compare their photocatalytic activity with commercially available TiO_2 (hombikat UV-100), the materials were added to an aqueous solution of methylene blue, at room temperature and atmosphere. Figure II.2.10 shows both, the adsorption percentage for methylene blue versus time in the dark, and its photocatalytic degradation versus time under simulated daylight conditions. Dye adsorption in the dark decreases 17, 25, 29, 31 and 35% after an equilibrium time of, respectively, 45 (hombikat UV-100), 120 (Cr-MIL-125-AC), 90 (Ag-MIL-AC), 120 (MIL-125-AC) and 135 minutes (NH_2-MIL-125) (Figure II.2.10b). The methylene blue color does not change after the addition of the catalyst, in the dark.

In contrast, under light irradiation, the methylene blue concentration decreases 29, 62, 74, 99 and 99.5 % after, respectively, an equilibrium time of 90 (hombikat UV-100), 60 (MIL-125-AC), 105 (NH_2-MIL-125), 120 (Cr-MIL-125-AC), 30 minutes (Ag-MIL-125-AC) (Figure II.2.10a). The reaction mixture changed from blue to milky white in the presence of Cr-MIL-125-AC and Ag-MIL-125-AC the degradation products were analyzed by using the GC/MS technique and it was found that the dye initially undergoes demethylation showing all the intermediates in the presence of Cr-MIL-125-AC, this findings agree with Rauf *et al* [41] but in the presence of Ag-MIL-125-AC, the results show only the last intermediate of demethylation, meaning that demethylation goes faster than Cr-MIL-125-AC. Also MB dye undergoes decomposition in the presence of both catalysts resulting in the formation of some degradation products, our findings are befit with Houas *et al*[42] and Chaudhuri *et al*[43](Scheme II.2.4).

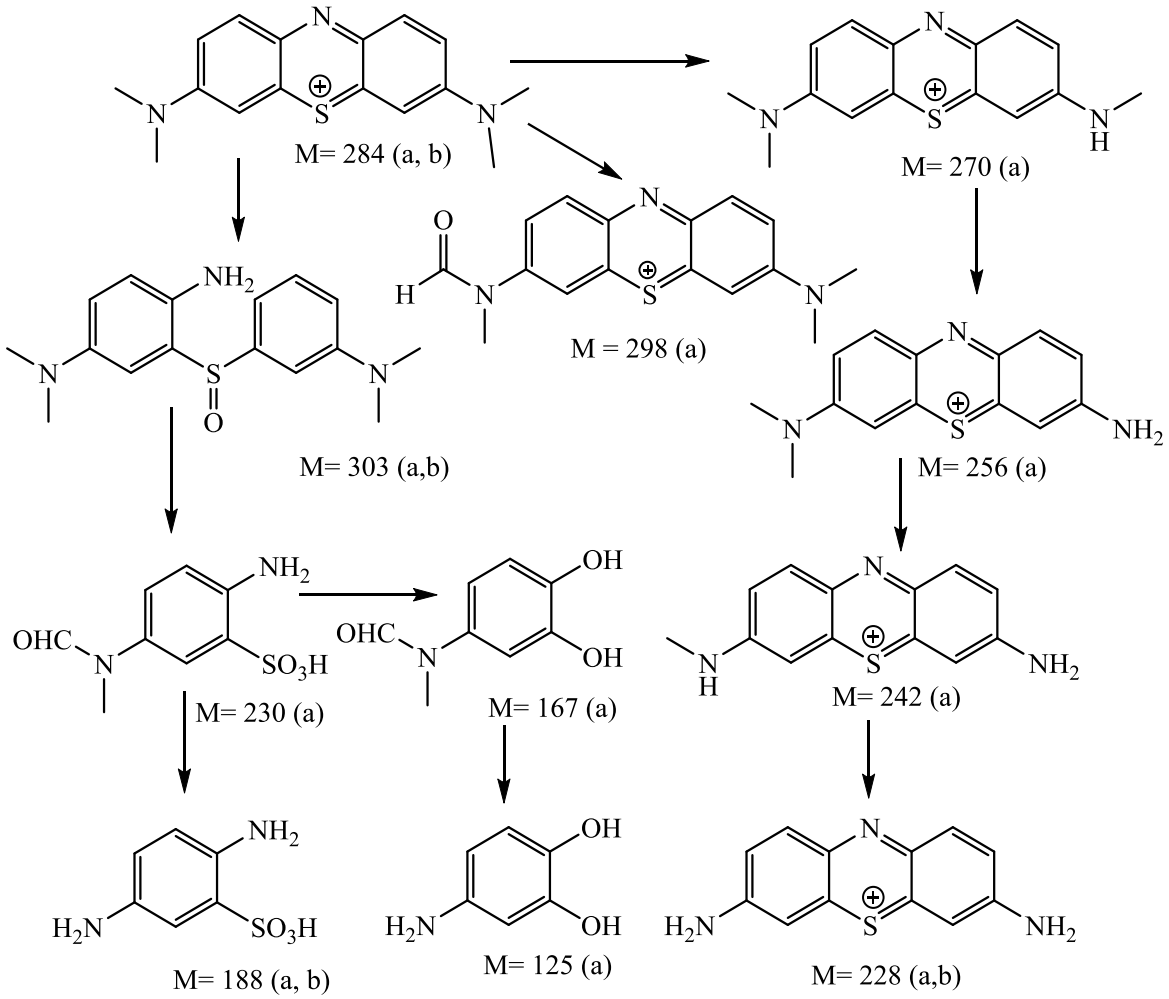

Scheme II.2.4 Photocatalytic degradation pathway of MB (analyzed by GC/MS) in presence of (a) Cr-MIL-125-AC, (b) Ag-MIL-125-AC.

Table II.2.1 lists the kinetic parameters for methylene blue adsorption and photocatalytic degradation. The former process follows a pseudo second-order kinetic model for the first 180 minutes and the measured rate constants (k_2) are the same for all working MOFs. This means that the adsorption kinetics is not the main factor determining the differences in the photocatalytic activity of the materials. The k_2 constant for hombikat UV-100 is 2.7 times higher than that of MIL-AC-Cr, presumably due to the short diffusion path for the former (*ca.* 10 nm), as compared with the micrometer scale particle size of MIL-AC-Cr.

Table II.2.1 Photocatalytic activity under simulated day light exposure in liquid phase and energy band gap (calculated from the Tauc plot) of the PSM of MIL-125.

	hombikat UV-100 (TiO_2)	NH_2-MIL-125	MIL-125-AC	Cr-MIL-125-AC	Ag-MIL-125-AC
k_1 X 10^{-2}, min^{-1}	0.48* ± 0.01	0.94* ± 0.03	0.82* ± 0.03	3.13** ± 0.02	10.31*** ± 0.09
r_{12}	0.98	0.94	0.94	0.99	0.95
q_2, mg/g	3.56 ± 0.03	7.44 ± 0.08	6.44 ± 0.10	5.47 ± 0.15	6.13 ± 0.15
K_2 X 10^{-2}, min. g/mg****	6.07 ± 0.08	2.57 ± 0.15	2.26 ± 0.09	2.25 ± 0.10	2.35 ± 0.10
r_{22}	0.99	0.99	0.99	0.99	0.99
Rate ratio to TiO_2	1	1.96	1.71	6.52	21.47
Catalytic quantum yield %	0.12	0.24	0.21	0.78	2.57
E_g (eV)	3.27	2.58	2.51	2.21	2.09

*fitting for the first 60 min.
**fitting for the first 150 min.
***fitting for the first 20 min.
****fitting for the first 180 min.

The methylene blue degradation-time curves were fitted with a pseudo-first-order kinetics model for: i) 20 minutes - Ag-MIL-AC; (ii) 60 minutes - TiO_2, NH_2-MIL-125 and MIL-125-AC-2; and (iii) 150 minutes Cr-MIL-AC. For convenience, the photocatalytic activities of MOF materials are compared by calculating the ratio of their rate constants k_1 to the hombikat UV-100 rate constant. Remarkably, Cr-MIL-125-AC and Ag-MIL-125-AC are 6.5 and 21.5 times larger than that of hombikat UV-100. At the end of the photocatalytic degradation of MB the Cr- and Ag-bearing photocatalysts were separated out from the solution by centrifugation and the latter was analyzed by ICP-AES, revealing

a negligible amount of leached metal (0.0043% for Cr after one cycle, 0.00083% for Ag after five cycles). One may contend that the photocatalytic activity of Cr-MIL-125-AC and Ag-MIL-125-AC should be compared with that of Cr- and Ag-doped TiO_2. This is not, however, possible because (i) the TiO_2 lattice does not accept the very high Cr loading of Cr-MIL-125-AC (typical loading for titanium oxide is 0.5 to 5%), while (ii) it is very difficult to ensure the formation of Ag nanoparticles over TiO_2 particles with similar coverage, particle size distribution, etc.

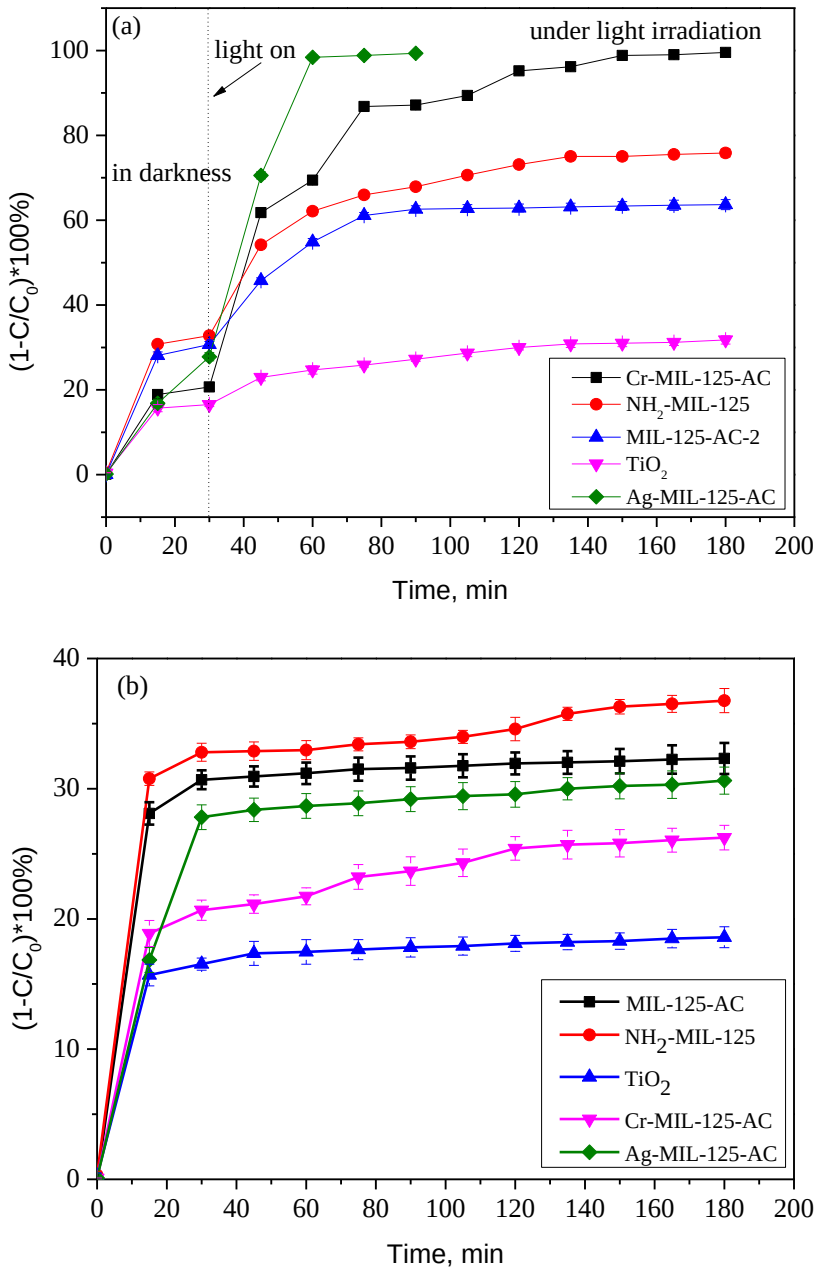

Figure II.2.10 a) Photocatalytic degradation of MB under daylight irradiation, and b) Adsorption of MB in dark.

The stability and activity during recycling reactions were studied for the best photocatalyst (Ag-MIL-AC, Figure II.2.11). After each cycle, the photocatalyst was centrifuged, separated, washed with ethanol and dried at 75 °C. The methylene blue photodegradation rate constant was the same, within experimental error, for the 5 cycles, *ca.* 0.10 min^{-1}.

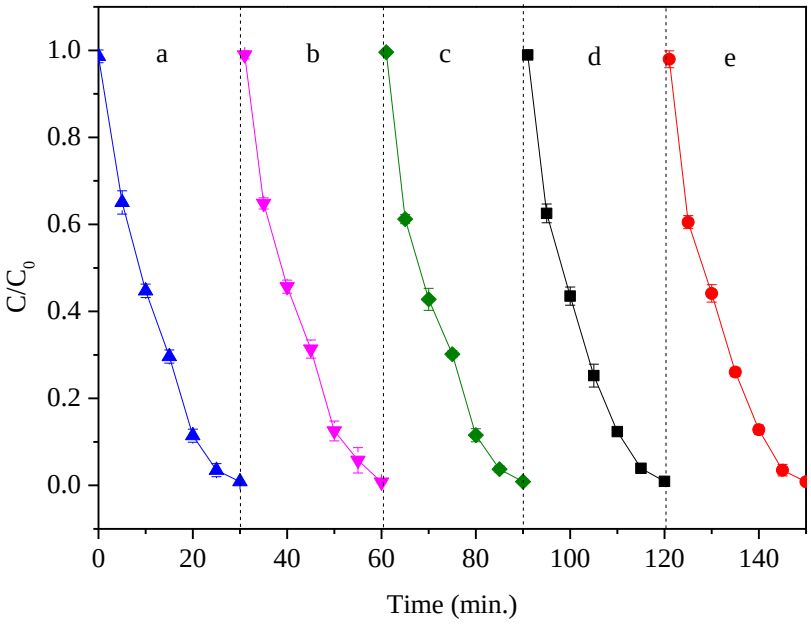

Figure II.2.11 Five repeated processes of using the Ag-MIL-AC for the photodegradation of MB under the simulated daylight irradiation conditions.

The study of the detailed mechanism of the photocatalytic methylene blue degradation is beyond the scope of this thesis. The presently accepted mechanism has been the subject of many studies and here we shall only highlight the basic ideas.[44-46] When light impinges on MIL materials with energy equal or greater than their band gaps the electrons (e^-) are excited from the valence band to the conduction band producing holes (h^+) in valence band. The latter diffuse to the materials surface and directly oxidize adsorbed organic molecules or react with water molecules or hydroxyl ions (OH^-) to generate hydroxyl radicals ($^{\bullet}OH$), which are strong oxidants and readily react with surface adsorbed organic molecules. On the other hand, photogenerated electrons may be trapped by molecular oxygen to form superoxide radicals ($O_2^{-\bullet}$), which also possess strong oxidant ability to decolorize the MB molecules.

Titanium organic frameworks raise interest as photocatalysts because of their relatively narrow band gap. As we have shown, embedding chromium in these materials via post-synthetic modification of MOFs increases their photocatalytic activity.

Chromium effectively extends the absorption from the ultraviolet to the visible light region. The photogenerated holes may migrate from the valence band of MIL-125-AC to the valence band of Cr(III), thus promoting the separation of holes and electrons and increasing the recombination time, and enhancing the MB photodegradation [Figure II.2.12 (left)]. This picture is a simplified one, particularly because it is likely that Cr-MIL-125-AC contains not only Cr(III) but also small amounts of other oxidation states.

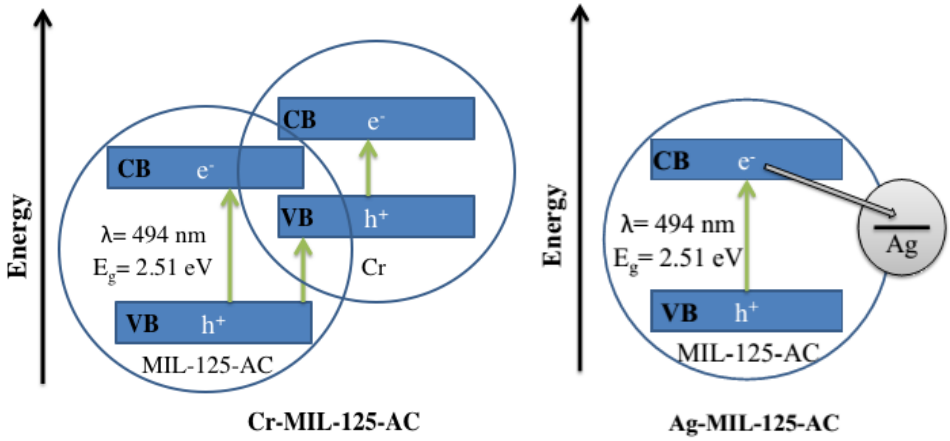

Figure II.2.12 Schematic illustrations of the charge separation in Cr-MIL-125-AC (left) and the possible role of silver nanoparticles in trapping the photogenerated electrons (right).

Decorating surfaces with Ag nanoparticles or incorporating silver nanoparticles into materials has been a common strategy for increasing photocatalytic activity by reducing the recombination reaction. It is well-known that silver may trap the excited electrons from TiO_2 leaving the holes for the degradation of organic species (Figure II.2.12, right). Ag particles may assist the electrons excitation by creating a local electric field and the plasmon resonance effect in metallic silver particles shows a reasonable enhancement in this electric field.[47] These facts help understanding the remarkable photocatalytic activity of Ag-MIL-AC.

References

[1] O. M. Yaghi, and Li, H. L. *J. Am. Chem. Soc*. **1995**, *117*, 10401−10402.

[2] O. M. Yaghi, G. Li and H. Li, *Nature*, **1995**, *378*, 703-706.

[3] a) R. B. Getman, Y.-S. Bae, C. E. Wilmer and R. Q. Snurr, *Chem. Rev*., **2012**, *112*,703-723., b) K. Sumida, D. L. Rogow, J. A. Mason, T. M. McDonald, E. D.

Bloch, Z. R. Herm, T.-H. Bae and J. R. Long, *Chem. Rev*., **2012**, *112*, 724-781. , c) M. P. Suh, H. J. Park, T. K. Prasad and D.-W. Lim, *Chem. Rev*., **2012**, *112*, 782-835., d) J.-R. Li, J. Sculley and H.-C. Zhou, *Chem. Rev*., **2012**, *112*, 869-932.

[4] a) P. Falcaro, D. Buso, A. J. Hill and C. M. Doherty, *Adv. Mat*., **2012**, *24*, 3153-3168., b) S. Eslava, L. P. Zhang, S. Esconjauregui, J. W. Yang, K. Vanstreels, M. R. Baklanov and E. Saiz, *Chem. Mat.*, **2013**, *25*, 27-33., c) M. D. llendorf, A. Schwartzberg, V. Stavila and A. A. Talin, *Chem. Eur. J.*, **2011**, *17*, 11372-11388., e) R. Ameloot, M. B. J. Roeffaers, G. De Cremer, F. Vermoortele, J. Hofkens, B. F. Sels and D. E. De Vos, *Adv. Mat.*, **2011**, *23*, 1788-1791.

[5] a) D. Buso, J. Jasieniak, M. D. H. Lay, P. Schiavuta, P. Scopece, J. Laird, H. Amenitsch, A. J. Hill and P. Falcaro, Small, **2012**, *8*, 80-88., b) B. Liu, *J. Mat. Chem*., **2012**, *22*, 10094-10101.; c) L. E. Kreno, K. Leong, O. K. Farha, M. Allendorf, R. P. Van Duyne and J. T. Hupp, *Chem. Rev*., **2012**, *112*, 1105-1125.

[6] S. Horike, D. Umeyama and S. Kitagawa, *Acc. Chem. Res*., **2013**, *46*, 2376–2384.

[7] C. Wang, T. Zhang and W. B. Lin, *Chem. Rev.*, **2012**, *112*, 1084-1104.

[8] a) C. M. Doherty, E. Knystautas, D. Buso, L. Villanova, K. Konstas, A. J. Hill, M. Takahashi and P. Falcaro, *J. Mat. Chem*., **2012**, *22*, 11470-11474., b) S.-H. Huo and X.-P. Yan, *Analyst*, **2012**, *137*, 3445-3451.

[9] a) P. Horcajada, T. Chalati, C. Serre, B. Gillet, C. Sebrie, T. Baati, J. F. Eubank, D. Heurtaux, P. Clayette, C. Kreuz, J.-S. Chang, Y. K. Hwang, V. Marsaud, P.-N. Bories, L. Cynober, S. Gil, G. Ferey, P. Couvreur and R. Gref, *Nat. Mat.*, **2010**, *9*, 172-178., b) J. Della Rocca, D. Liu and W. Lin, *Acc. Chem. Res*., **2011**, *44*, 957-968., c) P. Horcajada, R. Gref, T. Baati, P. K. Allan, G. Maurin, P. Couvreur, G. Ferey, R. E. Morris and C. Serre, *Chem. Rev*., **2012**, *112*, 1232-1268.

[10] a) J. Della Rocca and W. Lin, *Eur. J. Inorg. Chem*., **2010**, 3725-3734., b) T. D. Schladt, K. Schneider, H. Schild and W. Tremel, *Dalt. Trans*., **2011**, *40*, 6315-6343.

[11] Y. Ikezoe, G. Washino, T. Uemura, S. Kitagawa and H. Matsui, *Nat. Mat*., **2012**, *11*, 1081-1085.

[12] a)Y. Chen, V. Lykourinou, C. Vetromile, H. Tran, L.-J. Ming, R. W. Larsen and S. Ma, *J. Am. Chem. Soc*., **2012**, *134*, 13188-13191., b) V. Lykourinou, Y. Chen, X.-S. Wang, L. Meng, H. Tran, L.-J. Ming, R. L. Musselman and S. Ma, *J. Am. Chem. Soc*., **2011**, *133*, 10382-10385., c) W.-L. Liu, S.-H. Lo, B. Singco, C.-C. Yang, H.-

Y. Huang and C.-H. Lin, *J. Mat. Chem. B*, **2013**, *1*, 928-932., d) Y.-H. Shih, S.-H. Lo, N.-S. Yang, B. Singco, Y.-J. Cheng, C.-Y. Wu, I. H. Chang, H.-Y. Huang and C.-H. Lin, *Chempluschem*, 2012, **77**, 982-986. , e) C. M. Doherty, G. Grenci, R. Riccò, J. I. Mardel, J. Reboul, S. Furukawa, S. Kitagawa, A. J. Hill and P. Falcaro, *Adv. Mat.*, **2013**, *25*, 4701-4705.

[13] J.Y. Lee, O.K. Farha, J.Roberts, K. A. Scheidt, S.B. T. Nguyen and J. T. Hupp**,** *Chem. Soc. Rev. ,* **2009**, *38*, 1450-1459

[14] a) S. M. Cohen, *Chem. Rev*., **2012**, *112*, 970–1000; b) K. K. Tanabe and S. M. Cohen, *Chem. Soc. Rev*., **2011**, *40*, 498–519; c) S. M. Cohen, *Chem. Sci*., 2010, **1**, 32–36; d) Z. Wang, S. M. Cohen, *Chem. Soc. Rev.*, **2009**, *38*, 1315–1329.

[15] a) T. M. McDonald, D. M. D'Alessandro, R. Krishna andJ. R. Long, *Chem. Sci*., 2011, **2**, 2022–2028.; b) Z. Wang and S. M. Cohen, *J. Am. Chem. Soc*., **2009**, *131*, 16675–16677.

[16] Y. K. Hwang, D.-Y. Hong, J.-S. Chang, S. H. Jhung,Y.-K. Seo, J. Kim, A. Vimont, M. Daturi, C. Serre and G. Férey, *Angew. Chem., Int. Ed.*, **2008**, *47*, 4144–4148.

[17] R. M. Abdelhameed, L. D. Carlos, A. M. S. Silva, J. Rocha, *Chem. Commun*. **2013**, *49*, 5019-5021.

[18] T. Gadzikwa, O. K. Farha, C. D. Malliakas, M. G. Kanatzidis, J.T. Hupp, and S. T. Nguyen, *J. Am. Chem.Soc*., **2009**, *131*, 13613–13615

[19] K. M. L. Taylor-Pashow, J. D. Rocca, Z. Xie, S. Tran and W. Lin, *J. Am. Chem. Soc*., **2009**, *131*, 14261–14263.

[20] Z. Wang and S. M. Cohen, *J. Am. Chem. Soc*. **2009**, *131*, 16675–16677

[21] a) Y. Kataoka, K. Sato, Y. Miyazaki, K. Masuda, H. Tanaka, S. Naito and W. Mori, *Energy Environ Sci*, **2009**, *2*, 397–400.; b) J.H. Cavka, S. Jakobsen, U. Olsbye, N. Guillou, C. Lamberti, S. Bordiga, K.P. Lillerud, *J. Am. Chem. Soc.*, **2008**, *130*, 13850–13851.; c) C. Wang, K.E. deKrafft, W. Lin, *J. Am. Chem. Soc.*, **2012**, *134*, 7211–7214

[22] a) C .Wang, Z. Xie, K.E. deKrafft, W. Lin, *J. Am. Chem. Soc*., **2011**, *133*, 13445–13454.; b) Y. Fu, D. Sun, Y. Chen, R. Huang, Z. Ding, X. Fu, Z. Li , *Angew Chem Int Ed* **2012**, *51*, 3364–3367.

[23] a) J. Du, Y. Yuan, J. Sun, F. Peng, X. Jiang, L. Qiu, A. Xie, Y. Shen, J. Zhu , *J. Hazard. Mater.*, **2011**, *190*, 945–951.; b) M.C. Das, H. Xu, Z. Wang, G. Srinivas,

W. Zhou, Y. Yue, V.N. Nesterov, G. Qian, B. Chen, *Chem. Commun.*, **2011**, *47*, 11715–11717.

[24] a) H. Son, S. Jin, S. Patwardhan, S.J. Wezenberg, N.C. Jeong, M. So, C.E. Wilmer, A.A. Sarjeant, G.C. Schatz, R.Q. Snurr, O.K. Farha, G.P. Wiederrecht, J.T. Hupp, J. Am. Chem. Soc., **2013**, *135*, 862–869.; b) C.Y. Lee, O.K. Farha, B.J. Hong, A.A .Sarjeant, S.T. Nguyen, J.T. Hupp , J. Am. Chem. Soc., **2011**, *133*,15858–15861.; c) M. Xie, X. Yang, C. Zou, C. Wu, *Inorg Chem*., **2011**, *50*, 5318–5320.; d) P. Wu, C. He, J. Wang, X. Peng, X. Li, Y. An, C. Duan, *J. Am. Chem. Soc.*, **2012**, *134*, 14991–14999.

[25] M. Dan-Hardi, C. Serre, T. Frot, L. Rozes, G. Maurin, C. Sanchez, G. Férey, *J. Am. Chem. Soc*, **2009**, *131*, 10857-10859.

[26] C. Serre, J.A. Groves, P. Lightfoot, A.M.Z. Slawin, P.A. Wright, N. Stock, T. Bein, M. Haouas, F. Taulelle and G. Ferey, *Chem. Mater.*, **2006**, *18*, 1451-1457.

[27] J. Gao, J. Miao, P. Li, W. Y. Teng, L. Yang, Y. Zhao, B. Liu and Q. Zhang, *Chem. Commun.*, **2014**, *50*, 3786-3788.

[28] a)A. P. Smalley, D. G. Reid, J. C. Tan and G. O. Lloyd, *CrystEngComm*, **2013**, *15*, 9368-9371.; b) M.A. Nasalevich, M. G. Goesten, T. J. Savenije, F. Kapteijn and J. Gascon, *Chem. Commun.*, **2013**,*49*, 10575-10577.

[29] M. R. Hoffmann, S. T. Martin, W. Choi, and D. W. Bahneman, *Chem. Rev.*, **1995**, *95*, 69-96.

[30] C. H. Hendon, D. Tiana, M. Fontecave, C. Sanchez, L. D'arras, C. Sassoye, L. Rozes, C. Mellot-Draznieks, and A. Walsh, *J. Am. Chem. Soc*., **2013**, *135*, 10942−10945.

[31] a) J.F. Zhu, Z.G. Deng, F. Chen, J. Zhang, H. Chen, M. Anpo, J. Huang, L. Zhang, *Appl. Catal. B: Environ.*, **2006**, *62*, 329. ; b) K.T. Ranjit, B. Viswanathan, *J. Photochem. Photobiol. A: Chem.*, **1997**, *108*, 79. ; c) A. Di Paola, G. Marcı`, L. Palmisano, M. Schiavello, K. Uosaki, S. Ikeda, and B. Ohtani, *J. Phys. Chem. B*, **2002**, *106*, 637-645. ; d) X.B. Li, L.L. Wang, X.H. Lu, *J. Hazard. Mater.*, **2010**, *177*, 639.; e) Li Sa, P. Jena, *Phys. Rev. B*, **2009**, *79* , 201204.; f) L. Sangaletti, M.C. Mozzati, P. Galinetto, C.B. Azzoni, A. Speghini, Mbettinelli, *J. Phys. Condens. Matter.*, **2006**, *18*, 7643.; g) C.C. Pan, J.C.S. Wu, *Mater. Chem. Phys.*, **2006**, *100*, 102.

[32] J. R. Sohn and S. I. Lee, *J. Ind. Eng. Chem.*, **1997**, *3*, 198-202.

[33] S.F. Tayyari, F. Milani-nejad, *Spectrochimica Acta Part A,* **2000**, *56***,** 2679-2691.

[34] S. Bhattacharjee , D.-A. Yang and W.-S. Ahn, *Chem. Commun.,* **2011**, *47*, 3637-3639.

[35] a)Y. Fu, D. Sun, Y. Chen, R. Huang, Z. Ding, X. Fu and Z. Li, *Angew. Chem. In. Ed.*, **2012**, *51*, 3364-3367.; b) J. Gascon, M. D. Hernández-Alonso, A. R. Almeida, G. P. van Klink, F. Kapteijn and G. Mul, *ChemSusChem*, **2008**, *1*, 981-983.; c) H. Khajavi, J. Gascon, J. M. Schins, L. D. A. Siebbeles and F. Kapteijn, *J. Phys. Chem. C*, **2011**, *115*, 12487-12493.

[36] C. K. Brozek and M. Dinca, *J. Am. Chem. Soc.*, **2013**, *135*, 12886-12891.

[37] H. Fei, J. W. Shin, Y. S. Meng, M. Adelhardt, J. Sutter, K. Meyer, S. M. Cohen, *J. Am. Chem. Soc*. **2014**, *136*, 4965−4973.

[38] S. Eusti and M. A. El-Sayed, *Chem. Soc. Rev*., **2006**, *35*, 209–217.

[39] H. W. Chen, Y. Ku and Y. L. Kuo, *Chem. Eng. Technol.*, 2007, **30**, 1242–1247.

[40] S. Sen, S. Mahanty, S. Roy, O. Heintz, S. Bourgeois and D. Chaumont, *Thin Solid Films*, **2005**, *474*, 245–249.

[41] M. A. Rauf, M. A. Meetani, A. Khaleel, A. Ahmed, Chem. Eng. J., **2010,** *157*, 373–378.

[42] A. Houas, H. Lachheb, M. Ksibi, E. Elaloui,C. Guillard and J. Herrmann, *App. Cat. B: Environ.* **2001**, *31*, 145–157.

[43] R. G. Chaudhuri, S. Paria, *Dalton Trans.*, **2014**, *43*, 5526–5534.

[44] V. Luca, M. Osborne, D. Sizgek, C. Griffith, P. Z. Araujo, *Chem. Mater.* **2006**, *18*, 6132-6138.

[45] E. Haque, J. W. Jun, S. H. Jhung, *J. Hazard. Mater*. **2011**, *185*, 507–511.

[46] C. F. Zhang, L. G. Qiu, F. Ke, Y. J. Zhu, Y. P. Yuan, G. S. Xua, X. Jiang, *J. Mater. Chem. A*, **2013**, *1*, 14329–14334.

[47] M. K. Seery, R. George, P. Floris, and S. C. Pillai, *J. Photochem. Photobiol A: Chemistry*, **2007**, *189(2-3)*, 258 – 263.

Part III Experimental

Chapter III.1: Characterization Techniques

- **X**-Ray Diffraction (XRD).
- Electron Microscopy (Transmission and Scanning; TEM& SEM)
- Infrared (IR) Spectroscopy
- Elementary Analysis.
- ^{1}H, ^{13}C Nuclear Magnetic Resonance (^{1}H, ^{13}C NMR).
- Solid state nuclear magnetic resonance (CPMAS NMR)
- N_2 physisorption.
- X-ray photoelectron spectroscopy.
- Gas Chromatography/Mass spectroscopy (GC/MS).
- Photoluminescence spectroscopy
- Magnetic measurements
- DFT calculations

X-Ray Diffraction (XRD)

The powder diffraction X-ray (XRD) data were collected on an X'Pert MPD Philips diffractometer (Cu Kα X-radiation at 40 kV and 50 mA). PXRD analyses are essential (in the absence of suitable single crystal) to determine if the material possess the expected crystal structure.

Electron Microscopy (Transmission and Scanning; TEM& SEM)

EDS measurements were carried out on a SEM using a Hitachi SU-70 with a field emission gun. TEM was carried out on a Hitachi H-9000 microscope operating at 300 kV, high resolution microscopy was performed using a Jeol 2200 FS microscope with a field emission gun. The microscope was operated at 200 kV. The optical microscope examinations were carried out with Leica EZ4HD Digital Microscope-3.0 Megapixel.

Infrared (IR) Spectroscopy

Fourier transform infrared spectroscopy (FT-IR, Mattson 5000) was carried out in the range of 4000-350 cm^{-1} in transmission mode. The pellets were prepared by adding 1-2 mg of the MOFs to 200 mg of KBr. The mixture was then carefully mixed and compressed at a pressure of 10 kPa in order to form transparent pellets.

Elementary analysis (ICP-AES)

Elemental analysis was measured by Inductively Coupled Plasma Atomic Emission Spectroscopy (ICP-AES). The samples were dissolved in a boiling sulphuric and nitric acid mixture under reflux conditions and metal contents were analyzed using ICP-AES. Determination of C, H, and N content was determined by LECO CHNS-932 element analyzer.

^{1}H and ^{13}C Nuclear Magnetic Resonance (Solution NMR)

^{1}H and ^{13}C liquid NMR is a powerful tool to characterize the organic part of digested MOFs. Hence, it is mainly used after PSM to determine the post-functionalization yield. Solution NMR were recorded on Bruker Avance 300 spectrometer (300 MHz for ^{1}H NMR) using a solution prepared by digesting 7 mg of sample in mixture of d_6-DMSO (500 µL) and dilute DCl (100 µL, 35% DCl).

Solid state nuclear magnetic resonance (^{13}C CP/MAS NMR)

All ^{13}C CP/MAS spectra were recorded on a Bruker AVANCE-400 (DRX) NMR spectrometer operating at 100 MHz for carbon, using 7 mm CP/MAS Bruker double-bearing probes. All samples were finely ground before packing in the rotors. Rotors were spun at rates 9 kHz and the ^{13}C CP/MAS spectra were recorded using a proton 90° pulse length of 4.0 μs, 1 ms contact time and recycle time of 20 s.

N_2 physisorption

The apparent BET surface areas and the microporous volumes were obtained by N_2 adsorption at 77 K. Nitrogen adsorption-desorption isotherms were recorded at -196 ºC using a Gemini V 2.00 instrument model 2380. The materials were degassed overnight at 150 ºC to an ultimate pressure of 1024 mbar and then cooled to room temperature prior to adsorption.

X-ray photoelectron spectroscopy

The chemical state of the elements was analyzed by X-ray photoelectron spectroscopy (XPS, CEMUP – LAS Kratos Axis Ultra HSA) with an operating power of 90W and an Al Kα excitation source.

Gas Chromatography/Mass spectroscopy (GC/MS)

GC-MS analyses were performed using a Trace gas chromatograph (2000 series) equipped with a Thermo Scientific DSQ II mass spectrometer (Waltham, MA). Separation of compounds was carried out in a DB-1 J&W capillary column (30 m x 0.32 mm inner diameter, 0.25 μm film thickness) using helium as the carrier gas (35 cm s^{-1}). The chromatographic conditions were as follows: initial temperature, 80°C for 5 min; temperature rate, 4°C min-1 up to 285°C, which was maintained for 10 min; injector temperature, 250°C; transfer-line temperature, 290°C; split ratio, 1:50. The mass spectrometer was operated in the electron impact (EI) mode with energy of 70 eV, and data were collected at a rate of 1 scan s^{-1} over a range of m/z 33–750. The ion source was kept at 250°C.

Photoluminescence spectroscopy

The photoluminescence spectra in the visible and NIR spectral ranges were recorded at

room temperature with a modular double grating excitation spectrofluorimeter with a TRIAX 320 emission monochromator (Fluorolog-3, Horiba Scientific) coupled to a R928 and H9170 Hamamatsu photomultipliers, respectively, using a front face acquisition mode. The excitation source was a 450 W Xe arc lamp. The emission spectra were corrected for detection and optical spectral response of the spectrofluorimeter and the excitation spectra were corrected for the spectral distribution of the lamp intensity using a photodiode reference detector. The absolute emission quantum yields were measured at room temperature using a quantum yield measurement system C9920-02 from Hamamatsu with a 150 W Xenon lamp coupled to a monochromator for wavelength discrimination, an integrating sphere as sample chamber and a multi channel analyzer for signal detection. Three measurements were taken for each sample and the average value is reported. The method is accurate to within 10 %.

Magnetic measurements

Magnetic measurements were carried out with an SVSM Quantum Design SQUID magnetometer in the – 7 to + 7T and 1.8 K to 300 K ranges. Milligrams of powder samples were put in a gel cap. The magnetic susceptibility data were recorded applying a static magnetic field of 5000 Oe. All data were corrected from intrinsic diamagnetic contributions of the samples and that of the gel cap holder.

DFT calculations

Calculations were performed at the density functional theory (DFT) level with Gaussian09,[1] using the B3LYP functional and the 6-311++G(d,p) basis set on the C, H, N, O and Cl atoms and the LanL2DZ basis set (comprising an effective core potential) on La. The molecular model was composed of a deprotonated ethyl 2-oxo-2-(phenylamino)acetate anion, coordinated to an La^{+} cation (via the amino nitrogen and the acetate carbonyl) surrounded by four H_2O molecules, one Cl^{-} and one OH^{-} anion. Distinct conformations were geometry optimized with tight convergence criteria prior to the calculation of the corresponding vibration frequencies, which were then scaled by a factor of 0.9. Simulation of the spectra was performed using lorentzian profiles with FWHM of 20 cm^{-1}. All calculations were performed in the gas-phase.

Chapter III.2: Synthesis and Post-Synthetic Modification

- Synthesis of IRMOF-3
- Post-Synthetic Modification of IRMOF-3
- Complexation with lanthanides
- Synthesis of NH_2-MIL-125
- Post-Synthetic Modification of NH_2-MIL-125
- Adsorption and photocatalytic activity
- Recyclability test
- Optical properties of NH_2-MIL-125, MIL-125-AC, Cr-MIL-125-AC and Ag-MIL-125-AC

Synthesis of IRMOF-3

$Zn(NO_3)_2.6H_2O$ (1.795 g, 6 mmol) and 2-aminoterephthalic acid (0.37 g, 2 mmol) were dissolved in *N*,*N*-dimethylformamide (DMF, 50 mL) at room temperature. The obtained solution was sealed and placed in the oven at 100°C for 18 h. The obtained crystals were separated, washed with DMF (three times), chloroform (three times), then immersed into chloroform over night to remove DMF guest molecules from IRMOF-3, and finally stored under chloroform.

Post-synthetic modification of IRMOF-3

Synthesis of IRMOF-3-AC

A toluene solution of pentane-2,4-dione (0.6 mL, 6 mmol) was added dropwise at room temperature to IRMOF-3 (1.0 g, 3.3 mmol equiv of $–NH_2$) dispersed in toluene (15 mL), being the resulting mixture sealed and kept for 1 day at 60°C. The crystals were then washed with fresh toluene three times and finally stored under toluene.

Synthesis of IRMOF-3-OL

A $CHCl_3$ solution (15 mL) of 3-(2-hydroxyphenyl)-3-oxopropanal (656 mg, 4 mmol) was added dropwise at room temperature to IRMOF-3 (1.0 g, 3.3 mmol equiv of $–NH_2$) dispersed in $CHCl_3$ (15 mL), being the mixture refluxed for 2 days. The crystals were then washed with fresh $CHCl_3$ three times and finally stored under $CHCl_3$.

Synthesis of IRMOF-3-EOC

IRMOF-3 (1.0 g, 3.3 mmol equiv of $–NH_2$) was dispersed in $CHCl_3$ (15 mL). To this mixture, a solution of ethyl oxalyl monochloride (EOC) (0.67 mL, 6 mmol) and triethylamine (1.4 mL, 10 mmol) was dropwise added at room temperature, and the mixture was kept for 2 day at 40 °C. The crystals were then washed with fresh $CHCl_3$ three times and finally stored under $CHCl_3$.

Synthesis of IRMOF-3-EAA

IRMOF-3 (1.0 g, 3.3 mmol equiv of $–NH_2$) was dispersed in toluene (15 mL). To this mixture, a solution of ethyl acetoacetate (0.8 mL, 6 mmol) was dropwise added at room temperature, and the mixture was sealed and kept for 1 day at 80°C. The crystals were then washed with fresh toluene three times and finally stored under toluene.

Synthesis of IRMOF-3-CA

Freshly prepared IRMOF-3 (1.0 g, 3.3 mmol equiv of $–NH_2$) was dispersed in $CHCl_3$ (15 mL). To this mixture, a solution of chloroacetic acid (0.945 g, 10 mmol) and triethylamine (1 mL, 10 mmol) in $CHCl_3$ (15 mL) was dropwise added at room temperature, and the mixture was kept for 48h. The crystals were then washed with fresh $CHCl_3$ three times and finally stored under $CHCl_3$.

Synthesis of IRMOF-3-Gl

IRMOF-3 (1.0 g, 3.3 mmol equiv of $–NH_2$) was dispersed in CH_3CN (15 mL). To this mixture, a solution of glyoxylic acid monohydrate (0.61 g, 6.6 mmol) in CH_3CN (15 mL) was dropwise added at room temperature, and the mixture was sealed and kept for 48h at room temperature . The crystals were then washed with fresh CH_3CN three times and finally stored under CH_3CN.

Synthesis of IRMOF-3-Gl-R

Reductive amination using sodium triacetoxyborohydride was done by dispersing a sample IRMOF-3-GL (1.2 g) in a vial containing CH_3CN (15 mL). To this mixture, a solution of sodium triacetoxyborohydride (0.250 g, 1 mmol) in CH_3CN (15 mL) was dropwise added at room temperature, and the mixture was heated for 24h at 60 °C. The sample was washed twice with CH_3CN and dried in air.

Synthesis of IRMOF-3-EM

A toluene solution of diethyl (ethoxymethylene)malonate (0.6 mL, 6 mmol) was added dropwise at room temperature to IRMOF-3 (1.0 g, 3.3 mmol equiv of $–NH_2$) dispersed in toluene (15 mL), being the resulting mixture sealed and kept for 24 h at 80°C. The crystals were then washed with fresh toluene three times and exchange the solvent with chloroform, finally stored under chloroform.

Synthesis of IRMOF-3-MVK

Crystals of IRMOF-3 (1.0 g, 3.3 mmol equiv of $–NH_2$) were transferred inside the conical filter paper of the apparatus tube. Methyl vinyl ketone (MVK) (10 mL) was introduced with the help of a syringe on the bottom of the vessel avoiding any direct contact with the MOF. The system was heated overnight at 200 °C. The yellow crystals were washed three

times and then soaked in chloroform overnight to remove the excess MVK. The product was stored in fresh chloroform.

Complexation with lanthanides

Synthesis of Nd-IRMOF-3-AC

A DMSO (15 mL) solution of $NdCl_3.6H_2O$ (250 mg, 1 mmol) was added dropwise at room temperature to IRMOF-3-AC (340 mg, 1 mmol) dispersed in toluene (15 mL), being the resulting mixture stand for 3 days. The sample was washed twice with toluene and dried in air.

Synthesis of Nd-IRMOF-3-OL

An ethanolic solution (15 mL) of $NdCl_3.6H_2O$ (250 mg, 1 mmol) was added dropwise at room temperature to IRMOF-3-OL (420 mg, 1 mmol) dispersed in $CHCl_3$ (15 mL), being the resulting mixture stand for 3 days at room temperature. The sample was washed twice with $CHCl_3$ then washed with ethanol 3 times and dried in air.

Synthesis of Nd-Y-IRMOF-3-OL

An ethanolic solution (15 mL) of $NdCl_3.6H_2O$ (12.5 mg, 0.05 mmol) and YCl_3 (185.25 mg, 0.95 mmol) was dropwise added at room temperature to IRMOF-3-OL (420 mg, 1 mmol) dispersed in $CHCl_3$ (15 mL), being the resulting mixture stand for 3 days at room temperature. The sample was washed twice with $CHCl_3$ then washed with ethanol 3 times and dried in air.

Synthesis of Ln-IRMOF-3-EAA

A sample IRMOF-3-EAA (3.10 g, 3 mmol) was dispersed in three vials containing toluene (15 mL). To each portion this mixture, a solution of $EuCl_3.6H_2O$ (0.366 g, 1 mmol) or $TbCl_3.6H_2O$ (0.373 g, 1 mmol) or $NdCl_3.6H_2O$ (0.250 g, 1 mmol) in DMSO (15 mL) was dropwise added at room temperature, and the mixture was stand for 3 days. The sample was washed twice with toluene and dried in air.

Synthesis of Ln-IRMOF-3-EOC

A sample IRMOF-3-EOC (3.35 g, 3 mmol) was dispersed in three vials containing $CHCl_3$ (15 mL). To each portion of this mixture, a solution of $EuCl_3.6H_2O$ (0.366 g, 1 mmol) or

$TbCl_3.6H_2O$ (0.373 g, 1 mmol) or $NdCl_3.6H_2O$ (0.250 g, 1 mmol) in C_2H_5OH (15 mL) was dropwise added at room temperature, and the mixture was stand for 3 days. The sample was washed twice with CHCl3 and dried in air.

Synthesis of Ln-IRMOF-3-CA

A sample IRMOF-3-CA (1.2 g) was divided in two vials, each vial containing $CHCl_3$ (15 mL). To this mixture, a solution of $NdCl_3.6H_2O$ (0.250 g, 1 mmol) in C_2H_5OH (15 mL) or a solution of $EuCl_3.6H_2O$ (0.366 g, 1 mmol) in C_2H_5OH (15 mL) was dropwise added at room temperature, and the mixture was stand for 3 days. The sample was washed twice with $CHCl_3$ and dried in air.

Synthesis of Ln-IRMOF-3-GL

A sample IRMOF-3-GL (1.2 g) was dispersed in four vials containing CH_3CN (15 mL). To this mixture, a solution of $NdCl_3.6H_2O$ (0.250 g, 1 mmol) in C_2H_5OH (15 mL) or $EuCl_3.6H_2O$ (0.366 g, 1 mmol) in C_2H_5OH (15 mL) was dropwise added at room temperature, and the mixture was stand for 3 days. The sample was washed twice with CH_3CN and dried in air.

Synthesis of Ln-IRMOF-3-EM

A DMSO (15 mL) solution of $LnCl_3.6H_2O$ (250 mg, 1 mmol) [Ln= Eu, Nd] was added dropwise at room temperature to IRMOF-3-EM (340 mg, 1 mmol) dispersed in DMSO (15 mL), being the resulting mixture stand for 3 days. The sample was washed twice with DMSO and exchange with chloroform to remove the DMSO molecules from the pores of MOFs, and then dried in air.

Synthesis of Ln-IRMOF-3-MVK

A DMSO solution (15 mL) of $LnCl_3.6H_2O$ (250 mg, 1 mmol) [Ln= Eu, Nd] was added dropwise at room temperature to IRMOF-3-MVK (420 mg, 1 mmol) dispersed in DMSO (15 mL), being the resulting mixture stand for 3 days at room temperature. The sample was washed twice with DMSO then washed with chloroform 3 times and dried in air.

Synthesis of NH_2-MIL-125

This material was synthesized according to the method reported previously.[2] Titanium isopropoxide (1 mL, 3.38 mmol) and 2-aminoterephthalic acid (1 g, 5.5 mmol) were dissolved in a mixture of *N*,*N*-dimethylformamide (DMF, 50 ml) and methanol (25 ml) at room temperature. The obtained slurry was sealed and placed in the oven at 150 °C for 20 h. Finally, a light yellow product was obtained. The product was filtered off, and washed by DMF to remove the unreacted organic ligand, and then washed again with methanol to exchange DMF.

Post-synthetic modification of NH_2-MIL-125

A light yellow powder of NH_2-MIL-125 (400 mg, 0.22 mmol) was transferred inside the conical filter paper of the apparatus tube. Acetylacetone (5 mL) was introduced with the help of a syringe on the bottom of the vessel avoiding any direct contact with the MOF. The system was heated overnight at 200 °C. The dark yellow powder were washed three times and then soaked in methanol overnight to remove the excess acetyacetone.

Synthesis of Cr-MIL-125-AC

MIL-125-AC-Cr was prepared by stirring dry MIL-125-AC-2 (250 mg, 0.125 mmol) with $CrCl_2$ (15 mg, 0.125 mmol) in dry ethanol (15 mL) for 24 h under a nitrogen atmosphere. The green yellow-colored solid was formed, then filtered, dried in air at 120 °C, and washed with ethanol five times to remove any unreacted chromium species and dried in air at 120 °C.

Synthesis of Ag-MIL-125-AC

CH_3COOAg (20 mg, 0.125 mmol) was added to a mixture of CH_3CN (10 mL) and water (2.5 mL), then the solution was added to a suspension of MIL-125-AC-2 (250 mg, 0.125 mmol) in CH_3CN (10 mL), and stirring for 24 h at room temperature. The product solid was filtered, dried in air at 120 °C, and washed with CH_3CN five times to remove any unreacted silver species and washed with ethanol several times, then dried in air at 120 °C.

Adsorption and photocatalytic activity

The photocatalytic degradation of methylene blue (MB) was performed in a stirred pyrex reactor filled with MB aqueous solution (150 ml, 20 ppm of MB). The catalyst (60 mg/L)

was loaded in the reactor equipped with Philips 100W equivalent daylight lamp as the light source. The light intensity of the lamp is approximately 0.303 W m^{-2} in the λ range of 315-400 nm, and 325 W m^{-2} in the λ range of 400-1050 nm. The light intensity was measured with DELTA OHM - HD 2302.0 - Photo-Radiometer. The distance between the light source and the beaker containing reaction mixture was fixed at 15 cm. The pH value of the suspension was adjusted to neutral (pH = 7.0). All of the photocatalytic experiments were carried out after the adsorption of MB in the dark for 30 min under stirring. Under ambient conditions and rigorous stirring, the reactor was exposed to the light irradiation. A sample solution (3 mL) was taken at certain time intervals during the experiment and centrifuged to remove the catalyst completely. The solution was analyzed by measuring the absorption intensity at its maximum absorbance wavelength of λ= 664 nm on a UV-vis spectrophotometer (JASCO Co., USA). The solution was analyzed on a UV-vis spectrophotometer (JASCO Co., USA). The MB degradation percentages $(1-C/C_0)*100\%$ are plotted with time (C is the concentration of MB in solution at each irradiation time interval, while C_0 is the initial concentration). For a comparison of adsorption with photodegradation, MB adsorption in the dark was carried out with the same procedure as the photocatalytic experiments described above, but in the absence of light. The percentage removal by adsorption is reported as $(1-C/C_0)*100\%$ with time. For a comparison of our samples with commercial samples, hombikat UV-100, a commercial hombikat UV 100 photocatalyst powder (DE), anatase nanopowder, with a declared primary crystal size <10 nm, and specific surface area >250 m^2g^{-1}, and a commercial TiO_2 photocatalyst were tested for its adsorptivity and photocatalytic degradation of MB using the same procedure and conditions given above. The MB adsorption kinetic data and the MB degradation kinetic data were fitted by a pseudo-second-order model and the Lagergren pseudo first-order model respectively. The Lagergren pseudo first-order model and the pseudo-second-order model can be described by the equations (1) and (2), respectively.[3]

$$\mathrm{Log}\,(q_t - q_e) = \log q_e - \frac{k_1}{2.303}t \qquad (1)$$

Where t is time in min, q_t the amount of MB degraded at t in mg/g, q_e the amount of MB degraded at equilibrium in mg/g, and k_1 the first-order rate constant in min^{-1}.

We can obtain k_1 by applying MB photodegradation kinetics data to equation (1). The correlation coefficients r_{12}, values and standard errors (SE) of the fit were extracted.

$$\frac{t}{q_t} = \frac{1}{q_2^2 k_2} + \frac{1}{q_2}t \qquad (2)$$

Where *t* is time in min, q_t the amount of MB adsorbed at *t* in mg/g,q_2 the amount of MB adsorbed at equilibrium in mg/g, and k_2 the pseudo-second-order rate constant in min.g/mg.

We can obtain k_2 and q_2 by applying MB adsorption kinetics data in the dark to equation (2). The correlation coefficients r_{22}, values and standard errors (SE) of the fit were also extracted.

The quantum yield (ϕ) was calculated by the equation (3):

$$\emptyset = \frac{N_{cpr}}{N_{aph}} \qquad (3)$$

Where N_{cpr} is the rate of converted probe material, N_{aph} is the amount of photon energy absorbed by the photocatalyst.[4]

Recyclability test

Proving the stability of the catalyst, five cycles test is carried out. Ag-MIL-125-AC (60 mg/L) was suspended in water (150 mL) with methylene blue (20 ppm). The experiment was exposed to light for 30 min. After each cycle, the photocatalyst was centrifuged, separated, washed with ethanol and dried at 75 °C.

Optical properties of NH_2-MIL-125, MIL-125-AC, Cr-MIL-125-AC and Ag-MIL-125-AC

Optical spectra of the samples, and afterwards their E_g, were acquired on a JASCO UV 3100 spectrometer, in the UV-Vis range (250-700 nm), with 0.2 nm in step-size, and using $BaSO_4$ as reference. The Kubelka-Munk function was applied with the aim to convert the diffuse reflectance into the absorption coefficient α:

$$\alpha \approx \frac{K}{S} = \frac{(1-R_\infty)^2}{2R_\infty} \equiv F(R_\infty) \qquad (3)$$

where K and S are the absorption and scattering coefficients; the reflectance R_∞ is equal to $R_{sample}/R_{standard}$.[5] The E_g of the samples was calculated using the Tauc plot. This method assumes that the absorption coefficient α (Eq. 4) of a semiconductor can be expressed as:

$$(\alpha h\upsilon)^\gamma = A(h\upsilon - E_g) \qquad (4)$$

where A is a material constant, h is the Plank's constant, ν is the frequency of the light, E_g is the energy band gap of allowed transitions, and the power coefficient γ is characteristic of the type of transition. For nanoscale semiconductor materials, this value is accepted to

be equal to ½, since for such materials, the transition is assumed to be indirectly allowed.[6] Hence, plotting $[F(R_\infty)h\nu]^{0.5}$ against hν, one can obtain the energy band gap of the semiconductor material from the x-axis (α = 0) intercept of the line tangent to the inflection point of the curve. This was found by fitting the transformed Kubelka-Munk equation $[F(R_\infty)h\nu]^{0.5}$ versus the photon energy (hν), with a sigmoidal Boltzmann function. Afterwards, the Eg value was obtained from the x-axis intercept of the line tangent to the inflection point of that curve.

References

[1] Gaussian 09, Revision A.02, Frisch, M. J.; Trucks, G. W.; Schlegel, H. B.; Scuseria, G. E.; Robb, M. A.; Cheeseman, J. R.; Scalmani, G.; Barone, V.; Mennucci, B.; Petersson, G. A.; Nakatsuji, H.; Caricato, M.; Li, X.; Hratchian, H. P.; Izmaylov, A. F.; Bloino, J.; Zheng, G.; Sonnenberg, J. L.; Hada, M.; Ehara, M.; Toyota, K.; Fukuda, R.; Hasegawa, J.; Ishida, M.; Nakajima, T.; Honda, Y.; Kitao, O.; Nakai, H.; Vreven, T.; Montgomery, J. A., Jr.; Peralta, J. E.; Ogliaro, F.; Bearpark, M.; Heyd, J. J.; Brothers, E.; Kudin, K. N.; Staroverov, V. N.; Kobayashi, R.; Normand, J.; Raghavachari, K.; Rendell, A.; Burant, J. C.; Iyengar, S. S.; Tomasi, J.; Cossi, M.; Rega, N.; Millam, N. J.; Klene, M.; Knox, J. E.; Cross, J. B.; Bakken, V.; Adamo, C.; Jaramillo, J.; Gomperts, R.; Stratmann, R. E.; Yazyev, O.; Austin, A. J.; Cammi, R.; Pomelli, C.; Ochterski, J. W.; Martin, R. L.; Morokuma, K.; Zakrzewski, V. G.; Voth, G. A.; Salvador, P.; Dannenberg, J. J.; Dapprich, S.; Daniels, A. D.; Farkas, Ö.; Foresman, J. B.; Ortiz, J. V.; Cioslowski, J.; Fox, D. J. Gaussian, Inc., Wallingford CT, 20

[2] a) M. Dan-Hardi, C. Serre, T. Frot, L. Rozes, G. Maurin, C. Sanchez, G. Férey *J. Am. Chem. Soc*. 2009, **131**, 10857-10859. b) Y. Fu, D. Sun, Y. Chen, R. Huang, Z. Ding, X. Fu, Z. Li *Angew. Chem. Int. Ed.* 2012, **51**, 3364 –3367.

[3] a)Y. S. Ho, G. McKay *Chem. Eng. J.* 1998, **70**, 115–124.; b) A. S. Marfunin, *Physics of minerals and inorganic materials: an introduction*, Springer, Berlin, **1979**.

[4] H. Joo, *korean J. Chem. Eng.* **2006**, *23*, 931-934.

[5] N. Serpone, D. Lawless, R. Khairutdinov *J. Phys. Chem.* 1995, **99**, 16646-16654.

[6] A. Houas, H. Lachheb, M. Ksibi, E. Elaloui, C. Guillard, J.-M. Herrmann, *Appl. Catal. B: Environ.* 2001, **31**, 145–157.

Part IV: Conclusion and future work

- Conclusion
- Future work

Conclusions

The main goal of my scientific work has been to explore the potential of post-synthetic modification of nanoporous metal-organic frameworks as a new route for engineering light-emitting lanthanide (Ln) centres into organic-inorganic hybrid materials. Indeed, a distinct advantage of metal-organic frameworks is the possibility of post-synthetic covalent modification of the channel walls with suitable molecular species able to coordinate Ln^{3+} ions. I have shown that a judicious choice of these molecular entities allows boosting the emission properties of Ln^{3+} ions. In parallel, I have also explored the potential of post-synthetic modification for carrying out new types of organic reactions taking place in the constrained nanoreactors (nanochannels).

A successful post-synthetic covalent modification of the metal-organic framework IRMOF-3 amino group with pentane-2,4-dione and 3-(2-hydroxyphenyl)-3-oxopropanal, followed by the coordination of Nd^{3+}/Y^{3+}, was accomplished. The photoluminescence studies show that this method affords unusual near-infrared light-emitting materials. Next, IRMOF-3 was also post-synthetically modified by reaction with 1,2- and 1,3-dicarbonyl compounds. The introduced chelating fragments protruding into the micropores readily coordinate the Ln^3 ions, yielding also near-infrared and visible-light emitters. The post-synthetic modification of metal-organic frameworks is, thus, a promising method for engineering luminescence centers into hybrid materials.

The magnetic properties of the six MOFs [Ln-IRMOF-3-EOC, Ln-IRMOF-3-EAA, Ln = Eu, Tb, Nd] containing paramagnetic Ln^{3+} were investigated. Their behavior is typical of the rare-earth ions present in the structure. The temperature variation of the magnetic susceptibility of the Eu^{3+} derivatives Eu-IRMOF-3-EAA and Eu-IRMOF-3-EOC was fit with appropriate analytical relations. Refined values of the spin-orbit coupling are consistent with the energies of the electronic levels deduced from the photoluminescence spectra. The behaviou of the neodymium-based compounds, Nd-IRMOF-3-EAA and Nd-IRMOF-3-EOC, agrees with that of Nd^{3+} ions in the $^4I_{9/2}$ ground state. Below 80 K, the magnetic susceptibility shifts from the Curie-Weiss law due to the effect of crystal field splitting of the ground state to five Kramers doublets. The splitting value can be roughly evaluated by using the expression of the susceptibility known for the free ions in an axial symmetry. The magnetic susceptibility of Tb-IRMOF-3-EAA was fit as well. Yet, Tb-

IRMOF-3-EOC exhibits a peculiar magnetic behavior, which differs drastically from that of isolated Ln^{3+} ions as observed for the five other analogues.

In order to confirm the validity of my conclusions, I have extended the post-synthetic modification of metal-organic frameworks to a broader range of materials by covalently modifying the IRMOF-3 amino group with glyoxylic acid, 2-chloroacetic acid, diethyl (ethoxymethylene)malonate and methyl vinyl ketone (vapour), followed by the coordination to Ln^{3+} ions (Eu^{3+}, Tb^{3+} and Nd^{3+}). Once again, I have successfully developed lanthanide-organic framework emitting in the visible and near infrared.

On a separate line of research, the post-synthetic modification of Ti-bearing MOFs was shown to be a very promising route for designing and preparing efficient photocatalysts. For this purpose, NH_2-MIL-125 was successfully modified by the reaction with acetyl acetone vapour and subsequently doped with Cr^{3+} ions, acting as hole acceptors, or with Ag nanoparticles, acting as electron acceptors. The chelating fragments introduced by post-synthetic modification readily coordinate the Cr^{3+} ions. Alternatively, they enable the formation of Ag nanoparticles. The resultant materials are efficient photocatalysts in the methylene blue degradation.

Future work

It is clear that much work is needed to fully understand many of the fundamental aspects governing the referred unique chemical transformations. Further development of new post-synthetic modified metal-organic frameworks will establish whether or not these materials are the founders of a promising field of research. In my view, some of the future work must be concentrated on:

i) Developing simpler and more efficient synthetic methods of preparing metal-organic frameworks exhibiting large channels, based on aromatic carboxylates (or other linkers) with rigid and larger carbon skeletons. These materials would be useful for organizing large macromolecules - biomolecules, enzymes, proteins, polymers, and nanoparticles;

ii) Introducing a variety of building units such as chiral organocatalytic centres into a the crystalline solids by post-synthetic modification of known metal-organic frameworks for applications in asymmetric organic reactions;

iii) Using the modified metal-organic frameworks to trap and remove chemical and biological pollutants from non-potable water (smart water filters);

iv) Increasing the efficiency of the metal-organic frameworks-photocatalysts by immobilizing Bodipys;

v) Developing the encapsulation of metal-metal oxide-bimetallic nanoparticles in MOFs to increase the photocatalytic activity towards oxidation-[3+2] cycloaddition reactions.

Appendices

Table A1 Elemental analysis of IRMOF-3-AC, IRMOF-3-OL, Nd-IRMOF-3-AC, Nd-IRMOF-3-OL and Nd-Y-IRMOF-3-OL (%).

Sample	Metal & chloride ratio*				S	C	H	N
	Zn	Nd	Y	Cl				
IRMOF-3-AC $[Zn_4C_{30.9}H_{23.28}N_3O_{14.38}]=[Zn_4O(C_{13}H_{11}NO_5)_{1.38}(C_8H_5NO_4)_{1.62}]$	100	-	-	-	-	41.30 (39.98)	2.81 (2.53)	4.63 (4.53)
Nd-IRMOF-3-AC $[Zn_4C_{44.7}H_{63.3}Cl_{2.76}N_3Nd_{1.38}O_{21.28}S_{6.9}]=[Zn_4O(C_{23}H_{40}NO_{10}S_5NdCl_2)_{1.38}(C_8H_5NO_4)_{1.62}]$	49.14 ±3.43	33.92 ±2.88	-	16.94 ±1.78	12.60 (12.55)	30.55 (30.46)	3.58 (3.62)	2.41 (2.38)
IRMOF-3-OL $[Zn_4C_{48.3}H_{31.2}N_3O_{18.4}]=[Zn_4O(C_{17}H_{11}NO_6)_{2.7}(C_8H_5NO_4)_{0.3}]$	100	-	-	-	-	48.03 (47.96)	2.71 (2.60)	3.56 (3.47)
Nd-IRMOF-3-OL $[Zn_4C_{48.3}H_{25.8}N_3Nd_{0.9}O_{18.4}] = [Zn_4O(C_{17}H_9NO_6)_{2.7}Nd_{0.9}(C_8H_5NO_4)_{0.3}]$	81.63 ±2.13	18.36 ±1.12	-	-	-	43.85 (43.49)	2.10 (1.95)	3.34 (3.15)
Nd-Y-IRMOF-3-OL $[Zn_4C_{48.3}H_{25.8}N_3Nd_{0.05}Y_{0.85}O_{18.4}]=[Zn_4O(C_{17}H_9NO_6)_{2.7}Nd_{0.05}Y_{0.85}(C_8H_5NO_4)_{0.3}]$	81.64 ±2.13	1.02 ±0.20	17.34 ±1.12	-	-	45.21 (45.08)	2.05 (2.02)	3.25 (3.27)

*The percentage calculated from EDS and the results are expressed as mean ±SD for determination of 10 crystals. C, H, N percentages were measured for 3 samples and calculated value between brackets.

Table A2 Elemental analysis of IRMOF-3-EAA; IRMOF-3-EOC; Ln-IRMOF-3-EAA and Ln-IRMOF-3-EOC (Ln = Nd, Eu, Tb) (%)

Sample	Metal & chloride ratio*					S	C	H	N
	Zn	Nd	Eu	Tb	Cl				
IRMOF-3-EAA $Zn_4C_{35.7}H_{30.6}N_3O_{16.9}$ = $[Zn_4O(C_{14}H_{13}NO_6)_{1.95}(C_8H_5NO_4)_{1.05}]$	100	-	-	-	-	-	41.75 (41.49)	3.02 (2.98)	4.11 (4.07)
Nd-IRMOF-3-EAA $Zn_4C_{47.4}H_{63.75}Cl_{3.9}N_3Nd_{1.95}O_{22.75}S_{5.85}$= $[Zn_4O(C_{20}H_{30}NO_9S_3NdCl_2)_{1.95}(C_8H_5NO_4)_{1.05}]$	40.62 ±1.61	19.79 ±2.52	-	-	39.59 ±3.12	9.41 (9.83)	30.91 (29.83)	3.80 (3.37)	2.21 (2.20)
Eu-IRMOF-3-EAA $Zn_4C_{47.4}H_{63.75}Cl_{3.9}Eu_{1.95}N_3O_{22.75}S_{5.85}$= $[Zn_4O(C_{20}H_{30}NO_9S_3EuCl_2)_{1.95}(C_8H_5NO_4)_{1.05}]$	39.97 ±1.79	-	20.03 ±2.11	-	40.00 ±2.52	9.33 (9.75)	30.61 (29.60)	3.78 (3.34)	2.11 (2.18)
Tb-IRMOF-3-EAA $Zn_4C_{47.4}H_{63.75}Cl_{3.9}N_3O_{22.75}S_{5.85}Tb_{1.95}$= $[Zn_4O(C_{20}H_{30}NO_9S_3TbCl_2)_{1.95}(C_8H_5NO_4)_{1.05}]$	41.01 ±2.19	-	-	19.93 ±3.01	39.06 ±1.96	9.79 (9.68)	30.52 (29.39)	3.81 (3.32)	2.05 (2.17)
IRMOF-3-EOC $Zn_4C_{36}H_{27}N_3O_{22}$ = $[Zn_4O(C_{12}H_9NO_7)_3]$	100	-	-	-	-	-	39.12 (38.77)	2.51 (2.44)	3.72 (3.77)
Nd-IRMOF-3-EOC $Zn_4C_{36}H_{51}Cl_3N_3Nd_3O_{37}$= $[Zn_4O(C_{12}H_{17}NO_{12}NdCl)_3]$	39.80 ±1.81	30.04 ±2.71	-	-	30.16 ±1.91	-	22.62 (22.54)	2.81 (2.68)	2.16 (2.19)
Eu- IRMOF-3-EOC $Zn_4C_{36}H_{51}Cl_3Eu_3N_3O_{37}$= $[Zn_4O(C_{12}H_{17}NO_{12}EuCl)_3]$	40.06 ±2.61	-	29.91 ±2.11	-	30.03 ±2.31	-	21.28 (22.27)	2.69 (2.65)	2.14 (2.16)
Tb-IRMOF-3-EOC $Zn_4C_{36}H_{51}Cl_3N_3O_{37}Tb_3$= $[Zn_4O(C_{12}H_{17}NO_{12}TbCl)_3]$	40.15 ±1.71	-	-	29.93 ±2.01	29.92 ±1.31	-	22.06 (22.03)	2.75 (2.62)	2.12 (2.14)

*the percentage calculated from EDS and the results are expressed as mean ±SD for determination of 10 crystals. C, H, N percentages were measured for 3 samples and calculated value between brackets.

Table A3 Elemental analysis of IRMOF-3-CA, IRMOF-3-CA-Nd, IRMOF-3-CA-Eu, IRMOF-3-Gl, IRMOF-3-Gl-Nd, IRMOF-3-Gl-Eu (%).

Sample	Metal & chloride ratio *				C	H	N
	Zn	Nd	Eu	Cl			
IRMOF-3-CA $Zn_4C_{48}H_{51}N_5O_{19}$ = $[Zn_4O(C_{10}H_7NO_6)_3.(C6H15N)_2]$	100	-	-	-	45.75 (45.63)	4.12 (4.07)	5.51 (5.54)
Nd-IRMOF-3-CA $Zn_4C_{30}H_{51}Cl_3\,Nd_3N_3O_{40}$ = $[Zn_4O(C_{10}H_{17}NO_{12}NdCl)_3]$	39.44 ±1.61	30.10 ±2.52	-	30.46 ±1.91	18.91 (19.02)	2.89 (2.71)	2.36 (2.22)
Eu-IRMOF-3-CA $Zn_4C_{30}H_{51}Cl_3\,Eu_3N_3O_{40}$ = $[Zn_4O(C_{10}H_{17}NO_{12}EuCl)_3]$	41.17 ±1.79	-	29.91 ±2.11	28.92 ±2.31	19.01 (18.79)	2.98 (2.68)	2.51 (2.19)
IRMOF-3-Gl $Zn_4C_{28.5}H_{19.5}N_3O_{19.75}$ = $[Zn_4O(C_{10}H_7NO_7)_{2.25}(C_8H_5NO_4)_{0.75}]$	100	-	-	-	35.12 (34.88)	2.21 (2.00)	4.42 (4.28)
IRMOF-3-Gl-R $Zn_4C_{28.5}H_{19.5}N_3O_{17.5}$ = $[Zn_4O(C_{10}H_7NO_6)_{2.25}(C_8H_5NO_4)_{0.75}]$	100	-	-	-	36.52 (36.20)	2.11 (2.08)	4.46 (4.44)
Nd-IRMOF-3-Gl $Zn_4C_{55.5}H_{55.5}Cl_{2.25}N_{16.5}Nd_{2.25}O_{19.75}$ = $[Zn_4O(C_{22}H_{23}N_7O_7NdCl)_{2.25}(C_8H_5NO_4)_{0.75}]$	47.03 ±2.19	26.47 ±1.66	-	26.50 ±2.35	34.56 (34.44)	2.92 (2.89)	12.01 (11.94)
Eu-IRMOF-3-Gl $Zn_4C_{55.5}H_{55.5}Cl_{2.25}Eu_{2.25}N_{16.5}O_{19.75}$= $[Zn_4O(C_{22}H_{23}N_7O_7EuCl)_{2.25}(C_8H_5NO_4)_{0.75}]$	47.53 ±3.15	-	26.20 ±1.66	26.27 ±1.05	34.20 (34.13)	2.91 (2.86)	11.88 (11.83)

*the percentage calculated from EDS and the results are expressed as mean ±SD for determination of 10 crystals. C, H, N percentages were measured for 3 samples and calculated value between brackets.

Table A4 Elemental analysis of IRMOF-3-EM; IRMOF-3-MVK; Ln-IRMOF-3-EM and Ln-IRMOF-3-MVK (Ln = Nd, Eu) (%).

Sample	Metal & chloride ratio*				S	C	H	N
	Zn	Nd	Eu	Cl				
IRMOF-3-EM $Zn_4C_{43.2}H_{39}N_3O_{22.6}$ = $[Zn_4O(C_{16}H_{15}NO_8)_{2.4}(C_8H_5NO_4)_{0.6}]$	100	-	-	-	-	43.01 (42.42)	3.32 (3.21)	3.51 (3.43)
Nd-IRMOF-3-EM $Zn_4C_{62.4}H_{96.6}Cl_{7.2}N_3Nd_{2.4}O_{32.2}S_{9.6}$= $[Zn_4O(C_{24}H_{39}NO_{12}S_4NdCl_3)_{2.4}(C_8H_5NO_4)_{0.6}]$	29.44 ±2.35	17.64 ±1.12	- -	52.92 ±4.55	12.02 (11.96)	29.30 (29.11)	3.81 (3.78)	1.59 (1.63)
Eu-IRMOF-3-EM $Zn_4C_{62.4}H_{96.6}Cl_{7.2}N_3Eu_{2.4}O_{32.2}S_{9.6}$= $[Zn_4O(C_{24}H_{39}NO_{12}S_4EuCl_3)_{2.4}(C_8H_5NO_4)_{0.6}]$	28.99 ±3.55	-	17.99 ±1.13	53.02 ±4.15	11.89 (11.87)	29.02 (28.90)	3.72 (3.75)	1.65 (1.62)
IRMOF-3-MVK $Zn_4\ C_{33.12}H_{28.68}N_3O_{15.28}$ = $[Zn_4O(C_{12}H_{11}NO_5)_{1.38}(C_{12}H_{11}NO_5)_{0.9}(C_8H_5NO_4)^{0.72}]$	100	-	-	-	-	41.62 (40.81)	3.05 (2.97)	4.09 (4.31)
Nd-IRMOF-3-MVK $Zn_4C_{55.92}H_{94.8}Cl_{4.56}N_3Nd_{2.28}O_{26.68}S_{11.4}$= $[Zn_4O(C_{22}H_{40}NS_5O_{10}NdCl_2)_{1.38}(C_{22}H_{40}NS_5O_{10}NdCl_2)_{0.9}(C_8H_5NO_4)_{0.72}]$	36.88 ±3.21	21.08 ±1.18	-	42.04 ±2.05	15.65 (15.53)	28.66 (28.54)	4.12 (4.06)	1.82 (1.79)
Eu-IRMOF-3-MVK $Zn_4C_{55.92}H_{94.8}Cl_{4.56}Eu_{2.28}N_3O_{26.68}S_{11.4}$ = $[Zn_4O(C_{22}H_{40}NS_5O_{10}EuCl_2)_{1.38}(C_{22}H_{40}NS_5O_{10}EuCl_2)_{0.9}(C_8H_5NO_4)_{0.72}]$	37.05 ±3.19	-	19.93 ±1.10	43.02 ±2.19	15.31 (15.42)	28.44 (28.32)	4.09 (4.03)	1.81 (1.77)

*the percentage calculated from EDS and the results are expressed as mean ±SD for determination of 10 crystals. C, H, N percentages were measured for 3 samples and calculated value between brackets.

Table A5 Elemental analysis of MIL-125-AC-1, MIL-125-AC-2, Cr-MIL-125-AC and Ag-MIL-125-AC

Sample	Metal ratio*				C	H	N
	Ti	Cr	Ag	Cl			
MIL-125-AC-1 $[Ti_8O_8(OH)_4(C_{10}H_7NO_5)_{2.82}(C_{11}H_9NO_4)_{3.18}]$	100	-	-	-	40.01 (39.95)	2.76 (2.78)	4.45 (4.42)
MIL-125-AC-2 $[Ti_8O_8(OH)_4(C_{13}H_{11}NO_5)_{4.2}(C_{10}H_7NO_5)_{0.72}(C_8H_5NO_4)_{1.08}]$	100	-	-	-	42.30 (41.70)	2.98 (3.01)	4.19 (4.14)
Cr-MIL-125-AC $[Ti_8O_8(OH)_4(C_{19}H_{28}NO_8CrCl)_{4.2}(C_{10}H_7NO_5)_{0.72}(C_8H_5NO_4)_{1.08}]$	49.56 ±1.52	26.01 ±1.61	-	24.43 ±2.81	36.02 (35.37)	2.54 (2.38)	3.64 (3.51)
Ag-MIL-125-AC $[Ti_8O_8(OH)_4Ag_{2.15}(C_{10}H_7NO_5)_{1.77}(C_{11}H_9NO_4)_{4.23}]$	78.81 ±0.54	-	21.18 ±0.42	-	36.02 (36.23)	2.65 (2.58)	4.01 (3.95)

*the percentage calculated from ICP analysis (repeated 3 times) and EDS (10 crystals) the results are expressed as mean ±SD. C, H, N percentages were measured for 3 samples and calculated value between brackets.

Table A6 Electronic parameters deduced from the fit of the magnetic data for the 6 compounds. Eu(III) compounds: The spin–orbit coupling of the Eu(III) ions, λ(lum), deduced from the electronic transitions implying the low-lying states in Eu-IRMOF-3-EAA and Eu-IRMOF-3-EOC taken from the photoluminescence spectra and corresponding values deduced from the fit of the susceptibility with eq. 2, λ_{mag}(HT), and that of the low temperature χT product, λ_{mag}(LT), (eq. 3). Nd(III) and Tb(III) compounds: refined values of the Zeeman factor, g, and of the zero field splitting of the Stark levels, Δ.

Compound	g	Δ /K	$\lambda_{mag}(HT)$ / K	$\chi_M(LT)$ / emu mol^{-1}	$\lambda_{mag}(HT)$ /cm^{-1}	$\lambda_{mag}(LT)$ /cm^{-1}	λ_{lum} /cm^{-1}
Eu-IRMOF-3-EAA	-	-	447	0.0065	311	321	379
Eu-IRMOF-3-EOC	-	-	497	0.0059	345	354	379
Nd-IRMOF-3-EAA	0.8	3.9					
Nd-IRMOF-3-EOC	0.8	4.1					
Tb-IRMOF-3-EAA	1.5	0.5					
Tb-IRMOF-3-EOC	-	-					

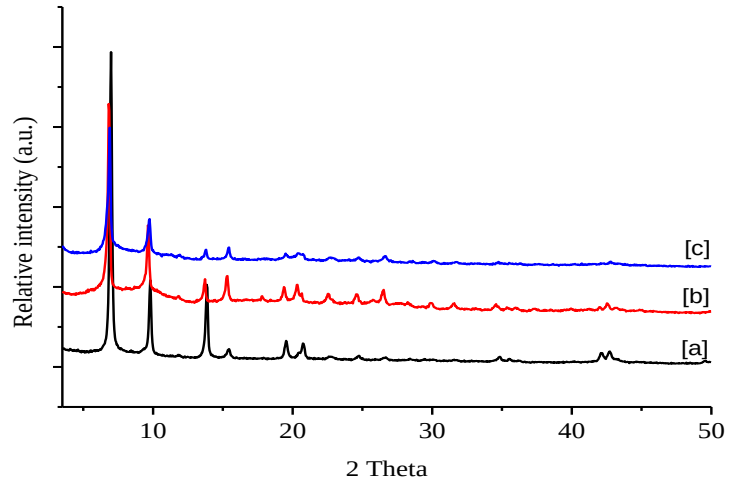

Figure A1 Powder XRD of (a) IRMOF-3; (b) IRMOF-3-AC and (c) Nd-IRMOF-3-AC.

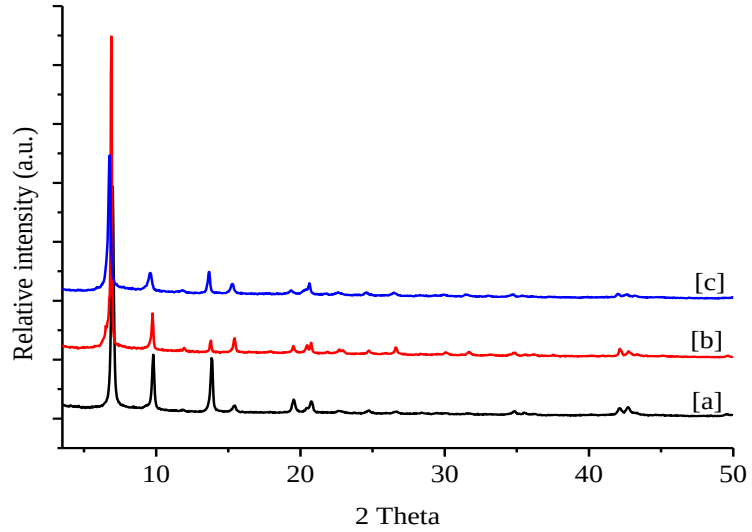

Figure A2 Powder XRD of (a) IRMOF-3; (b) IRMOF-3-OL and (c) Nd-IRMOF-3-OL

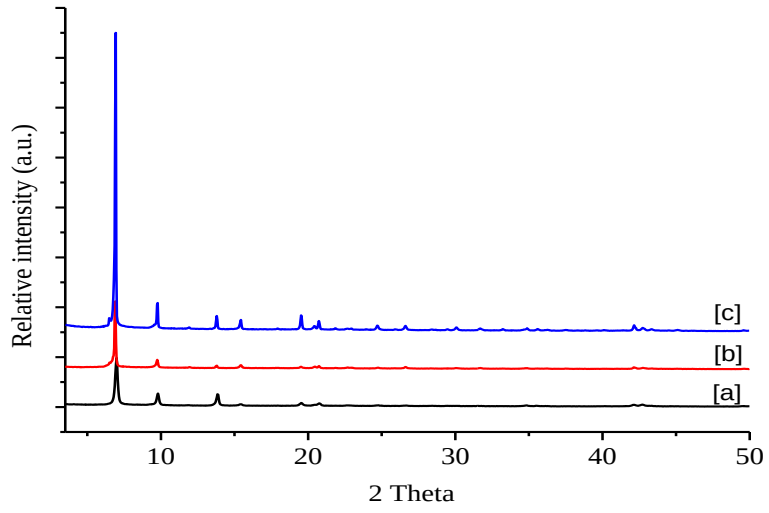

Figure A3 Powder XRD of (a) IRMOF-3; (b) IRMOF-3-OL and (c) Nd-Y-IRMOF-3-OL.

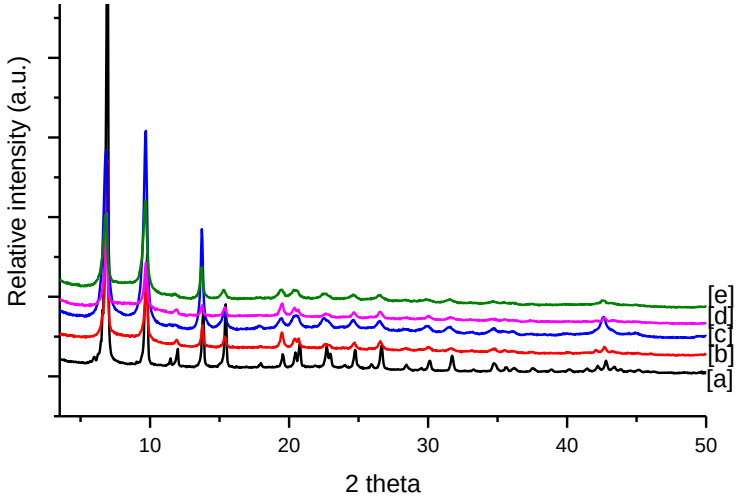

Figure A4 Powder XRD of (a) IRMOF-3; (b) IRMOF-3-EOC, (c) Nd-IRMOF-3-EOC, (d) Eu-IRMOF-3-EOC, and (e) Tb-IRMOF-3-EOC.

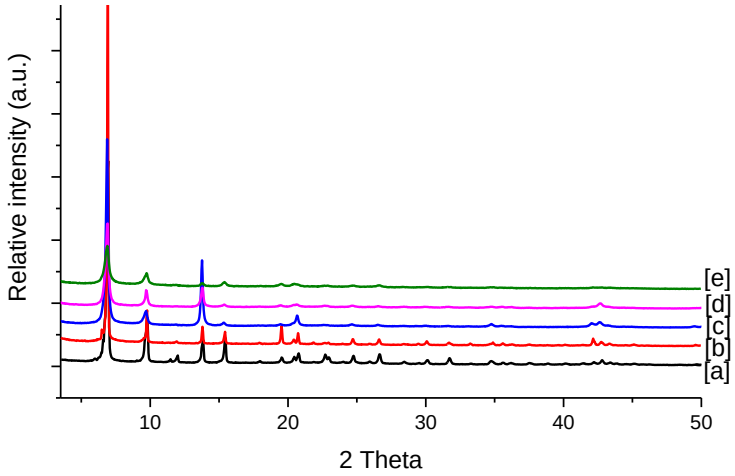

Figure A5 Powder XRD of (a) IRMOF-3, (b) IRMOF-3-EAA, (c) Nd-IRMOF-3-EAA, (d) Eu-IRMOF-3-EAA, and (e) Tb-IRMOF-3-EAA.

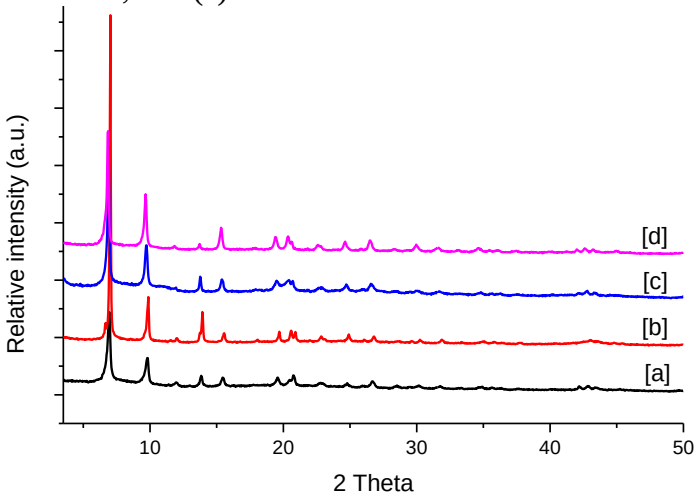

Figure A6 Powder XRD of (a) IRMOF-3; (b) IRMOF-3-CA; (c) Nd-IRMOF-3-CA and (d) Eu-IRMOF-3-CA.

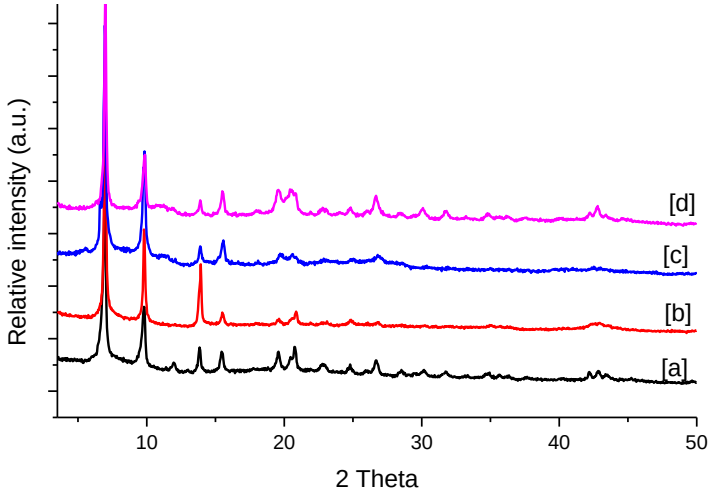

Figure A7 Powder XRD of (a) IRMOF-3, (b) IRMOF-3- GL, (c) Nd-IRMOF-3-GL and (d) Eu-IRMOF-3-GL.

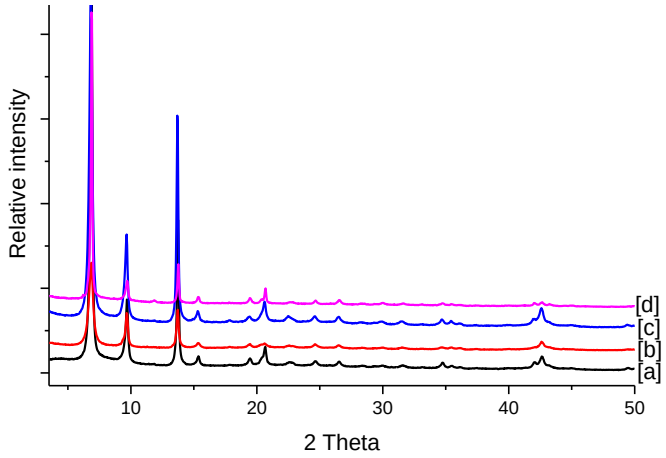

Figure A8 Powder XRD of [a] IRMOF-3, [b] IRMOF-3-MVK, [c] Eu-IRMOF-3-MVK [d] Nd-IRMOF-3-MVK

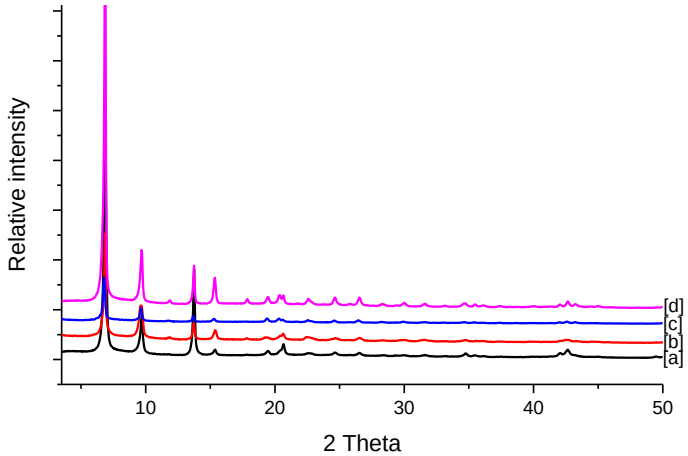

Figure A9 Powder XRD of [a] IRMOF-3, [b] IRMOF-3-EM, [c] Eu-IRMOF-3-EM [d] Tb-IRMOF-3-EM, [e] Nd-IRMOF-3-EM.

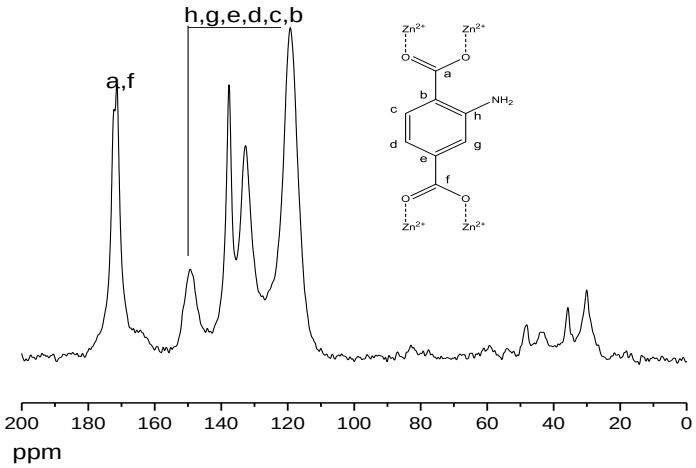

Figure A10 Solid state ^{13}C CP/MAS NMR spectrum of IRMOF-3.

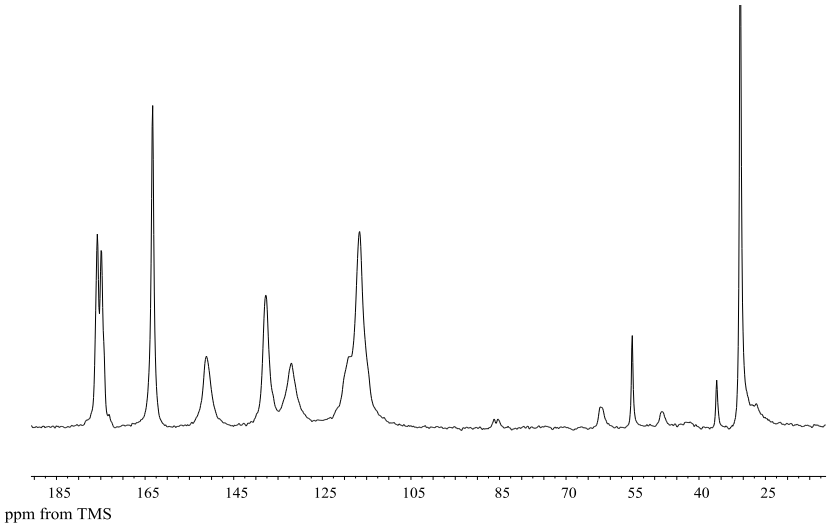

Figure A11. ^{13}C CP-MAS NMR spectrum of NH_2-MIL-125

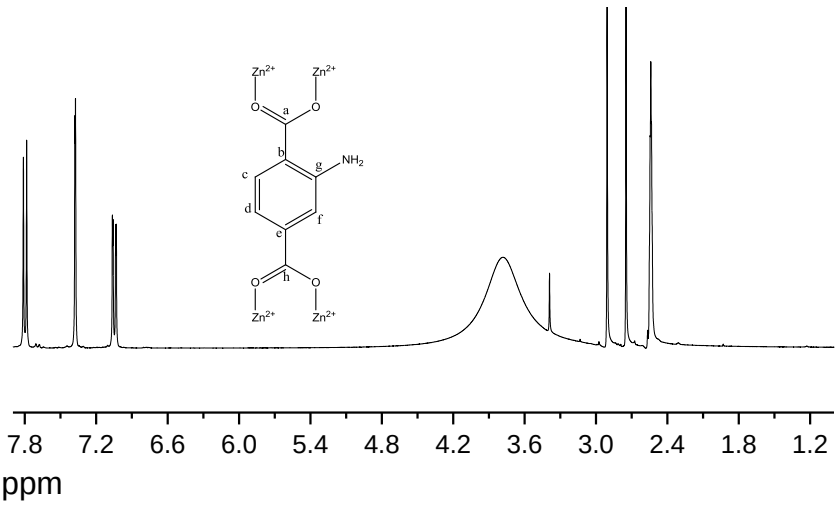

Figure A12 ^{1}H NMR of spectrum IRMOF-3.

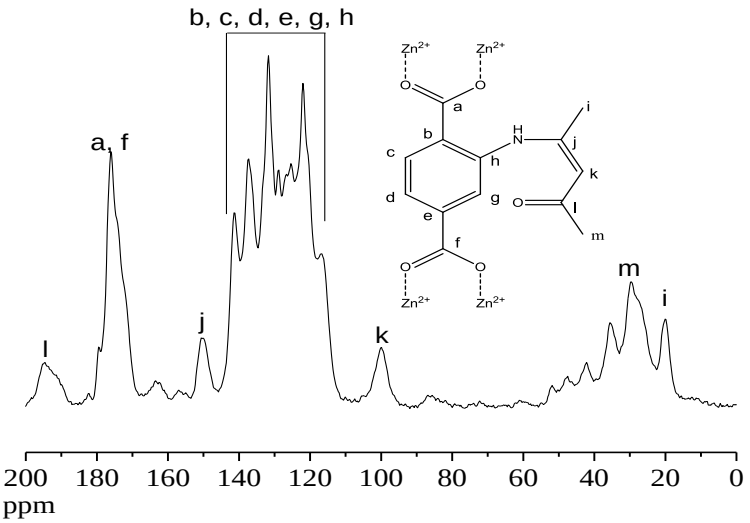

Figure A13 Solid-state ^{13}C CP/MAS NMR spectrum of IRMOF-3-AC.

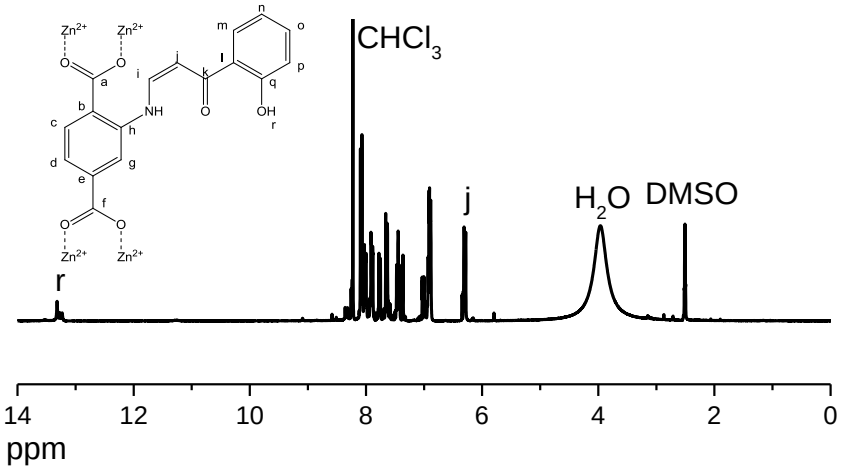

Figure A14 Solution ^{1}H NMR spectrum of acid-digested IRMOF-3-OL.

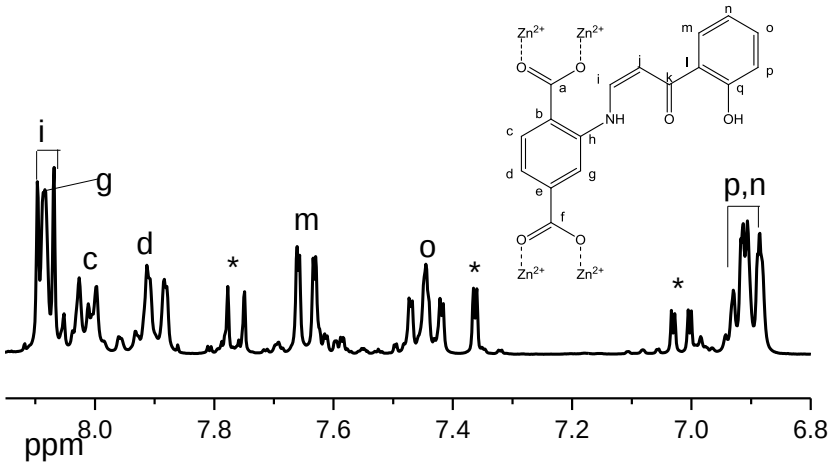

Figure A15 Solution ^{1}H NMR spectrum of acid-digested IRMOF-3-OL (expansion), *unmodified MOF.

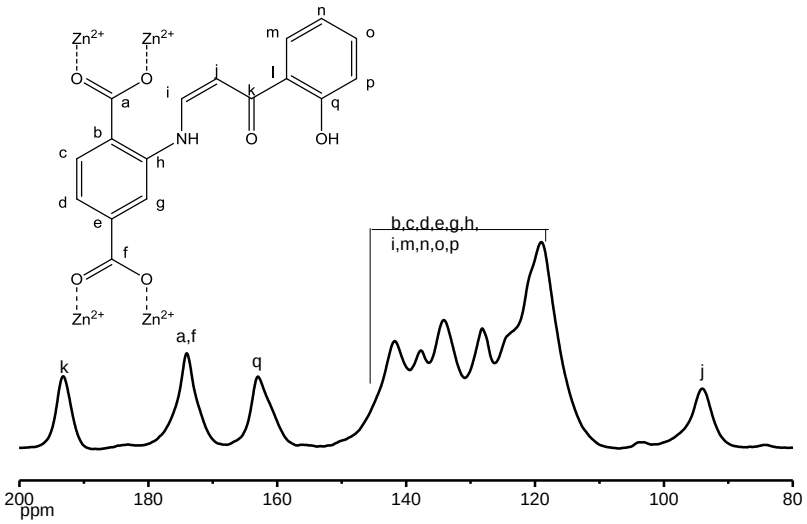

Figure A16 Solid-state ^{13}C CP/MAS NMR spectrum of IRMOF-3-OL

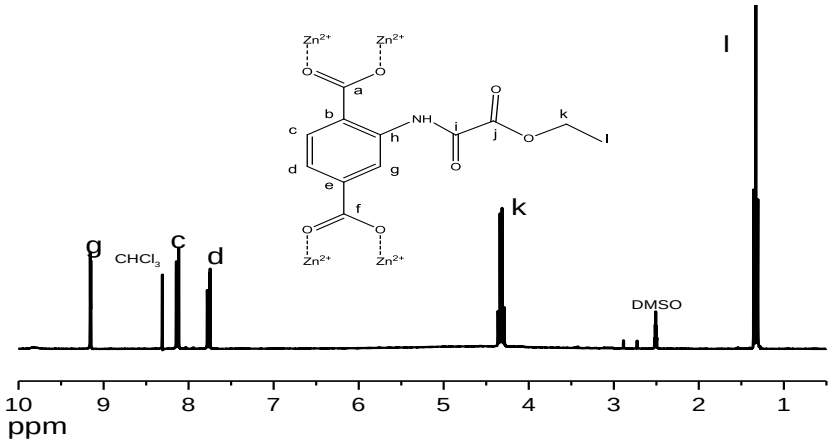

Figure A17 ^{1}H NMR spectrum of IRMOF-3-EOC.

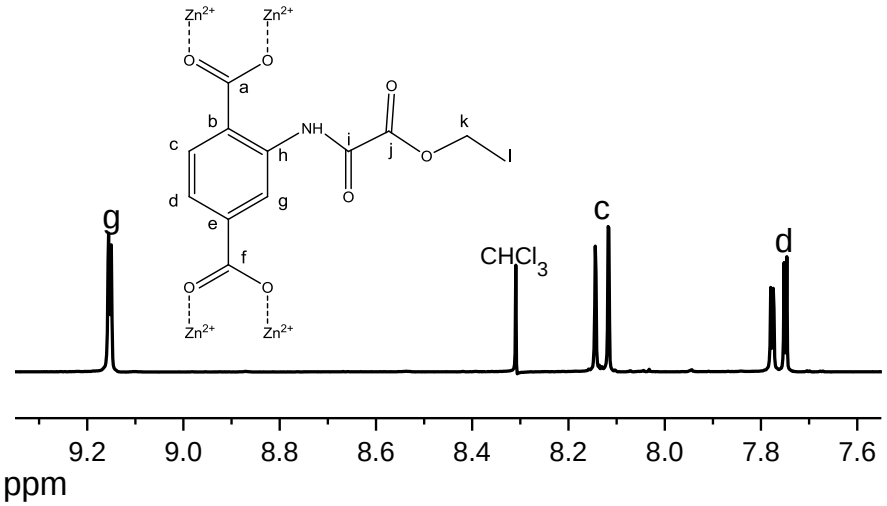

Figure A18 ^{1}H NMR spectrum of IRMOF-3-EOC (expansion).

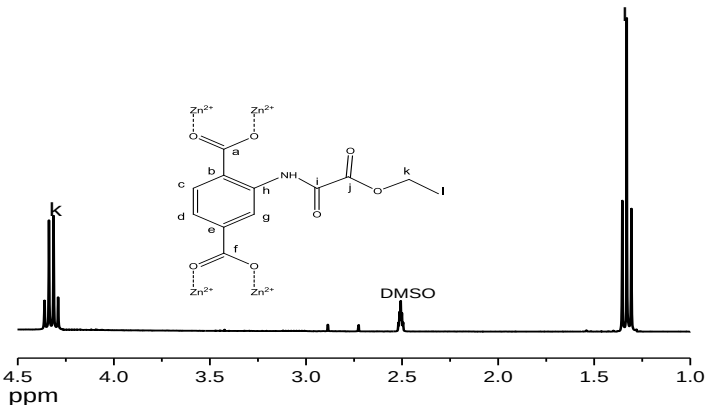

Figure A19 ^{1}H NMR spectrum of IRMOF-3-EOC (expansion).

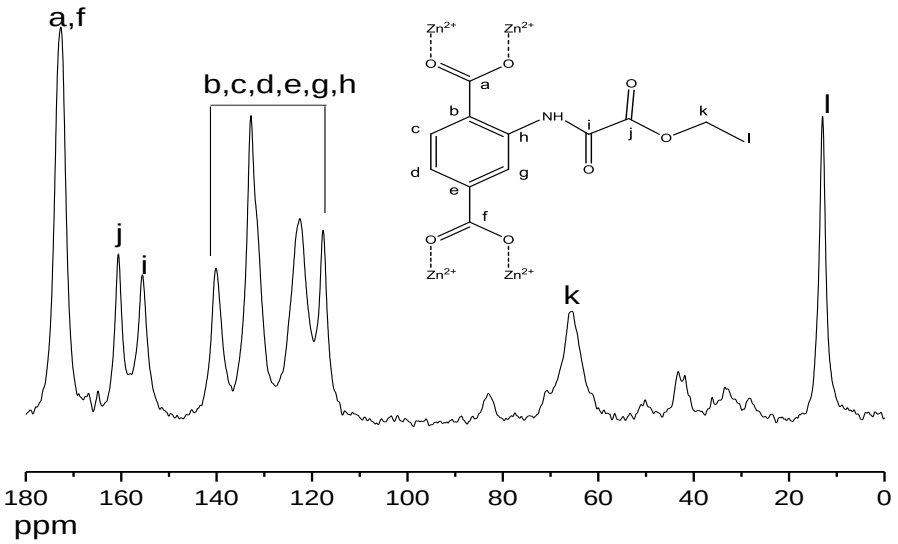

Figure A20 Solid state ^{13}C CP/MAS NMR spectrum of IRMOF-3-EOC.

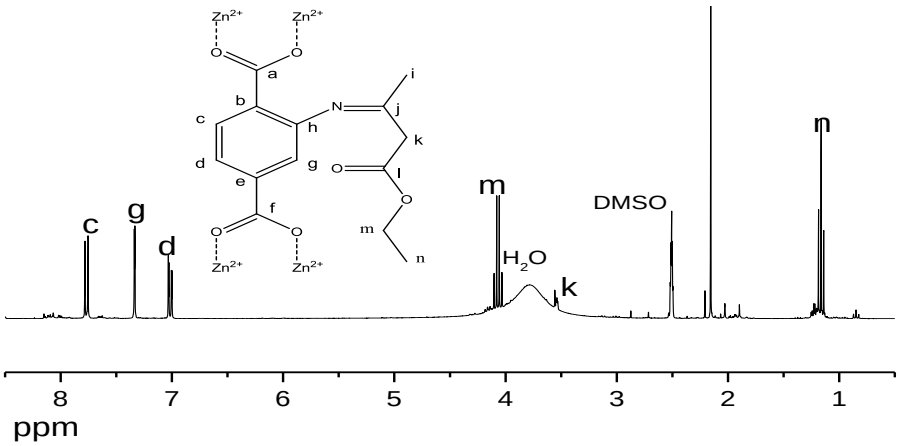

Figure A21 ^{1}H NMR spectrum of IRMOF-3-EAA.

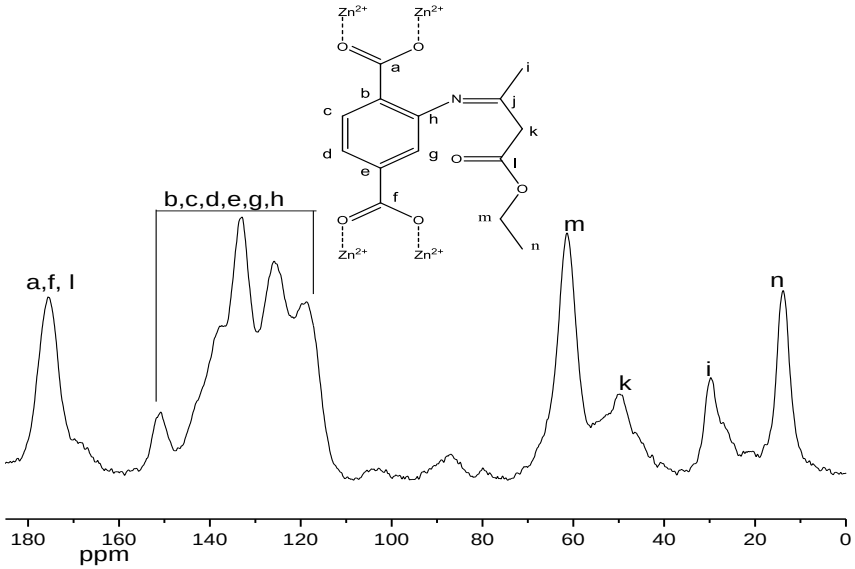

Figure A22 Solid state ^{13}C CP/MAS NMR spectrum of IRMOF-3-EAA.

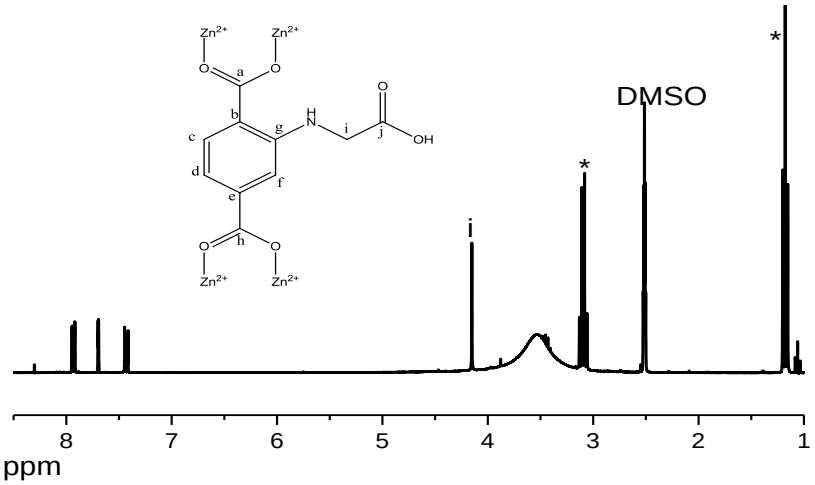

Figure A23 ^{1}H NMR spectrum of IRMOF-3-CA, *= triethylamine

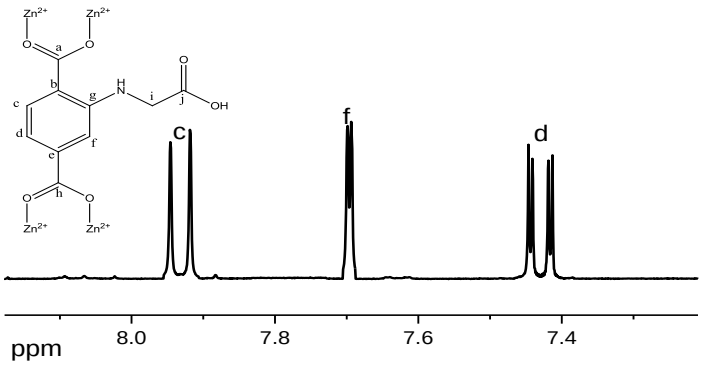

Figure A24 Aromatic zone of the ^{1}H NMR of spectrum IRMOF-3-CA.

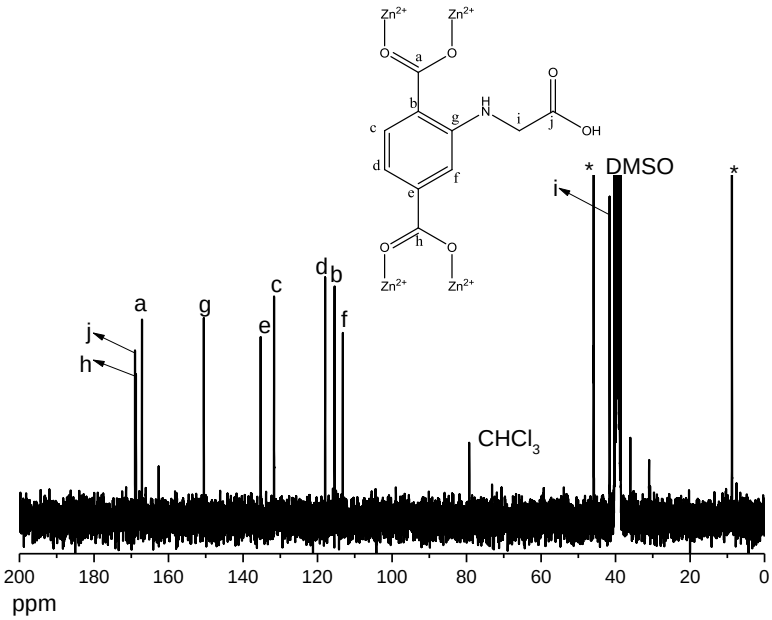

Figure A25 ^{13}C NMR spectrum of IRMOF-3-CA, *triethylamine.

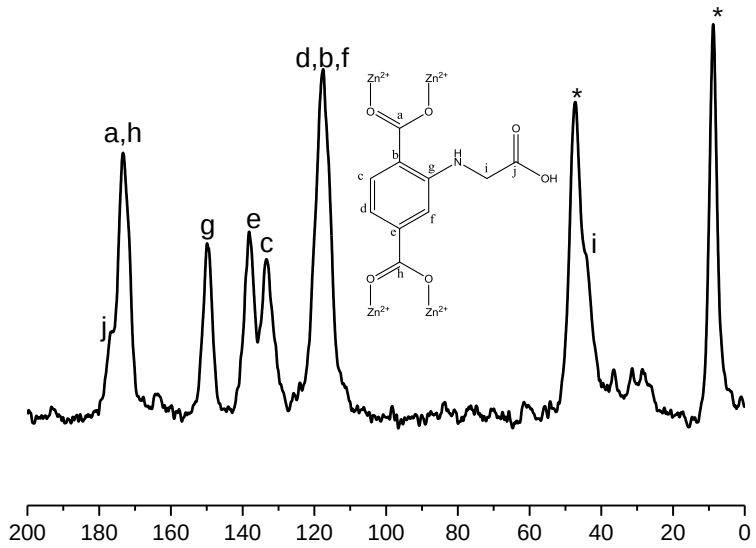

Figure A26 Solid state ^{13}C CP/MAS NMR spectrum of IRMOF-3-CA, *triethylamine.

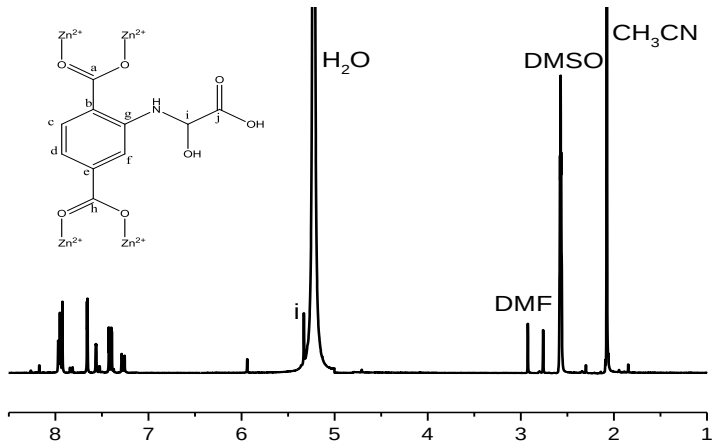

Figure A27 ^{1}H NMR spectrum of IRMOF-3-Gl.

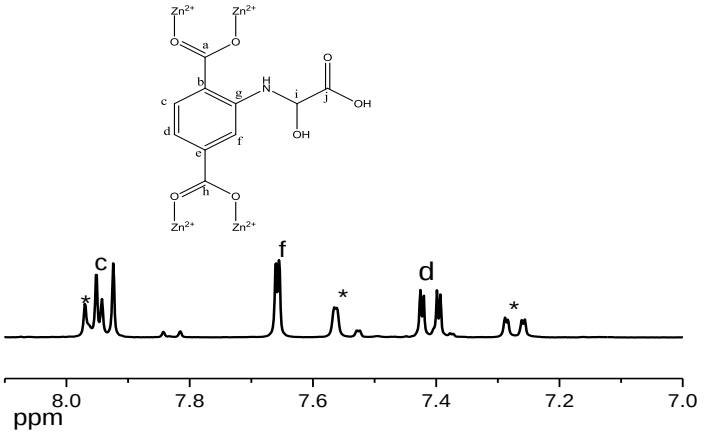

Figure A28 Aromatic zone of the ^{1}H NMR spectrum of IRMOF-3-Gl. * Unmodified IRMOF-3.

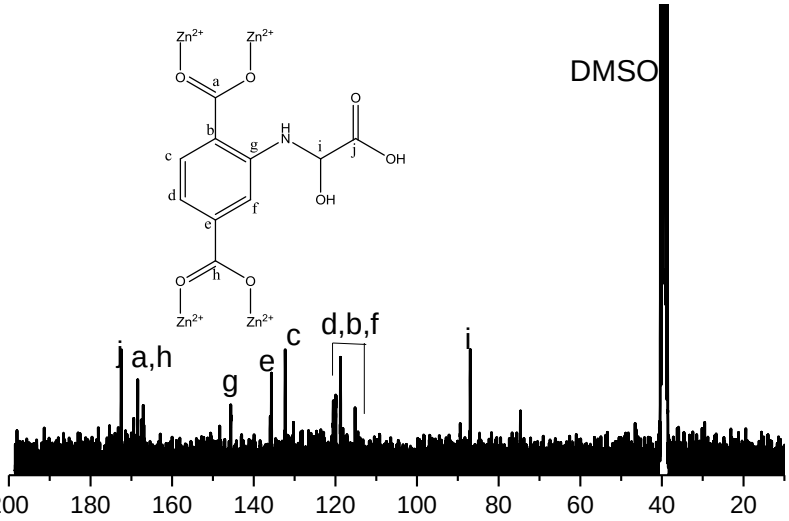

Figure A29 ^{13}C NMR spectrum of IRMOF-3-GL.

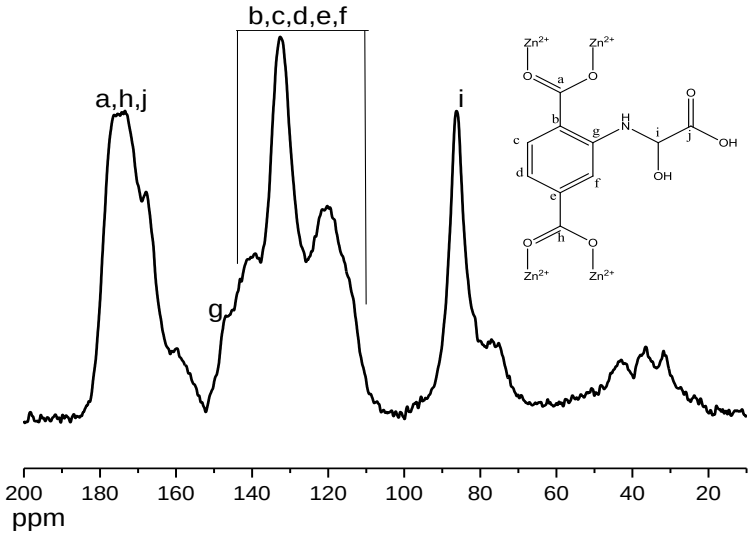

Figure A30 Solid state ^{13}C CP/MAS NMR spectrum of IRMOF-3-GL.

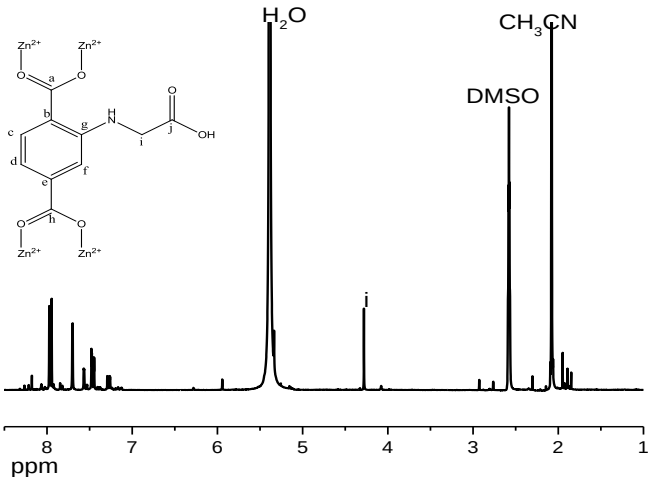

Figure A31 ^{1}H NMR spectrum of IRMOF-3-Gl-R.

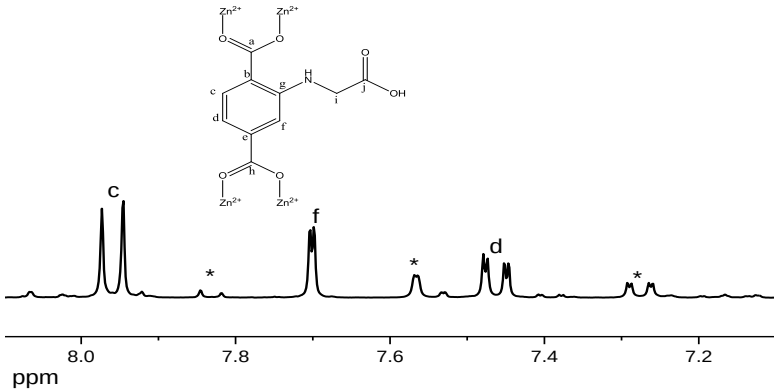

Figure A32 Aromatic zone of the ^{1}H NMR spectrum of IRMOF-3-Gl-R. * Unmodified IRMOF-3.

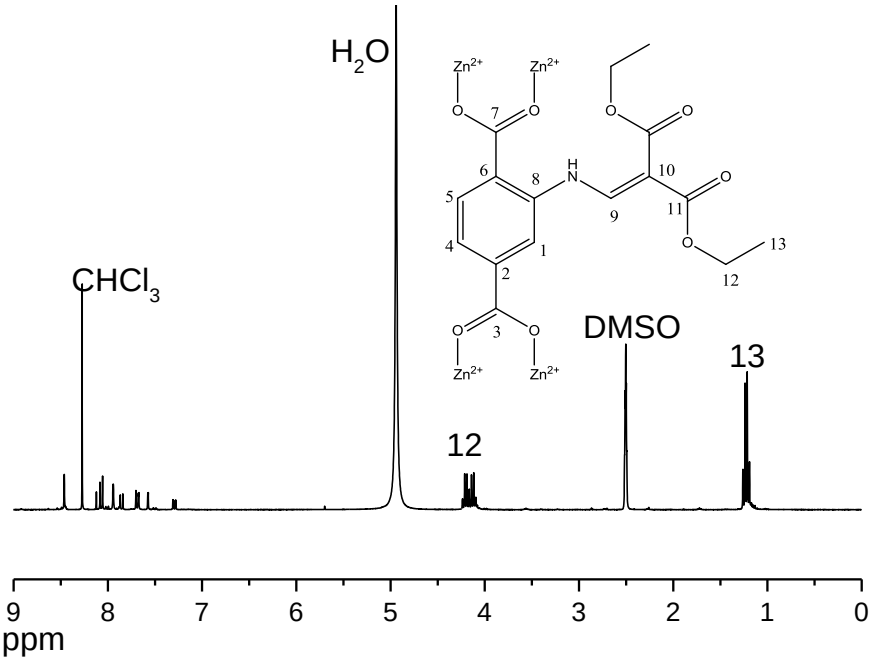

Figure A33 ^{1}H NMR spectrum of IRMOF-3-EM.

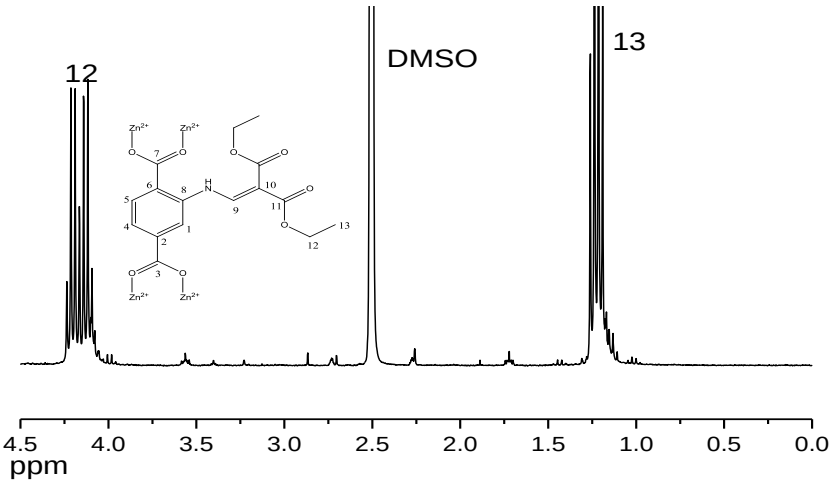

Figure A34 Aliphatic zone of the ^{1}H NMR spectrum of IRMOF-3-EM.

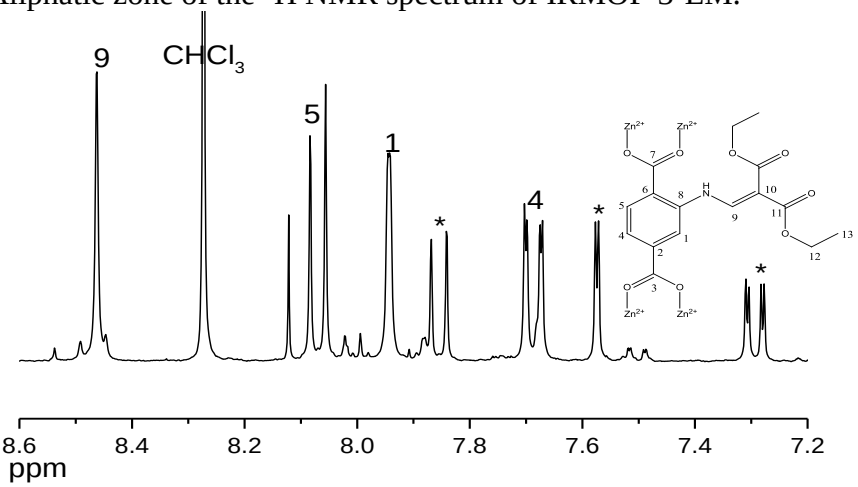

Figure A35 Aromatic zone of the ^{1}H NMR spectrum of IRMOF-3-EM. * Unmodified IRMOF-3.

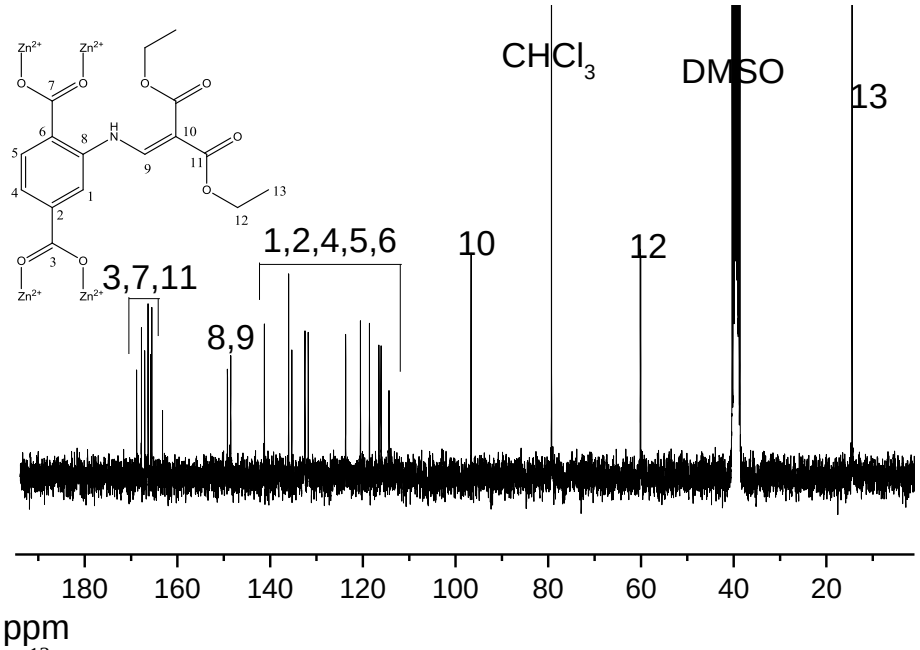

Figure A36 ^{13}C NMR spectrum of IRMOF-3-EM.

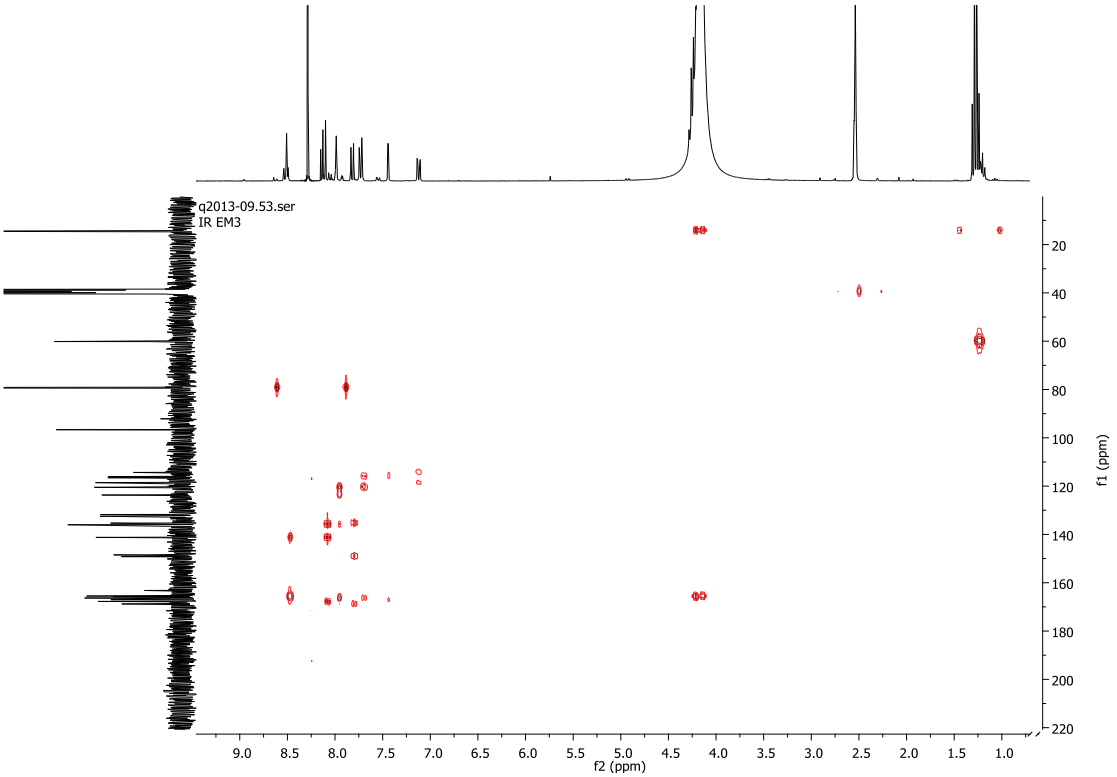

Figure A37 HMBC spectrum of IRMOF-3-EM.

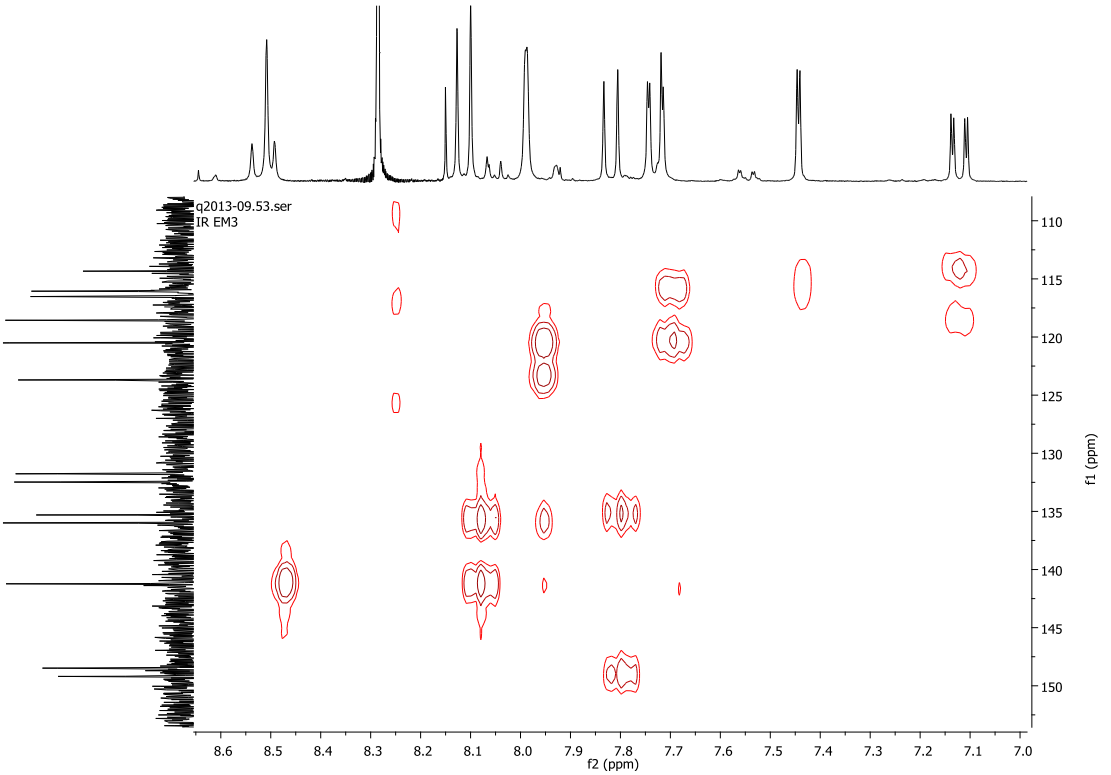

Figure A38 Expansion of HMBC spectrum of IRMOF-3-EM.

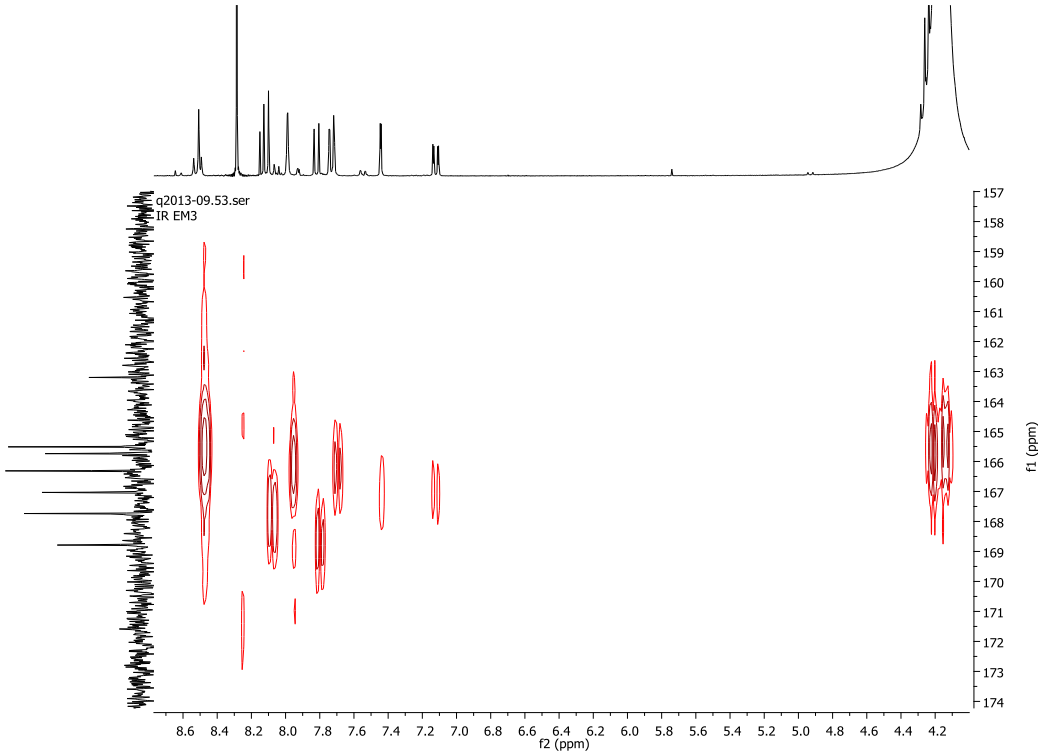

Figure A39 Expansion of HMBC spectrum of IRMOF-3-EM.

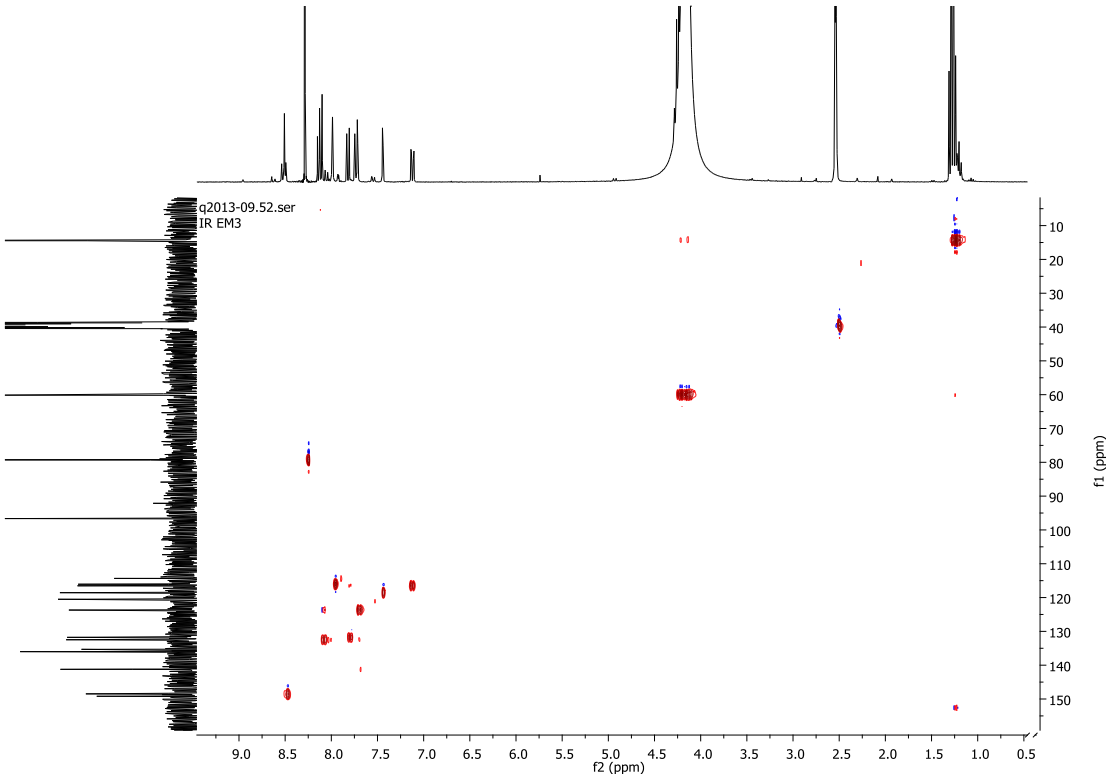

Figure A40 Expansion of HSQC spectrum of IRMOF-3-EM.

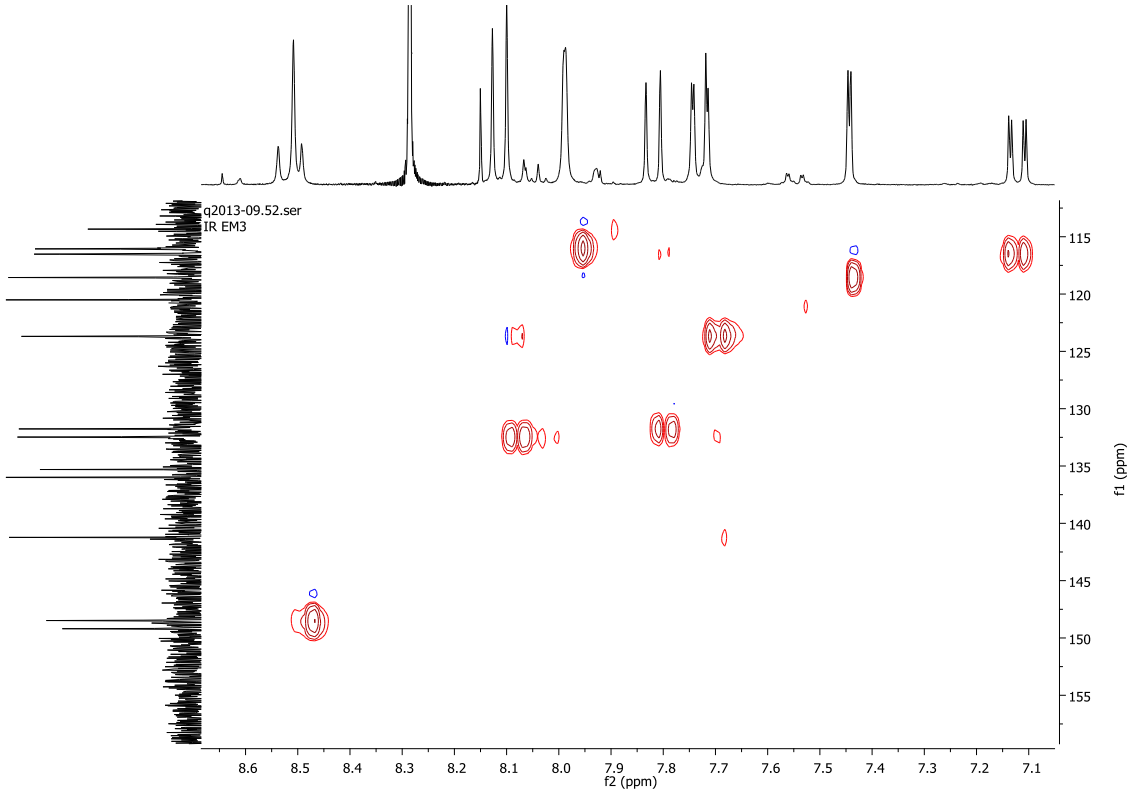

Figure A41 Expansion of HSQC spectrum of IRMOF-3-EM.

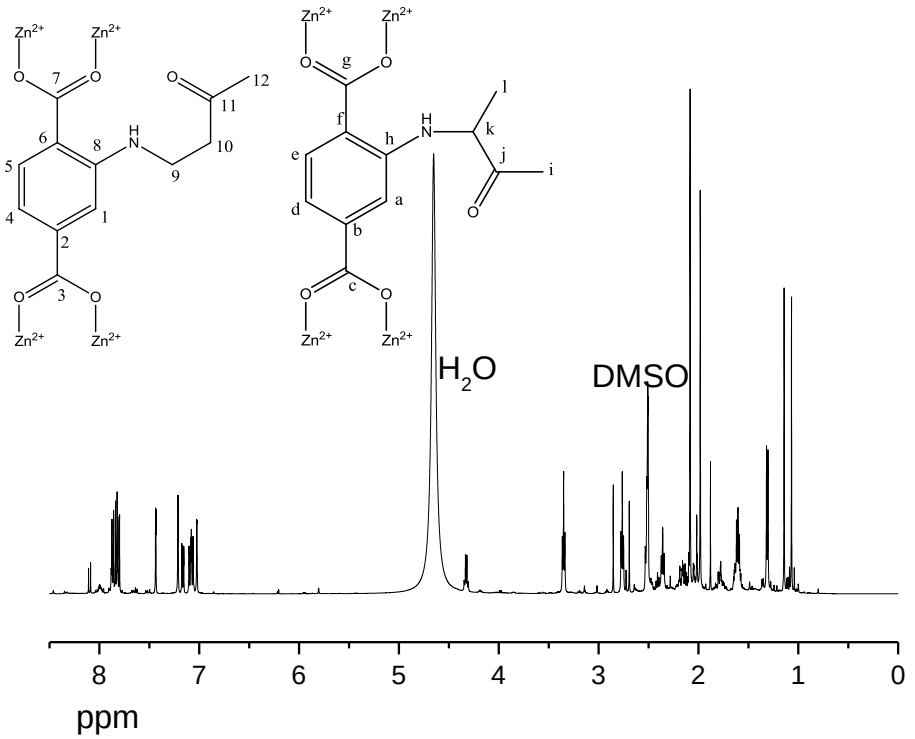

Figure A42 ^{1}H NMR spectrum of IRMOF-3-MVK.

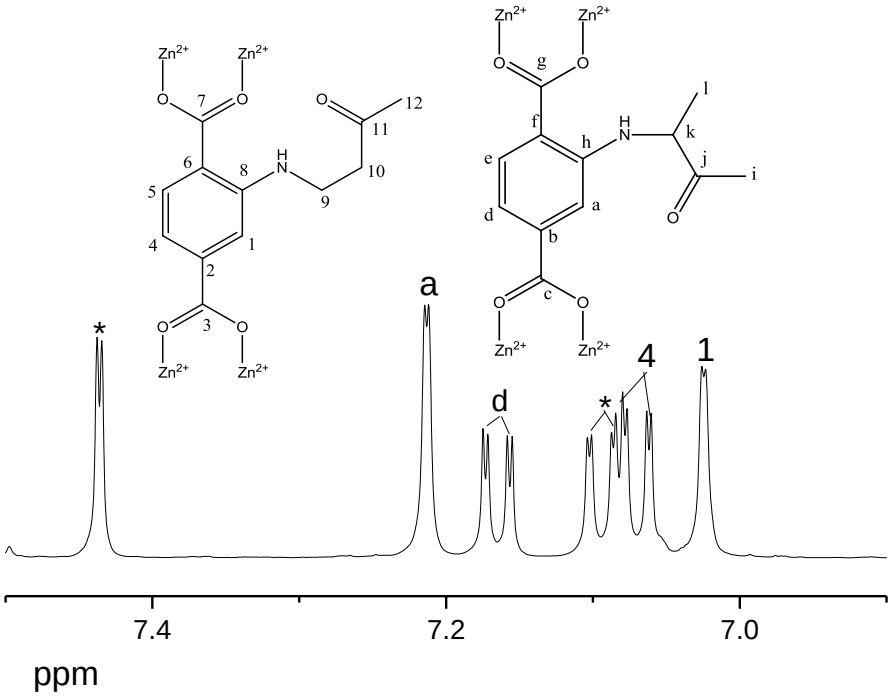

Figure A43 Expansion of the aromatic zone of the ^{1}H NMR spectrum of IRMOF-3-MVK. * Unmodified IRMOF-3.

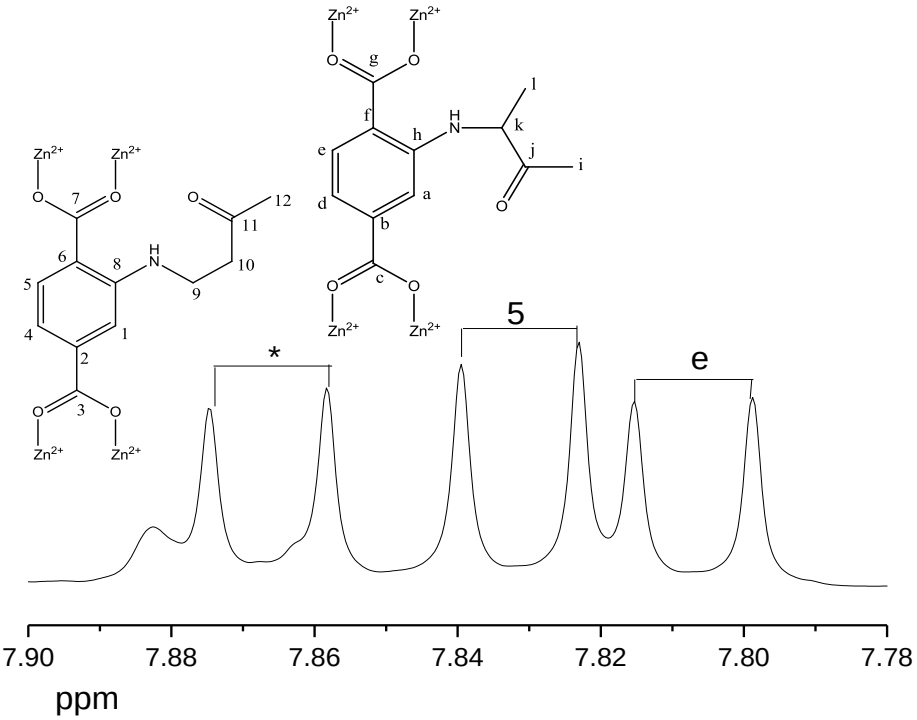

Figure A44 Expansion of the aromatic zone of the ^{1}H NMR spectrum of IRMOF-3-MVK. * Unmodified IRMOF-3.

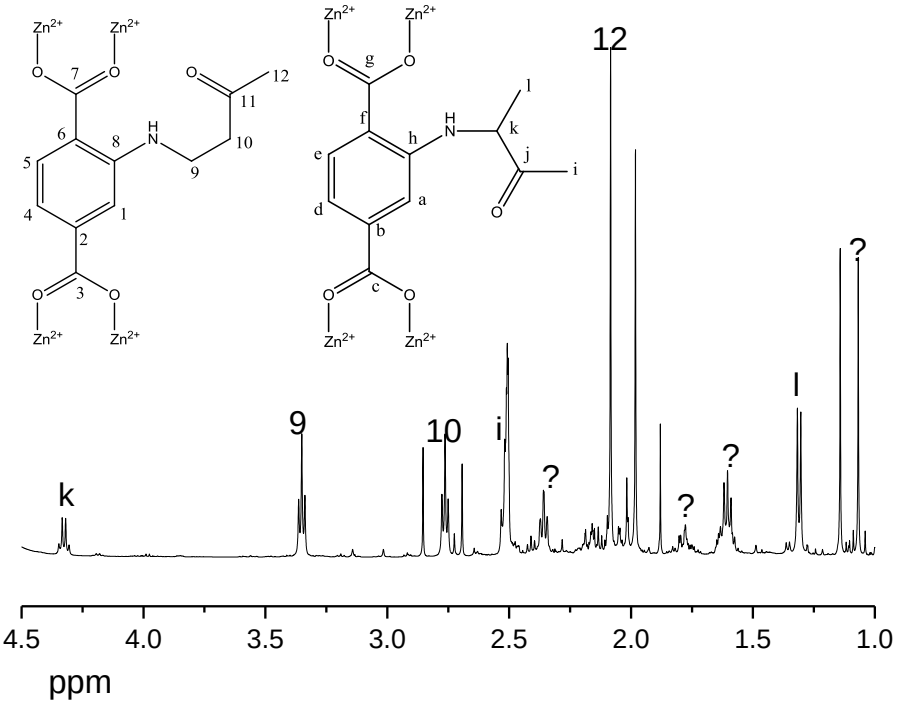

Figure A45 Aliphatic zone of the ^{1}H NMR spectrum of IRMOF-3-MVK.? = oligomers of MVK.

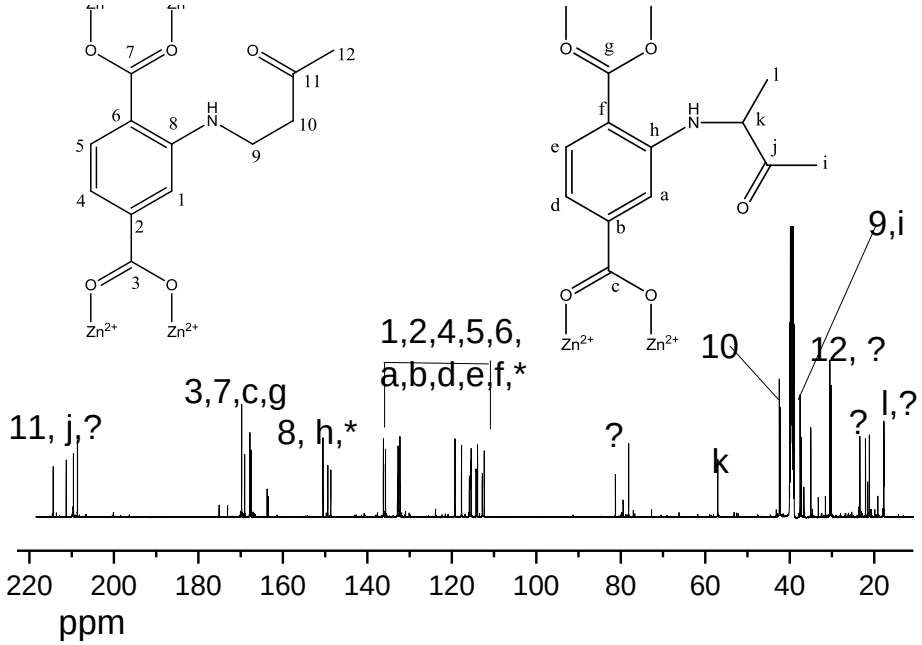

Figure A46 ^{13}C NMR spectrum of IRMOF-3-MVK.

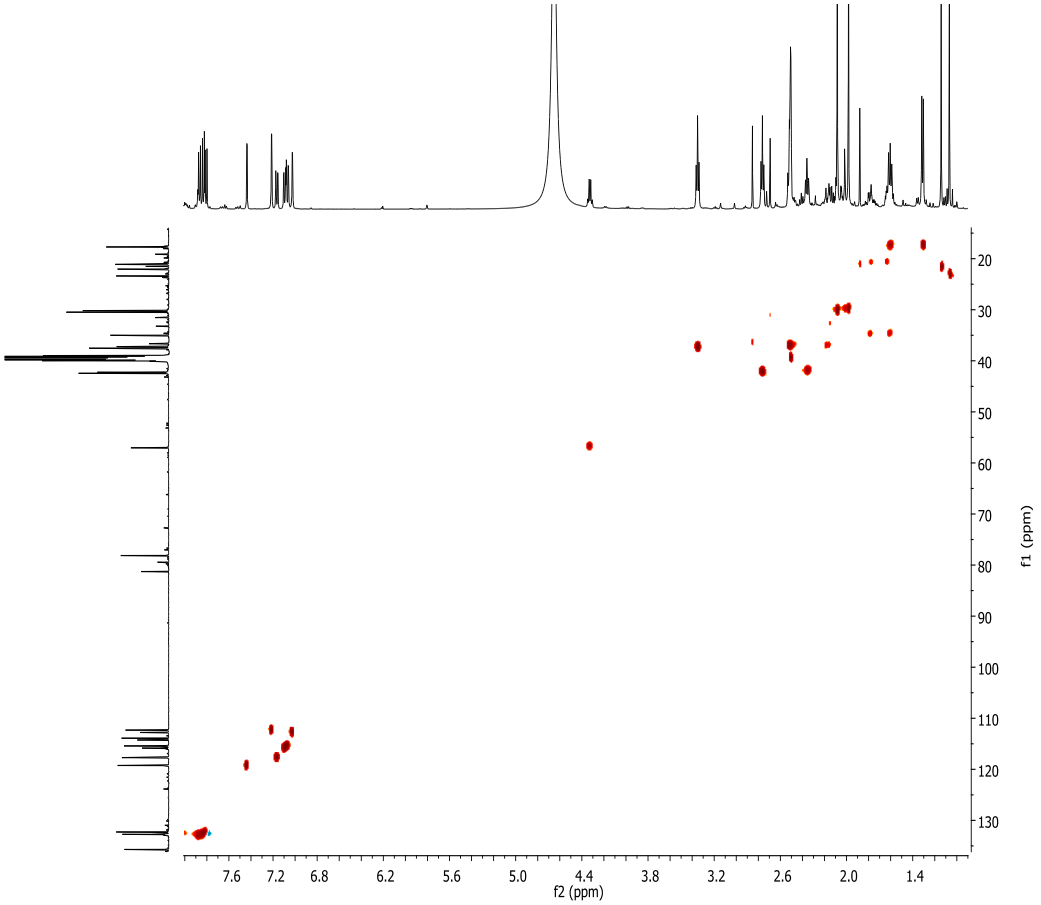

Figure A47 HSQC spectrum of IRMOF-3-MVK

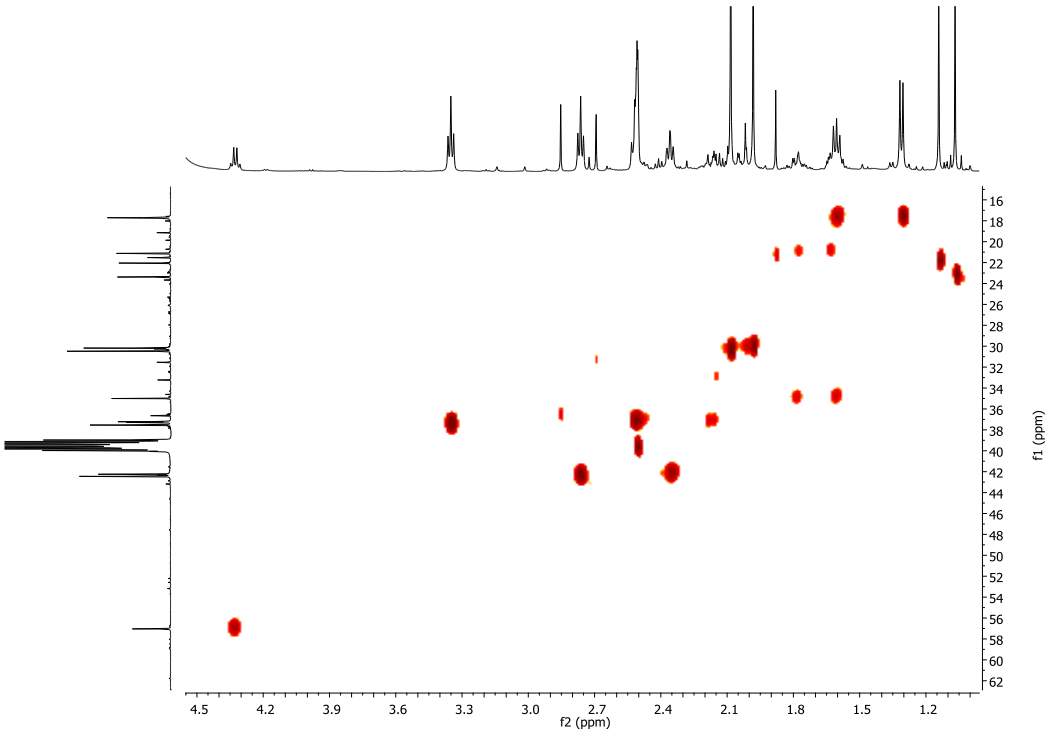

Figure A48 Expansion of the HSQC spectrum of IRMOF-3-MVK.

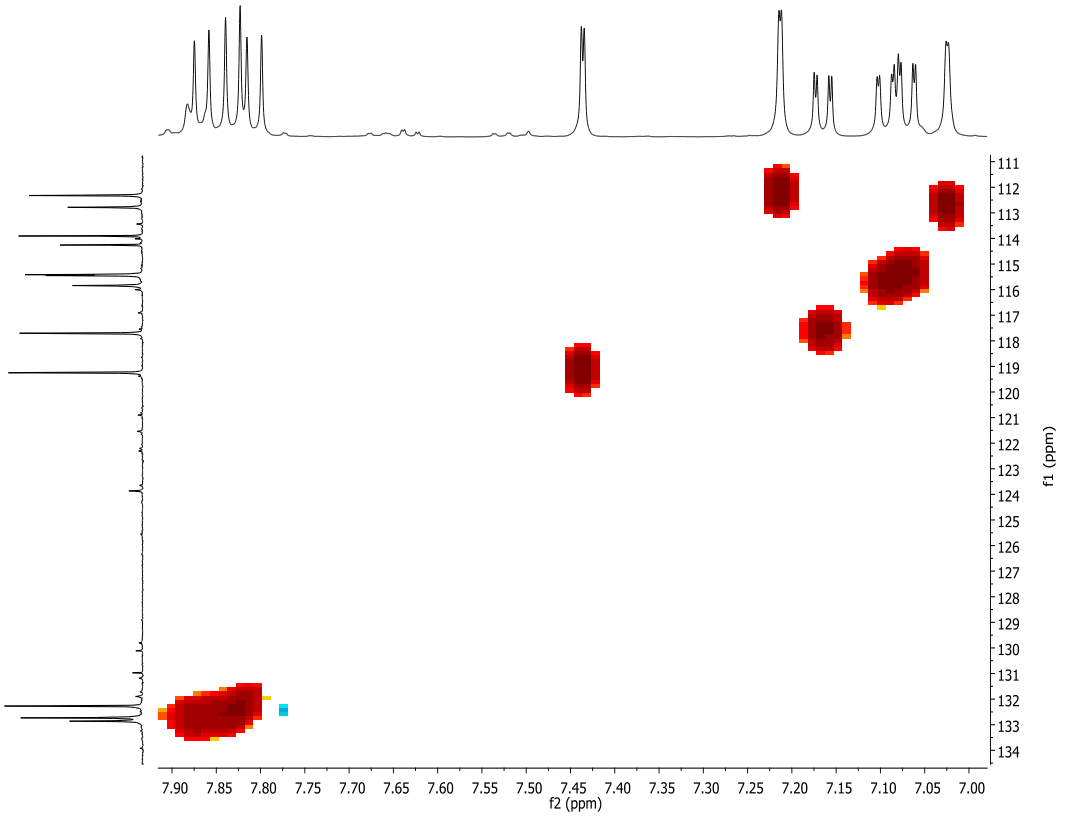

Figure A49 Expansion of the HSQC spectrum of IRMOF-3-MVK.

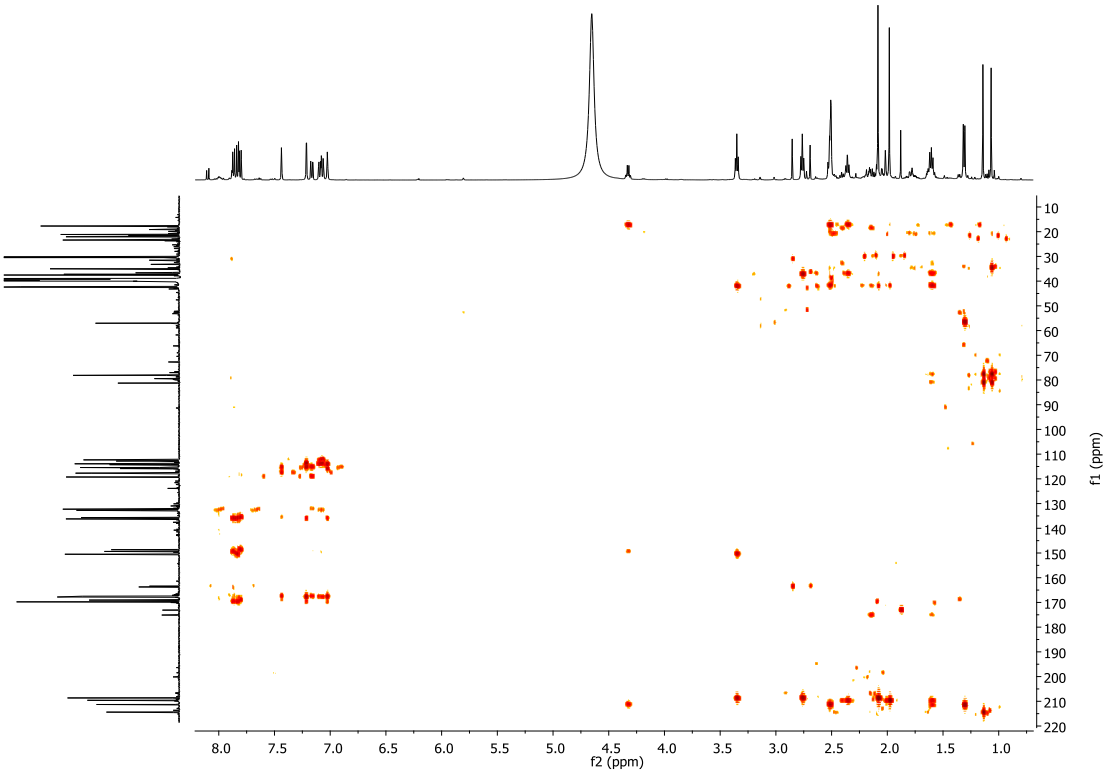

Figure A50 HMBC spectrum of IRMOF-3-MVK.

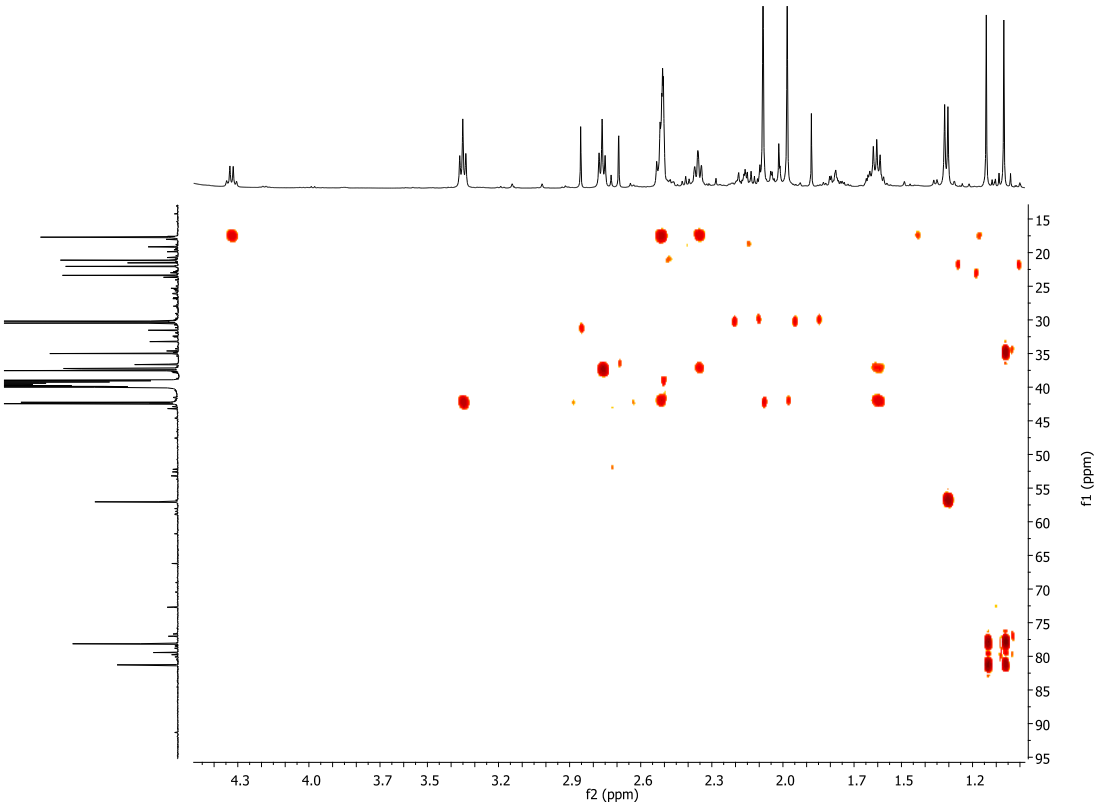

Figure A51 Expansion of the HMBC spectrum of IRMOF-3-MVK.

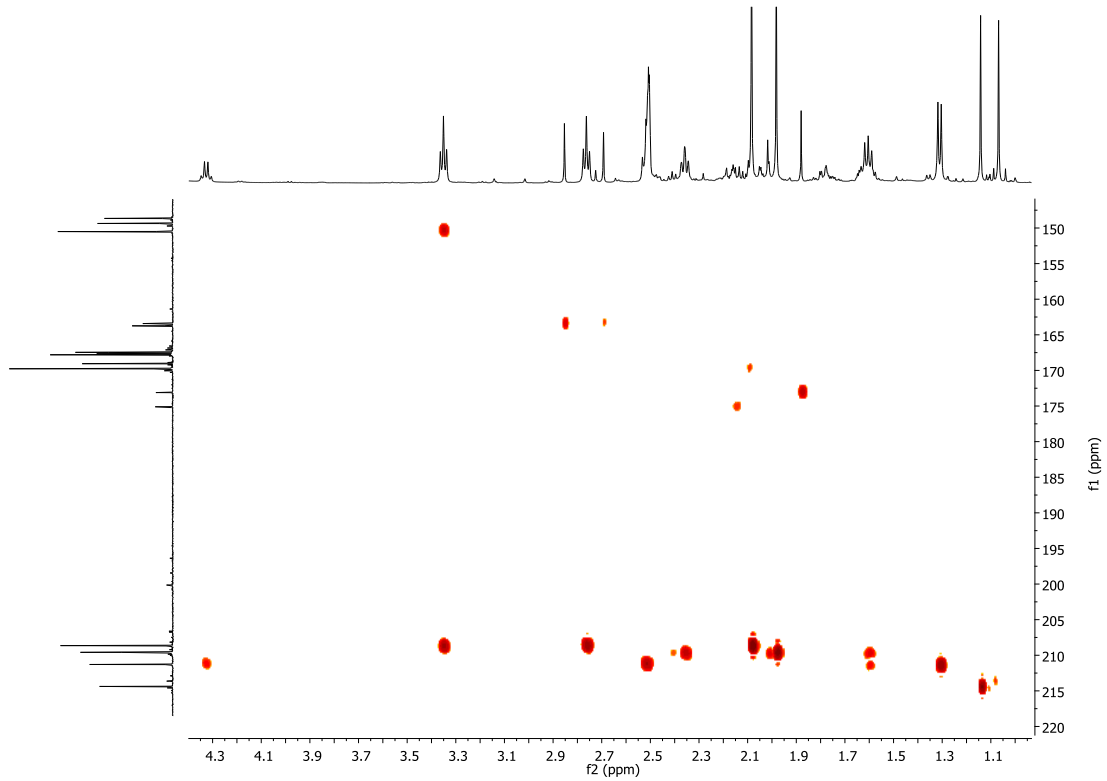

Figure A52 Expansion of the HMBC spectrum of IRMOF-3-MVK.

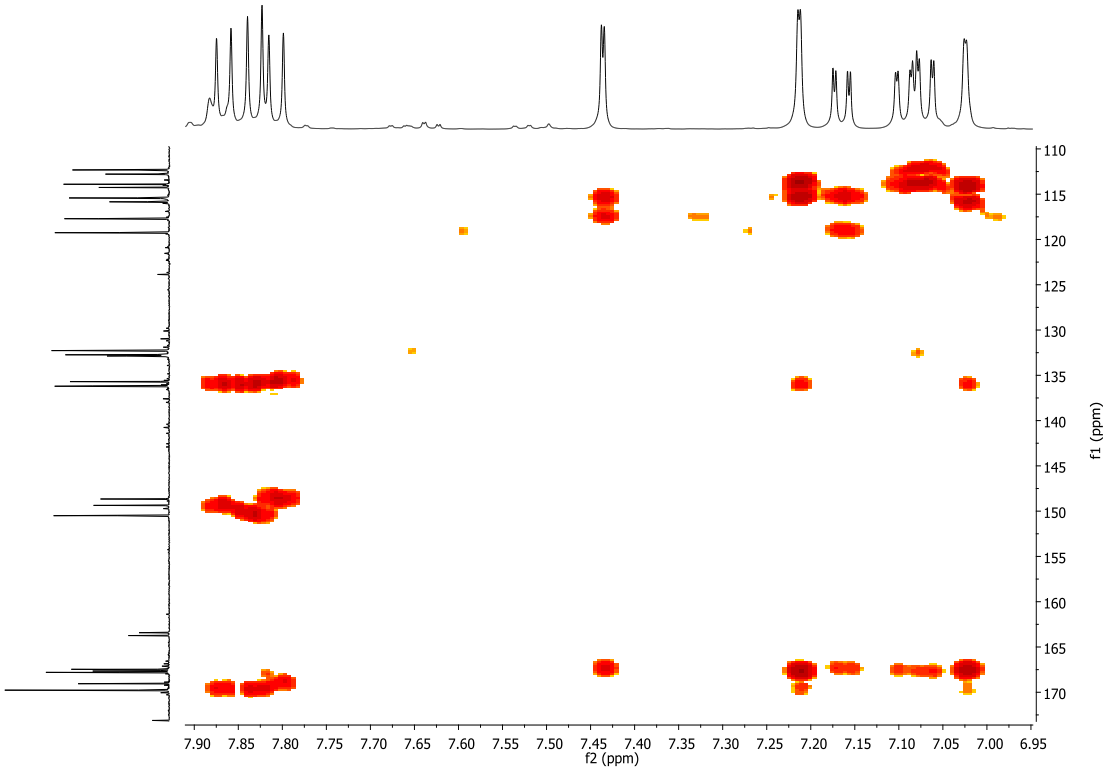

Figure A53 Expansion of the HMBC spectrum of IRMOF-3-MVK.

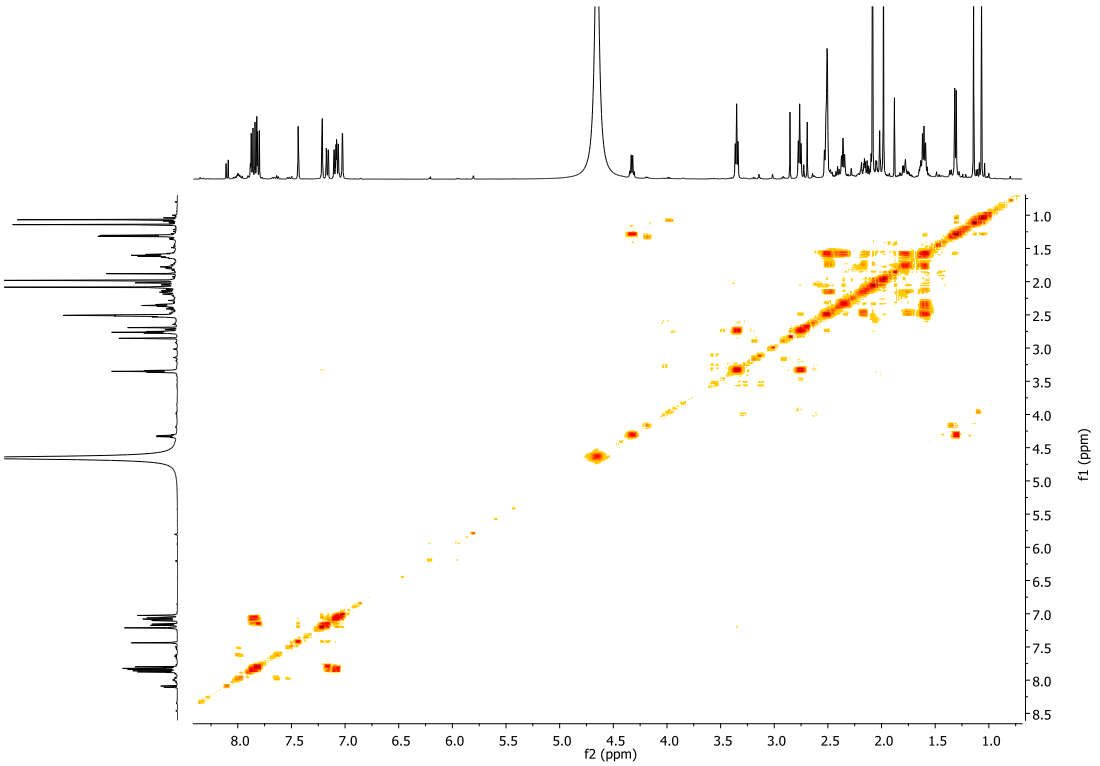

Figure A54 2D COSY spectrum of IRMOF-3-MVK.

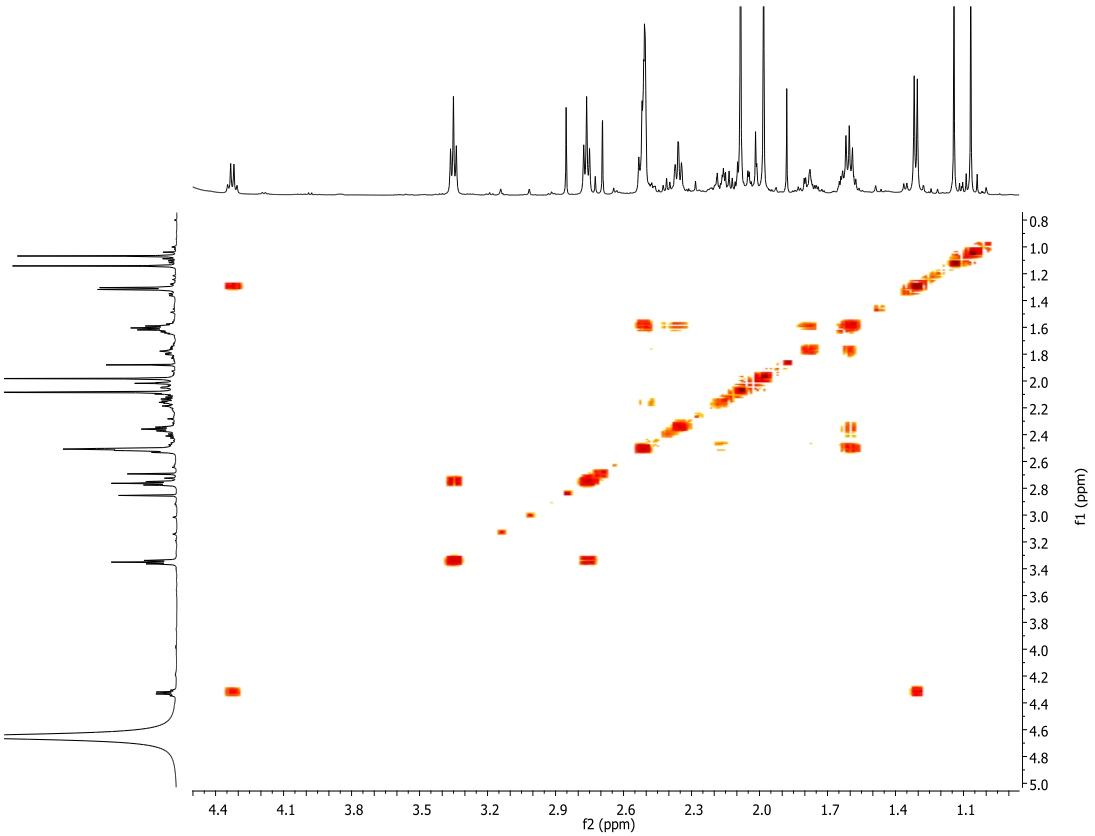

Figure A55 Expansion of the 2D COSY spectrum of IRMOF-3-MVK.

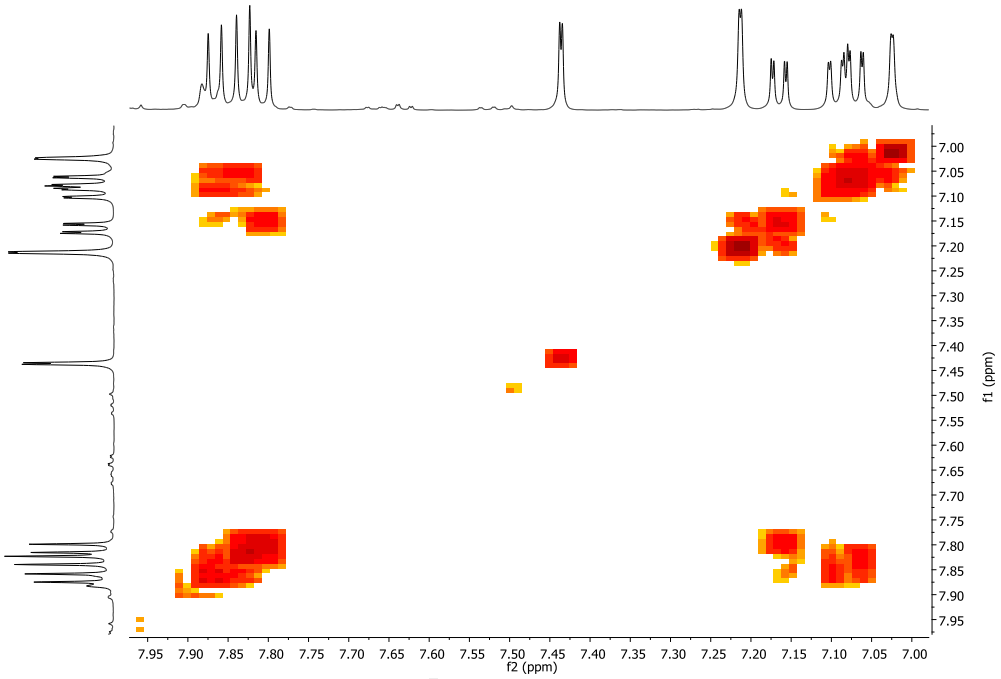

Figure A56 Expansion of the 2D COSY spectrum of IRMOF-3-MVK.

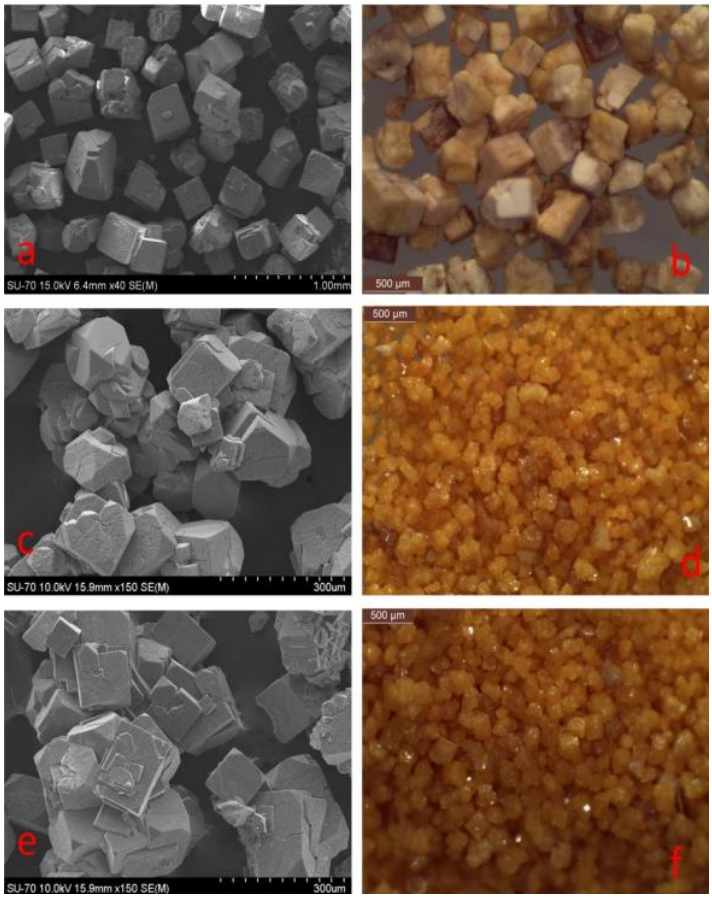

Figure A57 SEM of: (a) Nd-IRMOF-3-AC, (c) Nd-IRMOF-3-OL, (e) Nd-Y-IRMOF-3-OL and optical microscopy photographs of (b) Nd-IRMOF-3-AC, (d) Nd-IRMOF-3-OL, (f) Nd-Y-IRMOF-3-OL.

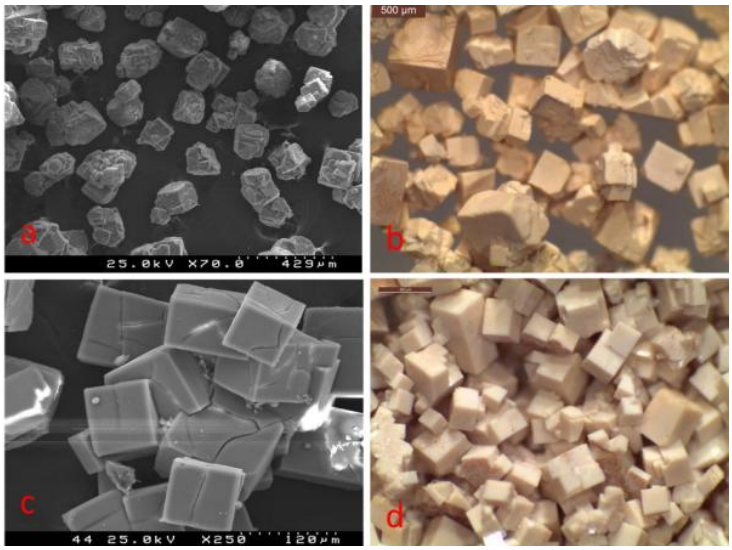

Figure A58 SEM of (a) Nd-IRMOF-3-EOC, (b) Nd-IRMOF-3-EAA & Optical microscopic photographs of (b) Nd- IRMOF-3-EOC, (d) Nd-IRMOF-3-EAA.

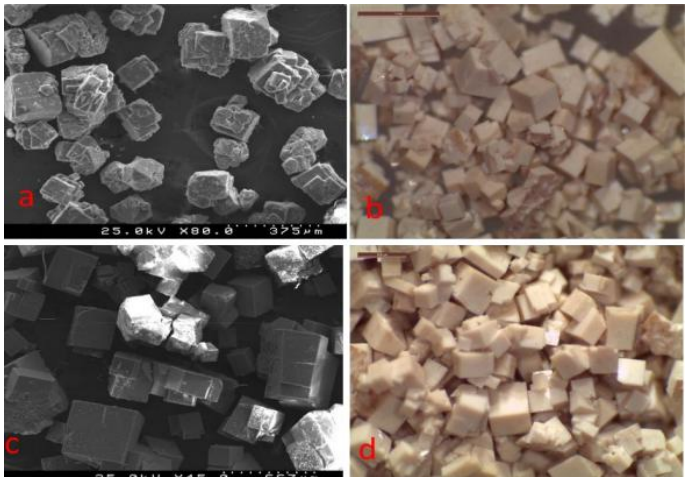

Figure A59 SEM of (a) Eu-IRMOF-3-EOC, (b) Eu-IRMOF-3-EAA & Optical microscopic photographs of (b) Eu-IRMOF-3-EOC, (d) Eu-IRMOF-3-EAA.

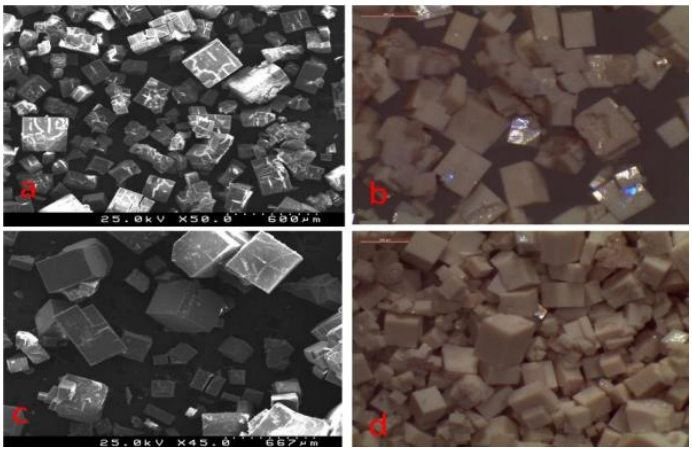

Figure A60 SEM of (a) Tb-IRMOF-3-EOC, (b) Tb-IRMOF-3-EAA & Optical microscopic photographs of (b) Tb-IRMOF-3-EOC, (d) Tb-IRMOF-3-EAA.

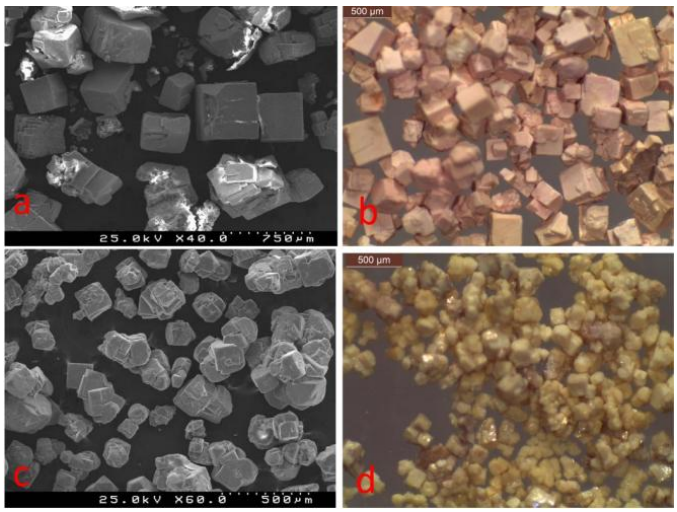

Figure A61 SEM of: (a) Nd-IRMOF-3-CA, (c) Nd-IRMOF-3-GL, and optical microscopy photographs of (b) Nd-IRMOF-3-CA, (d) Nd-IRMOF-3-GL.

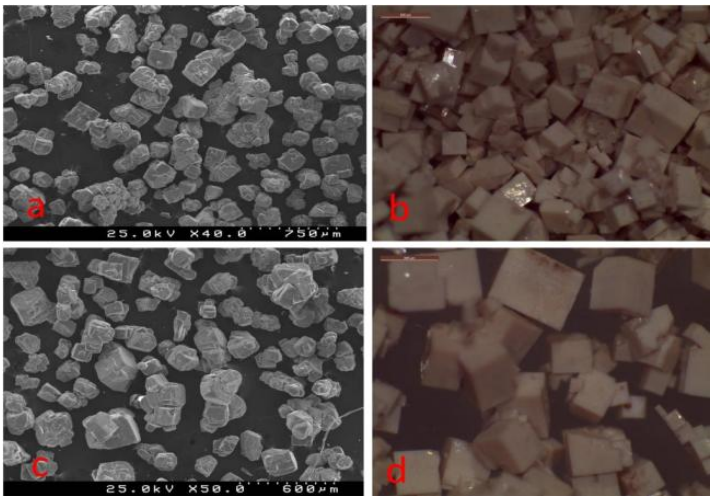

Figure A62 SEM of: (a) Eu-IRMOF-3-CA, (c) Eu-IRMOF-3-GL, and optical microscopy photographs of (b) Eu-IRMOF-3-CA, (d) Eu-IRMOF-3-GL.

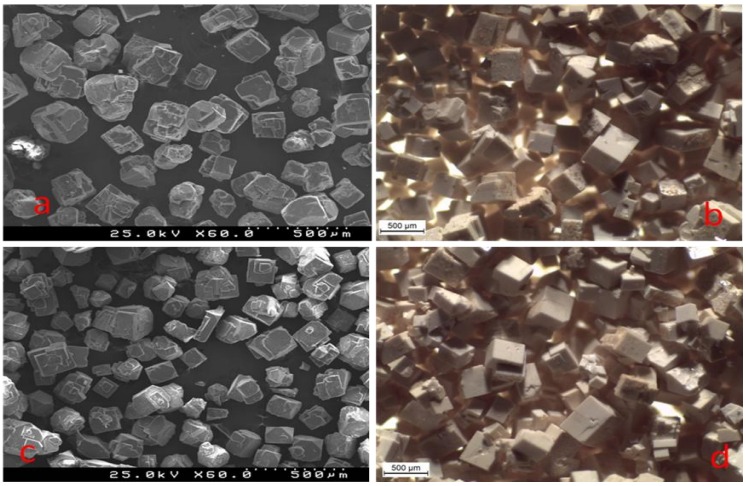

Figure A63 SEM of: (a) Nd-IRMOF-3-MVK, (c) Nd-IRMOF-3-EM, and optical microscopy photographs of (b) Nd-IRMOF-3-MVK, (d) Nd-IRMOF-3-EM.

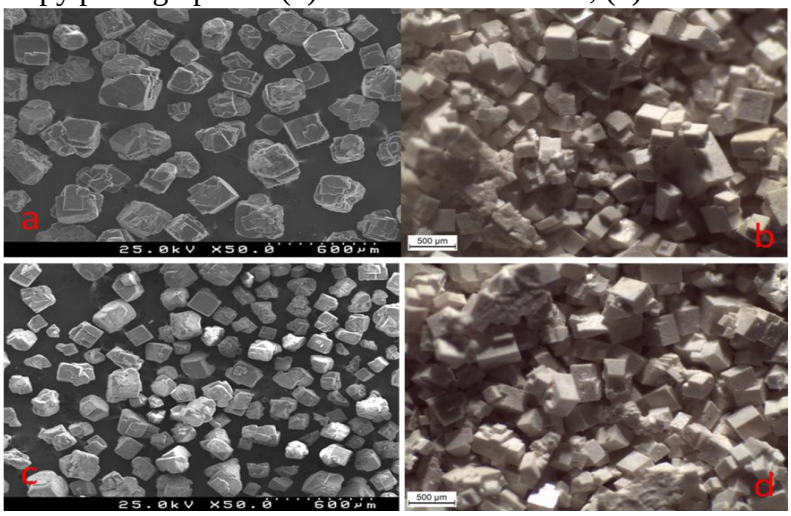

Figure A64 SEM of: (a) Eu-IRMOF-3-MVK, (c) Eu-IRMOF-3-EM, and optical microscopy photographs of (b) Eu-IRMOF-3-MVK, (d) Eu-IRMOF-3-EM.

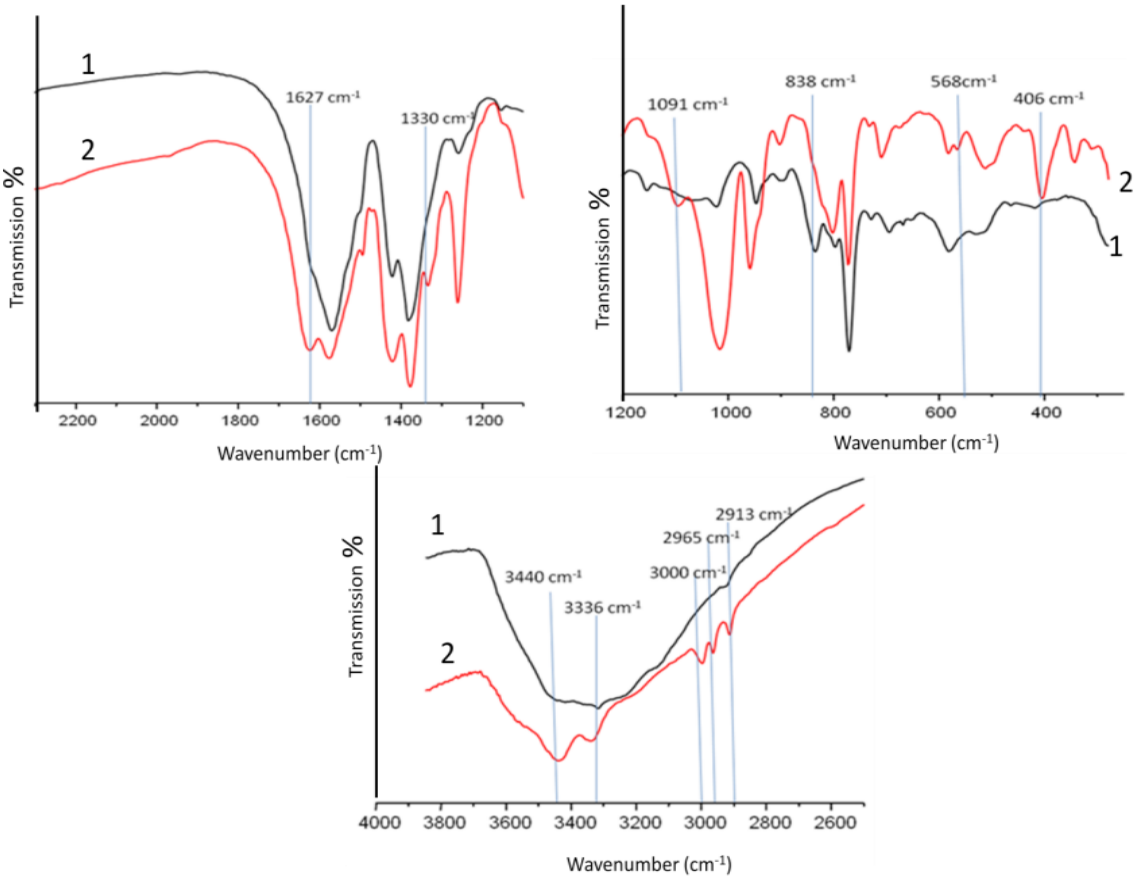

Figure A65 FTIR spectra of 1) IRMOF-3-AC and 2) Nd-IRMOF-3-AC.

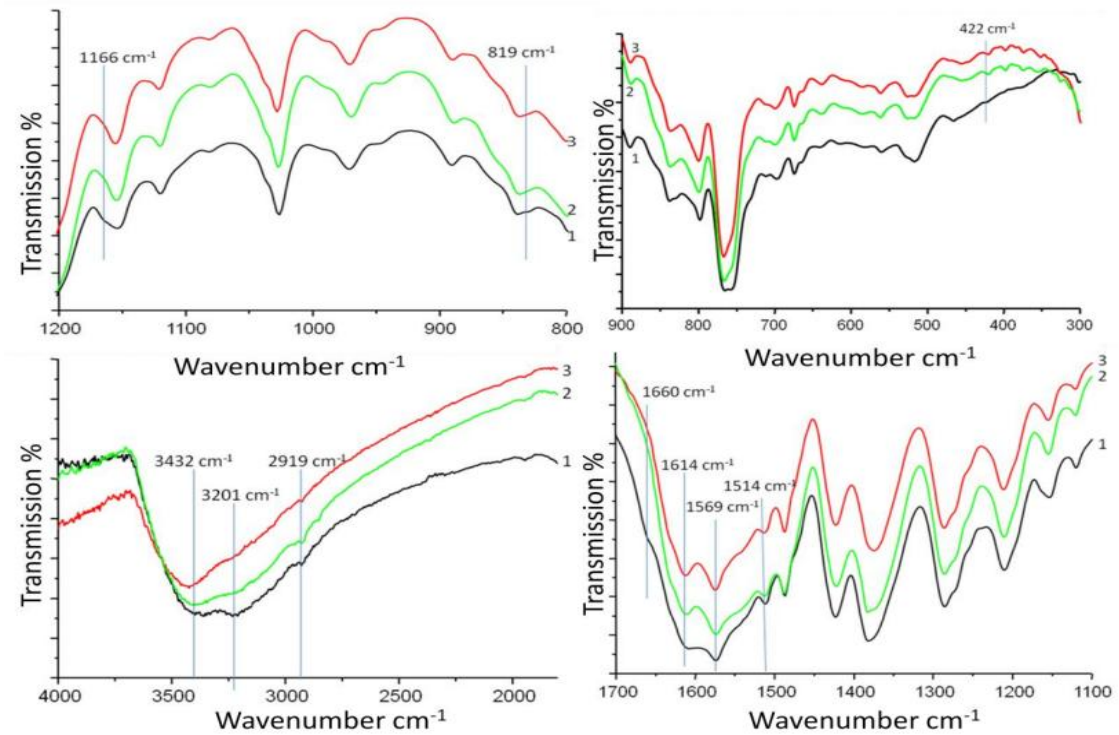

Figure A66 FTIR spectra of 1) IRMOF-3-OL, 2) Nd-IRMOF-3-OL and 3) Nd-Y-IRMOF-3-OL.

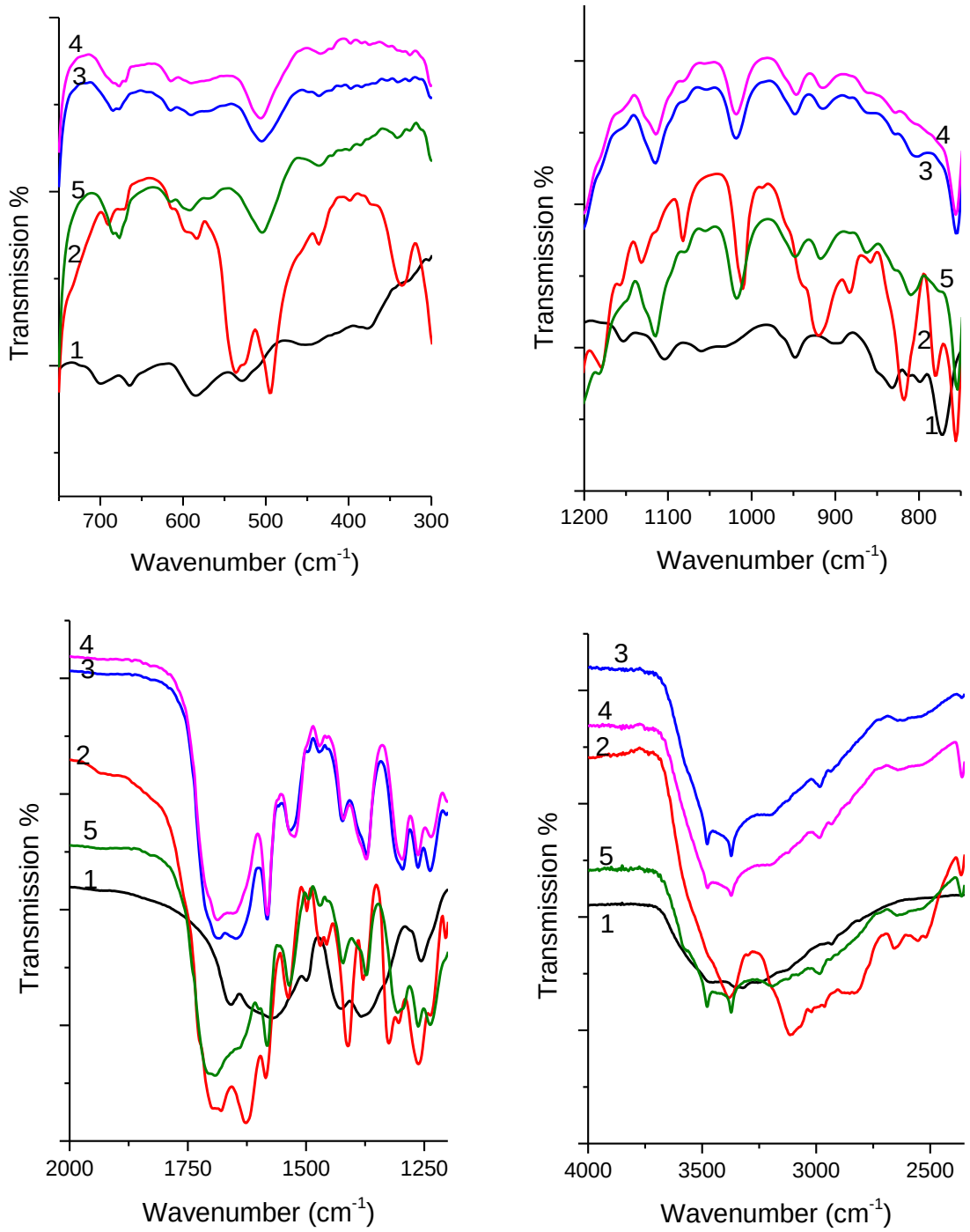

Figure A67 FTIR spectrum of 1) IRMOF-3, 2) IRMOF-3-EOC, 3) Eu-IRMOF-3-EOC, 4) Nd-IRMOF-3-EOC, and 5) Tb-IRMOF-3-EOC.

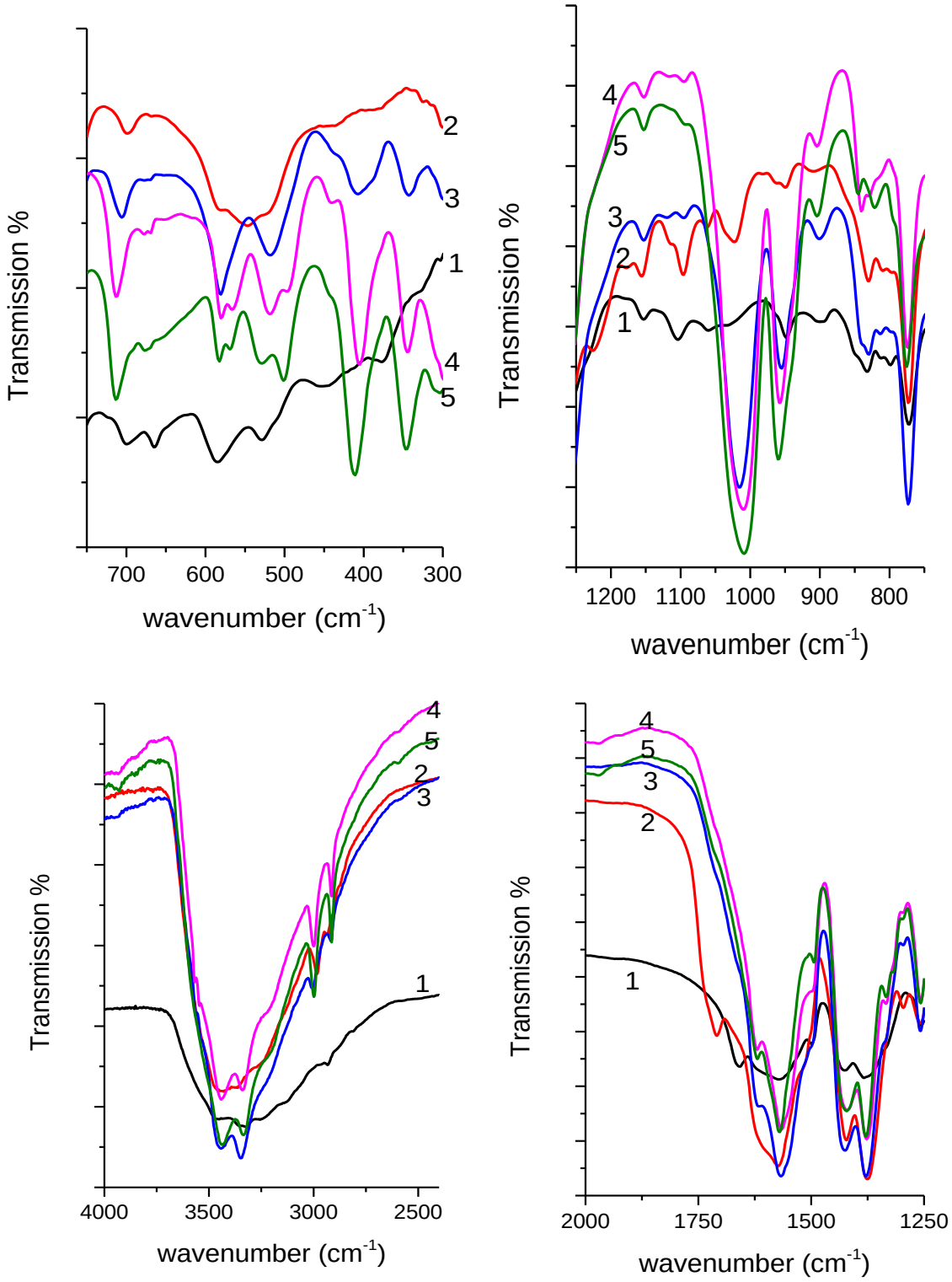

Figure A68 FTIR spectrum of 1) IRMOF-3, 2) IRMOF-3-EAA, 3) Eu-IRMOF-3-EAA, 4) Nd-IRMOF-3-EAA, and 5) Tb-IRMOF-3-EAA.

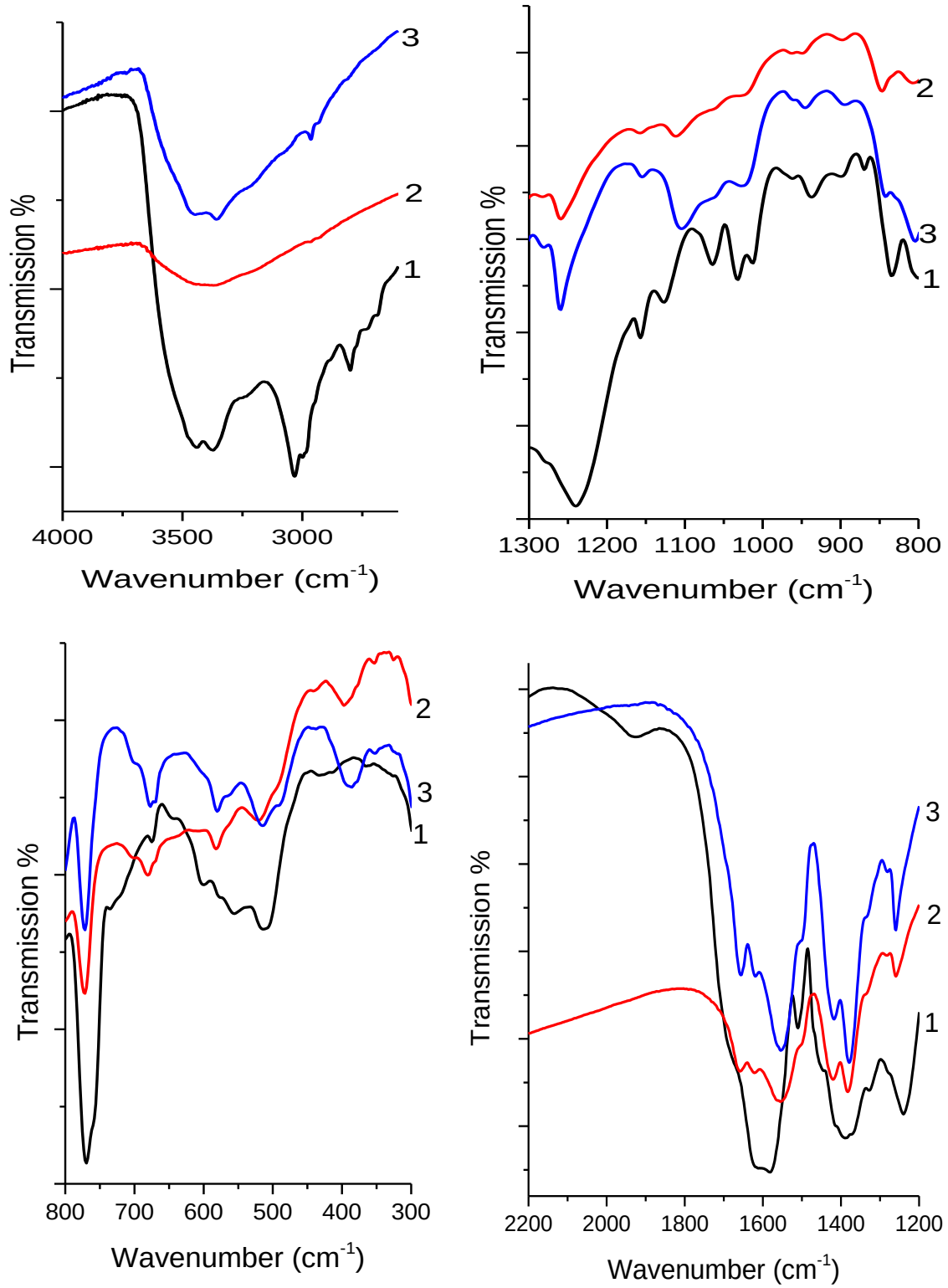

Figure A69 FTIR spectrum of 1) IRMOF-3-CA, 2) Nd-IRMOF-3-CA and 3) Eu-IRMOF-3-CA.

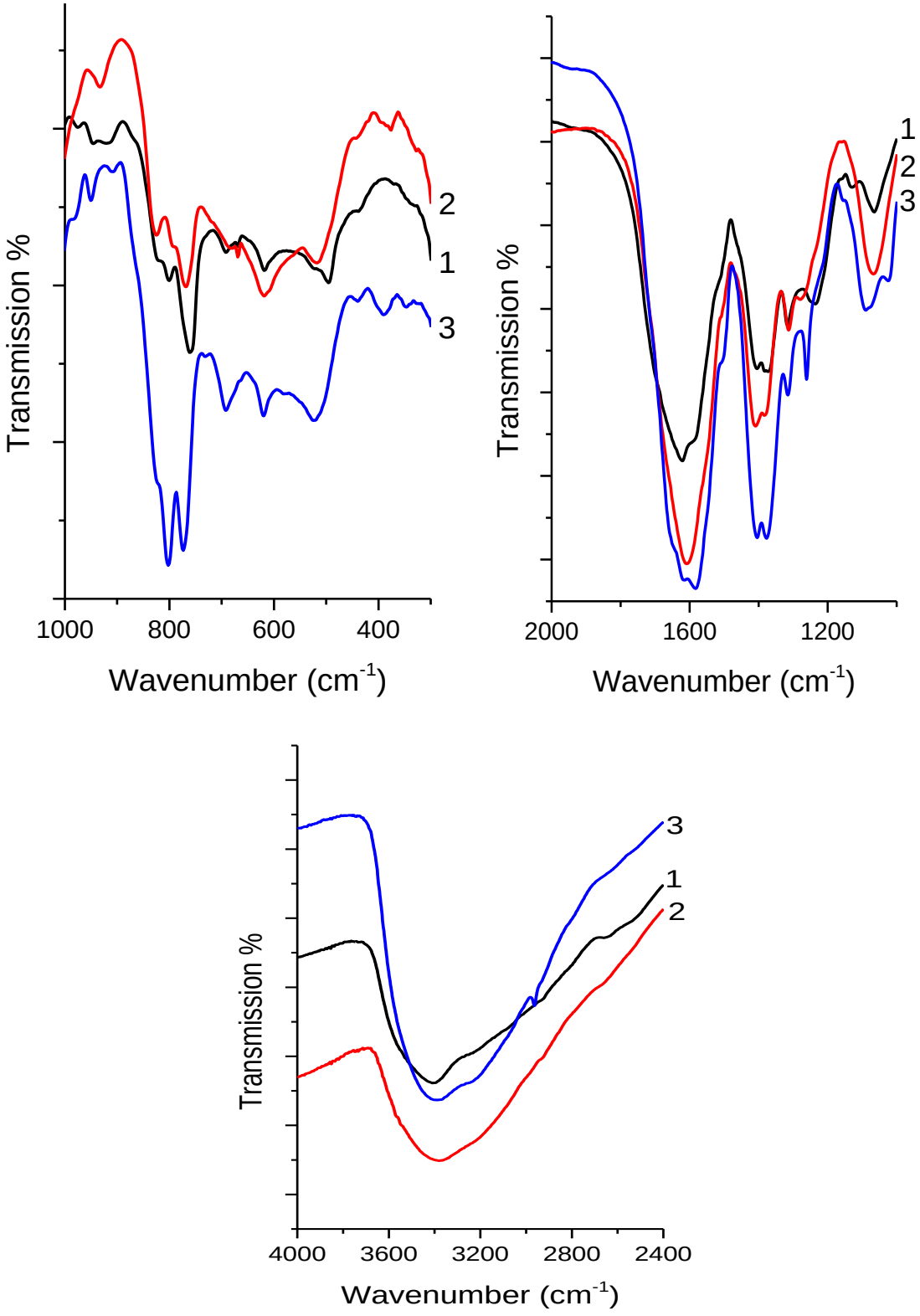

Figure A70 FTIR spectrum of 1) IRMOF-3-GL, 2) Nd-IRMOF-3-GL and 3) Eu-IRMOF-3-GL.

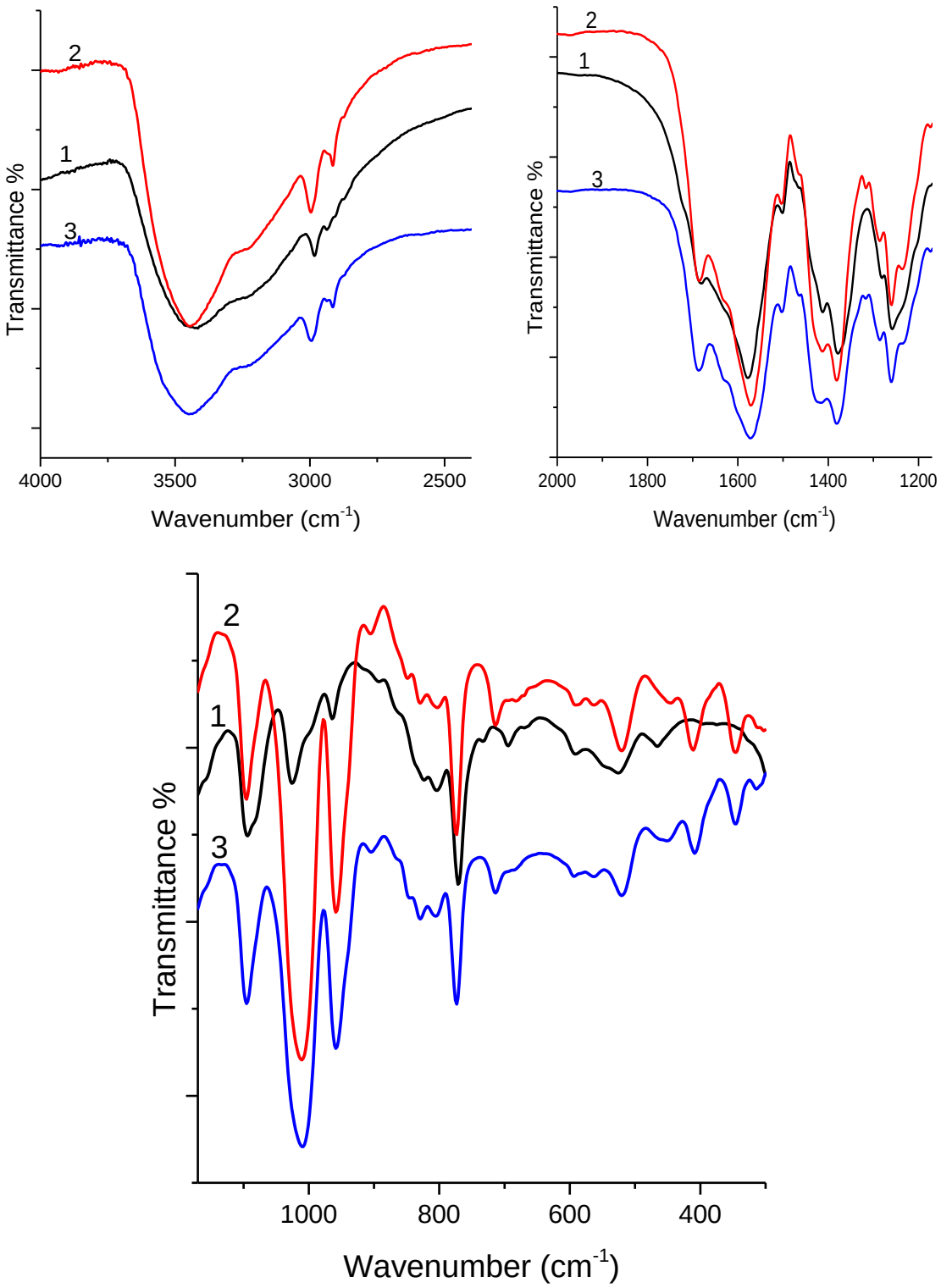

Figure A71 FTIR spectrum of 1) IRMOF-3-EM, 2) Eu-IRMOF-3-EM, and 3) Nd-IRMOF-3-EM.

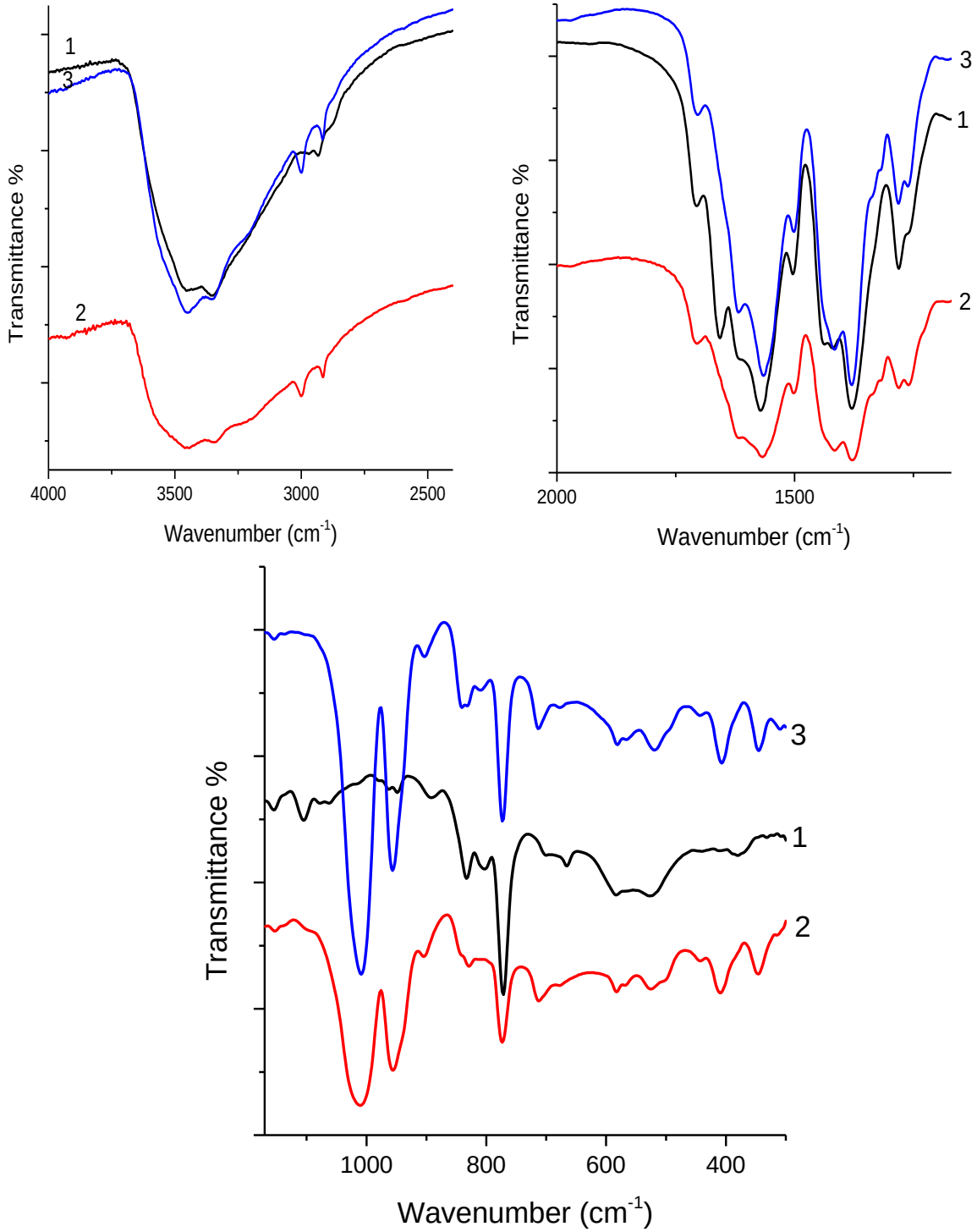

Figure A72 FTIR spectrum of 1) IRMOF-3-MVK, 2) Eu-IRMOF-3-MVK, 3) Nd-IRMOF-3-MVK.

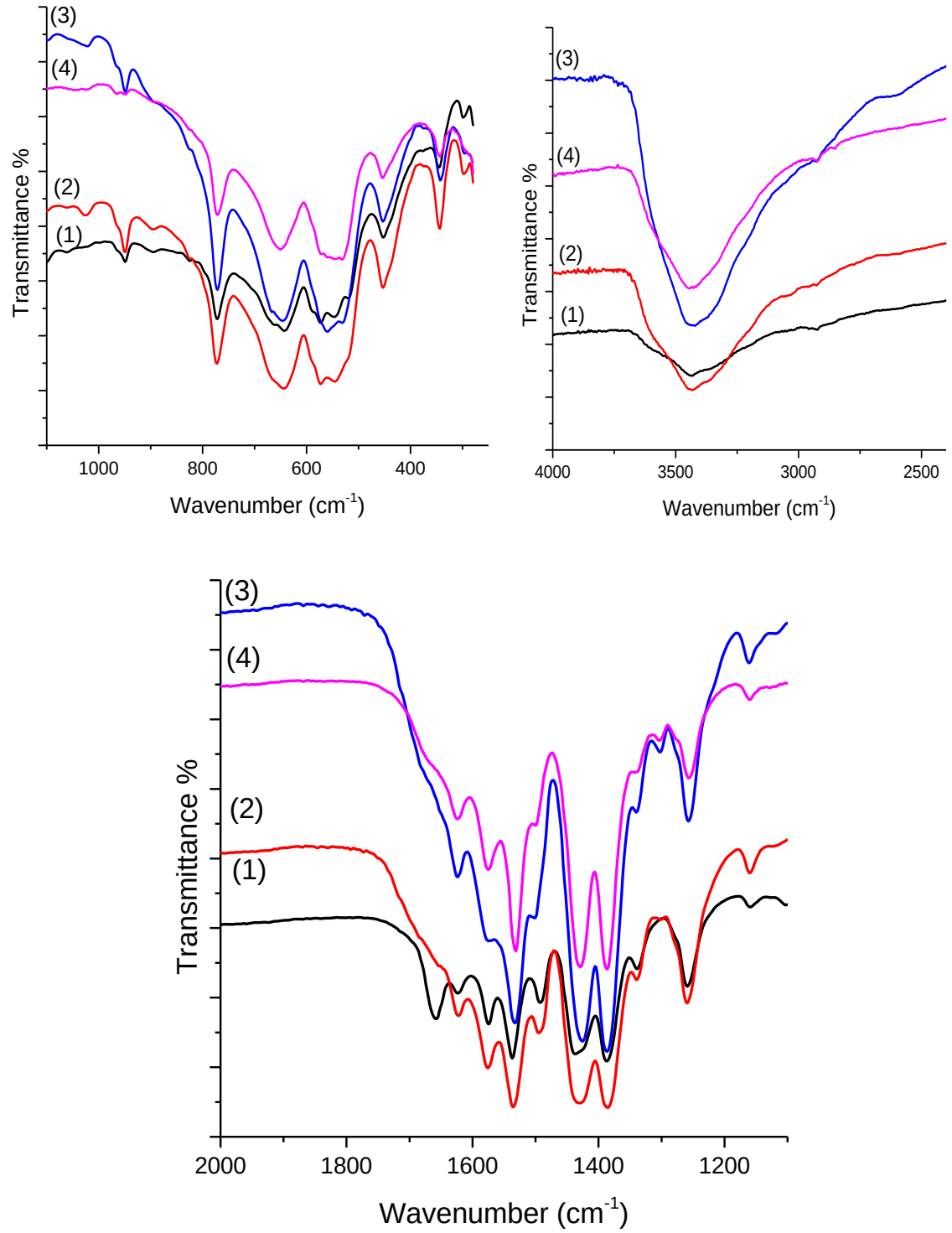

Figure A73 FTIR spectrum of 1) NH_2-MIL-125, 2) MIL-125-AC, and 3) Cr-MIL-125-AC, 4) Ag-MIL-125-AC.

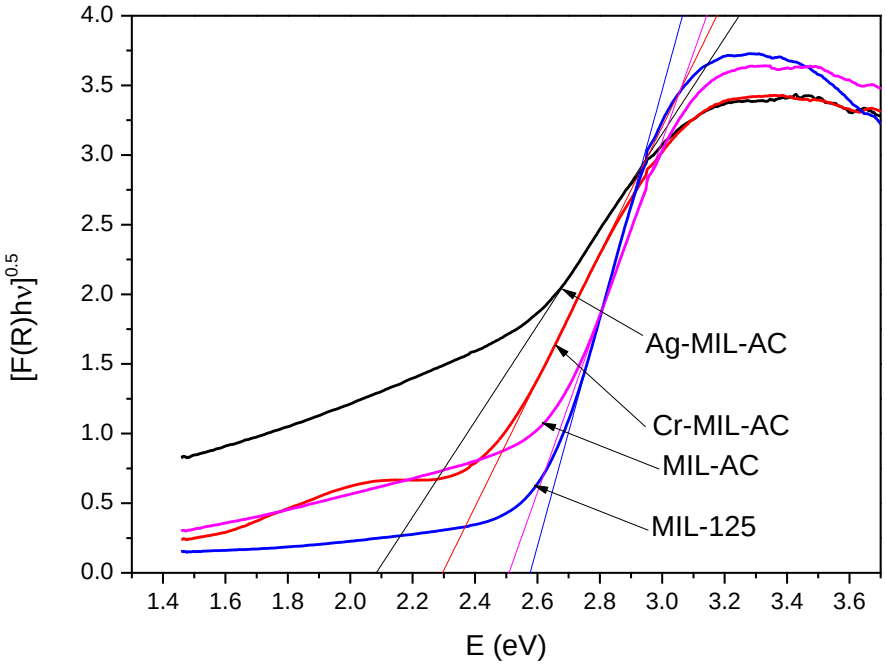

Figure A74 Tauc plot for the three photocatalysts: NH_2-MIL-125(MIL-125) ($E_g \approx 2.58$ eV), MIL-125-AC-2 (MIL-AC) ($E_g \approx 2.51$ eV), Cr-MIL-125-AC (Cr-MIL-AC) ($E_g \approx 2.21$ eV), Ag-MIL-125-AC (Ag-MIL-AC) ($E_g \approx 2.09$ eV).

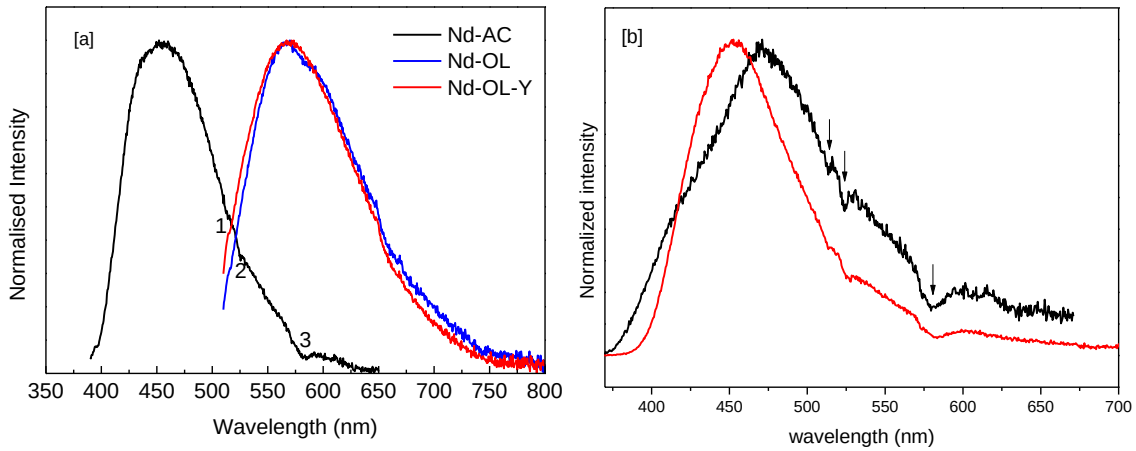

Figure A75 (a) Emission spectra of Nd-IRMOF-3-AC (Nd-AC), Nd-IRMOF-3-OL (Nd-OL) and Nd-Y-IRMOF-3-OL (Nd-Y-OL) MOFs excited at 370 nm (Nd-AC) and 490 nm (Nd-OL, Nd-Y-OL). The intra-4*f* ^{3} $^4I_{9/2} \rightarrow {}^4G_{7/2}$ (1), $^4I_{9/2} \rightarrow {}^2K_{13/2}$ (2), and $^4I_{9/2} \rightarrow {}^2G_{7/2}$ (3) self-absorptions are discerned. (b) Emission spectra of Nd-IRMOF-3-EAA (black) and Nd-IRMOF-3-EOC (red) excited at 340 nm. The $^4I_{9/2} \rightarrow {}^4G_{7/2}$, $^2K_{13/2}$, $^4G_{5/2}/{}^2G_{7/2}$ transitions observed at, respectively, 513, 524 and 580 nm are assigned to self-absorptions.

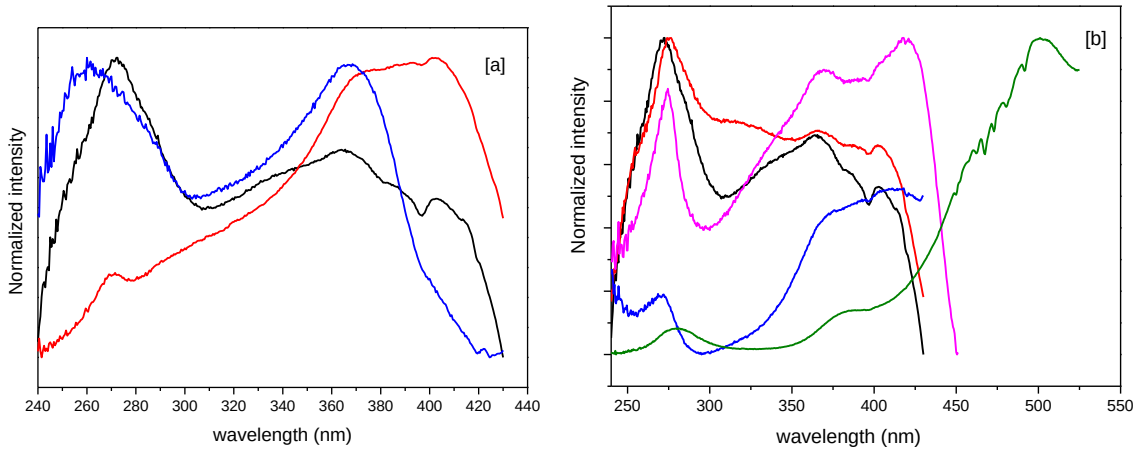

Figure A76 Room temperature (300K) excitation spectra of [a]IRMOF-3 (black) at 450 nm, IRMOF-3-EAA (red) at 470 nm and IRMOF-3-EOC (blue) at 465 nm, [b] IRMOF-3 (black) at 450 nm, IRMOF-3-GL (blue) at 475 nm, IRMOF-3-CA (red) at 460 nm, IRMOF-3-MVK (purple) at 471 nm and IRMOF-3-EM (green) at 545 nm.

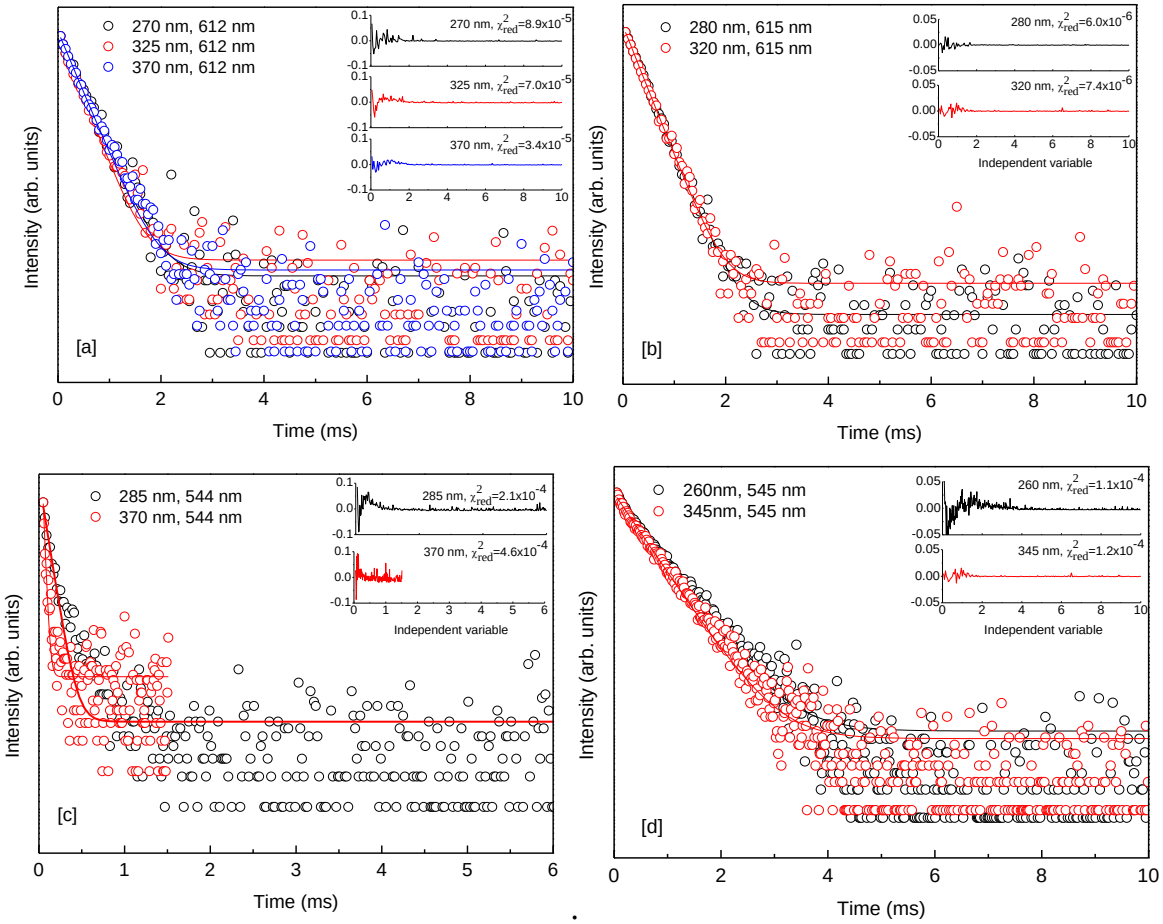

Figure A77 Room temperature (300K) emission decay curves of [a] Eu-IRMOF-3-EAA monitored at 612 nm under excitation within 270-370 nm, **[b]** Eu-IRMOF-3-EOC monitored at 615 nm under excitation at 280 and 320 nm**; [c]** Tb-IRMOF-3-EAA monitored at 544 nm under excitation at 285 and 370 nm; [d] Tb-IRMOF-3-EOC monitored at 545 nm under excitation at 280 and 345 nm.

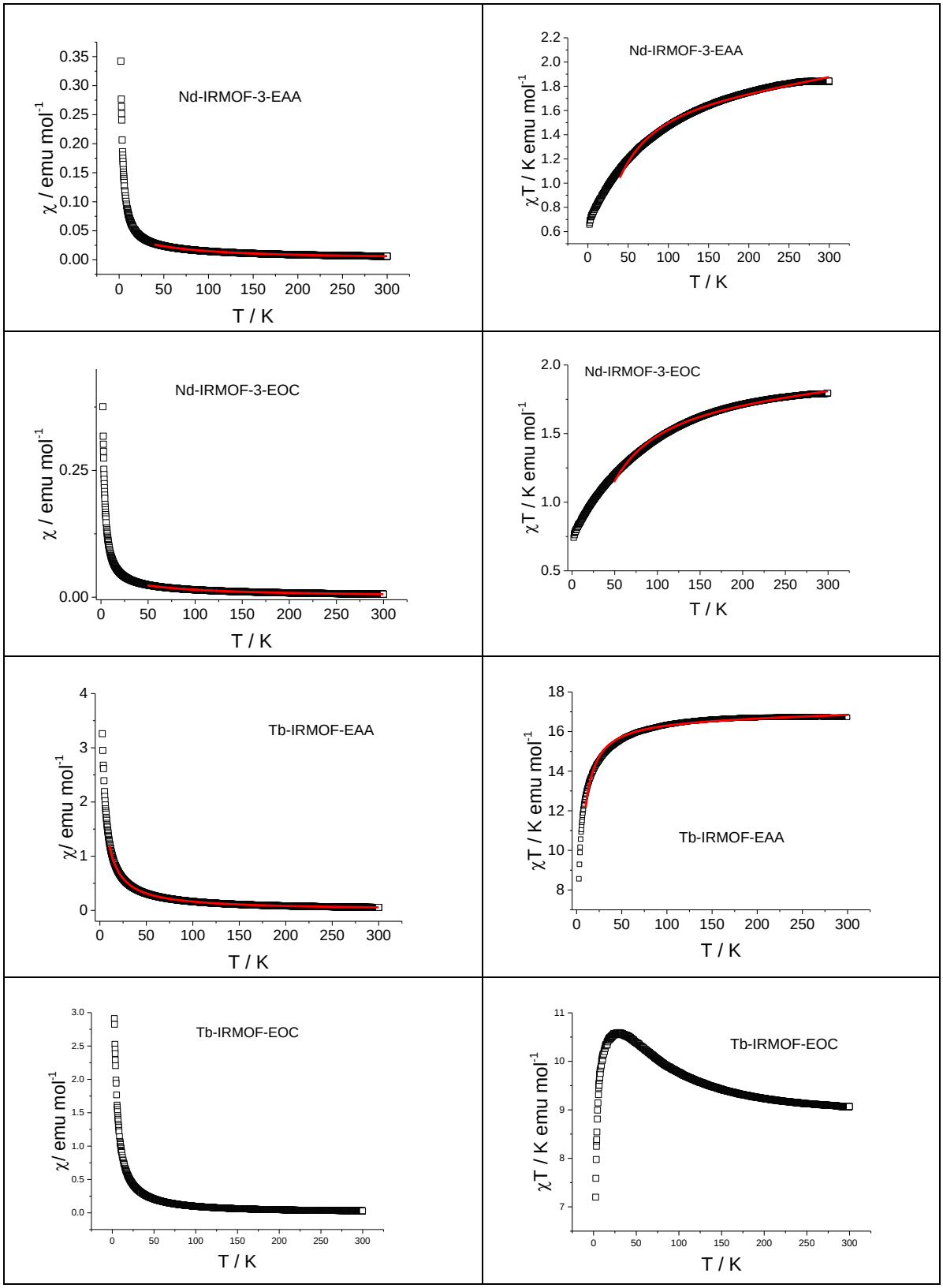

Figure A78 Temperature variation of the magnetic susceptibility of the Nd and Tb compounds. μThe full lines correspond to the best fit using the analytical expressions above. The data for the Eu analogues are given in the main text.

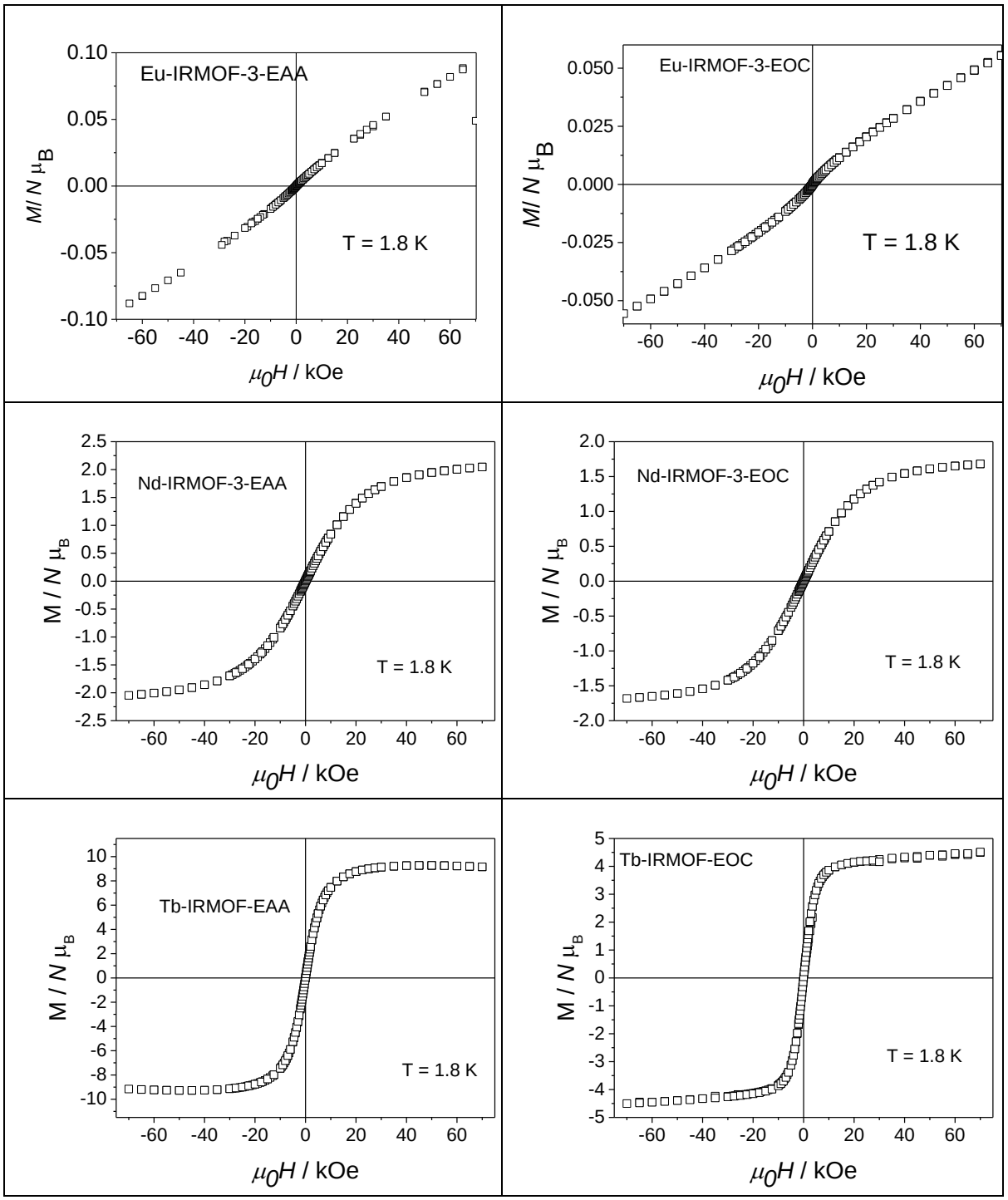

Figure A79 Temperature variation of the magnetic susceptibility and magnetization versus field curve at 1.8 K of the Eu, Nd and Tb compounds.

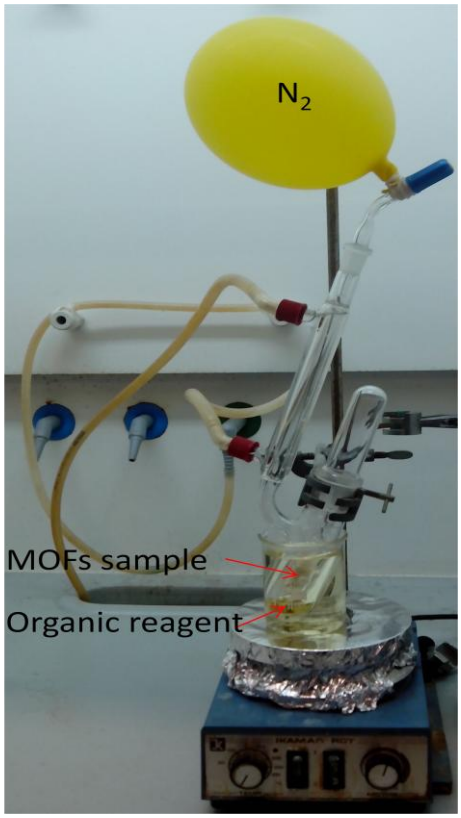

Figure A80 Vapor reactor at work

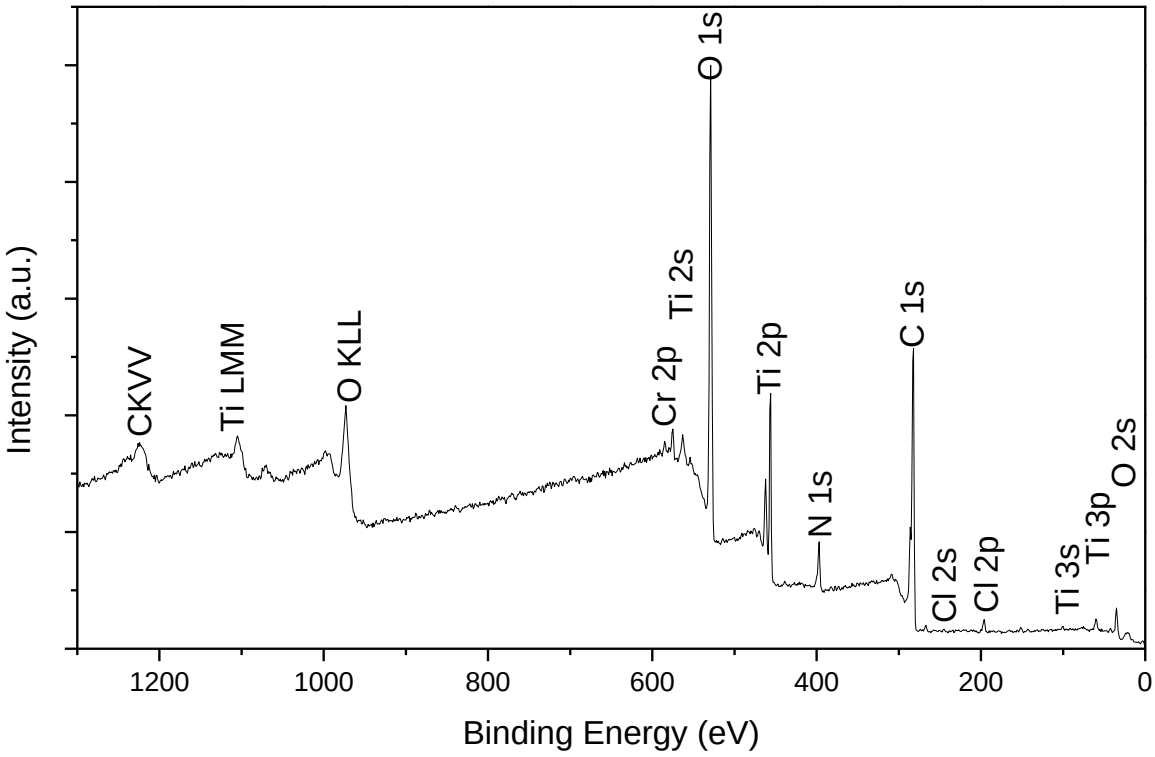

Figure A81 XPS survey spectrum of Cr-MIL-125-AC.

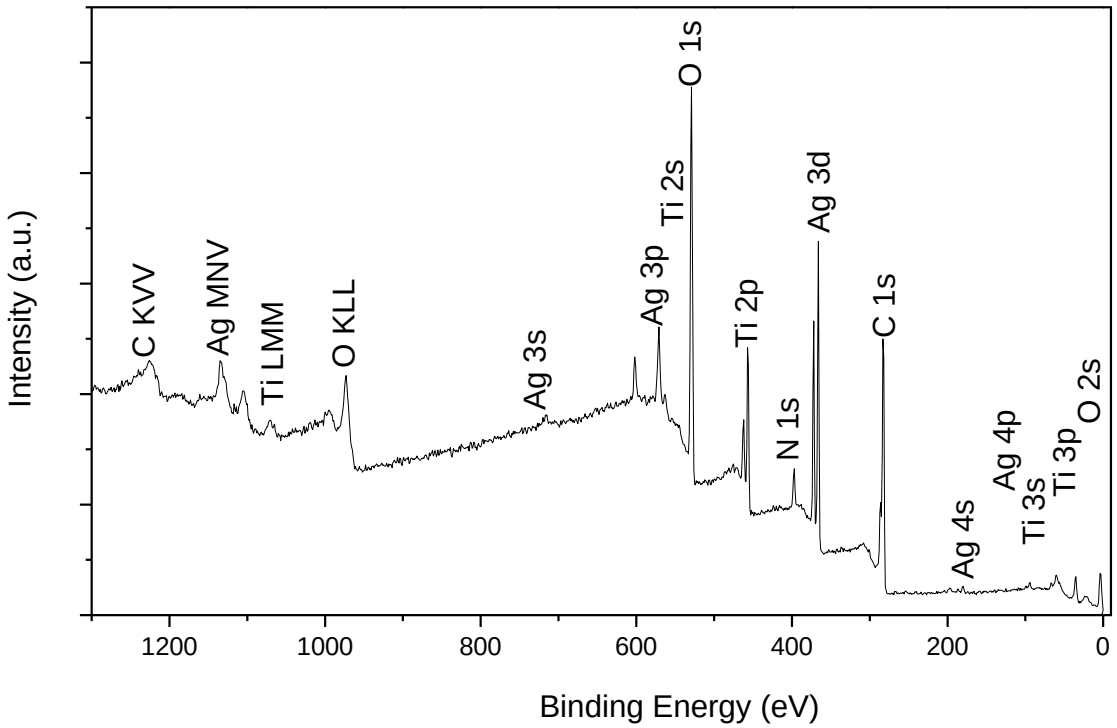

Figure A82 XPS survey spectrum of Ag-MIL-125-AC.

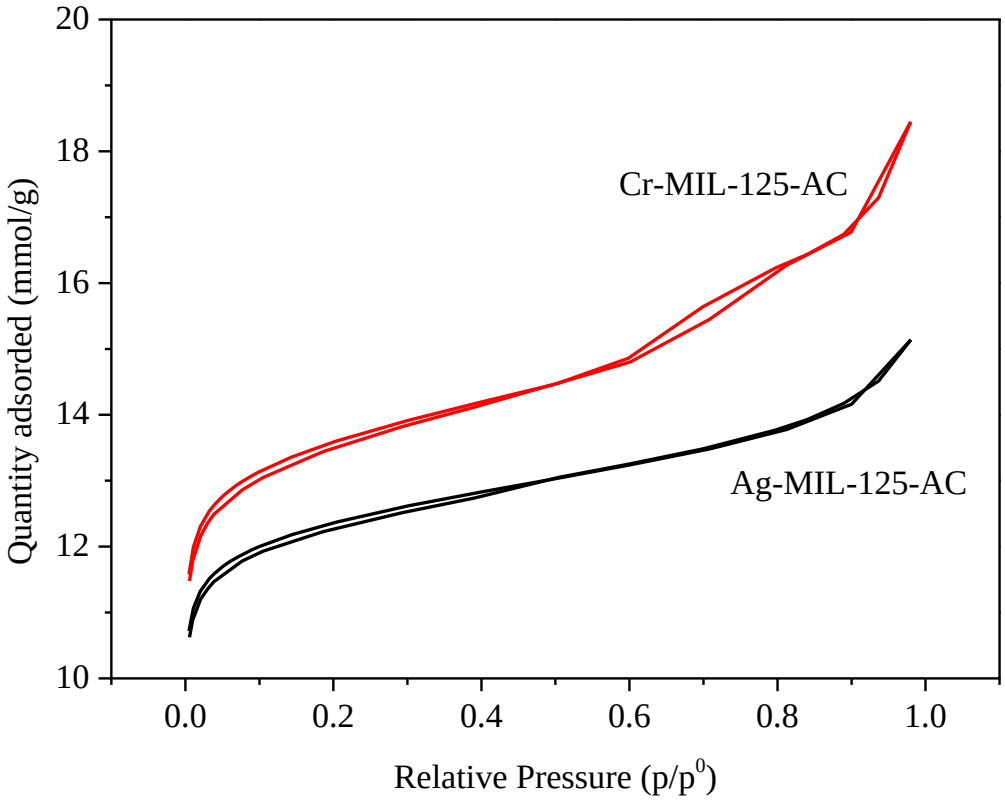

Figure A83 Nitrogen adsorption/desorption isotherms